

NATIONAL CENTER FOR EARTHQUAKE  
ENGINEERING RESEARCH

State University of New York at Buffalo

---

---

# CYCLIC UNDRAINED BEHAVIOR OF NONPLASTIC AND LOW PLASTICITY SILTS

by

A. J. Walker and H. E. Stewart

Department of Structural Engineering  
School of Civil and Environmental Engineering  
Cornell University  
Ithaca, New York 14853

Technical Report NCEER-89-0035

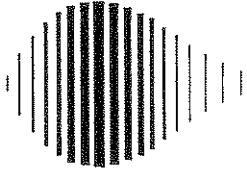
July 26, 1989

This research was conducted at Cornell University and was partially supported by the National Science Foundation under Grant No. ECE 86-07591.

## NOTICE

This report was prepared by Cornell University and as a result of research sponsored by the National Center for Earthquake Engineering Research (NCEER). Neither NCEER, associates of NCEER, its sponsors, Cornell University, or any person acting on their behalf:

- a. makes any warranty, express or implied, with respect to the use of any information, apparatus, method, or process disclosed in this report or that such use may not infringe upon privately owned rights; or
- b. assumes any liabilities of whatsoever kind with respect to the use of, or the damage resulting from the use of, any information, apparatus, method or process disclosed in this report.



---

CYCLIC UNDRAINED BEHAVIOR OF  
NONPLASTIC AND LOW PLASTICITY SILTS

by

A.J. Walker<sup>1</sup> and H.E. Stewart<sup>2</sup>

July 26, 1989

Technical Report NCEER-89-0035

NCEER Contract Number 88-1503

NSF Master Contract Number ECE 86-07591

and

NSF Grant Number R94433

- 1 Geotechnical Engineer, Golder Associates, Ltd., Ontario, Canada, formerly Graduate Research Assistant, School of Civil and Environmental Engineering, Cornell University
- 2 Assistant Professor, School of Civil and Environmental Engineering, Cornell University

NATIONAL CENTER FOR EARTHQUAKE ENGINEERING RESEARCH  
State University of New York at Buffalo  
Red Jacket Quadrangle, Buffalo, NY 14261

---



## PREFACE

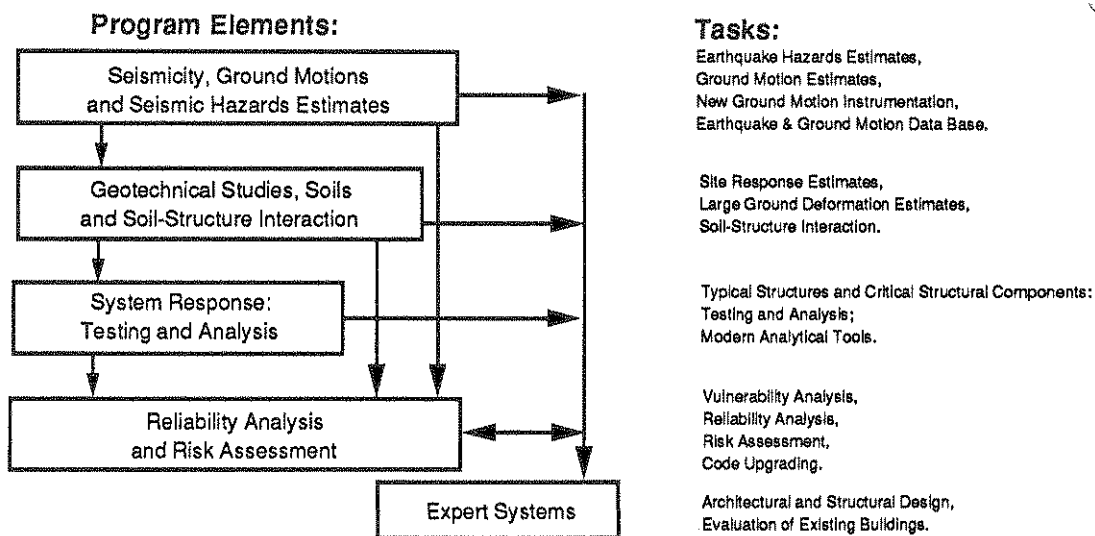
The National Center for Earthquake Engineering Research (NCEER) is devoted to the expansion and dissemination of knowledge about earthquakes, the improvement of earthquake-resistant design, and the implementation of seismic hazard mitigation procedures to minimize loss of lives and property. The emphasis is on structures and lifelines that are found in zones of moderate to high seismicity throughout the United States.

NCEER's research is being carried out in an integrated and coordinated manner following a structured program. The current research program comprises four main areas:

- Existing and New Structures
- Secondary and Protective Systems
- Lifeline Systems
- Disaster Research and Planning

This technical report pertains to Program 1, Existing and New Structures, and more specifically to geotechnical studies.

The long term goal of research in Existing and New Structures is to develop seismic hazard mitigation procedures through rational probabilistic risk assessment for damage or collapse of structures, mainly existing buildings, in regions of moderate to high seismicity. The work relies on improved definitions of seismicity and site response, experimental and analytical evaluations of systems response, and more accurate assessment of risk factors. This technology will be incorporated in expert systems tools and improved code formats for existing and new structures. Methods of retrofit will also be developed. When this work is completed, it should be possible to characterize and quantify societal impact of seismic risk in various geographical regions and large municipalities. Toward this goal, the program has been divided into five components, as shown in the figure below:



Geotechnical studies constitute one of the important areas of research in Existing and New Structures. Current research activities include the following:

1. Development of linear and nonlinear site response estimates.
2. Development of liquefaction and large ground deformation estimates.
3. Investigation of soil-structure interaction phenomena.
4. Development of computational methods.
5. Incorporation of local soil effects and soil-structure interaction into existing codes.

The ultimate goal of projects concerned with geotechnical studies is to develop methods of engineering estimation of large soil deformations, soil-structure interaction, and site response.

*This report contains a study of cyclic strain-controlled tests (resonant column and torsional shear) on clayey silt of various clay contents. The results show that the general dynamic response of silts is similar to that of sands. In addition, an extensive literature survey is presented on the subject of cyclic behavior of fine-grained soils.*

## ABSTRACT

This report describes dynamic testing carried out on plastic and non-plastic silts. The plastic silt was prepared by mixing nonplastic silt with controlled amounts of Kaolin clay. Testing was carried out using a quasi-static resonant column/torsional shear device, which has the capability of measuring dynamic properties over a wide range of strain amplitudes.

The main parameters investigated in this study were the effects of cyclic shear strain amplitude on the potential for pore pressure generation, and the variation of shear modulus and damping ratio, for different specimen plasticities. The dynamic tests consisted of a resonant column testing phase which was concluded at the initiation of excess pore pressure generation, followed by strain control torsional shear testing.

Results showed that the general dynamic response of the silts was similar, in some respects, to that of sands. In particular, pore pressure generation response with varying strain level was found to resemble closely that of a sand of similar relative density. This indicates that silt, despite having a grain size distribution which is outside the generally accepted boundaries for soils susceptible to liquefaction, has a potential for liquefaction very similar to that of sand. Increasing plasticity was found to reduce the silt's level of pore pressure response. This reduction, however, was not significant for plasticity indices of 5 or less.





## ACKNOWLEDGMENTS

This study was sponsored in part by a grant from the National Center for Earthquake Engineering. This support is appreciated greatly. The experimental portions were conducted in the Takeo Mogami Geotechnical Laboratory, which is supported partially through the generosity of Mr. P. Y. Hsu, and the School of Civil and Environmental Engineering at Cornell University. The support and assistance of Matthew F. Kleinmann with the instrumentation, and Paul Jones and Glen Darling of the machine shop is appreciated. The availability and assistance of V. P. Drnevich in equipment details is appreciated. A. K. Hussein, Graduate Research Assistant, provided invaluable assistance in reviewing several details and assisting with the experimental equipment and testing. K. J. Stewart and A. Avcişoy have done outstanding work in preparing the manuscript and drafting the figures.

The overall support for this program by K. Jacob at Lamont Geological Observatory and P. Gergely at Cornell University is deeply appreciated and acknowledged.



## TABLE OF CONTENTS

SECTION	TITLE	PAGE
<b>1</b>	<b>INTRODUCTION</b> .....	1-1
<b>2</b>	<b>LITERATURE REVIEW</b> .....	2-1
2.1	Introduction .....	2-1
2.2	Cyclic Triaxial Testing .....	2-3
2.2.1	Stress Conditions .....	2-3
2.2.2	Cyclic Strength Determination .....	2-7
2.2.3	Testing Problems .....	2-9
2.3	Liquefaction .....	2-11
2.3.1	Definitions of Liquefaction .....	2-11
2.3.2	Factors Affecting Liquefaction Potential .....	2-17
2.3.2.1	Soil Type .....	2-17
2.3.2.2	Soil State .....	2-20
2.3.2.3	Threshold Shear Strain .....	2-21
2.3.2.4	Testing Techniques .....	2-25
2.3.3	Liquefaction Failure Mechanism .....	2-26
2.3.4	Liquefaction Pore Pressure Models .....	2-31
2.4	Resonant Column Testing .....	2-35
2.4.1	Introduction .....	2-35
2.4.2	Types of Resonant Column Systems .....	2-38
2.4.3	Shear Modulus and Damping Ratio Determination .....	2-40
2.5	Cyclic Torsional Testing .....	2-45
2.5.1	Introduction .....	2-45
2.5.2	Stress States .....	2-46
2.5.3	Types of Torsional Shear Systems .....	2-49
2.5.4	Liquefaction by Torsional Shear Device .....	2-52
2.6	Liquefaction of Fine-Grained Soils .....	2-58
2.6.1	Introduction .....	2-58
2.6.2	Stress-Strain Behavior of Clay, Silt, and Sand .....	2-59
2.6.3	Dynamic Properties of Clays .....	2-64
2.6.4	Dynamic Properties of Silts .....	2-69
2.7	Conclusions .....	2-77
<b>3</b>	<b>EXPERIMENTAL PROGRAM</b> .....	3-1
3.1	Test Apparatus .....	3-1
3.1.1	Resonant Column System .....	3-4
3.1.2	Torsional Shear System .....	3-6
3.2	Material Properties .....	3-10
3.2.1	Plasticity Control .....	3-12
3.2.2	Specimen Preparation .....	3-15
3.3	Testing Procedures .....	3-16
3.4	Summary .....	3-18

TABLE OF CONTENTS (Cont'd)

SECTION	TITLE	PAGE
4	<b>TEST RESULTS</b> .....	4-1
4.1	Introduction .....	4-1
4.1.1	Test Conditions .....	4-1
4.1.2	Normalization Procedure .....	4-3
4.2	Resonant Column and Torsional Shear Results .....	4-8
4.2.1	Effect of Cyclic Shear Strain Level .....	4-8
4.2.2	Effect of Number of Loading Cycles .....	4-12
4.2.3	Effects of Plasticity .....	4-14
4.3	Comparisons with Sand and Clay .....	4-19
4.4	Summary and Conclusions .....	4-23
5	<b>CONCLUSIONS AND RECOMMENDATIONS</b> .....	5-1
5.1	General Conclusions .....	5-1
5.2	Equipment Recommendations .....	5-2
5.3	Areas for Further Research .....	5-3
6	<b>NOTATION</b> .....	6-1
7	<b>REFERENCES</b> .....	7-1
<b>APPENDIX A</b>	<b>TRANSDUCERS</b> .....	A-1
A.1	Introduction .....	A-1
A.2	Calibration of Kaman Transducers .....	A-2
A.3	Torque Transducer Calibration .....	A-11
<b>APPENDIX B</b>	<b>GENERAL OPERATIONS</b> .....	B-1
B.1	Solid Specimen Preparation .....	B-1
B.2	Apparatus Assembly .....	B-6
B.2.1	General Setup .....	B-6
B.2.2	Assembly Procedure .....	B-6
B.3	Saturation Procedure .....	B-11
B.3.1	Setup .....	B-11
B.3.2	B-Determination .....	B-12
B.4	Specimen Consolidation .....	B-14
B.5	Pressure Test .....	B-15
B.6	Apparatus Disassembly Procedure .....	B-15
<b>APPENDIX C</b>	<b>RESONANT COLUMN OPERATION</b> .....	C-1
C.1	Introduction .....	C-1
C.2	Testing Procedure .....	C-2
C.3	Data Reduction .....	C-4

TABLE OF CONTENTS (Cont'd)

SECTION	TITLE	PAGE
APPENDIX D	TORSIONAL SHEAR TESTING .....	D-1
D.1	Introduction .....	D-1
D.2	Data Retrieval .....	D-2
D.3	Stress and Strain Distributions .....	D-7
D.4	Determination of Shear Modulus and Damping Ratio .....	D-10



## LIST OF FIGURES

FIGURE	TITLE	PAGE
2-1	Shearing Strain Amplitude Capabilities of Laboratory Apparatus .....	2-3
2-2	Idealized Stress Conditions for Element of Soil Below Ground Surface During an Earthquake .....	2-4
2-3	Stress Components in Cyclic Triaxial Test Specimens ...	2-5
2-4	Effect of Stress Reversal on Failure Mode .....	2-6
2-5	Typical Results of Dynamic Triaxial Test .....	2-6
2-6	Stress Ratio versus Number of Cycles to Initial Liquefaction .....	2-8
2-7	Axial Strain After Initial Liquefaction for Pulsating Load Tests at Three Densities .....	2-8
2-8	Stress-Controlled Cyclic Triaxial Tests of Saturated Crystal Silica Sand .....	2-10
2-9	Compilation Summary of Pore Pressure Buildup Data .....	2-10
2-10	Redistribution of Relative Density in Cyclic Triaxial Specimen .....	2-11
2-11	Liquefaction Due to Monotonic or Cyclic Loading .....	2-13
2-12	Plot of Data for One Undrained Test on Contractive Specimen to Determine Steady-State Strength .....	2-13
2-13	Expanded Record and Results of Cyclic Triaxial Test ...	2-15
2-14	State Diagram Showing Liquefaction Potential Based on Undrained Tests of Saturated Sands .....	2-16
2-15	Changes in Fabric During Cyclic Loading .....	2-18
2-16	Limits in the Gradation Curves Separating Liquefiable and Unliquefiable Soils .....	2-18
2-17	Steady-State Lines for Sands .....	2-19
2-18	Generalized Relationship Between Peak Cyclic Stress and Number of Cycles to Cause Cyclic Mobility Failure .....	2-21
2-19	Influence of Initial Principal Stress Ratio on Stresses Causing Pore Pressure Ratio of 100% in Simple Shear Tests .....	2-23
2-20	Relationship Between Cyclic Strength and OCR Value ...	2-23
2-21	Excess Pore Pressures After Ten Loading Cycles, Cyclic Triaxial Strain-Controlled Tests .....	2-24
2-22	Cyclic Stress Ratio versus number of Cycles for Different Compaction Procedures .....	2-27
2-23	Undrained Stress Paths Characterizing Two States .....	2-28
2-24	Sands Beneath Impermeable Soils .....	2-29
2-25	Example of a Potential Situation for Mechanism B Failure .....	2-30

LIST OF ILLUSTRATIONS (Cont'd)

FIGURE	TITLE	PAGE
2-26	Relationship Between Cyclic Stress Ratio and Number of Cycles Required to Cause Liquefaction for Simple Shear Tests on Medium Sand at Different Relative Densities .....	2-33
2-27	Normalized Curves from Pore Pressure Buildup Equation .....	2-35
2-28	Liquefaction Due to Cyclic Loading and Cyclic Mobility Due to Cyclic Loading .....	2-36
2-29	Limited Liquefaction Due to Cyclic Loading .....	2-36
2-30	Characteristic Behavior of Saturated Sand Under Undrained Monotonic Loading .....	2-37
2-31	Common Resonant Column Boundary Conditions .....	2-39
2-32	Schematic of Resonant Column End Conditions .....	2-39
2-33	Summary of Normalized Shear Modulus Variation with Shearing Strain .....	2-43
2-34	Summary of Normalized Damping Ratio Variation with Shearing Strain .....	2-43
2-35	Summary of Excess Pore Water Pressure Buildup versus Shear Strain Amplitude .....	2-44
2-36	Stress Conditions in Strain-Controlled Test .....	2-47
2-37	Mohr's Diagram Representation of Stresses .....	2-48
2-38	Torsional Simple Shear Device, Short Specimen .....	2-50
2-39	Torsional Simple Shear Device, Long Specimen .....	2-51
2-40	Typical Liquefaction Data for Low B and High B Values .....	2-53
2-41	Results of ICT- and ACT-Tests .....	2-54
2-42	Pore Pressure Buildup With and Without Initial Shear .....	2-55
2-43	Typical Cyclic Torsional Test Data .....	2-56
2-44	Number of Cycles, $n_c$ , of Cyclic Shear Strain, $\gamma_{cy}$ , Needed to Trigger Liquefaction Flow Failure .....	2-58
2-45	General Stress-Strain Behavior of Clays .....	2-60
2-46	Cyclic Loading of Contractive Sand and Clay Specimens Leads to Failure when Pore Pressures Increase .....	2-60
2-47	A Comparison of the State Paths of Contractive Sand and Clay Specimens Subjected to Cyclic Loading .....	2-62
2-48	General Behavior of Contractive Soils Under Cyclic Loading .....	2-62
2-49	Critical Level of Repeated Loading (CLRL) for Undrained Tests of Contractive Soils .....	2-64



LIST OF ILLUSTRATIONS (Cont'd)

FIGURE	TITLE	PAGE
2-50	Relationship Between Modulus Increase Rate and Plasticity Index .....	2-69
2-51	$G/G_{max}$ versus $\log \tau$ Relationships for Normally Consolidated Specimens .....	2-70
2-52	Shear Strain versus Plasticity Index Relationships for Different Modulus Ratios .....	2-71
2-53	Strain-Dependent Changes of Damping Ratio for Normally Consolidated Specimens .....	2-71
2-54	Influence of Shearing Strain Amplitude, Relative Density, and Confining Pressure on Dynamic Response .....	2-73
2-55	Influence of Number of Loading Cycles on Dynamic Response .....	2-74
2-56	Degradation of Shear Modulus Ratio .....	2-76
2-57	Comparison of Shear Moduli Measured by Torsional Shear and Resonant Column Tests .....	2-76
2-58	Relationship Between Cyclic Strength and Plasticity Index of Tailings .....	2-78
3-1	Quasi-Static Torsional Shear/Resonant Column Device ...	3-2
3-2	Wiring Schematic for Hardin Resonant Column .....	3-5
3-3	Definition of Secant Modulus, $G$ , and Hysteretic Damping Ratio, $\lambda$ .....	3-10
3-4	Grain Size Distributions for Silt Testing .....	3-11
3-5	Energy/Unit Weight versus Energy .....	3-13
3-6	Liquid Limit versus Percentage Clay .....	3-14
3-7	Plasticity Index versus Liquid Limit for Various Silt/Clay Mixes .....	3-14
4-1	Stress Paths for an Isotropic Undrained Monotonic Torsional Shear Test .....	4-5
4-2	Shear Stresses versus Shear Strain for a Monotonic Torsional Shear Test .....	4-6
4-3	Effective Stress Path and Failure Envelope for a Monotonic Torsional Shear Test on Silt .....	4-6
4-4	Pore Pressure Change versus Shear Strain for a Monotonic Torsional Shear Test .....	4-7
4-5	Pore Pressure Parameter $A$ versus Shear Strain for a Monotonic Torsional Shear Test .....	4-7
4-6	Normalized Shear Strain versus Normalized Shear Modulus for 0% Clay .....	4-9
4-7	Normalized Shear Strain versus Pore Pressure Ratio for 0% Clay .....	4-10

LIST OF ILLUSTRATIONS (Cont'd)

FIGURE	TITLE	PAGE
4-8	Normalized Damping Ratio versus Normalized Shear Strain for 0% Clay .....	4-11
4-9	Cyclic Shear Stress versus Cyclic Shear Strain for 0% Clay and Various Levels of Pore Pressure Ratio .....	4-11
4-10	Number of Cycles versus Shear Modulus for 0% Clay and Different Levels of $\gamma_{cy}$ .....	4-13
4-11	Number of Cycles versus Pore Pressure Ratio for 0% Clay and Different Levels of $\gamma_{cy}$ .....	4-13
4-12	Number of Cycles versus Damping Ratio for 0% Clay and Different Levels of $\gamma_{cy}$ .....	4-15
4-13	Normalized Shear Modulus versus Normalized Shear Strain for One Cycle of Torsional Shear Loading and Clay Fractions of 0%, 10%, and 20% .....	4-15
4-14	Pore Pressure Ratio versus Normalized Shear Strain for One Cycle of Torsional Shear Loading and Clay Fractions of 0%, 10%, and 20% .....	4-16
4-15	Normalized Damping Ratio versus Normalized Shear Strain for One Cycle of Torsional Shear Loading and Clay Fractions of 0%, 10%, and 20% .....	4-17
4-16	Shear Modulus versus Number of Loading Cycles for $\gamma_{cy} = 0.17\%$ and Clay Fractions of 0%, 10% and 20% ....	4-18
4-17	Pore Pressure Ratio versus Number of Load Cycles for $\gamma_{cy} = 0.17\%$ and Clay Fractions of 0%, 10% and 20% ....	4-18
4-18	Damping Ratio versus Number of Load Cycles for $\gamma_{cy} = 0.17\%$ and Clay Fractions of 0%, 10% and 20% .....	4-20
4-19	Shear Modulus versus Shear Strain for a Range of Materials .....	4-20
4-20	Pore Pressure Ratio versus Cyclic Shear Strain for Sand, Clay and Silt .....	4-21
4-21	Damping Ratio versus Shear Strain; Ranges for Sand, Clay, and Silt .....	4-21
A-1	Example of Linear Range Rotation Transducer Calibration .....	A-9
A-2	Example of Nonlinear Range Rotation Transducer Calibration .....	A-9
A-3	Theoretical versus Actual Torque Transducer Readings ..	A-10
A-4	Theoretical versus Corrected Torque Transducer Readings for 0.8 Correction Factor .....	A-10
B-1	Sample Preparation and Test Data .....	B-4
C-1	Example RC6-0987 Output .....	C-5

LIST OF ILLUSTRATIONS (Cont'd)

FIGURE	TITLE	PAGE
D-1	Axial Load versus Time .....	D-4
D-2	Axial Deformation versus Time .....	D-4
D-3	Torque versus Time .....	D-5
D-4	Rotation versus Time .....	D-5
D-5	Torque versus Rotation .....	D-6
D-6	Effective Pressure versus Time .....	D-6
D-7	Stress versus Strain .....	D-7
D-8	Shearing Deformation in a Test Specimen .....	D-8
D-9	Definition of Equivalent Hysteretic Shear Modulus and Damping Ratio .....	D-11
D-10	Measurements of Hysteresis Loop .....	D-12



## LIST OF TABLES

TABLE	TITLE	PAGE
2-1	Differences Between Liquefaction and Cyclic Mobility ..	2-22
2-2	Threshold Shear Strain, $\gamma_t$ , for Dry and Saturated Sands .....	2-24
2-3	Summary of Failure Mechanisms .....	2-31
2-4	Earthquake Magnitude and Corresponding Values of $N_{eq}$ and Shaking Duration.....	2-33
2-5	Relationships Between Torsional Moments and Average Shear Stress .....	2-48
3-1	Stress and Deformation Limits of the Apparatus .....	3-8
3-2	Properties of PGS 120 Silt .....	3-12
3-3	Plasticity Properties of Mixes .....	3-16
4-1	Test Summary .....	4-2
4-2	Summary of Cyclic Loading Results .....	4-22
B-1	Additional Axial Load Requirements .....	B-14
D-1	Comparison Between Methods of Damping Ratio Calculation .....	D-12



## SECTION 1 INTRODUCTION

Ground liquefaction during earthquakes can cause major damage to buildings and earth structures, as well as failures in natural slopes. Seed and Idriss [1967] described the 1964 Niigata, Japan earthquake, which caused liquefaction of the sand underlying foundations, resulting in severe building settlement and tilting. Study of ground response during earthquakes has concentrated on the dynamic behavior and liquefaction potential of clean granular materials. To a lesser extent, clay soils have been investigated, with the emphasis on permanent strain accumulation due to long-term dynamic loading. Silts have been studied to an even lesser degree, as they are considered on the borderline between liquefiable and nonliquefiable soils. However, Shen, et al. [1985] describe the 1976 Tangshan, China earthquake, where severe building damage occurred because of liquefaction in silt. The behavior of silts during undrained cyclic loading has not been investigated thoroughly.

The goal of this research was to characterize the dynamic behavior of plastic and nonplastic silts. Two basic silts, a nonplastic silt and a low plasticity silt, were used as control materials. The low plasticity silt was prepared by mixing the nonplastic silt with controlled amounts of Kaolin clay, which resulted in a predominantly silt-sized mixture having low plasticity properties. By combining fractions of these two basic silts, specimens having controlled plasticity properties were tested. Descriptions of several dynamic tests, the basic definition of liquefaction, and information available on the dynamic testing of silt are presented in Section 2.

A quasi-static torsional simple shear/resonant column device was used to investigate the dynamic properties of the silts. The device is capable of testing both solid and hollow samples in either strain or stress control, and under either monotonic or cyclic loading. The resonance oscillator can be operated independently from the torsional

loading system, enabling measurements of shear modulus and damping throughout testing. A full description of the equipment and the experimental program is presented in Section 3.

The main parameters investigated in this study were the effects of cyclic shear strain amplitude on the potential for pore pressure generation for various plasticity properties. In addition, dynamic shear modulus and damping were determined for the same sample variables. Presentation and analysis of results are outlined in Section 4. Conclusions and recommendations for future study are discussed in Section 5.



## SECTION 2 LITERATURE REVIEW

### 2.1 INTRODUCTION

Many problems in engineering require a knowledge of dynamic soil properties. These problems span a wide range of situations and amplitudes of motion. At one end are small amplitude machine vibrations and at the other, earthquake or blast motions. Woods [1978] lists the major soil properties and characteristics needed to predict ground motions from a given dynamic loading. They include:

- a) dynamic moduli - Young's modulus, shear modulus, bulk modulus, and constrained modulus,
- b) Poisson's ratio,
- c) damping and attenuation,
- d) liquefaction parameters - cyclic shearing stress ratio, cyclic deformation, and pore pressure response, and
- e) shearing strength in terms of strain rate effects.

A variety of laboratory and field measuring techniques are required to determine these properties. Some of these properties are best measured in the field, others in the laboratory, and some can be measured in both the laboratory and with in-situ techniques.

Ideally, the specimen used for laboratory testing should behave as an element of soil in the field would during dynamic excitation. This goal is very difficult, and in some cases, impossible to achieve. In particular, laboratory machines always introduce boundary effects from the platens and membranes, which do not occur in-situ [Saada and Townsend, 1981]. However, laboratory parametric studies are necessary for a better understanding of dynamic soil behavior, and most of these studies would be too costly or difficult to do in the field.

A major problem with dynamic laboratory testing is that it is difficult to establish general relationships, due to the many sample

variables involved. Factors which should be accounted for include grain size distribution, relative density, state of stress, stress history, fabric, aging, and anisotropy. Additionally, for cohesive soils, chemical and plasticity properties should be considered. For both cohesive and cohesionless soils, "undisturbed" sampling is very difficult to achieve. DeAlba, et al. [1984] report that the liquefaction resistance of a given deposit is highly dependent on its stress history, and that stress history effects are largely removed by current sampling techniques. Thus, most testing to date has been done with reconstituted samples, where the effect of varying the sample properties can be evaluated systematically.

Several testing devices have been developed to study dynamic properties over a wide strain range. The Hardin [1970] resonant column can be used for strains between 0.0001% to 0.01%. For larger strains (0.01% to 10%), equipment such as cyclic triaxial, simple shear, or torsional shear devices must be used. Resonant columns typically operate at high frequencies (100+ Hz), while the larger strain cyclic tests generally operate at lower frequencies (0.001 to 1 Hz). This disparity of operating frequencies is due to pore pressure generation and liquefaction that occurs at higher strains. Longer cycle times allow for pore pressure equalization within the sample, as well as close study of the effects of the number of cycles.

The laboratory techniques available for testing are summarized in Figure 2-1. The strain ranges suggested by this figure are potential levels only. For example, a resonant column operating at 1% strain is not of any practical benefit, as an undrained specimen could fail immediately, due to the high loading frequency.

The aim of this review is to cover briefly the development of cyclic testing and liquefaction studies. In particular, resonant column and cyclic torsional testing are reviewed in some detail. Finally, information relating to silt and silty clay behavior are discussed.

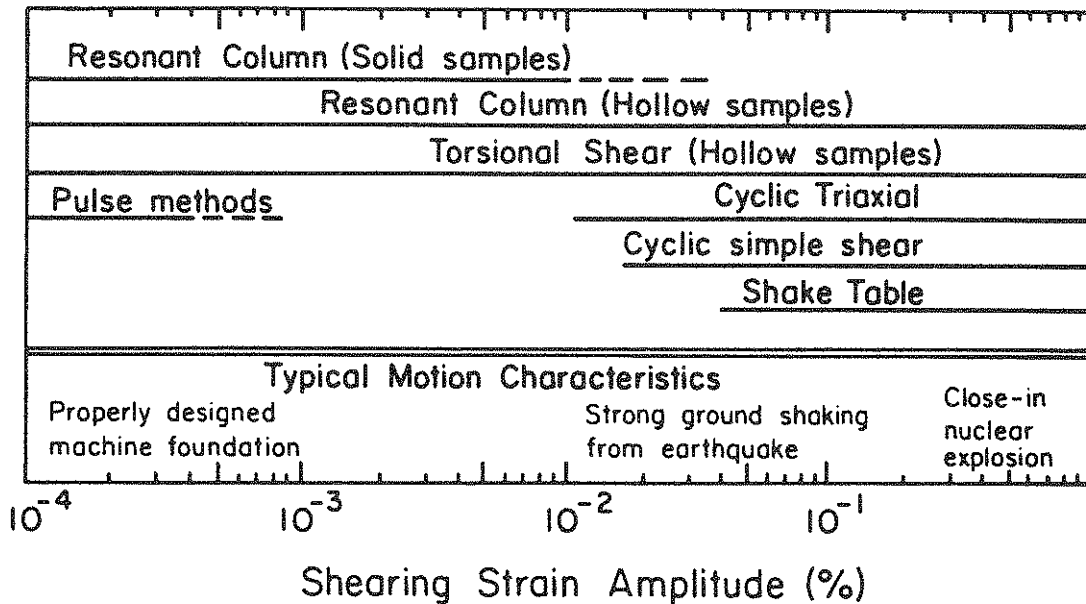


FIGURE 2-1. Shearing Strain Amplitude Capabilities of Laboratory Apparatus [after Woods, 1978]

## 2.2 CYCLIC TRIAXIAL TESTING

### 2.2.1 Stress Conditions

An element of soil in the ground during an earthquake is subjected to a complex system of deformations resulting from the erratic sequence of earthquake-induced ground motions. However, the major element of soil deformation may be attributed to upward propagating shear waves. Thus, an element of soil, as shown in Figure 2-2, may be considered subject to a series of cyclic shear stresses. If the ground surface is horizontal with no imposed surface loading, then there is no shear stress on the horizontal plane. During an earthquake, the total normal stress on this plane remains constant, while cyclic shear stresses may exist for the duration of the shaking. Such deformation conditions were approximated by Seed and Lee [1966] using cyclic triaxial tests.

The stress conditions for a cyclic triaxial test on an isotropically or anisotropically consolidated sample are shown in Figure 2-3a and 2-3b, respectively. Under isotropic consolidation, the major

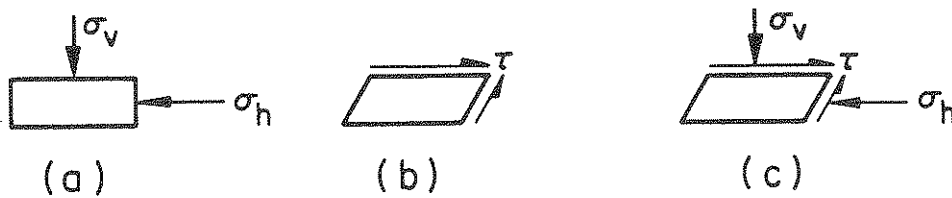
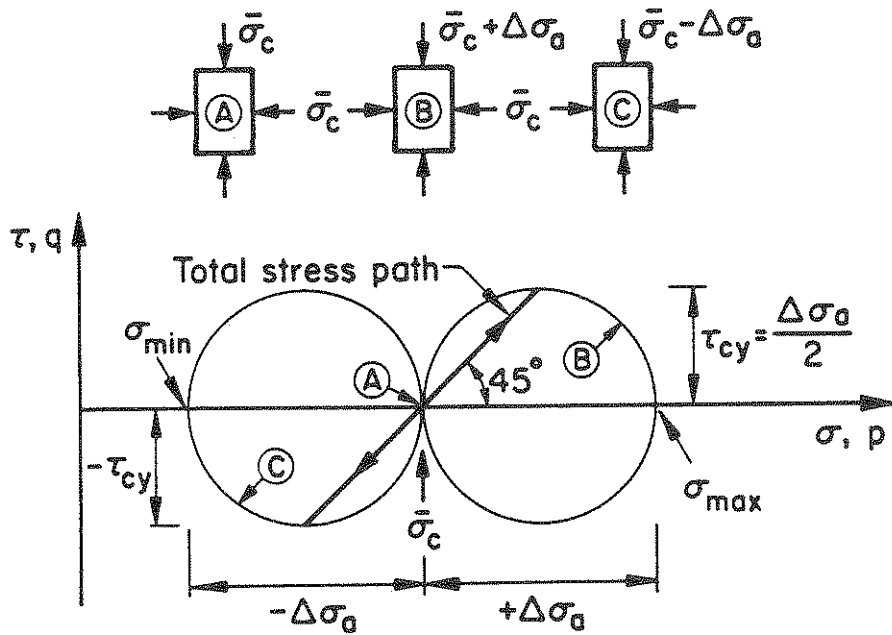


FIGURE 2-2. Idealized Stress Conditions for Element of Soil Below Ground Surface During an Earthquake

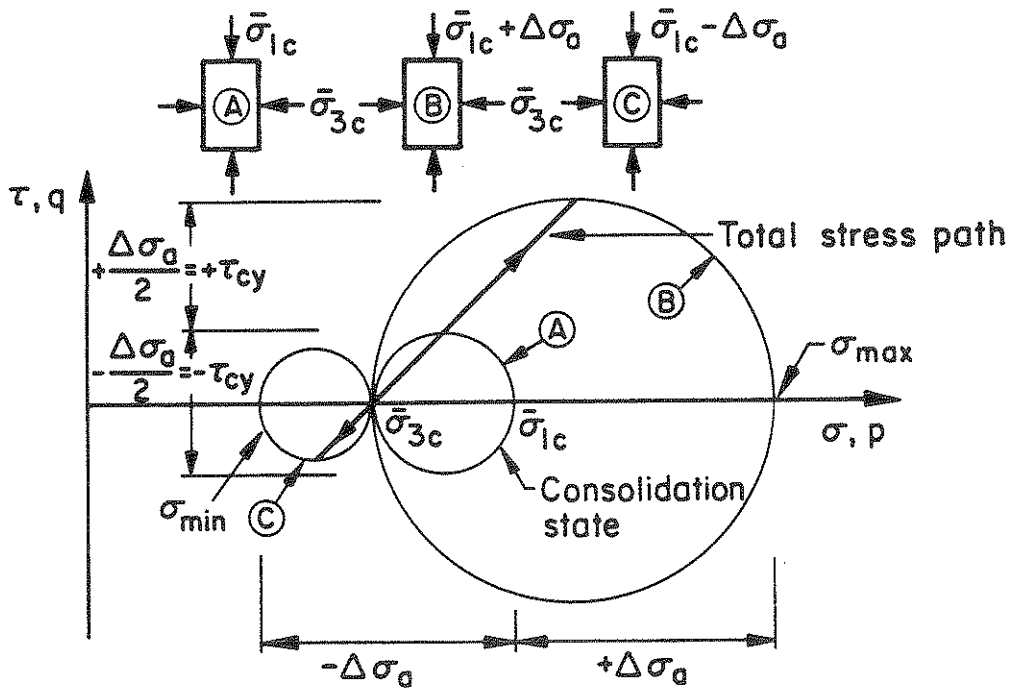
principal stress,  $\sigma_1$ , acts alternately in the vertical and horizontal directions. When  $+\Delta\sigma_a$  is applied the maximum shear stress,  $+\tau_{cy}$ , which is equal to  $\Delta\sigma_a/2$ , develops on a 45 degree plane in the specimen. Then  $-\Delta\sigma_a$  is applied and the shear stress reverses, and a symmetrically reversing shear stress condition is obtained. Under anisotropic consolidation, as shown in Figure 2-3b, if  $\Delta\sigma_a$  is smaller than  $\sigma_{dc}$  ( $\sigma_{dc} = \sigma_{1c} - \sigma_{3c}$ ), the major principal stress acts in the vertical direction throughout the loading cycle (i.e., no shear stress reversals take place). If  $\Delta\sigma_a$  is larger than  $\sigma_{dc}$ , then the net axial stress acting on the specimen will become less than the lateral stress during a portion of the loading cycle, and shear stress reversal will occur.

Failure modes due to undrained cyclic loading and for a variety of static and cyclic stress conditions are shown in Figure 2-4 ( $\sigma_{df}$  = deviator stress at failure). These modes were discussed in more detail by Selig and Chang [1981]. The solid circles indicate tests in which failure occurred by cyclic strain, and the open circles indicate tests in which failure occurred by permanent strain accumulation. The transition was defined precisely by the condition of shear stress reversal. When no shear stress reversal occurred ( $\Delta\sigma_a < \sigma_{dc}$ ), the permanent axial strain was greater than the cyclic axial strain. When shear stress reversal occurred ( $\Delta\sigma_a > \sigma_{dc}$ ), the cyclic strain was greater than the permanent strain.

Park and Silver [1975] described the dynamic properties obtainable from the cyclic triaxial test, as shown in Figure 2-5, for a typical constant strain amplitude test on a dry sand sample. The resulting



a) Isotropically Consolidated



b) Anisotropically Consolidated

FIGURE 2-3. Stress Components in Cyclic Triaxial Test Specimens

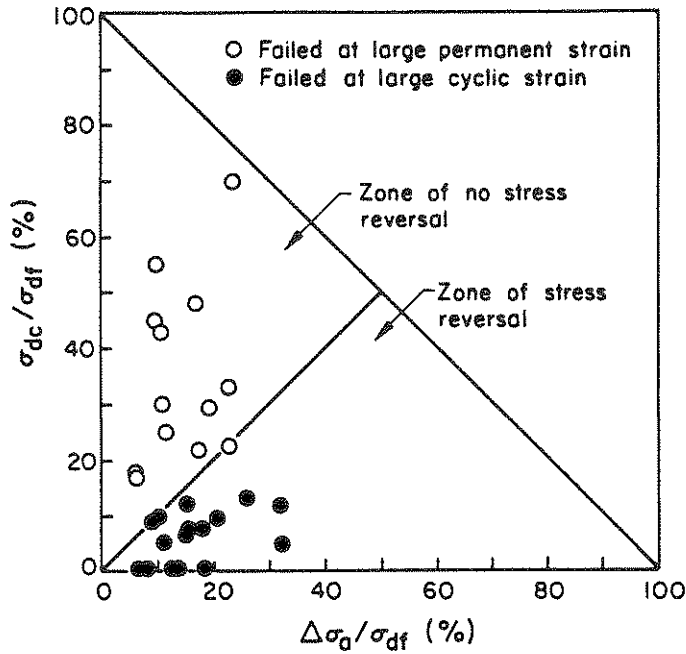


FIGURE 2-4. Effect of Stress Reversal on Failure Mode [after Selig and Chang, 1981]

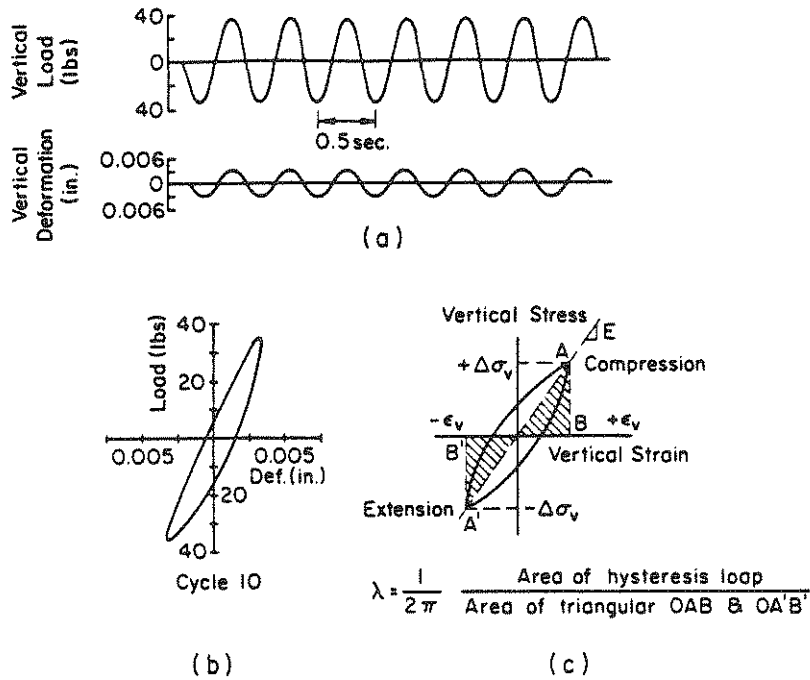


FIGURE 2-5. Typical Results of Dynamic Triaxial Test: (a) Record of Deformation and Load During Dynamic Triaxial Test; (b) Corresponding Hysteresis Loop; (c) Definition of Equivalent Stress-Strain Properties [after Park and Silver, 1975]

load-deformation hysteresis loop is shown in Figure 2-5b. Young's modulus, E, can be determined by measuring the slope of the line connecting the extreme points of the stress-strain hysteresis loop, as shown in Figure 2-5c. The same hysteresis loop can be used to calculate hysteretic damping by calculating the loop areas and using the equation shown in the figure.

Since the behavior of soil is strain dependent, the modulus and damping values are related to the single amplitude vertical strain,  $\epsilon_v$ . For dynamic analysis, it is often more convenient to convert values of Young's modulus and vertical strain to values of shear modulus, G, and shear strain,  $\gamma$ , respectively. From elasticity theory:

$$G = E/2(1 + \mu) \quad (2-1)$$

and

$$\gamma = (1 + \mu)\epsilon_v \quad (2-2)$$

in which  $\mu$  = Poisson's Ratio.

### 2.2.2 Cyclic Strength Determination

Cyclic undrained strength has often been defined from cyclic triaxial tests. The cyclic undrained strength often is expressed as the relationship between the cyclic stress ratio (R) and the number of cycles required to induce liquefaction ( $N_L$ ), or some value of limiting strain, in which R is the ratio of the cyclic deviator stress,  $\Delta\sigma_a$ , to twice the initial effective confining pressure. This is also equal to the cyclic shear stress,  $\tau$ , divided by the initial effective confining pressure,  $\bar{\sigma}_0$ . Curves relating R to  $N_L$  for, say, different relative densities, can be determined as shown in Figure 2-6. The influence of sand density on the strain amplitude following liquefaction is shown in Figure 2-7. In this test series [Seed and Lee, 1966], three samples with different initial densities were cycled at stresses sufficient to cause initial liquefaction at about the same number of cycles. Initial liquefaction was defined as when effective stress is first reduced to zero due to pore pressure buildup. As relative

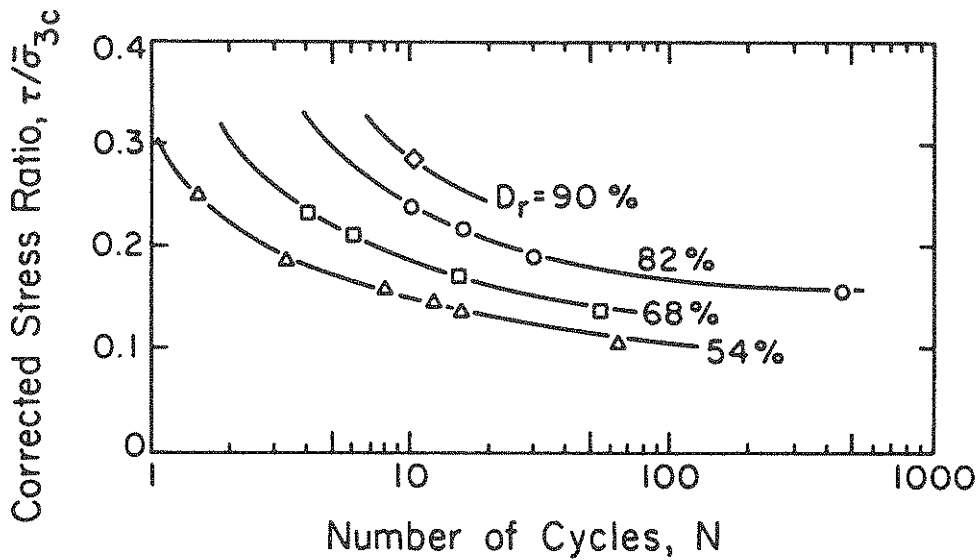


FIGURE 2-6. Stress Ratio versus Number of Cycles to Initial Liquefaction [after De Alba, et al., 1976]

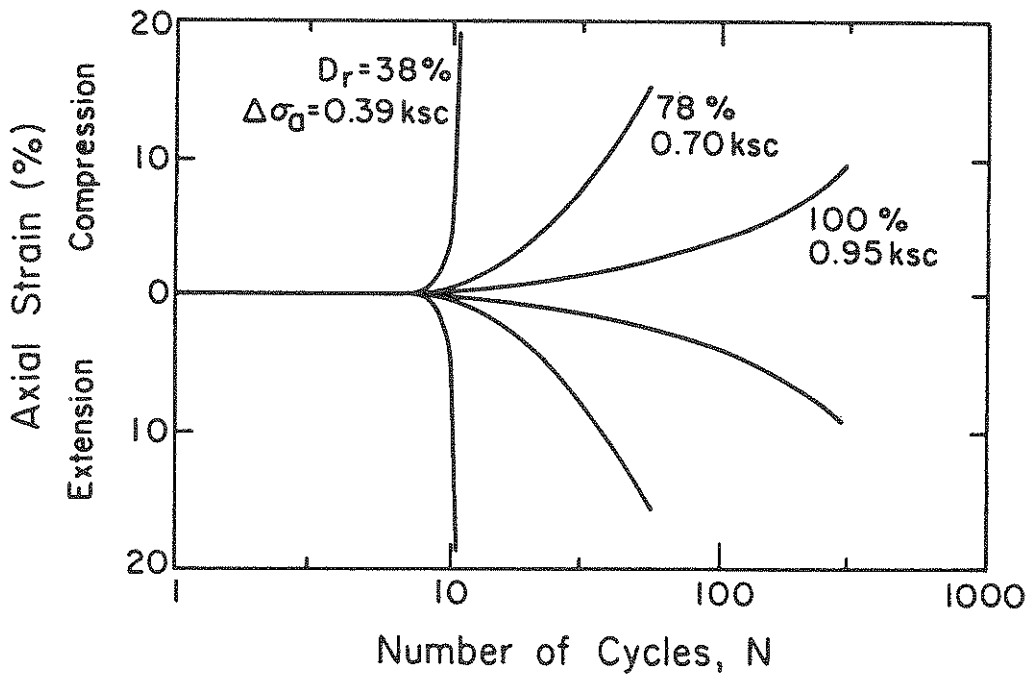


FIGURE 2-7. Axial Strain After Initial Liquefaction for Pulsating Load Tests at Three Densities [after Seed and Lee, 1966]



density increased, the rate of deformation decreased, and larger stress ratios were required to cause initial liquefaction.

The relationship between pore pressure ratio,  $(\Delta u/\bar{\sigma}_{3c})$ , and cyclic stress ratio,  $R$ , has also been studied for varying numbers of load cycles, as shown in Figure 2-8. Figure 2-8 also shows the effect of two methods of sample preparation [Dobry, et al., 1982]. Lee and Albaisa [1974] summarized several cyclic tests for design purposes, as shown in Figure 2-9, to illustrate the relationship between pore pressure ratio and cycle ratio,  $N/N_L$ , where  $N$  = number of cycles. They found that all such curves from one soil fell within a narrow band, and that this shape is similar for different soils. In addition, the position of the curves was largely insensitive to the type of soil, relative density, confining pressure, and number of cycles to cause liquefaction.

### 2.2.3 Testing Problems

Despite the wide use of cyclic triaxial tests in liquefaction studies, there are difficulties with respect to the accurate modeling of in-situ stresses. Casagrande [1975] and Castro [1975] investigated certain specific problems with the test. Figure 2-10 illustrates the radical redistribution of water content and of corresponding relative density in a cyclic triaxial test specimen. This redistribution was determined to occur because of the combined effects of three factors:

- a) stress gradients within the test specimen generated by nonuniform stress distribution on the specimen boundary,
- b) the high pore pressures and softening which develop as the specimen is cycled through a state of hydrostatic stress, and
- c) a pumping-like action which draws water to the top of the specimen.

Problem (a) is present to some extent in all cyclic testing, but seems to be particularly severe in cyclic triaxial tests, as extension may cause necking, and hence a soft zone at the top of the specimen.

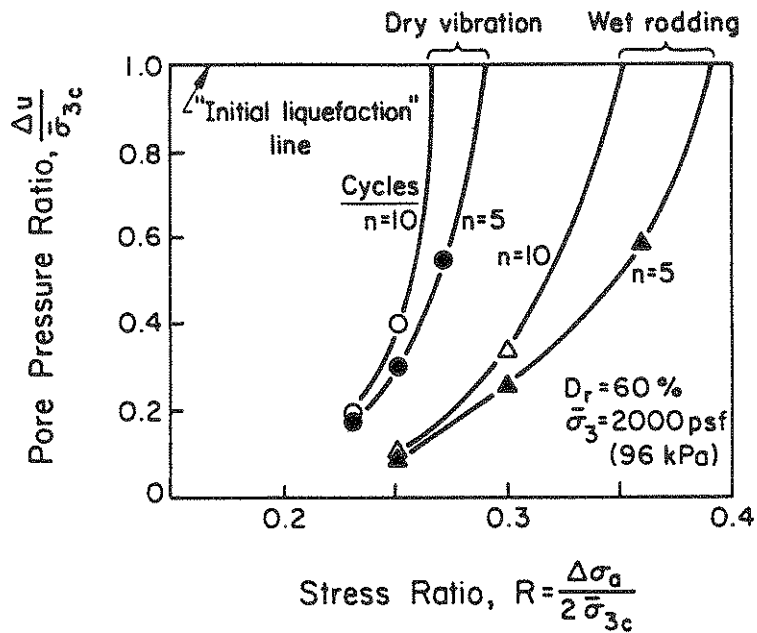


FIGURE 2-8. Stress-Controlled Cyclic Triaxial Tests of Saturated Crystal Silica Sand [after Dobry, et al., 1982]

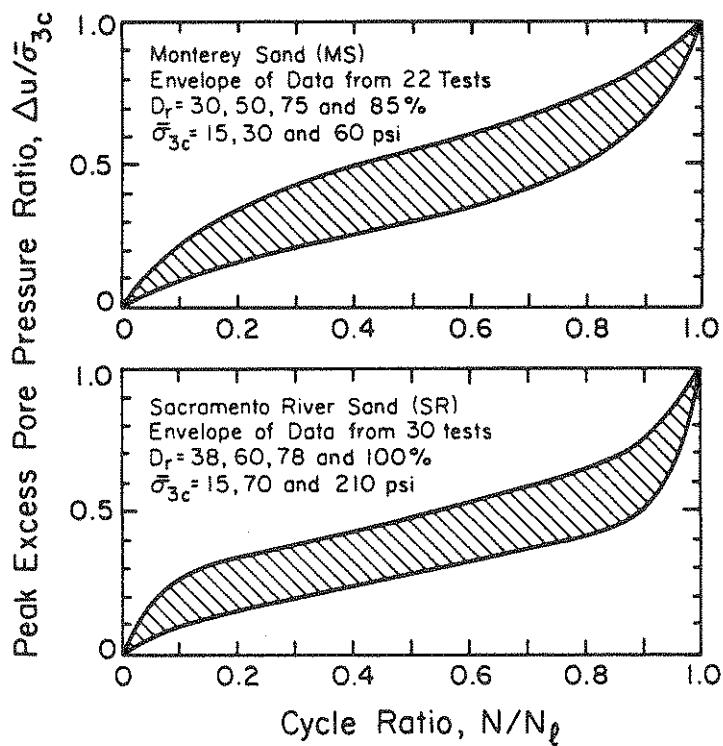
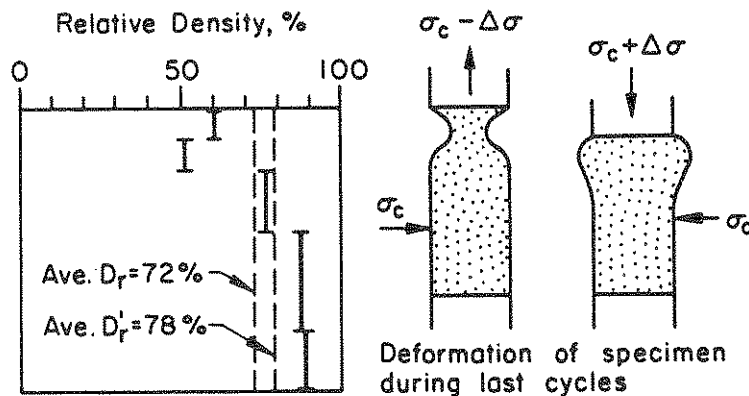


FIGURE 2-9. Compilation Summary of Pore Pressure Buildup Data (1 psi = 6.9 kN/m<sup>2</sup>) [after Lee and Albaisa, 1974]



Average Relative Density of Specimen:

- 1) As prepared and during cyclic test  $D_r = 72\%$
- 2) After reconsolidation under  $\sigma_c$  at end of test  $D_r' = 78\%$

Test Procedure:

After 14 load cycles, which produced 14% total strain amplitude, specimen was reconsolidated under  $\sigma_c$ , then frozen, cut into segments, and water contents determined. The corresponding relative densities are shown by the heavy vertical bars.

FIGURE 2-10. Redistribution of Relative Density in Cyclic Triaxial Specimen [after Casagrande, 1975]

Additional deviations from in-situ behavior include different pore pressure responses to triaxial compression and extension, rotation of the principal stress directions, and possible lack of plane strain conditions.

## 2.3 LIQUEFACTION

### 2.3.1 Definitions of Liquefaction

The term liquefaction has already been used on several occasions, yet only one definition has been mentioned. Initial liquefaction was defined as the point at which effective stress is first reduced to zero due to increased pore pressure. Unfortunately, this definition represents only one side of two distinctly different approaches.

On one side, liquefaction is defined as a phenomenon in which a loose saturated sand loses a large proportion of its shear resistance, due

to either undrained monotonic or cyclic loading, and flows like a liquid until the shear stresses acting on the mass are as low as its reduced shear resistance [Casagrande, 1975; Castro, 1977; and Poulos, et al., 1985]. This behavior is also referred to as flow failure, and is accompanied by strain softening behavior, as shown in Figure 2-11 (i.e., a reduction in strength beyond the peak in a stress strain curve).

Poulos, et al. [1985] state that only soils that have a tendency to decrease in volume during shear (contractive soils) are susceptible to liquefaction flow failure. However, even contractive soils are not susceptible to liquefaction unless the driving in-situ shear stresses are sufficiently large. Soils which have a tendency to increase in volume due to shearing (dilative soils) are not susceptible to flow failure, because their undrained strength is greater than their drained strength.

The essence of Casagrande's [1975] definition of liquefaction flow failure is steady-state strength. The steady-state of deformation is that state in which a mass of particles is deforming at constant volume, constant normal effective stress, constant rate of strain, and constant shear stress. The steady-state of deformation is achieved only after all particle orientation effects have reached a steady-state condition and after all possible particle breakage. The steady-state can be attained in either drained or undrained loading, but only during deformation. Figure 2-12 illustrates the steady-state strength concept for a contractive soil. The steady-state line is the line drawn through points that show the steady-state void ratio versus the effective minor principal stress during steady-state deformation. Therefore, liquefaction is only possible, for this concept, when the steady-state strength is less than the driving shear stress. This approach, as discussed by Poulos, et al. [1985], implies that cyclic load tests are unnecessary in determining whether a soil mass is susceptible to liquefaction flow failure, and that only several monotonic tests are required in order to determine the position of the steady-state line. On the other hand, a liquefaction hypothesis can

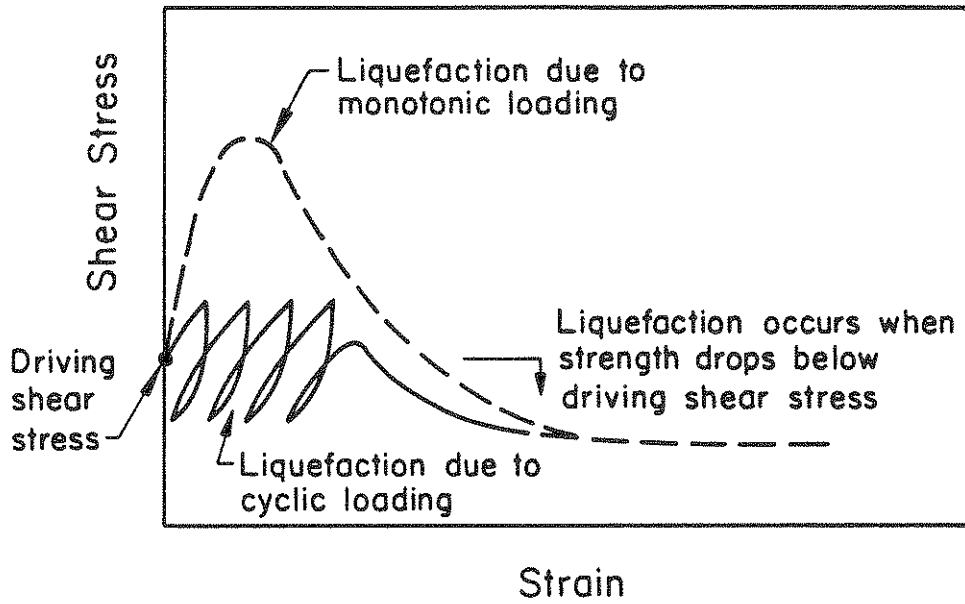


FIGURE 2-11. Liquefaction Due to Monotonic or Cyclic Loading (Schematic) [after Poulos, et al., 1985]

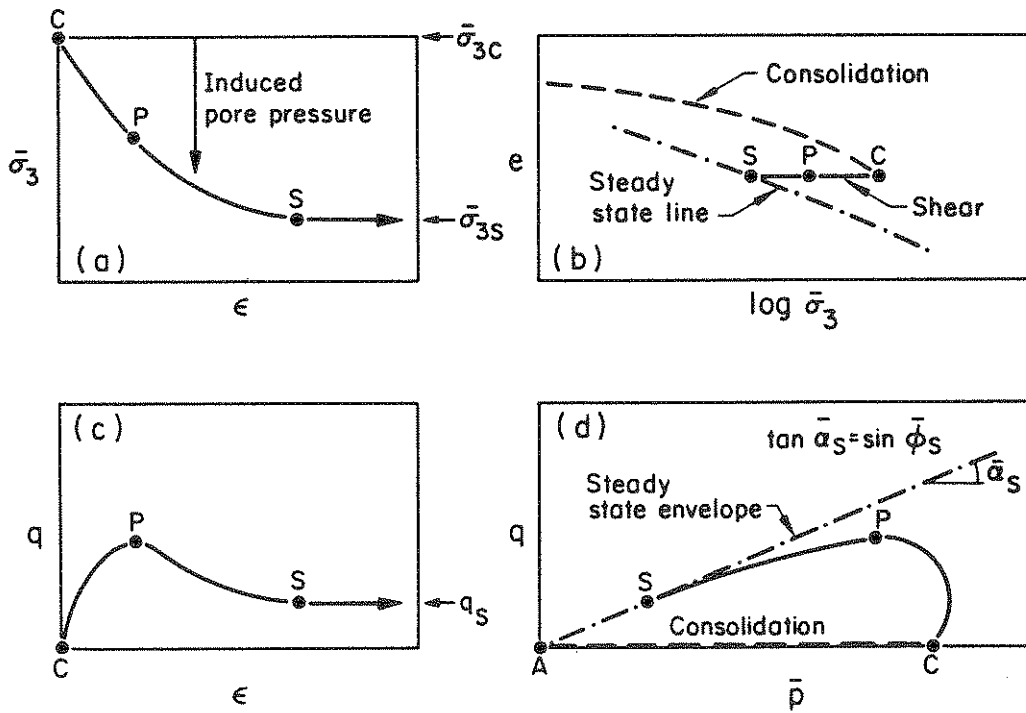


FIGURE 2-12. Plot of Data for One Undrained Test on Contractive Specimen to Determine Steady-State Strength (Schematic): a) Effectiveness Stress; b) State; c) Stress-Strain; d) Stress Path [after Poulos, et al., 1985]

be built on observations from laboratory testing. Figure 2-13 shows a typical stress-controlled cyclic triaxial test on either a loose or dense (contractive or dilative) sand, which illustrates an alternate liquefaction definition. The definition states that initial liquefaction occurs the first time the value of the pore pressure, at zero deviator stress, is momentarily equal to the confining pressure, i.e., the effective stress drops to zero and the stresses are hydrostatic. After initial liquefaction, the strains during each subsequent cycle become progressively larger as more cycles of load are applied. During each cycle, a point is reached where effective stress becomes zero, but increases again when either axial compression or extension is applied, such as in a cyclic triaxial test.

Casagrande [1975] and Castro [1975] suggested using the term cyclic mobility for the definition of liquefaction based on zero effective stress. (In this report, liquefaction or cyclic mobility will refer to the zero effective stress definition, and flow failure, or liquefaction flow failure, will refer to the Casagrande [1975] and Castro [1975] definition.) In cyclic mobility, loads cause a buildup of pore pressures in medium to high density saturated sands and induce strains in specimens that ordinarily exhibit a dilative response under static loading. Thus, cyclic stresses, if they are large enough and for a sufficient duration (number of cycles), can cause even dilative sands to lose strength.

There are a variety of test types used to investigate cyclic responses. Cyclic simple shear (CSS) tests were also used in the investigation of cyclic mobility, and provided data which confirmed the trends apparent in the cyclic triaxial tests. CSS tests are considered to simulate more closely actual field stress conditions, even though nonuniform stress and strain distributions may exist within the specimen [Saada and Townsend, 1981]. In the CSS test, after consolidation under a vertical stress, a cyclic horizontal shear stress is applied at the top or bottom of a laterally constrained specimen. The differences in stress conditions between cyclic triaxial and CSS tests have been the subject of much research [e.g., Peacock and Seed, 1971;

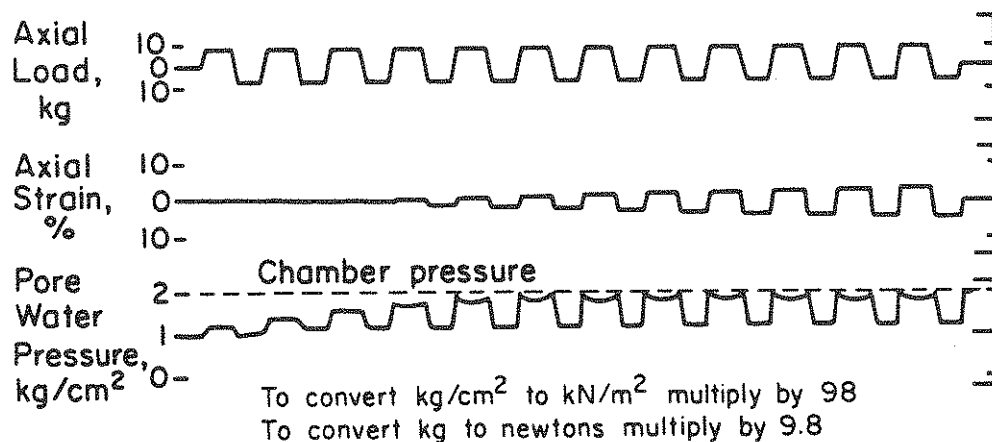


FIGURE 2-13. Expanded Record and Results of Cyclic Triaxial Test  
[after Seed and Lee, 1966]

Finn, et al., 1971; Park and Silver, 1975; and Castro, 1975]. Peacock and Seed [1971] found that the cyclic stress required to cause initial liquefaction under simple shear conditions was considerably less than that required under triaxial conditions. A comparative study of cyclic testing equipment was carried out by Bhatia, et al. [1985], and is discussed in more detail in Section 2.5.4.

Liquefaction flow failure and cyclic mobility are illustrated together in Figure 2-14. Soils with void ratios and effective stresses lying above and to the right of the steady-state line are contractive, and thus may be susceptible to liquefaction flow failure. For example, a specimen with an initial state at point C, when either monotonically or cyclically loaded, develops positive excess pore pressure and moves toward point A on the steady-state line. Flow failure may occur in this case, depending on the shape of the stress-strain curve. However, a dense dilative specimen originally at point D below the steady-state line will move towards a condition of zero effective stress, point B, during cyclic shearing (cyclic mobility). If the same sample was loaded monotonically, then the loading path would go in the opposite direction towards the steady-state line.

It is interesting to note Casagrande's [1975] opinion of cyclic mobility. Casagrande stated that "progressive increase of cyclic pore pressures and softening in test specimens in various types of cyclic

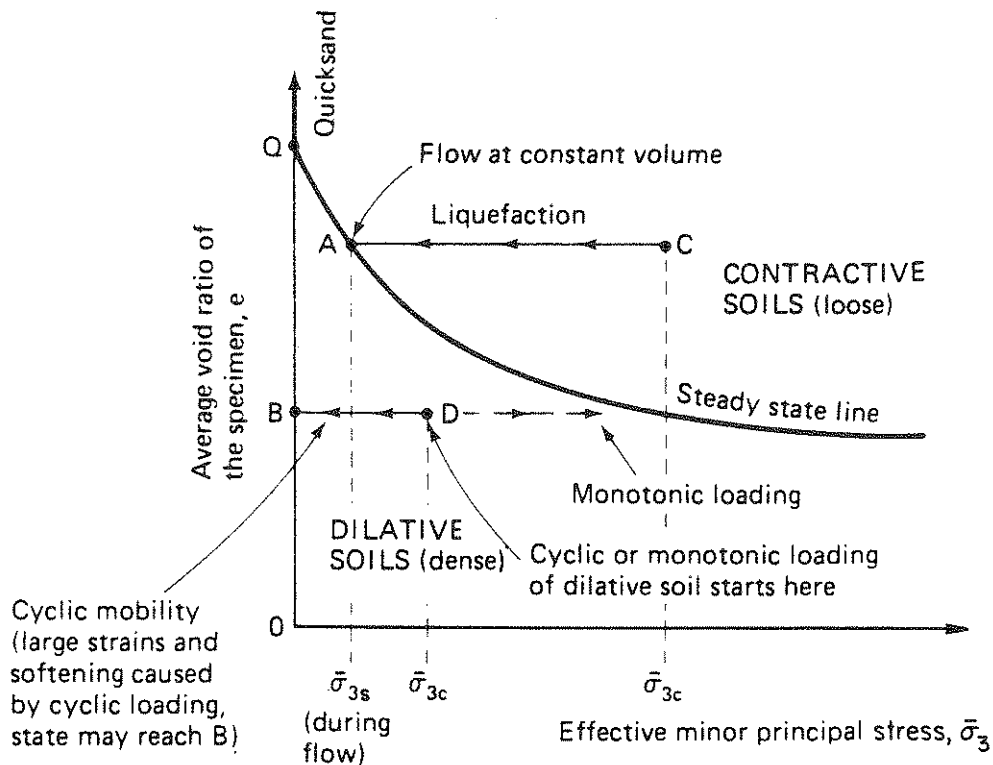


FIGURE 2-14. State Diagram Showing Liquefaction Potential Based on Undrained Tests of Saturated Sands [after Holtz and Kovacs, 1981]

tests, including cyclic liquefaction in triaxial tests, are caused by radical redistribution of the water content which is generated by mechanisms that are normally not active in-situ." This would mean that cyclic mobility is due to void ratio redistributions within a test specimen, and that such an effect is unlikely to occur in actual conditions. There is little doubt that void ratio redistributions occur during cyclic testing. However, Mulilis, et al. [1977] found that no water content redistribution occurred before the development of failure. After failure, however, the same nonuniform conditions as observed by Casagrande [1975] and Castro [1975] (i.e., necking and bulging) developed. This suggests that in-situ pore pressure rise does occur in a uniform dilatant sand. Whitman and Lambe [1982] have also shown, using a shaking table, that excessive settlements of model structures occur even in dilatant saturated sands. Poulos, et al. [1985] concede that the strains measured in undrained cyclic load



tests are "related" to the deformations that occur in-situ due to cyclic loading. However, they consider testing errors to be so large that extrapolation to field performance is unwarranted.

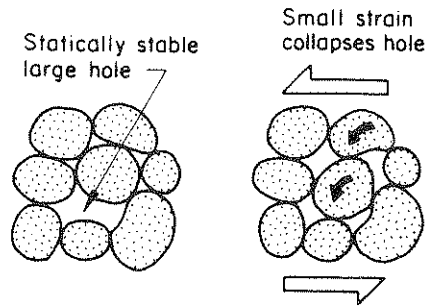
Cyclic mobility is simply the tendency of a loose or dense soil to densify during cyclic loading. The exact mechanism by which a dilatant soil densifies under cyclic loading is explained by Youd [1977] and Nemat-Nasser and Takahashi [1984]. Dilatancy tendencies are due to particles attempting to roll or slide up and over one another, as shown in Figure 2-15a, which under constant volume causes a reduction in pore pressure, creating larger voids locally near the dilating zones. On stress reversal, most of these unstable holes collapse, producing an increase in pore pressure, as shown in Figure 2-15b. This increase may also be due to a net downward movement of the soil grains upon unloading, and therefore a tendency for volume reduction.

### 2.3.2 Factors Affecting Liquefaction Potential

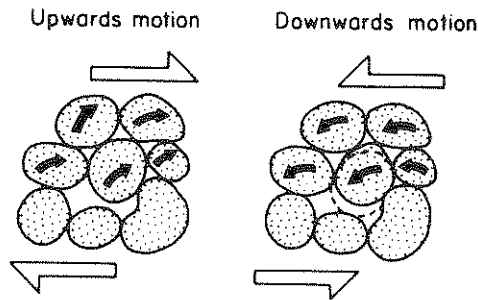
#### 2.3.2.1 Soil Type

Tsuchida [1970] studied the grain size distributions of several soils that did or did not liquefy during an earthquake. Figure 2-16 shows boundary curves, identified by Tsuchida, for most liquefiable and potentially liquefiable soils. The presence of large amounts of fines, especially cohesive fines, has been found to impede particle rearrangement during cyclic straining. However, Ishihara [1984] found that even fine-grained tailings sand was susceptible to liquefaction, and that the values of cyclic strength (defined as cyclic stress ratio causing 5% strain in 20 cycles) obtained were nearly independent of grain size distribution. Cyclic strength was, nonetheless, found to increase slightly with increasing plasticity index. Therefore, although Figure 2-16 is a useful guide, it should be realized that even finer soils have been found to be susceptible to liquefaction.

Castro [1977] and Poulos, et al. [1985] have also looked at the effect of grain size distribution and grain shape on the position of the steady-state line. Figure 2-17 shows the effect of grain shapes



a) Changes in Initial Fabric at Small Strains



b) Changes in Fabric due to Dilatancy at Large Strains

FIGURE 2-15. Changes in Fabric During Cyclic Loading [after Youd, 1977]

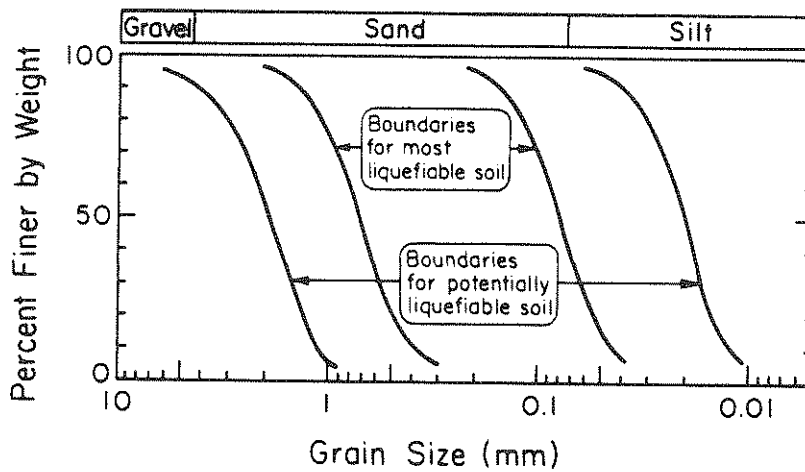


FIGURE 2-16. Limits in the Gradation Curves Separating Liquefiable and Unliquefiable Soils [after Tsuchida, 1970]

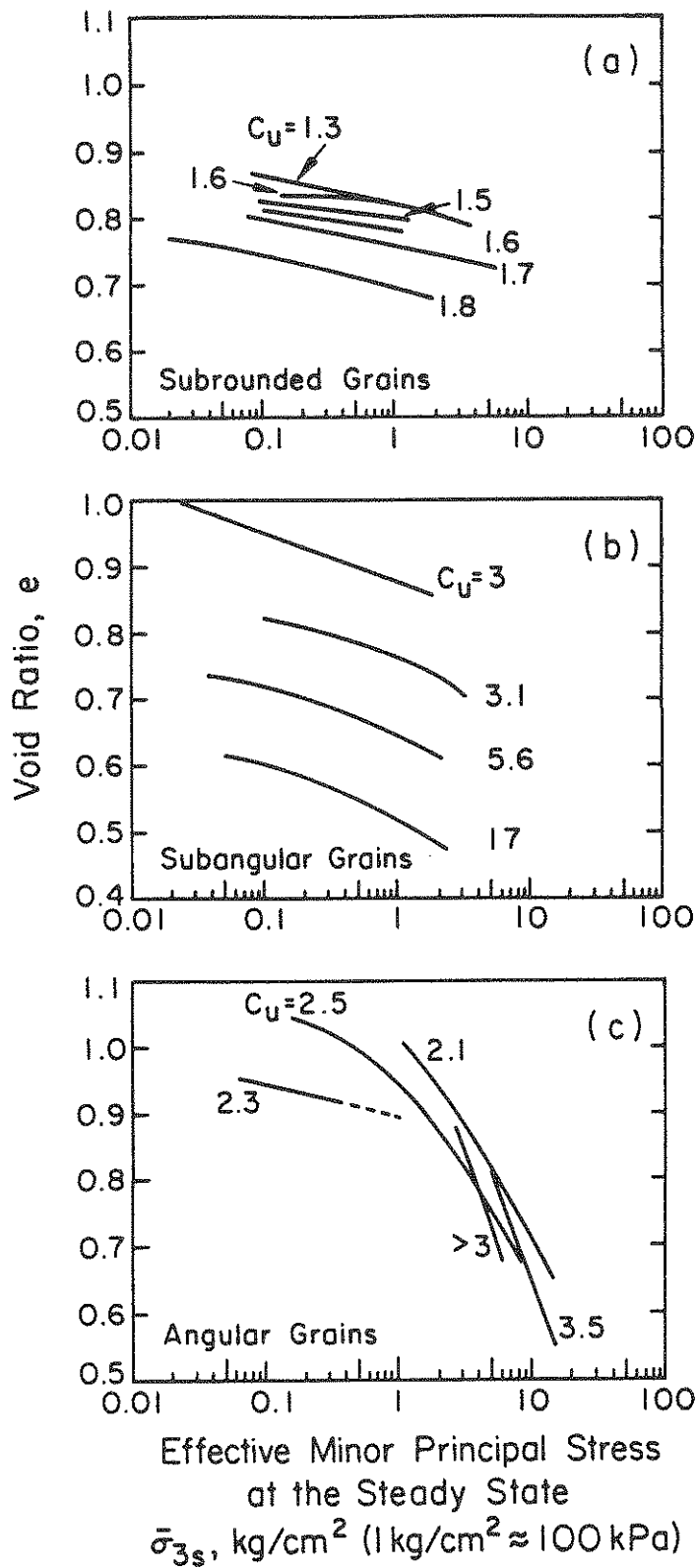


FIGURE 2-17. Steady-State Lines for Sands [after Poulos, et al., 1985]

(subrounded, subangular, and angular) and grain size distribution (defined by the uniformity coefficient,  $C_u = D_{60}/D_{10}$ , where  $D_n$  = grain diameter at n% passing) on the position of the steady-state line. The slope of the steady-state line was found to be affected mainly by the shape of a given soil's grains, and the vertical position of the line was affected by changes in grain-size distribution. Thus, a soil's grain characteristics have a large effect on the steady-state behavior of a soil.

#### 2.3.2.2 Soil State

Typical effects of confining stress and relative density are shown in a generalized form in Figure 2-18. As the peak cyclic stress is decreased, more cycles are required to "fail" the sample. As the relative density and/or confining pressure is increased, a higher cyclic stress is required to fail the specimen in a given number of cycles. Figure 2-6 showed a similar trend for cyclic stress ratio against relative density.

The findings given above apply to cyclic mobility only. For static loading, flow failure potential increases with increasing confining pressure, i.e., increasing the effective confining pressure on an initially dense sand tends to cause contractive type behavior. Castro and Poulos' [1977] conclusions regarding the factors likely to influence flow failure and liquefaction are shown in Table 2-1. The conclusions with respect to the effect of  $K_c = \bar{\sigma}_{1c}/\bar{\sigma}_{3c}$  on cyclic mobility deserve attention. It would be reasonable to expect that, as  $K_c$  increases, a larger value of shear stress must be applied to cause stress reversals. This effect was shown by Ishibashi and Sherif [1974], and summarized by Seed [1979], as shown in Figure 2-19. Also, Ishihara and Takatsu [1979] studied the effect of  $K_c$  and OCR on the liquefaction characteristics of sands using a torsional shear device. Ishihara and Takatsu's [1979] results (Figure 2-20) also show that for an increasing  $K_c$  and/or OCR value, liquefaction resistance increases. The fact that Castro and Poulos' [1977] results are different can only be explained by dissimilar test procedures, sample preparation

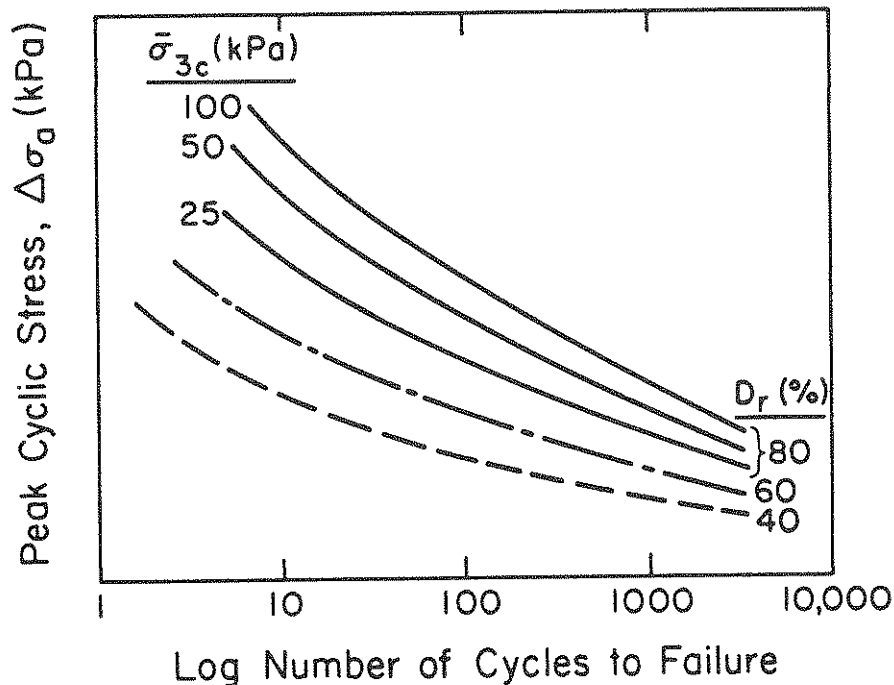


FIGURE 2-18. Generalized Relationship Between Peak Cyclic Stress and Number of Cycles to Cause Cyclic Mobility Failure [after Holtz and Kovacs, 1981]

techniques, and testing equipment.

### 2.3.2.3 Threshold Shear Strain

The threshold shear strain,  $\gamma_t$ , is the strain amplitude needed to initiate a pore pressure buildup in a saturated cohesionless soil, or densification of dry sand [Dobry, et al., 1981]. Research carried out to study the effect of initial state of stress and relative density on the threshold shear strain has been done using strain-controlled cyclic tests. Strain control tests are tests where a specimen is subjected to uniform cycles of deformation, and axial or torsional stress varies. In stress-control tests, a sample is subjected to uniform stress cycles, and deformation varies. Table 2-2 and Figure 2-21 summarize the cyclic laboratory testing data available concerning  $\gamma_t$  in sands. Table 2-2 is a compilation of data for three distinct sands, at different relative densities, prepared using different

TABLE 2-1. Differences Between Liquefaction and Cyclic Mobility  
[Holtz and Kovacs, 1981]

	Liquefaction Flow Failure	Cyclic Mobility/ Liquefaction
General	Most likely in uniform, fine, clean, loose sand. Static load can cause liquefaction. Cyclic loads causing shear stresses larger than the steady-state strength also can cause liquefaction.	Any soil in any state can develop cyclic mobility in the laboratory if the cyclic stresses are large enough.
Effect of $\bar{\sigma}_{3c}$ at constant void ratio for $\bar{\sigma}_{1c}/\bar{\sigma}_{3c} = 1.0$	Increased $\bar{\sigma}_{3c}$ means larger deformations if liquefaction is induced.  The magnitude and/or number of cyclic loads needed to cause liquefaction increases with $\bar{\sigma}_{3c}$ . Cyclic loads smaller than the steady-state strength cannot cause liquefaction but may cause cyclic mobility.	Increased $\bar{\sigma}_{3c}$ means increased cyclic mobility. But the cyclic mobility ratio <sup>1</sup> usually decreases with increasing $\bar{\sigma}_{3c}$ .
Effect of $\bar{\sigma}_{1c}/\bar{\sigma}_{3c}$ at constant void ratio and $\bar{\sigma}_{3c}$	Smaller additional loads are needed to cause liquefaction as $\bar{\sigma}_{1c}/\bar{\sigma}_{3c}$ increases. When $\bar{\sigma}_{1c}/\bar{\sigma}_{3c}$ is large, a soil is more unstable and may, in the extreme, be susceptible to "spontaneous liquefaction."	In soils that have low permeability, increased $\bar{\sigma}_{1c}/\bar{\sigma}_{3c}$ seems to result in somewhat smaller cyclic mobility stresses, which is a reasonable trend. In clean sands, cyclic mobility stress increases with $\bar{\sigma}_{1c}/\bar{\sigma}_{3c}$ . This unusual result for clean sands is postulated to be due to the substantial test error due to redistribution of void ratio in the laboratory specimens.

<sup>1</sup>  $[(\sigma_1 - \sigma_3)/2]/\bar{\sigma}_{3c}$ , where  $(\sigma_1 - \sigma_3)$  is the dynamic principal stress difference, or the cyclic mobility stress.

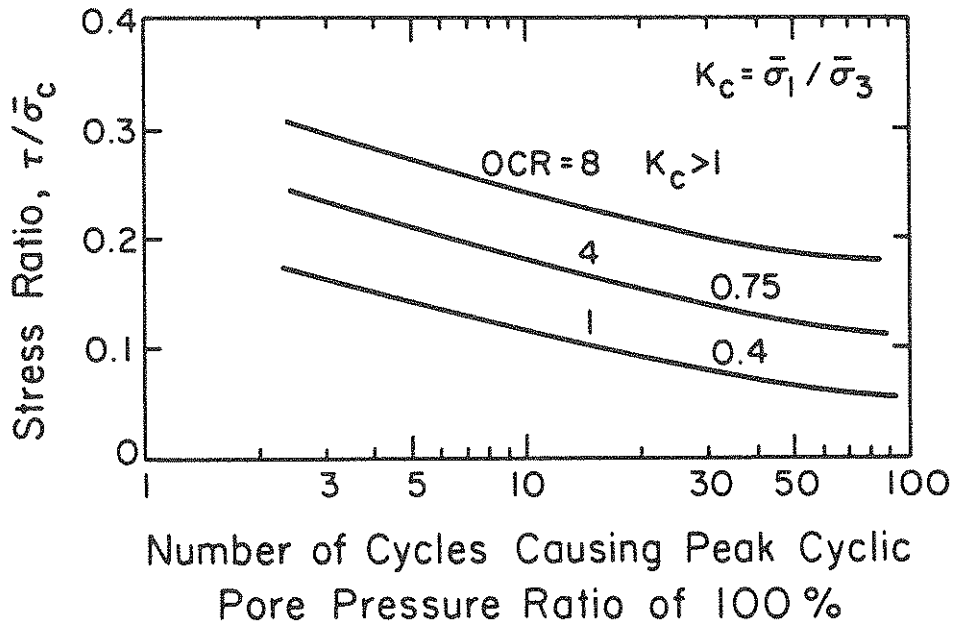


FIGURE 2-19. Influence of Initial Principal Stress Ratio on Stresses Causing Pore Pressure Ratio of 100% in Simple Shear Tests [after Seed, 1979]

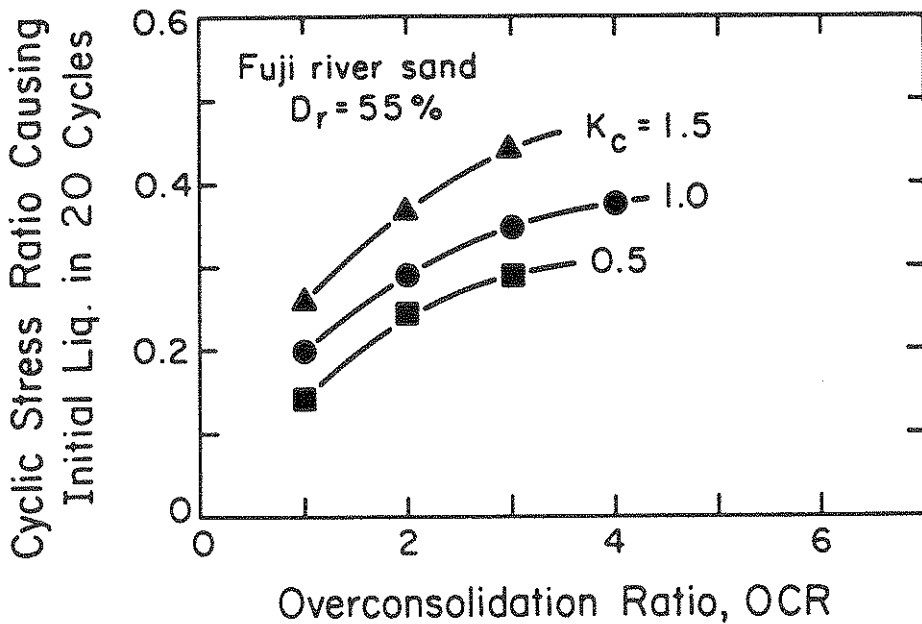


FIGURE 2-20. Relationship Between Cyclic Strength and OCR Value [after Ishihara and Takatsu, 1979]

TABLE 2-2. Threshold Shear Strain,  $\gamma_t$ , for Dry and Saturated Sands [after Dobry, et al., 1981]

Sand	Testing Technique	$\gamma_t$	Reference
Dry Ottawa Sand	Resonant Column	$1 \times 10^{-2}\%$	Drnevich and Richart [1970]
Dry Crystal Silica Sand	Cyclic Simple Shear	$2 \times 10^{-2}\%$	Silver and Seed [1971]
Dry and Saturated Ottawa Sand	Cyclic Simple Shear (Drained)	$1 \times 10^{-2}\%$	Youd [1972]
Dry Monterey Sand	Cyclic Simple Shear Shaking Table	$1 \times 10^{-2}\%$	Pyke [1973]
Saturated Monterey Sand	Cyclic Triaxial (Undrained)	$1.1 \times 10^{-2}\%$	Dobry, et al. [1982]

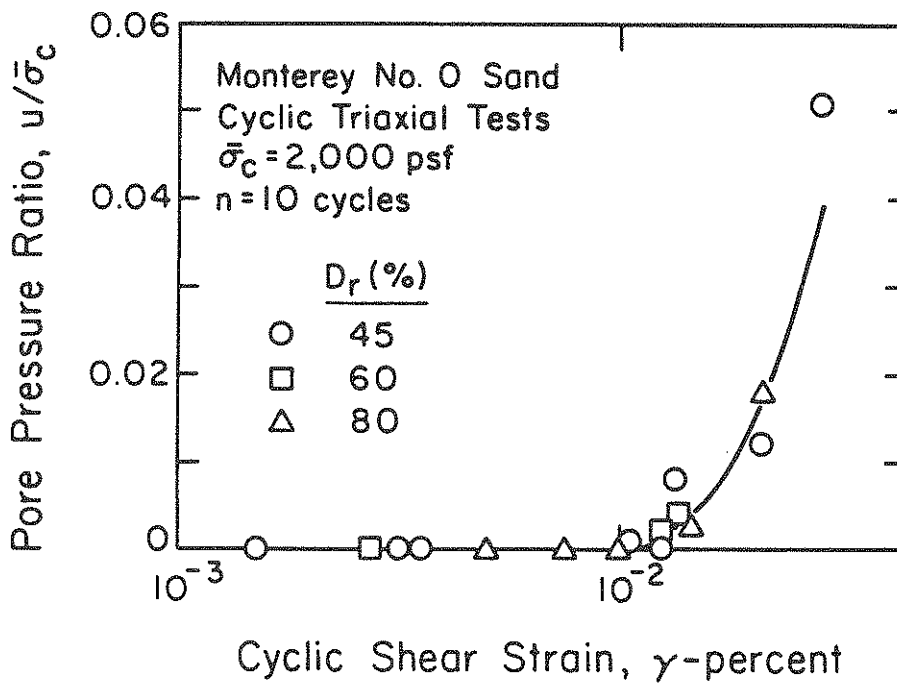


FIGURE 2-21. Excess Pore Pressures After Ten Loading Cycles, Cyclic Triaxial Strain-Controlled Tests [after Dobry, et al., 1981]



placement methods and consolidated to various confining pressures. Despite these differences, consistent values for  $\gamma_t$  of between 0.01% and 0.02%, for normally consolidated clean sands, were obtained. Figure 2-21 indicates that a threshold shear strain of about 0.01%, for 10 loading cycles, was essentially independent of relative density. Results from a test program carried out by Dyvik, et al. [1984] indicated  $\gamma_t$  between 0.008% and 0.015% for normally consolidated sands. In tests on overconsolidated specimens of Monterey No. 0 sand,  $\gamma_t$  was shown to increase with OCR, with  $\gamma_t = 0.03\%$  for OCR = 8.

The concept of a threshold shear stress also occurs in stress control tests. However, unlike threshold shear strain, the critical stress varies over a wide range, depending on confining stress, sand type, and relative density.

#### 2.3.2.4 Testing Techniques

The major tests available for the study of liquefaction, cyclic triaxial, torsional shear, and cyclic simple shear, should be regarded as index tests only, and not exact representations of in-situ soil behavior. Each type of test will give a different liquefaction potential for the same soil type, although the tests usually exhibit the same general trends. A comparative study of the different testing techniques by Bhatia, et al. [1985] indicated that, in general, triaxial tests predict the largest liquefaction resistance, and simple shear the lowest, with torsional shear test results between the two. The differences between the tests are essentially due to the ways in which the in-situ stress conditions and the earthquake loadings are modeled. Torsional shear tests are considered to represent stress conditions most closely, and will be discussed in more detail in Section 2.5.

Details that affect all of the testing methods include:

1. Test Frequency - It is important to cycle at a low enough frequency to allow pore pressure equalization within the sample. A frequency of 0.1 Hz or lower is appropriate for less permeable samples requiring longer equalization times;

2. Wave Form of Loading Cycles - The type of wave form has not been found to have a large effect on liquefaction, although a sine wave is preferred, as it enables a smooth load variation;

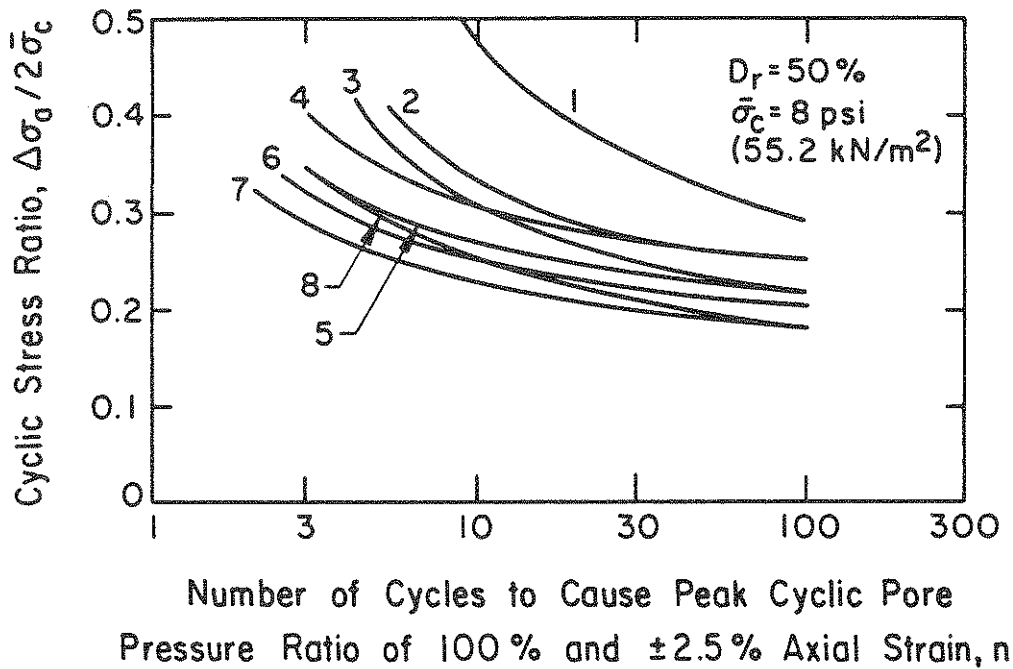
3. Saturation -  $B > 0.9$  is usually recommended for undrained testing ( $B = \Delta u / \Delta \sigma_3$ ). However, Chung, et al. [1984] recommended a minimum of 0.95 to obtain more consistent results. Achieving saturation is not a problem for clean sands, but can be difficult to attain in finer-grained materials; and

4. Sample Preparation - Obtaining "undisturbed" samples is extremely difficult to achieve economically for cohesionless materials, and thus samples used for research usually are reconstituted in the laboratory. The report by Mulilis, et al. [1977] on the effects of sample preparation procedures indicates that the manner of preparation has a major effect on a samples liquefaction characteristics. Several preparation techniques, including pluviation through air or water, and using vibration or tamping to densify a sample, were investigated. Figure 2-22 indicates the wide range of cyclic strengths obtained from the different preparation techniques. Ladd [1977] concluded that the method of specimen preparation had a large effect on cyclic triaxial strength. However, flow failure concepts based on steady-state strength are reported to be unaffected by sample preparation methods.

### 2.3.3 Liquefaction Failure Mechanisms

The National Research Council publication, "Liquefaction of Soils During Earthquakes," [1985], and Whitman [1985] have helped to categorize types of failure mechanisms and stress-strain behavior. State I and State II behaviors were described by Whitman [1985].

State I stress-strain behavior, as shown in Figure 2-23a, consists of the undrained monotonic loading defining a peak in the stress-strain curve, and then falling off to a steady-state value which is below the consolidation value of shear stress. It is characterized by an undrained stress path, with  $\bar{p} = (\bar{\sigma}_1 + \bar{\sigma}_3)/2$  monotonically decreasing, and a peak shear resistance larger than the final resistance,  $q_{cr}$  [ $q =$



<u>Curve No.</u>	<u>Method of Compaction</u>
1	High frequency vibrations on moist samples
2	Moist tamping
3	Moist rodding
4	Low frequency vibrations on dry samples
5	High frequency vibrations on dry samples
6	Pluviated-water
7	Pluviated-air
8	Dry rodding

FIGURE 2-22. Cyclic Stress Ratio versus Number of Cycles for Different Compaction Procedures [after Mulilis, et al., 1977]

$(\sigma_1 - \sigma_3)/2]$ . The second type of stress-strain behavior, as shown in Figure 2-23b, consists of the shear resistance under monotonic undrained loading initially rising sharply, then leveling off at larger strains, with a constant resistance being reached at high strains. State II is therefore characterized by monotonically increasing  $q$ . A sand in State I can sustain a static shear stress,  $q_s$ , greater than the steady-state resistance,  $q_{cr}$ . However, a sand in State II has a steady-state resistance larger than  $q_s$ . Therefore, State I describes loose or contractive behavior, and State II describes dense or dilative behavior.

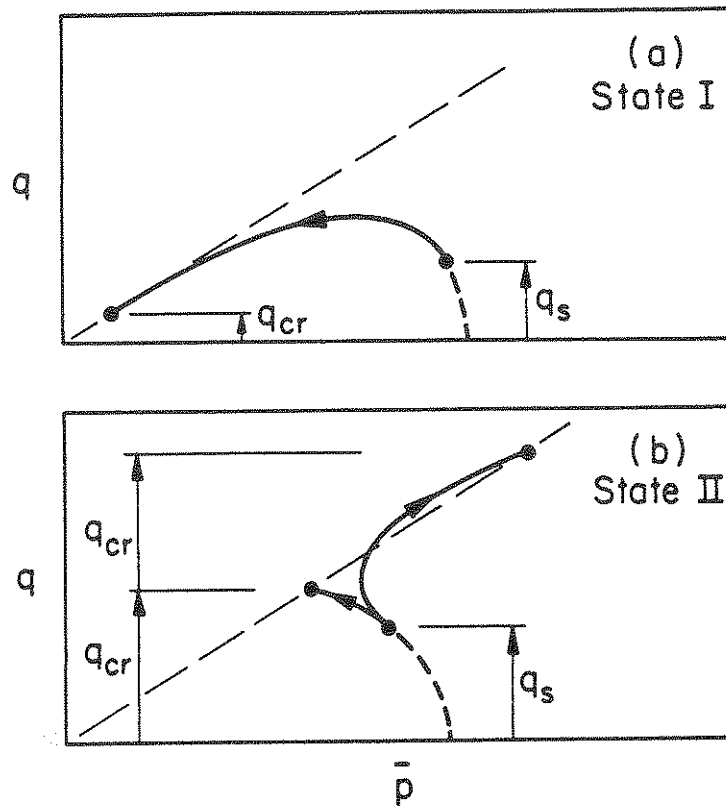


FIGURE 2-23. Undrained Stress Paths Characterizing Two States [after Whitman, 1985]

Whitman [1985] defined two types of failure, disintegrative and non-disintegrative. Disintegrative failure describes the condition in which a soil mass can deform continuously at a shear stress less than the static shear stress, i.e., a flow failure. This type of condition causes slope instability and bearing capacity-type failures. Nondisintegrative failures involve unacceptably large permanent displacements or settlements during or after an earthquake, but the earth mass remains stable.

Soil in State I is susceptible to disintegrative failures. Cyclic loading of sufficient amplitude and duration can reduce the resistance to the steady-state value. Thus, for an infinite slope, as shown in Figure 2-24a, a flow slide can occur if the static shear stress,  $q_s$ , is greater than  $q_{cr}$ . This is also referred to as failure Mechanism A.

For the other situations shown in Figure 2-24, disintegrative failures

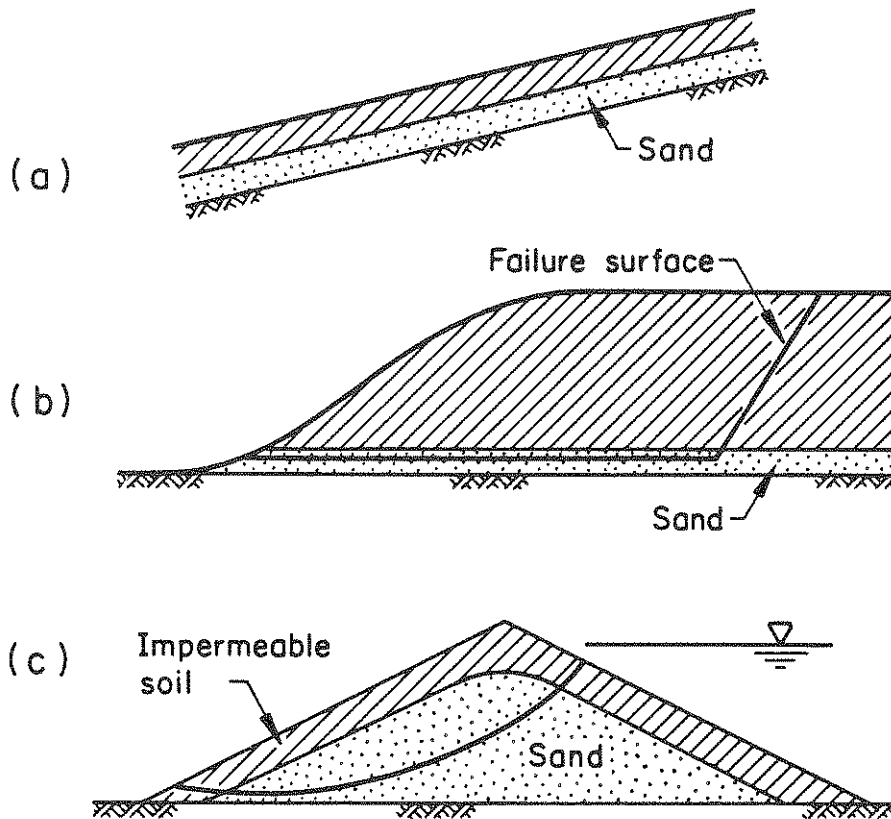


FIGURE 2-24. Sands Beneath Impermeable Soils [after Whitman, 1985]

can occur if the total shear force required for equilibrium along failure surfaces exceeds the steady-state strength of the soil in State I plus the shear resistance of the unaffected soil. Soil in State II is not likely to suffer disintegrative failures unless there is redistribution of void ratio within the soil, in which case there are two main types of failure.

If a sand layer is enclosed by relatively impervious soil, i.e., undrained in a global sense, then during or after shaking, instability may occur due to a loosening of the upper portion and densification of the lower portion of the layer, as shown in Figure 2-25. The result is that the steady-state resistance of the upper portion of the layer is reduced because of this redistribution of void ratio. Failure will occur if the shear resistance becomes less than the static shear stress. This is referred to as Mechanism B.

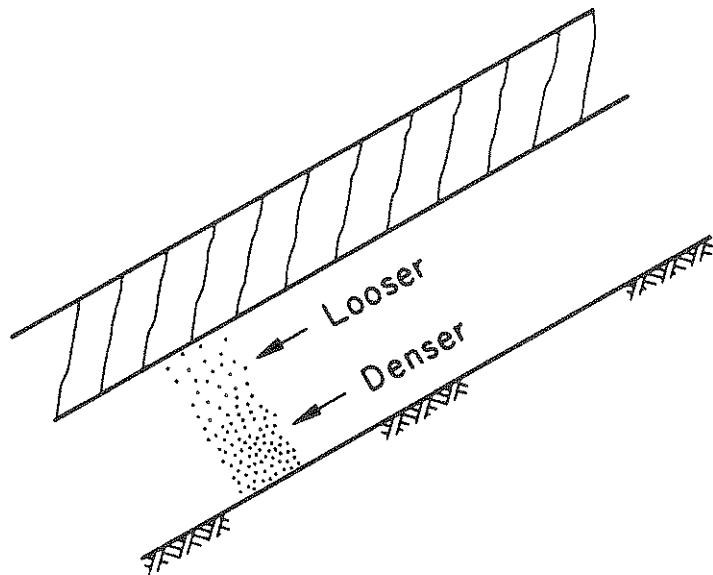


FIGURE 2-25. Example of a Potential Situation for Mechanism B Failure [after Committee on Earthquake Engineering, 1985]

If high excess pore pressures develop in a cohesionless material, then the pore pressures in the surrounding soil are likely to increase as well, thus reducing their shear resistance. Upward pressures may cause overlying cohesive soils to crack, and sand may be carried upward through these cracks to the surface (sand boils). The result is that the soil loses strength as a mass, and if this loss is great enough, instability may occur. This is referred to as Mechanism C. Permanent deformations large enough to be classified as nondisintegrative failures may occur because of accumulation of cyclic strains, buildup of plastic deformations (if the applied cyclic stress is large enough), or from excessive movements caused by a cohesionless soil softening due to pore pressure rise. Table 2-3 summarizes the failure mechanisms discussed above. Mechanism A is the Casagrande definition of liquefaction flow failure discussed in Section 2.3.1. Mechanism C is a restatement of the zero effective stress failure process.

Mechanism B has been observed to occur in many laboratory experiments [Castro, 1975], but its existence in the field is more speculative.

TABLE 2-3. Summary of Failure Mechanisms [after Whitman, 1985]

DRAINAGE CONDITIONS	STATE I	STATE II	
	DISINTEGRATIVE	DISINTEGRATIVE	NON-DIS-INTEGRATIVE
Undrained Locally	Mechanism A	Not Possible	Excessive Deformation But Not Instability
Undrained Globally	X	Mechanism B	
Diffusion of Pore Press.	X	Mechanism C	

#### 2.3.4 Liquefaction Pore Pressure Models

Many researchers have developed models to predict pore pressure rise during an earthquake. Seed, et al. [1976] developed the relationship:

$$r_u = 0.5 + (1/\pi) \arcsin[2r(1/\alpha) - 1] \quad (2-3)$$

where:

$$r_u = \Delta u / \bar{\sigma}_{3c},$$

$r$  = number of cycles (N)/number of cycles to liquefaction ( $N_L$ ),

and

$\alpha$  = shape factor, defined as equal to 0.7.

This equation is based on the  $r_u$  versus  $r$  relationship discussed earlier, and shown previously in Figure 2-9.  $N_L$  is a function of stress ratio,  $R$ , and relative density,  $D_r$ . It is a simplified and somewhat

empirical relationship which has been applied to all types of sands.

The following procedure may be used with Equation 2-3 to determine the rate of pore pressure generation in a soil deposit during an earthquake:

1. The time record of horizontal shear stresses developed by the design earthquake is evaluated by any appropriate procedure, e.g., a ground response analysis or a simplified procedure [Seed and Idriss, 1971].

2. Using a weighting procedure, the effects of the actual stress history is then represented by an equivalent number of uniform stress cycles,  $N_{eq}$ , having a peak stress amplitude,  $\tau_{eq}$ , developed over a selected duration of sampling characterized by a period,  $T_{eq}$ . Seed, et al. [1976] suggested that  $\tau_{eq}$  can be taken as 65% of the maximum shear stress developed. Corresponding values of  $N_{eq}$  and shaking duration for different earthquake magnitudes are given in Table 2-4.

3. Then, for the known conditions of overburden pressure, density, and  $\tau_{eq}$ , the number of cycles required to produce a condition of initial liquefaction in a sand layer can be determined from experimental results, such as those shown in Figure 2-26. If the soil layer is undrained, the rate of development of pore pressures in the layer can be determined. For  $N_L < N_{eq}$ , the layer will liquefy before shaking is completed after a time of  $N_L \times T_{eq}$ . For  $N_L > N_{eq}$ , the pore water pressure without any allowance for dissipation would develop as predicted by Equation 2-3. A procedure has also been developed [Seed, et al., 1976] using Terzaghi's one-dimensional consolidation theory to take account of the dissipation of the excess pore pressure and settlement occurring with time.

Finn, et al. [1978] extended Equation 2-3 to take into account anisotropic consolidation stress effects by varying  $\alpha$  with  $K_c$ . Since anisotropically consolidated samples rarely reach initial liquefaction, Finn, et al. [1978] decided to use  $N_{50}$  (number of cycles to develop a pore water pressure equal to 50% of the confining stress,  $\bar{\sigma}_{3c}$ ), instead of  $N_L$  in Equation 2-3. For a particular test sand, Figure



TABLE 2-4. Earthquake Magnitude and Corresponding Values of  $N_{eq}$  and Shaking Duration [after Seed, et al., 1976]

Earthquake Magnitude	$N_{eq}$	Duration of Strong Shaking (seconds)
5½ - 6	5	8
6½	8	14
7	12	20
7½	20	40
8	30	60

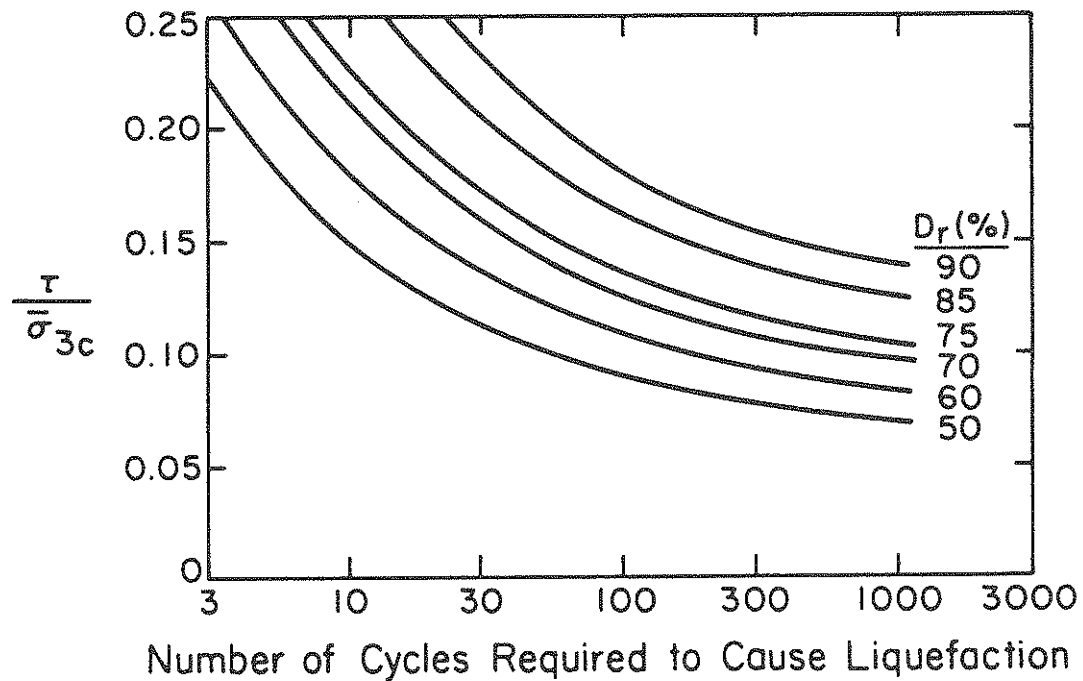


FIGURE 2-26. Relationship Between Cyclic Stress Ratio and Number of Cycles Required to Cause Liquefaction for Simple Shear Tests on Medium Sand at Different Relative Densities [after Seed, et al., 1976]

2-27 illustrates pore pressure ratio versus  $N/N_{50}$  for varying  $K_c = \bar{\sigma}_{1c}/\bar{\sigma}_{3c}$  values, using the modified equation as shown. Chang, et al. [1983] found that these modifications applied only to low values of  $K_c$ , and therefore extended Finn, et al.'s work to include more general anisotropic conditions.

For higher values of  $K_c$ , the pore pressure buildup will be less than 50% of  $\bar{\sigma}_{3c}$ . Therefore, instead of using  $N_{50}$ , a more general form was suggested, where  $N_{50} = \Delta u/u_f$ . The limiting value of residual pore pressure,  $u_f$ , that can occur in a sample for a given  $K_c$  condition is dependent on the effective stress friction angle ( $\bar{\phi}$ ) and  $\bar{\sigma}_{3c}$ .

Equation 2-3 was based mainly on cyclic triaxial tests. Ishibashi and Sherif [1974] developed expressions to predict pore pressure buildup based on torsional shear testing. Ishibashi, et al. [1977] developed predictive equations for both uniform and nonuniform cyclic loading, which gave good agreement with experimental values for Ottawa sand. Sherif, et al. [1978] extended these equations to use with Ottawa sand at varying relative densities. Ishibashi, et al. [1982] produced a more general form of the pore pressure rise model to cover a wider range of sands.

Vaid and Chern [1985] presented an attempt to unify the monotonic and cyclic loading response of saturated sands. A three-dimensional effective stress state diagram for sand using effective normal stress, shear stress, and void ratio space was devised to provide a link between monotonic and cyclic loading responses. The diagram featured boundary surfaces separating states which are contractive from those which are dilative. Critical stress conditions that marked the onset and arrest of contractive deformation were also identified. The model was based on cyclic and monotonic triaxial tests on two types of sand, and therefore is not as generally applicable as that given by Seed, et al. [1976] or Ishibashi, et al. [1982].

Vaid and Chern [1985] defined a new term, "limited liquefaction." Liquefaction flow failure and cyclic mobility are defined in the usual

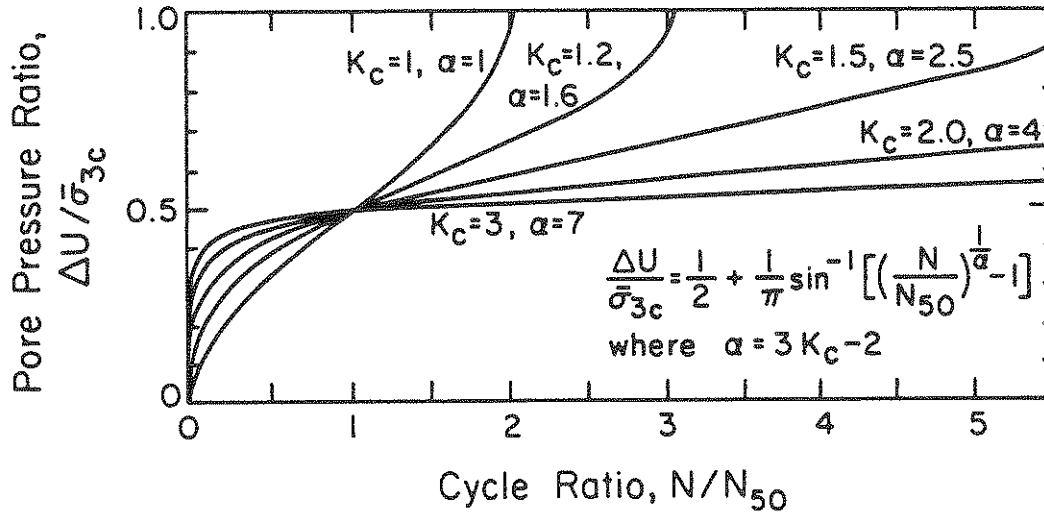


FIGURE 2-27. Normalized Curves from Pore Pressure Buildup Equation [after Finn, et al., 1978]

way, as shown in Figure 2-28. Limited liquefaction is liquefaction flow which develops over a limited strain range. This type of response is characterized by a temporary loss of shear resistance that is regained with further straining, as shown in Figure 2-29 ( $\sigma_d$  = deviator stress, and  $\epsilon_v$  = axial strain). This type of response occurs "in between" purely dilative and contractive behavior, and is shown as line 2 in Figure 2-30. Therefore, during cyclic loading, deformation may be due to limited liquefaction, cyclic mobility, or a combination of both.

## 2.4 RESONANT COLUMN TESTING

### 2.4.1 Introduction

The aim of the resonant column test is to determine the modulus and damping properties of a soil by means of wave propagation in a cylindrical specimen. The frequency of an applied vibration is varied until "resonance" develops. For these tests, resonance is defined as the frequency at which there is a  $\pi/2$  phase angle between the forcing function and resulting displacement. This frequency, the magnitude of applied force, and the resulting strain are used to calculate modulus and damping. When axial compression is applied, Young's modulus and

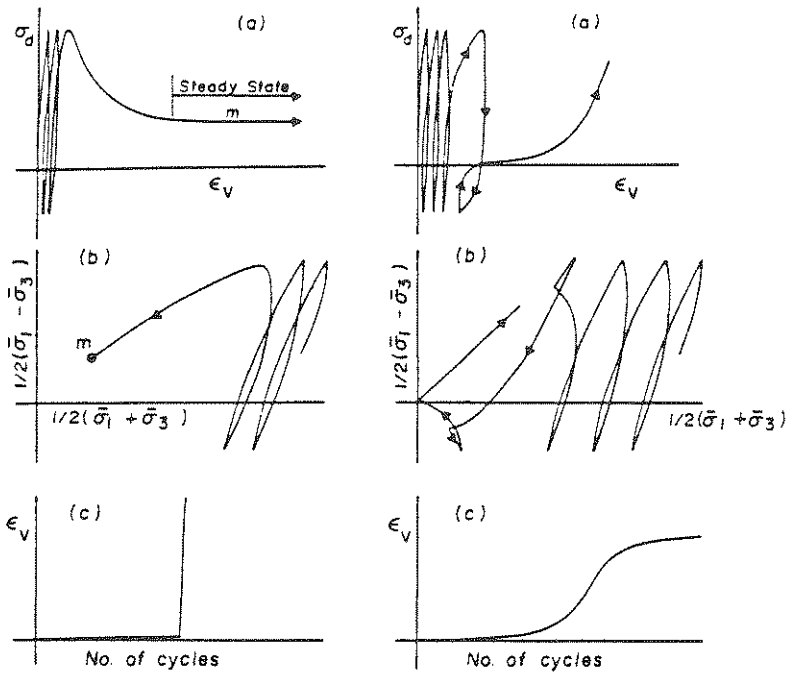


FIGURE 2-28. (a) Liquefaction Due to Cyclic Loading, and (b) Cyclic Mobility Due to Cyclic Loading [after Vaid and Chern, 1985]

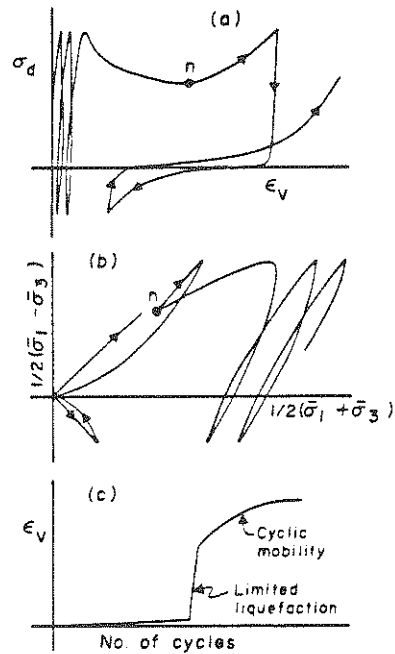


FIGURE 2-29. Limited Liquefaction Due to Cyclic Loading [after Vaid and Chern, 1985]

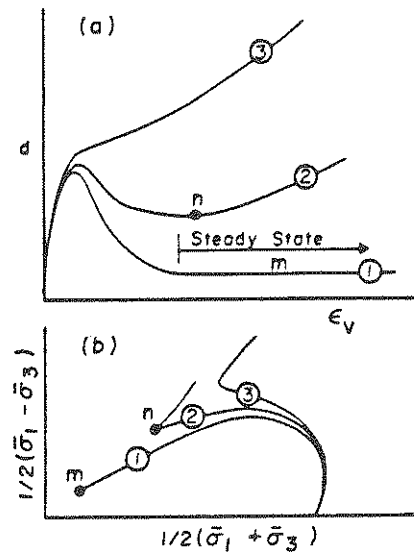


FIGURE 2-30. Characteristic Behavior of Saturated Sand Under Undrained Monotonic Loading [after Vaid and Chern, 1985]

damping due to rod compression are obtained as functions of axial strain amplitude. If torsion is applied, shear modulus and shear damping are obtained as functions of shear strain amplitude. Resonant column tests can give accurate results for strain amplitudes as low as 0.0001% and as high as 0.1%, or higher using hollow specimens.

To excite and measure the vibration of a system, the system itself must be altered by the required measurement transducers and excitation device [Hardin, 1965]. Therefore, the observed vibration is not the response of the soil specimen alone, but of the system and attached apparatus, e.g., platens, pressure tubing, o-rings, etc. Hence, to interpret the frequency response in terms of specimen parameters, the contribution of all of the other elements in the system must be accounted for. Drnevich [1978; 1985] presents methods and procedures which can be used to calibrate and reduce data from resonant column devices.

A test is carried out on a specimen which has a complex constitutive relationship. Therefore, a model for the system must be assumed,

including parameters to describe the apparatus, the specimen, and the excitation. The model is used by assuming the unknown parameters (modulus and damping ratio), and varying the assumed values until the motion of the model matches the motion measured in the test. Early work in resonant column testing for low amplitudes assumed the specimen to be elastic, and therefore the theory of propagation of waves in elastic bars could be used to interpret the results. However, for higher strain amplitudes and with the increased importance of damping, a generalized linear viscoelastic model (Kelvin-Voigt) is used. This model is straightforward to use and can describe accurately the behavior of soils excited by steady-state sinusoidal motion, although it is inadequate to describe highly nonlinear stress-strain responses.

#### 2.4.2 Types of Resonant Column Systems

Several resonant column devices have been developed using different boundary conditions. Three commonly used boundary conditions are shown in Figure 2-31. The most widely used configurations are the systems with one end of the specimen fixed, as shown in Figure 2-31a and b. In the "fixed-free" type, vibration is applied and the response is measured at the top platen (active-end), and the bottom platen is rigidly fixed (passive-end). The distribution of angular rotation along the sample, in the specimen of a "fixed-free" device, is a 1/4 sine wave, as shown in Figure 2-32a. By adding a mass with polar moment,  $J_0$ , to the top of the specimen, as shown in Figure 2-32b, the variation of angular rotation along the sample becomes almost linear. Therefore, most "fixed-free" models use end mass effects to obtain uniform strain distribution throughout the specimen.

The mass attached to one or both ends of the specimen represents the platen, the equipment used to apply the force or torque, and the transducers used to measure the resulting motion. The springs and dashpots attached to the mass are to account for damping, and for springs which may be used to support the upper platen. Springs can be used to provide anisotropic stress conditions, although they tend to limit the strain amplitude capabilities of the apparatus [Drnevich,

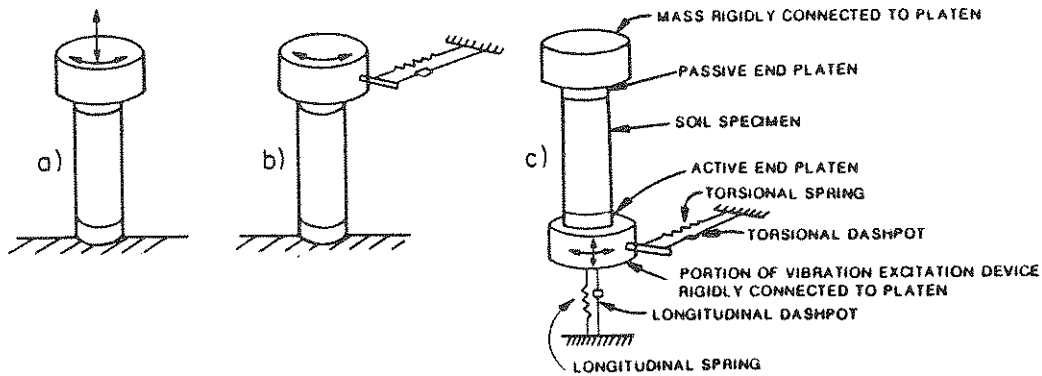


FIGURE 2-31. Common Resonant Column Boundary Conditions: (a) Fixed-Free; (b) Fixed Spring Top; (c) Free-Free [after Drnevich, 1985]

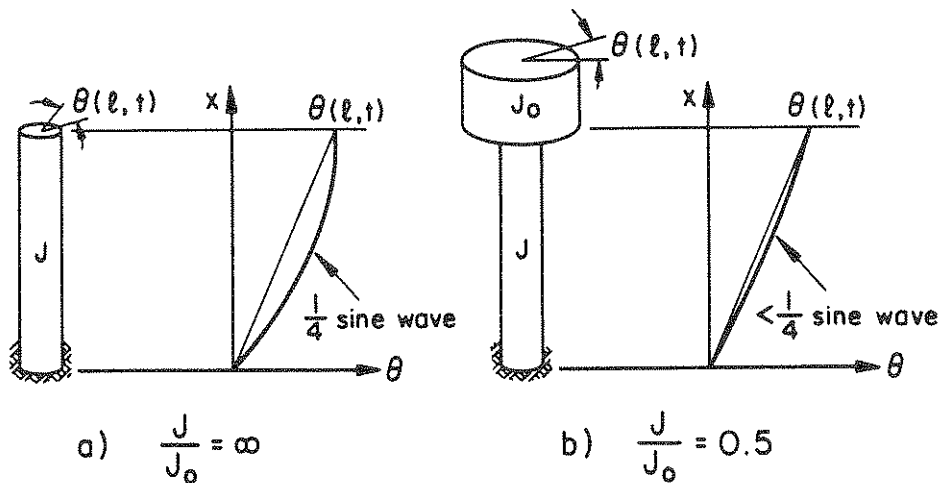


FIGURE 2-32. Schematic of Resonant Column End Conditions [after Woods, 1978]

1985]. If a single spring is used to support the upper platen and excitation device, a single degree of freedom system, which is easier to calibrate, is created.

Figure 2-31c shows a system where neither end is fixed, i.e., a "free-free" type apparatus. This type of system is advantageous for testing

large size specimens and specimens that are unusually stiff, such as shales, rock, concrete, asphalt, and cemented soils.

Other types of low strain testing equipment include a free torsional vibration system developed by Shen, et al. [1985]. In this system, an initial torque applied to a specimen by an electromagnetic oscillator. When the torque is released, the system undergoes free vibration. The acceleration decay of the system is recorded so that shear modulus and damping ratio of the system may be calculated. Saada, et al. [1978] describe a hybrid loading system in which both dynamic resonance and quasi-static testing are applied to the same specimen. Systems which utilize the same electromagnetic system for both quasi-static and resonance testing are described by Drnevich [1972] and Isenhower, et al. [1987]. The torque for quasi-static testing is determined by measuring the current applied to the drive system, and displacements are measured using non-contacting transducers. These types of hybrid systems are, by their nature, torque rather than rotation-controlled, so that as high pore pressures build up, large uncontrolled strains occur.

Drnevich [1985] developed another type of hybrid system which incorporates a Hardin-type oscillator and a rotation or torque controlled quasi-static loading system. A stepper motor provides rotation to the loading piston, which is fastened to the inertial reaction mass of the oscillator. This combined system can study the effects of strain amplitudes ranging from 0.0005% to 10%. This system is described more fully in Section 3.

Despite the different configurations, Skogland, et al. [1976] and Woods [1978] reported that all devices used for resonant column testing produced consistent results. Also, results from resonant column testing appear to be consistent with results found from other methods of cyclic testing [Iwasaki, et al., 1978; Alarcon-Guzman, 1986].

#### 2.4.3 Shear Modulus and Damping Ratio Determination

A number of practical testing problems occur when using the resonant



column device. Problems such as membrane penetration [Vaid and Negusse, 1984], saturation problems, and air migration through the membrane are similar to those encountered during standard triaxial testing. Problems specific to resonant column testing are discussed by Drnevich [1978]. Saada and Townsend [1981] review details about specimen geometry and suggest that, while length-to-diameter ratios of 2.5 are sufficient for solid cylindrical specimens, research testing using hollow cylindrical specimens will be influenced by end effects unless:

$$L \geq 5.44 (r_o^2 + r_i^2)^{0.5} \quad (2-4)$$

and

$$r_i/r_o \geq 0.65 \quad (2-5)$$

where:

- L is the specimen length,
- $r_i$  is the inside radius, and
- $r_o$  is the outside radius.

However, Saada [1985] suggests that these restrictions are too stringent, and that length to diameter ratios of 1.5 are sufficient to ensure uniformity of stresses.

The general use of hollow cylindrical samples for torsional shear and resonant column testing has been discussed in detail by Saada [1985]. The basic advantage of the hollow sample is that the average shearing strain on any horizontal cross-section is not greatly different from the maximum or minimum, and shearing strain is uniform along the height of the specimen. This is an improvement from the solid cylindrical samples, where shear strain varies from zero at the center to a maximum at the outer surface, and where the distribution of shear strain across the sample must be assumed. However, hollow samples are more difficult to prepare and, because of their increased membrane area, are more susceptible to membrane penetration effects. Chung, et al. [1984] and Alarcon-Guzman [1986] found no significant differences in the test results between the two types of specimens.

The problem of insufficient coupling between the specimen and both end platens can cause slipping. If slipping occurs, lower shear moduli and higher damping values would result. However, special end platens, porous disks with embedded razor blades, are only required for exceptional cases. Drnevich [1978] developed a criterion based on the mobilization of a minimum coefficient of friction between soils of 0.2 to determine when the use of normal roughened porous disks was unacceptable. Therefore, to determine if full coupling exists for a strain amplitude,  $\gamma$ , and for a specimen with a shear modulus,  $G$ ,

$$\gamma G / \bar{\sigma}_a < 0.2 \quad (2-6)$$

where  $\bar{\sigma}_a$  is the effective axial stress applied by the platen to the specimen. For cases where the above equation is not satisfied, special top and bottom platens are required.

Many researchers have used the resonant column to study the shear modulus, damping ratio, and pore pressure generation characteristics of soil. In particular, Chung, et al. [1984] have summarized the findings of several researchers on the determination of shear modulus.

$G_{\max}$  is the value of the shear modulus at the lowest measured shear strain amplitude. Shear modulus is usually normalized by  $G_{\max}$  when plotted against shear strain, to allow for different confining pressures and relative densities. In a similar way, damping ratio can be divided by the minimum damping ratio when plotted against shear strain amplitude. Stokoe, et al. [1980] presented several researchers' results which show the typical shapes of curves obtained from resonance testing. Figure 2-33 shows normalized shear modulus versus shearing strain, and Figure 2-34 shows normalized damping ratio versus shearing strain.

Chung, et al. [1984] studied the pore pressure buildup in resonant column tests for Monterey No. 0 sand. Figure 2-35 is a summary of stabilized excess pore pressure ratio against shear strain. Stabilized values are values obtained for a large number of cycles before

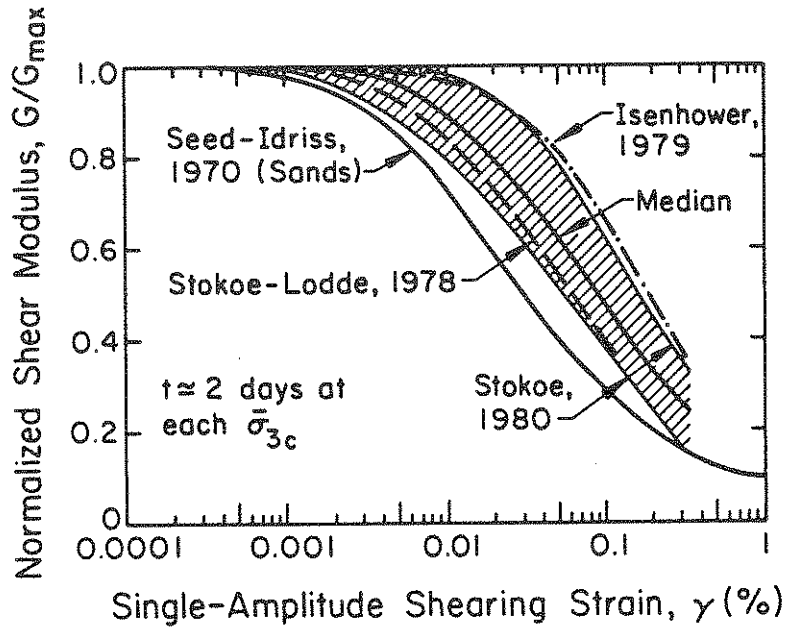


FIGURE 2-33. Summary of Normalized Shear Modulus Variation with Shearing Strain [after Stokoe, et al., 1980]

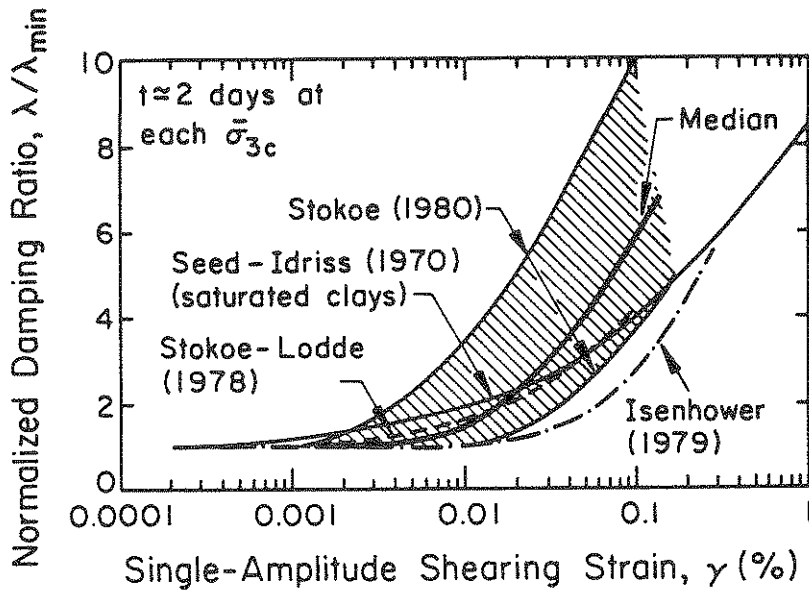


FIGURE 2-34. Summary of Normalized Damping Ratio Variation with Shearing Strain [after Stokoe, et al., 1980]

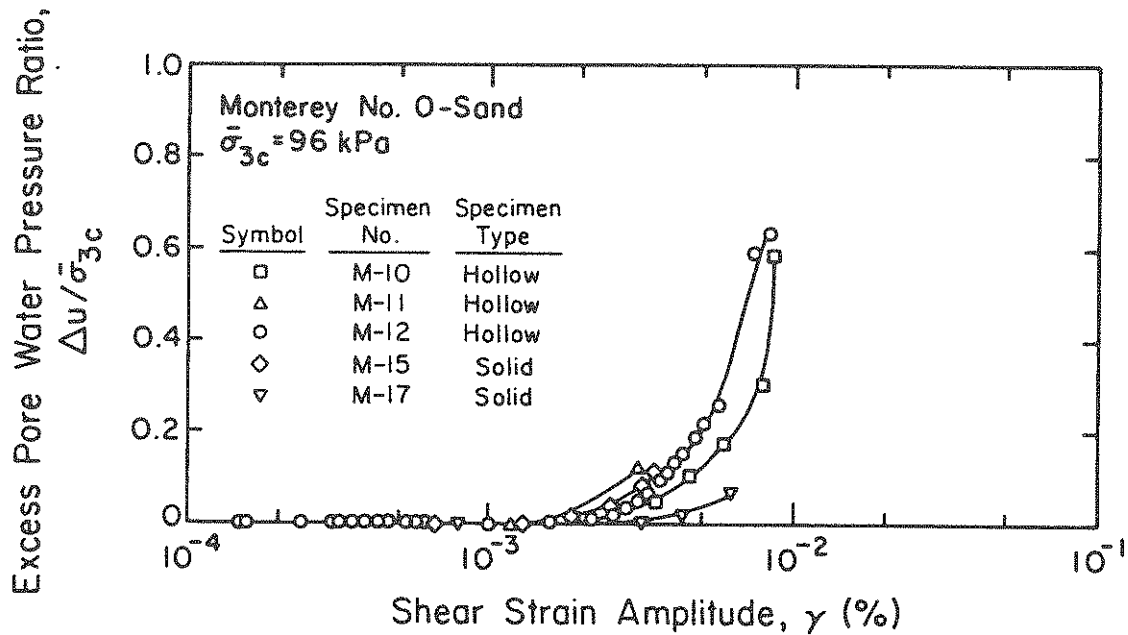


FIGURE 2-35. Summary of Excess Pore Water Pressure Buildup versus Shear Strain Amplitude [after Chung, et al., 1984]

liquefaction occurs. Two main observations can be made from this figure:

1. The threshold strain amplitude for excess pore pressure generation under a very large number of strain cycles was approximately 0.002%. The threshold strain level suggested by Dobry, et al. [1981], 0.01%, is much larger because it was referenced to only 10 loading cycles. This suggests that the number of loading cycles has an effect on the threshold shear strain level, and

2. At cyclic strain amplitudes larger than the threshold strain but smaller than approximately 0.0085%, the excess pore pressure ratio increased to a level smaller than unity and stabilized at that level.

Since resonant column tests operate at frequencies usually more than 100 Hz, they are not used normally to study pore pressure buildup, as pore pressure rise occurs too rapidly at cyclic strains above the threshold shear strain. Therefore, although other cyclic tests which operate at much lower frequencies more normally are used to study the

rate of pore pressure buildup, resonant column tests can still be used to study the parameters which affect threshold shear strain, such as type of sand, initial confining pressure, relative density, number of loading cycles, and specimen preparation method.

Dobry, et al. [1981] used the concepts of threshold strain and modulus reduction curves, with in-situ measurement of shear modulus,  $G$ , to determine the liquefaction potential of a site. The resonant column test is one of the few lab tests that operates at a low enough strain amplitude to be comparable to geophysical in-situ testing, and that can be used to determine the low strain portion of the modulus reduction curve. Threshold strain also can be determined by the resonant column test, although the concept, as presented by Dobry, et al. is referenced to 10 loading cycles using cyclic torsional tests, which makes it appropriate for earthquake loading. Resonant column tests usually subject a specimen to thousands of loading cycles.

Due to sampling effects and testing procedures,  $G_{lab}$  is generally found to be less than  $G_{field}$ . Richart, et al. [1977] developed an empirical relationship relating  $G_{lab}$  to  $G_{field}$  using in-situ shear wave measurements and resonant column results. De Alba [1984] discussed the idea that elastic wave velocities respond to minor changes in soil structure or fabric, and therefore can be used for determining the effects of sample disturbance. Also, the measurement of  $G_{max}$  by resonant columns has been used to judge if laboratory specimens replicate field conditions, or to what extent the fabric of a reconstituted specimen is similar to that of the in-situ material. When working with reconstituted specimens, the use of resonant columns has been recommended to investigate the effects of factors such as stress or strain history, aging, and anisotropic effects [Drnevich, 1979; 1985].

## 2.5 CYCLIC TORSIONAL TESTING

### 2.5.1 Introduction

The problems in representing in-situ stresses during an earthquake

with cyclic triaxial tests were discussed in Section 2.2. As an improvement on the cyclic triaxial test, Peacock and Seed [1968] proposed the use of the simple shear test to study liquefaction. In a cyclic simple shear test, the specimen is  $K_0$ -consolidated ( $K_0 = \bar{\sigma}_h / \bar{\sigma}_v$ ), and then subjected to a cyclic shear stress applied on a horizontal plane. The results of these tests gave a resistance to liquefaction of about one third, under analogous conditions, of that found in cyclic triaxial tests.

Despite the apparent accuracy with which the in-situ stress conditions during an earthquake are represented, the cyclic simple shear test has limitations. The lateral stress cannot be controlled directly, so the effects of non- $K_0$  conditions on liquefaction potential cannot be investigated independently. Also, the generation of nonuniform boundary stresses may cause specimens to fail at lower stresses than required for failure in the field. These issues and subsequent developments in simple shear testing have been discussed in detail by Woods [1978] and Saada and Townsend [1981].

The torsional shear test was developed by Ishihara and Li [1972] as an improvement to the existing cyclic tests. As such, the test allows the reproduction of the most general stress conditions. A torque (stress control) or a rotation (strain control) is cycled to simulate earthquake loadings and the resulting rotations of the planes of principal stress. Applying a torque, along with a confining pressure and an axial load, allows the reproduction of almost any desired stress state or stress path. Additionally, the large strains which occur during liquefaction flow failure can also be duplicated under either monotonic or cyclic shear loading.

### 2.5.2 Stress States

The stress state in solid cylindrical samples for an anisotropic cyclic torsional test is shown in Figure 2-36a. Where  $\bar{\sigma}_{1c}$  is the effective axial stress,  $\bar{\sigma}_{3c}$  is the effective confining pressure, and  $\tau_{cy}$  is the applied cyclic stress. For strain control tests,  $\gamma_{cy}$  is

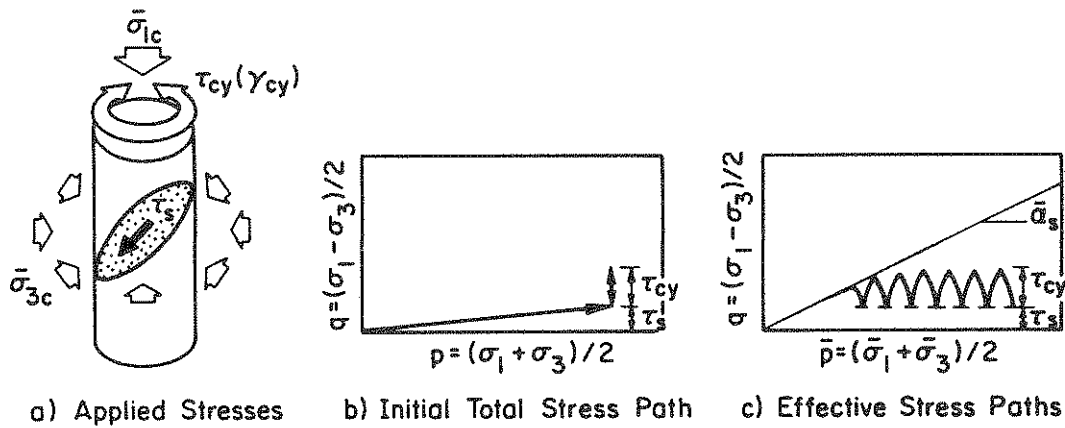



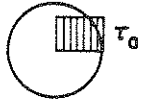
FIGURE 2-36. Stress Conditions in Strain-Controlled Test [after Dobry, et al., 1985]

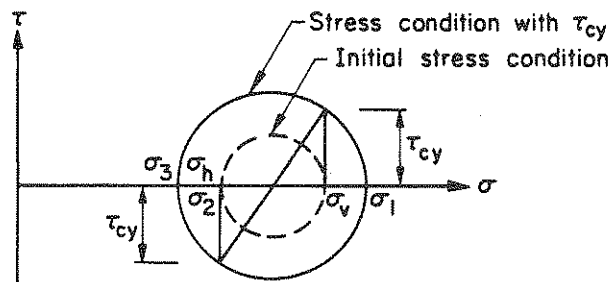
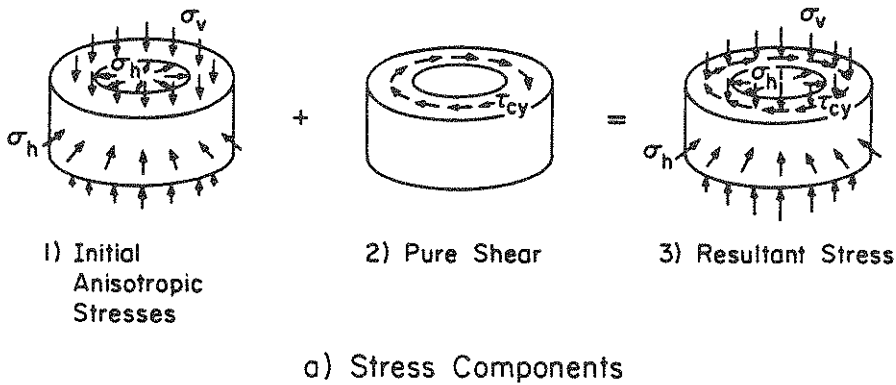
the applied shear strain, and  $\gamma_s$  represents the static shear stress which exists in the field before the earthquake. The total and effective stress paths are shown for a typical test undergoing torsional stress-controlled loading in Figure 2-36b and c.

In solid specimens, the shear strains vary from zero at the center to a maximum at the outside radius. The resulting variation in shear stresses will depend on the stress-strain properties of the specimen, making the stress distribution across the specimen nonlinear and strain-dependent. However, taking the two extreme stress distribution cases, a linear variation (elastic model for low strains), and a uniform level of shear stress (rigid plastic model for higher strains), the difference between the average shear stresses, shown in Table 2-5, is only 11% [Ishihara and Li, 1972].

Tests using hollow cylindrical specimens were developed to reduce the problems with nonuniformities in the solid sample, and have been discussed briefly in Section 2.4.3. Hollow specimens also help to reduce pore pressure gradients within the sample during testing. Figure 2-37a shows the stress components for a hollow sample with an initial anisotropic loading,  $\bar{\sigma}_h$  and  $\bar{\sigma}_v$ , and an incremental torsional loading,  $\tau_{cy}$ . The Mohr's diagram representing this anisotropic stress state is shown in Figure 2-37b. The internal and external pressures acting on

TABLE 2-5. Relationships Between Torsional Moments and Average Shear Stress [after Ishihara and Li, 1972]

	Distribution of Stress	Maximum Shear Stress $\tau_o$	Average Shear Stress $\tau_{av}$	$\frac{\tau_{av}}{\tau_o}$
Linear - Elastic		$2.0 \frac{M}{\pi a^3}$	$1.33 \frac{M}{\pi a^3}$	0.67
Rigid - Plastic		$1.5 \frac{M}{\pi a^3}$	$1.50 \frac{M}{\pi a^3}$	1.00



b) Mohr's Diagram Representation of Stresses

FIGURE 2-37. Mohr's Diagram Representation of Stresses [after Ishibashi and Sherif, 1974]



the sample are normally the same, although Hight, et al. [1983] constructed a torsional shear device where the internal and external pressure could be varied independently. The stress conditions and equations used for data reduction are discussed in more detail in Appendix D.

Strain control tests using a torsional cyclic shear strain to simulate seismic action recently have become preferred to stress control tests [Dobry, et al., 1985]. It has been shown that cyclic strain is a more fundamental parameter than cyclic stress in controlling pore pressure buildup in saturated sands, due to the existence of a threshold cyclic shear strain below which no excess pore pressures are generated. Also, the use of  $\gamma_{cy}$  makes the test results much less sensitive to several factors, including specimen preparation method and relative density.

### 2.5.3 Types of Torsional Shear Systems

There are two main types of system which have been used for torsional simple shear testing. Figure 2-38 illustrates the system configuration and specimen shape used and developed by Ishibashi and Sherif [1974]. The short hollow specimen with different inner and outer heights was designed so that uniform shearing strains throughout the specimen would be developed during torsional shearing. The bottom taper is proportional to the inner and outer radii.

The second main type of system is shown in Figure 2-39, the major difference being that a long hollow specimen with equal inner and outer heights is used. Ishihara and Yashuda [1975] and Iwasaki, et al. [1978] have developed and used this configuration.

Both of these types of systems have drawbacks and advantages. Woods [1978] notes that "undisturbed" specimens can be constructed more easily for the shorter cylindrical sample than the taller configuration. However, the smaller sample is subject to greater boundary effects and stress concentrations, along with nonuniformities caused by varying vertical strain throughout the specimen. For the larger

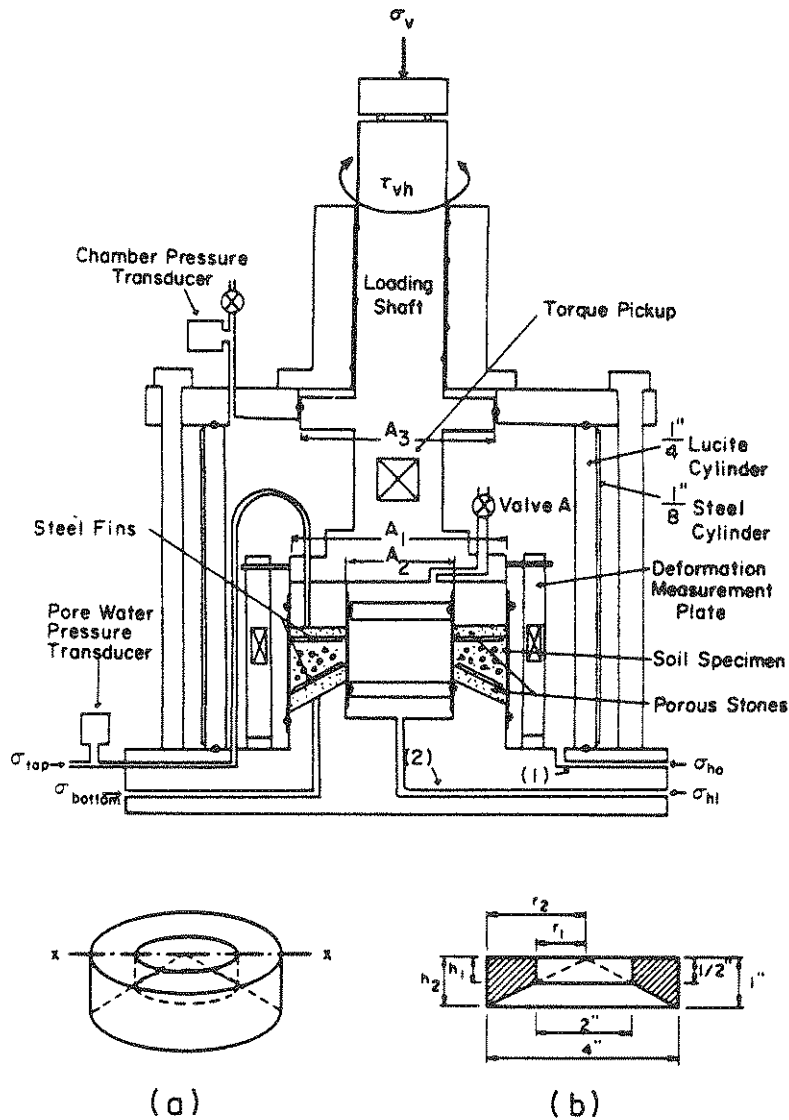


FIGURE 2-38. Torsional Simple Shear Device Short Specimen:  
 a) Specimen Shape, and b) Cross-Section [after  
 Ishibashi and Sherif, 1974; Ishibashi, et al., 1985]

specimen, Wright, et al. [1978] developed criteria, given in Equations 2-4 and 2-5, which ensure that a central zone is free of end effects. The larger specimen will therefore suffer proportionally less boundary disturbance than the smaller specimen. A more detailed discussion on sample shape, equipment configuration, and testing effects is given by Ishibashi, et al. [1985].

The hybrid resonant column/torsional shear devices, which also use long specimens, have been discussed in Section 2.4.2. Note that the

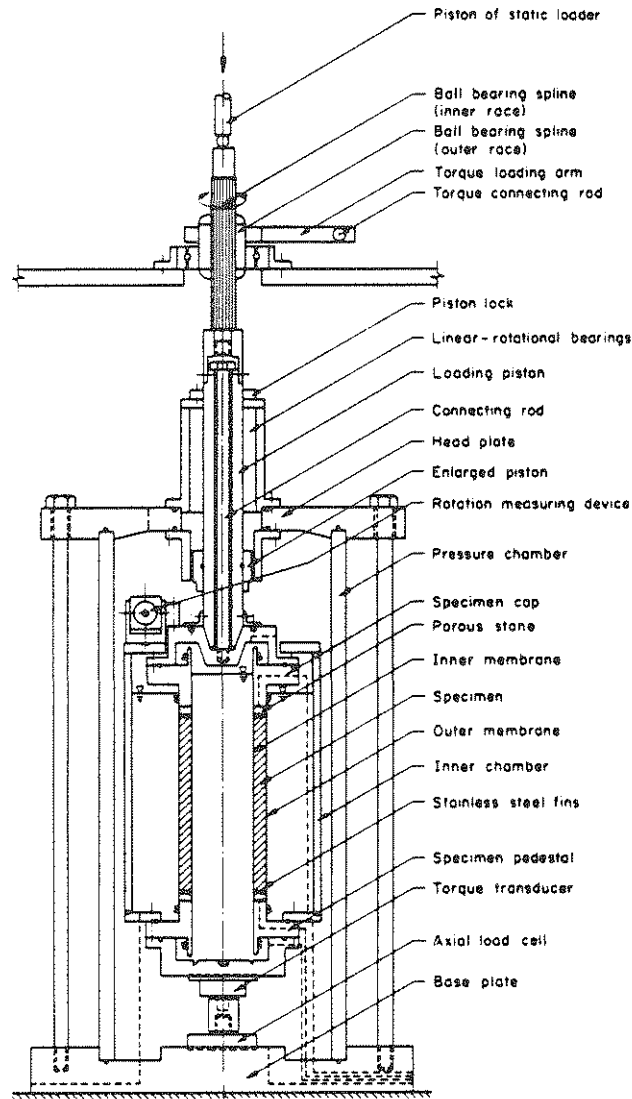


FIGURE 2-39. Torsional Simple Shear Device Long Specimen [after Ishibashi, et al., 1985]

torsional shear device is an improvement on the cyclic triaxial test in that end effects have been reduced greatly and in-situ stress conditions are modeled more accurately. These types of devices also improve upon cyclic simple shear devices, as different anisotropic consolidation stresses can be modelled, boundary nonuniformities (e.g., sidewall friction) have been reduced, and the pore pressure parameter,  $B$ , can be measured during the saturation procedure. It is important to achieve  $B > 0.9$  during saturation procedures, as liquefaction potential is dependent on the degree of saturation. The

effect of B on liquefaction potential is shown in Figure 2-40 and discussed by Sherif, et al. [1977].

#### 2.5.4 Liquefaction by Torsional Shear Device

The torsional shear device has been used to study a number of the factors affecting liquefaction potential. For example, Ishihara and Li [1972] studied the effects of initial stress anisotropy on pore pressure buildup in saturated solid sand samples using strain control torsional shear tests. For isotropically consolidated torsion tests (ICT-test), specimens were consolidated under an ambient pressure and then subjected to a constant cyclic shear strain under undrained conditions. In anisotropically consolidated torsional tests (ACT-test), specimens were consolidated under different axial and lateral confining stresses, and then sheared undrained while the axial stress was kept constant. The results of ICT and ACT tests, reported by Ishihara and Lee [1972], are shown in Figure 2-41, which gives normalized shear stress, pore pressure rise, and axial strain against number of cycles (note that the ICT tests have a  $K = 1.0$ , where  $K = \bar{\sigma}_3/\bar{\sigma}_1$ ). The figure suggests that ICT tests develop the largest increase in pore pressure and reduction in sustainable shear stress, although ACT tests ( $K = 0.5$  and  $0.75$ ) show the largest axial displacements. Note that pore pressure increase in the ACT tests reaches a constant value after a certain number of loading cycles. Therefore, increased anisotropy increases resistance to initial liquefaction, and thus agrees with the cyclic triaxial test findings discussed in Section 2.3.2.

Ishihara and Yasuda [1975] studied the effects of irregular torsional excitation on the liquefaction characteristics of saturated sands. The acceleration records from several earthquakes were used as load histories, and reproduced by an electro-hydraulic loading system. Two basic types of earthquake loading were studied: shock or single impulse loading, and vibration loading. In pore pressure buildup studies, it was found that vibration-type loadings produced behavior similar to that observed under the equivalent sinusoidal loading patterns. Shock-type earthquake loading, however, was found to produce

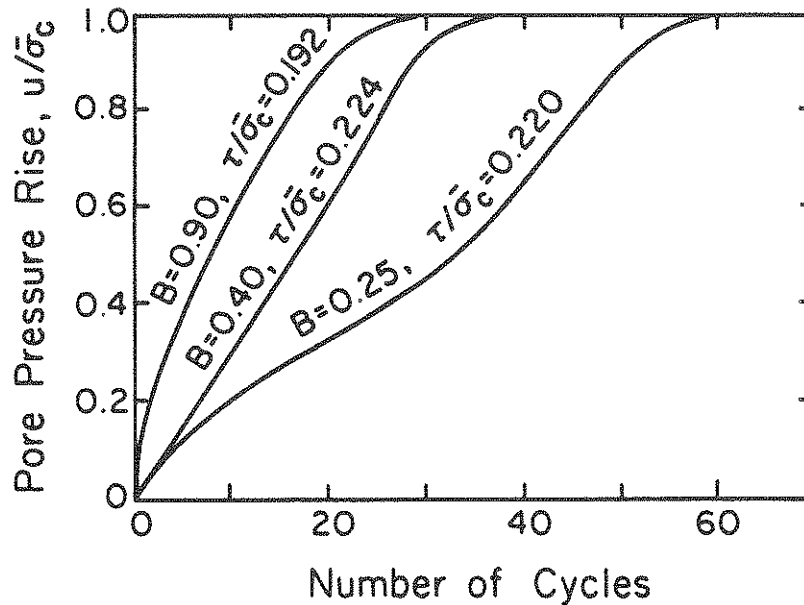


FIGURE 2-40. Typical Liquefaction Data for Low B and High B Values [after Sherif, et al., 1977]

much less pore pressure buildup.

Ishibashi, et al. [1985] used a long hollow cylinder torsional shear device to study the liquefaction potential of sands under initial,  $\gamma_{ini}$ , and cyclic,  $\gamma_{cy}$ , shear strains. Figure 2-42 illustrates the results of undrained strain control tests, and indicates that pore pressure buildup is not influenced greatly by the existence of initial static shear applications.

Dobry, et al. [1985] used solid samples and strain control tests to study liquefaction flow failure in saturated silty sands under isotropic and anisotropic conditions. Three different soils were tested. Sands A, B, and C were sampled from the same deposit, but with different nonplastic silt contents of 13%, 32%, and 63%, respectively. Cyclic and monotonic tests were used to determine the steady-state lines of the sands. Compared to monotonic tests, cyclic tests provide additional information on the rate of pore pressure buildup, number of cycles to flow failure, and state of stresses at triggering of flow

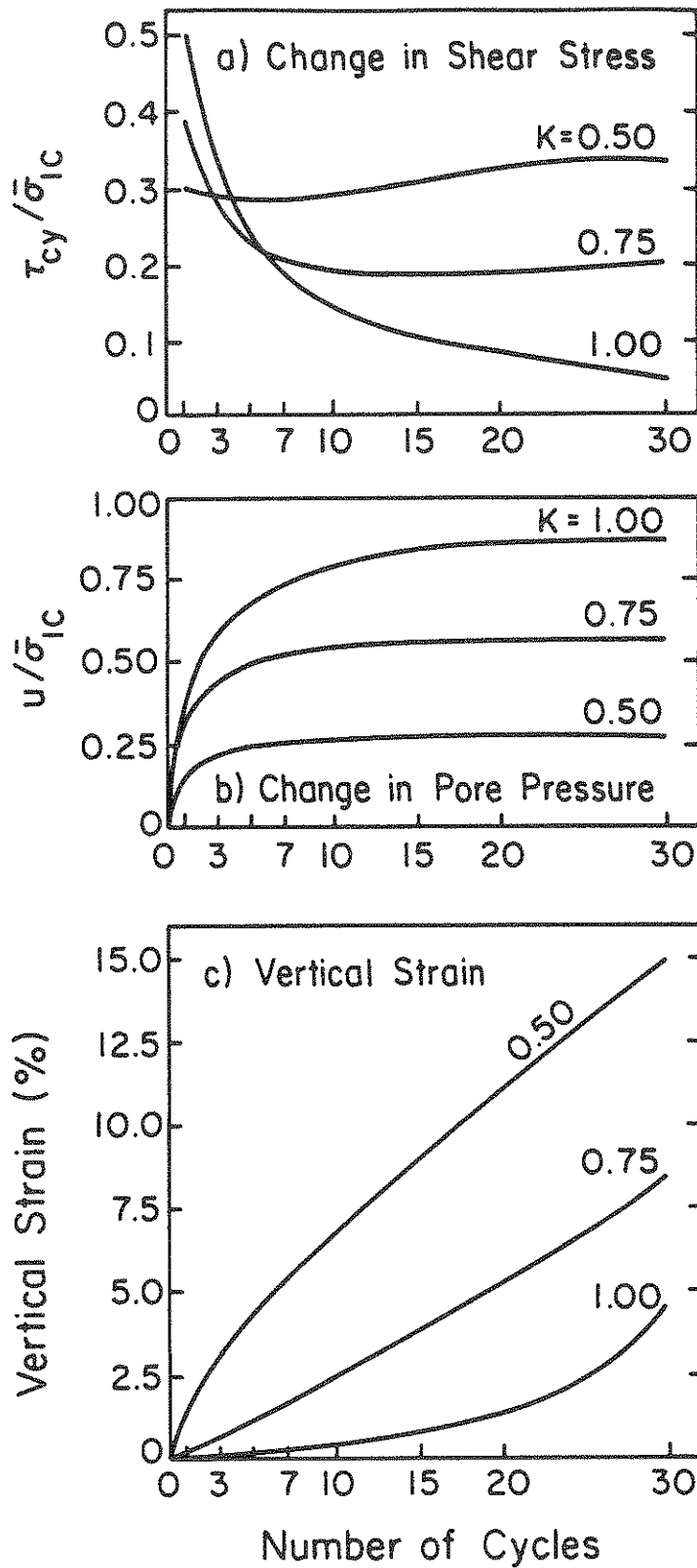


FIGURE 2-41. Results of ICT- and ACT-Tests [after Ishihara and Li, 1972]

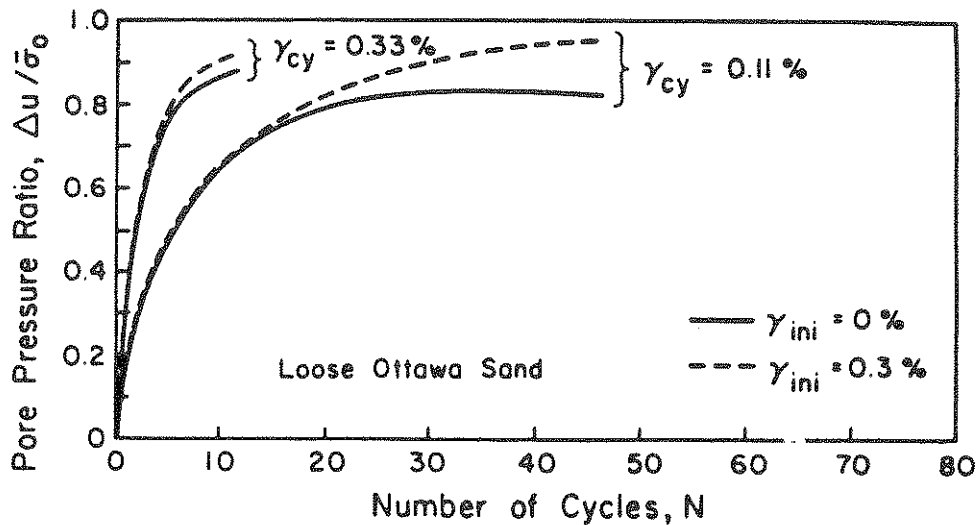
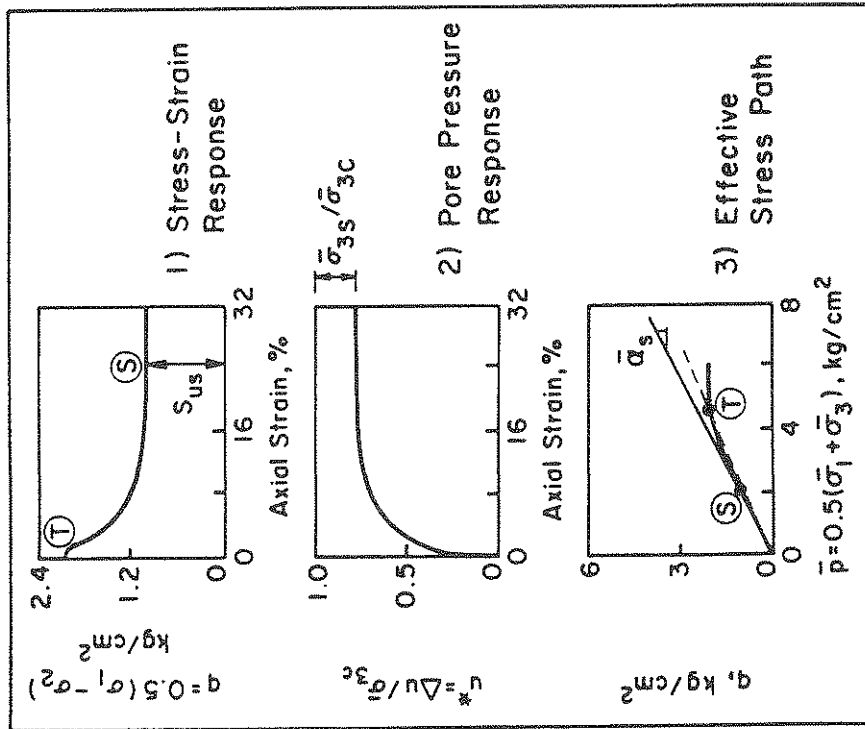


FIGURE 2-42. Pore Pressure Buildup With and Without Initial Shear [after Ishibashi, et al., 1985]

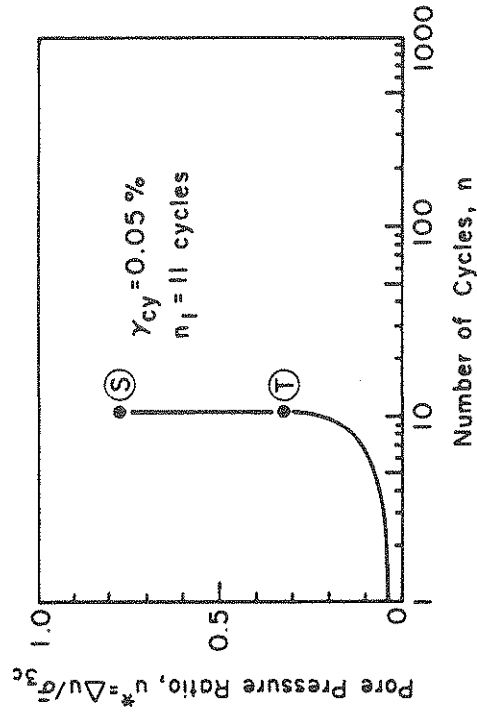
failure.

Figure 2-43a shows a typical anisotropic test on a contractive specimen of sand A. The figure shows the gradual pore pressure increase during cyclic straining, until flow failure is triggered at point T after 11 cycles. After triggering, axial deformation increased rapidly to 20%, the shear stress decreased to the steady-state shear strength,  $S_{US}$ , and the pore pressure ratio ( $u^* = \Delta u / \bar{\sigma}_{3C}$ ) increased from  $u^*_T = 0.32$  to  $u^*_S = 0.77$  (Figure 2-43b). Note that point S corresponds to the steady-state condition, and that this agrees with  $S_{US}$  and  $u^*_S$  obtained from monotonic tests, thus confirming the hypothesis that the state of steady deformation is unique, and that the steady-state can be triggered in either cyclic or monotonic loading.

Dobry, et al. [1985] also found that the slopes of the steady-state lines of the sands become flatter with increasing silt content. Thus, for siltier sands, the determination as to whether a sand is contractive or not becomes very sensitive to the void ratio, and therefore depends upon accurate in-situ density determinations. Ishihara and Li [1972], whose results were discussed above, used dilative rather than contractive sand specimens, and therefore did not observe flow



a) Test on Sand A ( $e = 0.75, \bar{\sigma}_{3c} = 4.07 \text{ kg/cm}^2, \bar{\sigma}_{1c} = 8.34 \text{ kg/cm}^2, K_c = 2.05, \gamma_{cy} = 0.05\%$ )



b) Pore Pressure Buildup During Test on Sand A Shown in A

FIGURE 2-43. Typical Cyclic Torsional Test Data [after Dobry, et al., 1985]



failure. Dobry, et al. [1985] determined the threshold shear strain for all the silty sands tested to be approximately 0.01%, that is, if the applied cyclic shear strain is less than 0.01%, then negligible pore pressure buildup occurs. For all the silty sands tested, Figure 2-44 shows cyclic shear strain against number of cycles to flow failure triggering,  $n_t$ , and shows that  $n_t$  becomes large as 0.01% is reached. This figure illustrates the importance of the strain level induced by the earthquake on the number of cycles required to trigger flow failure in a contractive material. Also, the percentage of silt is suprisingly shown to have very little influence on liquefaction flow potential.

The papers discussed above are only an indication of the range of applications for torsional shear testing. However, the problem still exists of relating the data obtained from these tests to cyclic triaxial and cyclic simple shear results. Ishibashi, et al. [1974] and Ishihara and Li [1972] both tried to produce correlations between cyclic triaxial and torsional shear testing. Different types of shearing devices tend to produce dissimilar results, and thus such relationships are only significant in a very broad sense (i.e., basic trends should be the same). Bhatia, et al. [1985] made a comparative study of the different cyclic testing devices using both strain and stress control test results, and came to the following general conclusions:

1. Twice the shear stress is generated in torsional shear tests than simple shear tests for the same cyclic strain amplitude,
2. Expressing the cyclic stress required to cause liquefaction in terms of the octahedral stress [ $\bar{\sigma}_{oct} = 1/3(\bar{\sigma}_1 + \bar{\sigma}_2 + \bar{\sigma}_3)$ ] appears to predict most accurately the liquefaction resistance of the soil,
3. Triaxial tests give the largest liquefaction resistance, simple shear the least, and torsional shear somewhere in between, and
4. Strain-controlled tests give a better insight into the cyclic behavior of a soil and provide a better evaluation of cyclic strength than stress controlled tests.

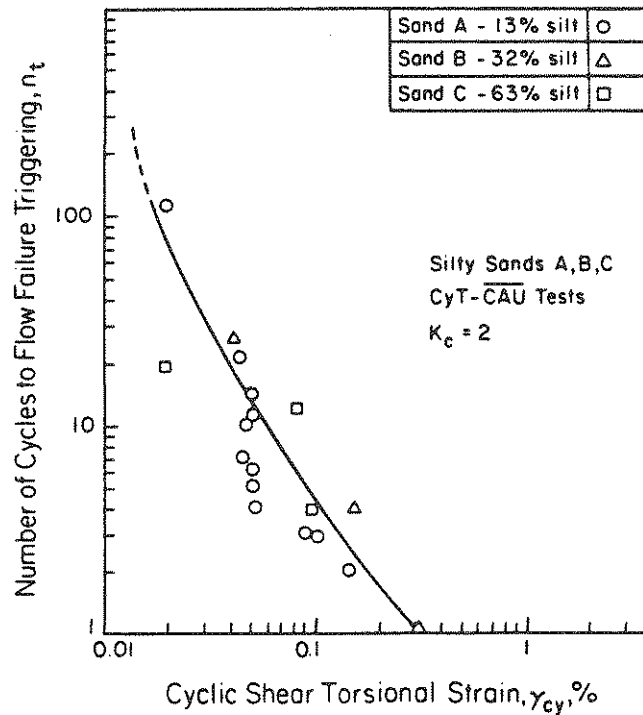


FIGURE 2-44. Number of Cycles,  $n_t$ , of Cyclic Shear Strain,  $\gamma_{cy}$ , Needed to Trigger Liquefaction Flow Failure [after Dobry, et al., 1985]

## 2.6 LIQUEFACTION OF FINE-GRAINED SOILS

### 2.6.1 Introduction

The bulk of cyclic testing has concentrated on the parameters affecting cyclic mobility or liquefaction flow failure in sands. Most research on fine-grained soils has concentrated on the dynamic response of clays. However, silty soils commonly are encountered. Shen, et al. [1985] reported that the 1978 Tangshan, China earthquake caused severe building damage because of liquefaction which occurred in a silt deposit.

This section discusses selected information on the cyclic behavior of clay, including the concept of critical stress level, variation of shear modulus with applied strain, time effects on shear modulus, and plasticity effects. Silt, silty clay, and silty sands also are discussed with regard to shear modulus and pore pressure buildup.

Also, the stress-strain behavior of silt and clay is compared to that of sand.

### 2.6.2 Stress-Strain Behavior of Clay, Silt, and Sand

Sangrey, et al. [1969] investigated the response of a clay soil due to repeated loading using stress-controlled cyclic triaxial tests. Undisturbed samples were used in a series of isotropically consolidated tests in which very low loading frequencies were used to enable full pore pressure equalization. The concept of critical stress level (CSL) of repeated stress was developed to distinguish two types of observed behavior:

1. Below the CSL, a state of nonfailure equilibrium was reached in which the stress-strain curves followed closed hysteresis loops, and no further excess pore pressure was generated, and
2. Above the CSL, failure occurred, and each additional loading cycle produced increased pore pressure and deformations.

Figure 2-45 shows a graph of cyclic stress level versus axial strain for the clay, and indicates that if the stress level is increased above point P (the CSL), then failure occurs and equilibrium is no longer possible.

Sangrey, et al. [1978] extended their study of repeated loading, using critical state concepts, to produce a general effective stress behavioral model to explain the cyclic loading responses of clays, silts, and sands. Stress-controlled isotropically consolidated cyclic triaxial tests were used as the standard reference test. Figure 2-46 shows normalized stress difference and pore pressure plotted versus axial strain for contractive clay and sand specimens ( $\sigma_d$  = deviator stress, and  $\sigma_{o-oct}$  = reference effective octahedral stress). For both the sand and the clay, liquefaction flow failure occurred when the excess pore pressures resulted in an effective stress condition at the cyclic limit state for each soil. The cyclic limit state, CLS, is a reference state for failure induced by cyclic loading. The CLS for a clay has been determined from test data to be its remolded strength, and

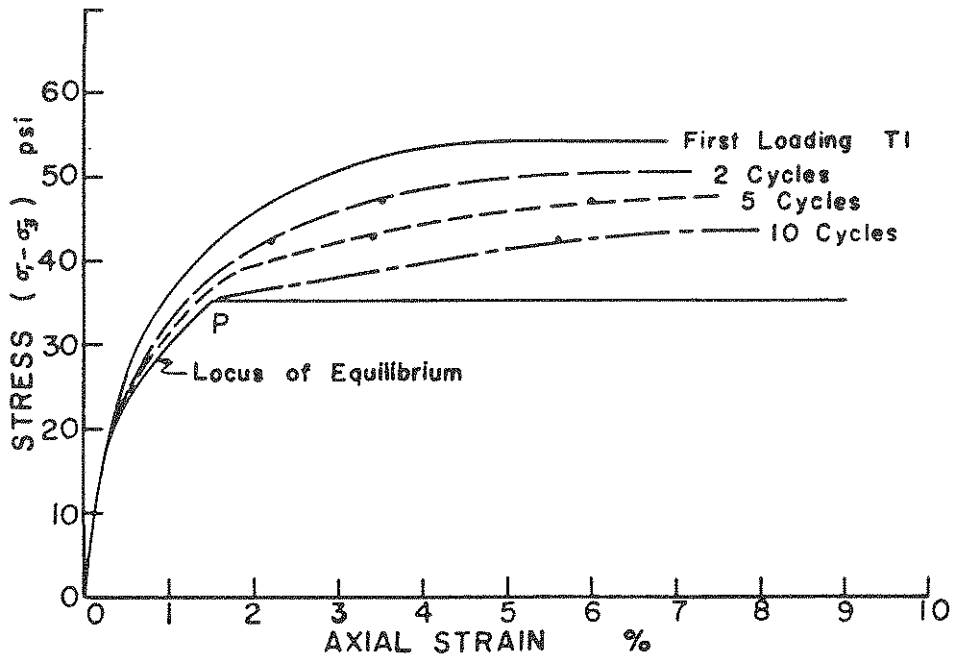


FIGURE 2-45. General Stress-Strain Behavior of Clays [after Sangrey, et al., 1969]

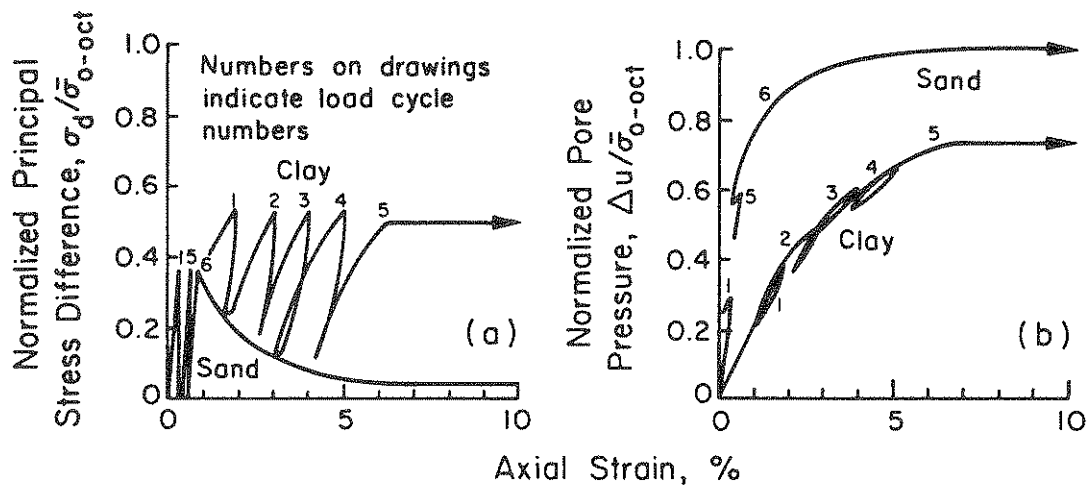


FIGURE 2-46. Cyclic Loading of Contractive Sand and Clay Specimens Leads to Failure When Pore Pressures Increase [after Sangrey, et al., 1978]

not, as might be expected, its steady-state strength. For a sand, the cyclic limit state coincides with the steady-state strength.

The differences and similarities between sand and clay soils are illustrated in Figure 2-47. A series of tests were required to define the position of the CLS lines for both the sand and clay. In each case, there was an accumulation of pore pressure, until the CLS lines were reached at point k, where large strains developed and failure occurred. The differences between the two tests were that the clay was cycled at a much higher normalized stress level, and that the rate of development and maximum level of excess pore pressure generation were much less than that for the sands. In Figure 2-47a and 2-47b, it is apparent that the CLS line for the sand is much flatter than the one for the clay, and because of this, the distance between the initial condition, j, and the failure condition, k, on a contour of constant volume, is much larger for the sand than the clay. This horizontal distance is related directly to the amount of excess pore pressure generation.

Thus, the general behavior of sand and clay in cyclic loading has been considered for only one level of cyclic stress. As discussed by Sangrey, et al. [1969], a clay can respond to cyclic loading by either failing or by reaching a nonfailure equilibrium condition. This equilibrium condition develops when excess pore pressure builds up to a stable level which is smaller than that required to cause an effective stress failure.

The range of response to different cyclic stress levels is shown in Figure 2-48. Note that maximum cyclic stress,  $\Delta\sigma_a$ , and excess pore pressure have been normalized by undrained monotonic peak strength,  $(\sigma_1 - \sigma_3)_{pk}$ . At low levels of stress, only a limited amount of pore pressure increase occurs, and nonfailure equilibrium is reached quickly. For progressively higher levels of cyclic stress, the equilibrium pore pressure values get larger and the stress path approaches failure, until the strength envelope (CLS line) is intersected and strains increase rapidly.

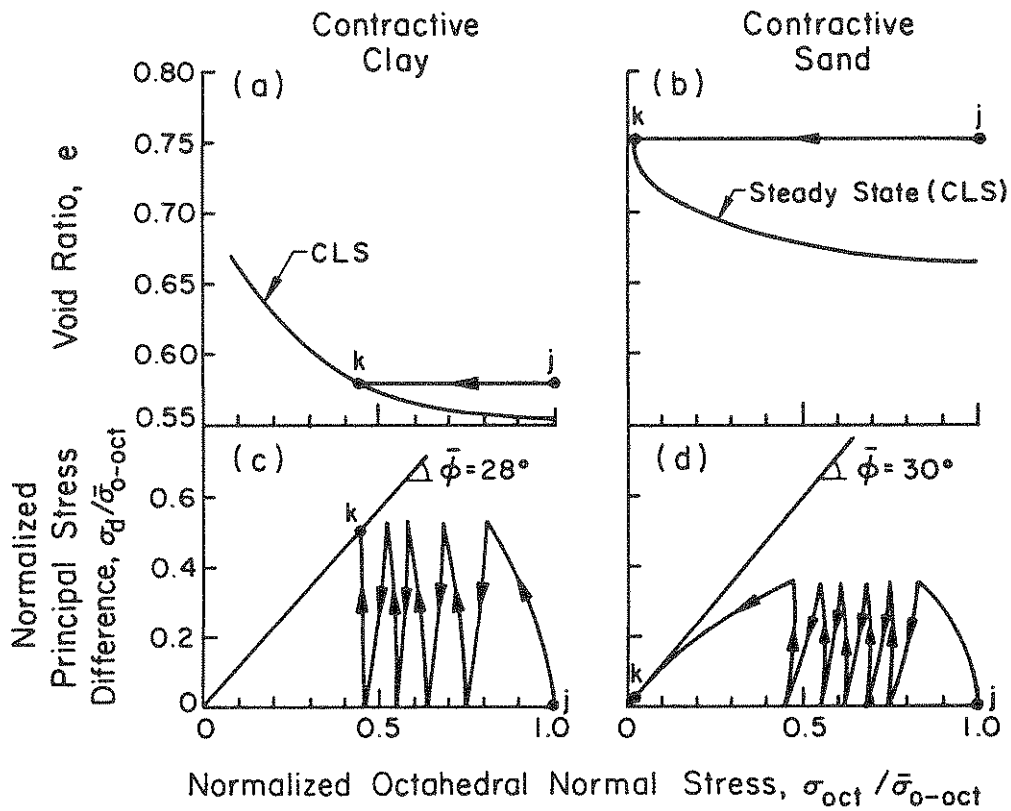


FIGURE 2-47. A Comparison of the State Paths of Contractive Sand and Clay Specimens Subjected to Cyclic Loading [after Sangrey, et al., 1978]

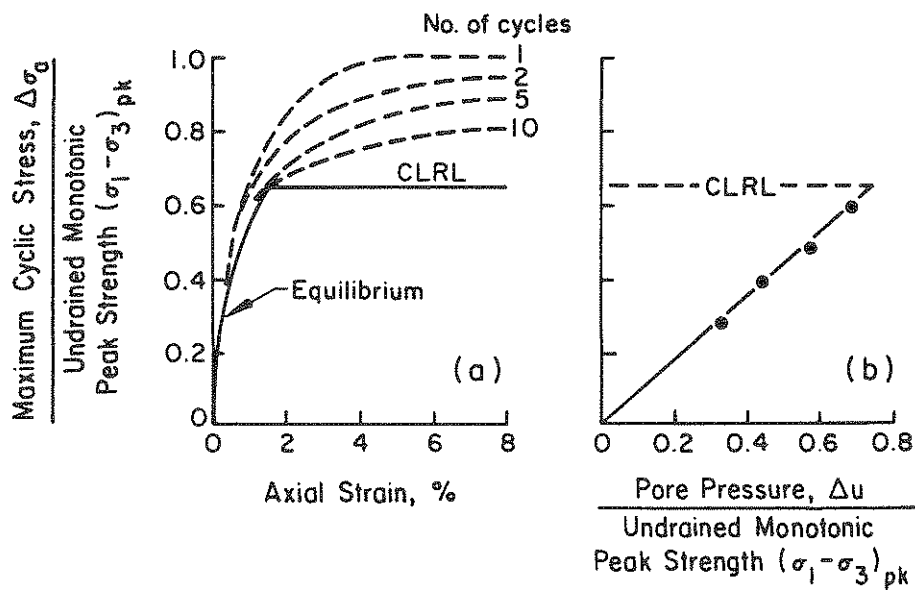


FIGURE 2-48. General Behavior of Contractive Soils Under Cyclic Loading [after Sangrey, et al., 1978]

The boundary between nonfailure equilibrium and failure is defined as the critical level of repeated loading (CLRL), which equals the principal stress difference at the CLS. Above the CLRL, variables such as number and frequency of stress cycles become important. Sangrey, et al. [1978] illustrate the differences between contractive sands, silts, and clays when cyclically loaded under undrained conditions by comparing their CLRL levels.

Figure 2-49 shows normalized CLRL values plotted against compressibility ( $\kappa$  is the recompression index expressed on a natural logarithm scale, i.e.,  $C_r/2.3$ , where  $C_r$  is the average slope of the recompression line on an  $e$  versus  $\log \sigma_v$  plot), and illustrates why cyclic loading is more severe for sands than clays, as sands can only sustain low levels of cyclic stress before failure occurs. As might be expected, silt strength lies somewhere between clay and sand, as shown by the solid square symbols in Figure 2-49.

In general, dilative soils are not subject to the same magnitudes of pore pressure and strain accumulation that affect contractive soils. Dilative clays tend to accumulate strain under cyclic loading, although the rates of strain accumulation are small for maximum cyclic stress levels less than 0.85 of the undrained compressive strength. Sangrey, et al. [1978] concluded that for dilative clays, the CLRL and the undrained shear strength are approximately equal. Dilative sands cycled at even very low stress levels of between 0.05 to 0.3 times the undrained cyclic strength tend to accumulate large deformations, although samples do not experience flow failure or a significant strength reduction. Dilative nonplastic silts were reported to exhibit behavior similar to sands, except that they were reported to accumulate strains and pore pressures at a much lower rate.

Egan and Sangrey [1978] described a mathematical model for predicting the pore pressure increase, in any type of soil, under a given cyclic loading. The suggested model combines critical state concepts with the CLS and CLRL ideas discussed above. Although the model and approach to the problem are useful to describe the differences between

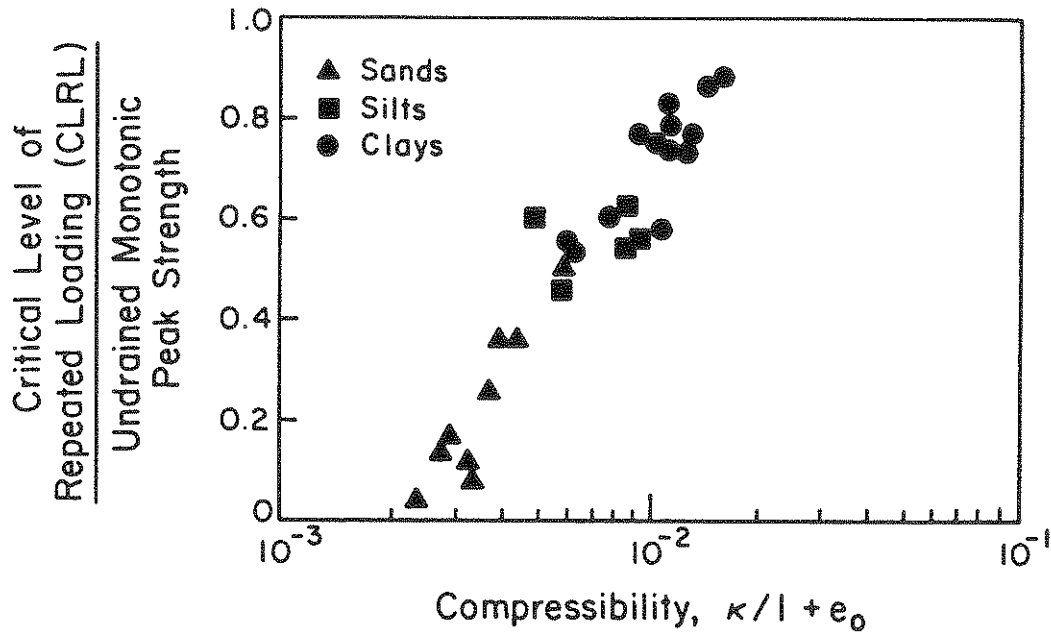


FIGURE 2-49. Critical Level of Repeated Loading (CLRL) for Undrained Tests of Contractive Soils [after Sangrey, et al., 1978]

soil types, it has several drawbacks:

1. Cyclic triaxial tests, as discussed previously, are not the most accurate nor best available type of test for modeling of in-situ stresses and earthquake loading,
2. Considering only isotropic normally consolidated tests considerably limits the field applicability, and
3. Stress-controlled tests, upon which the model is based, are more susceptible to errors caused by variations in sample preparation techniques [Mulilis, et al., 1977].

### 2.6.3 Dynamic Properties of Clays

The dynamic properties of clays vary in more complicated ways than sands. Parameters such as time duration of loading, consolidation, anisotropy, and saturation have a large effect on dynamic response. Research has concentrated on trying to isolate and quantify the effects of the many variables involved.

Kovacs, et al. [1971] used cyclic simple shear tests with both forced



and free vibrations to study the basic dynamic and stress-strain response of a soft clay. The clay was reconstituted in the laboratory from a mixture of three parts kaolinite and one part montmorillonite, and all tests were run 24 hours after clay placement. The basic conclusions drawn about the clay's responses were that the dynamic modulus was dependent on shear strain and the number of cycles, but was independent of the frequency of oscillation in the strain range 0.01% to 2%. Also, the modulus decreased as shear strain increased, and for a given strain level, the modulus decreased as the number of cycles increased, with the largest change in modulus occurring in the first few cycles. These conclusions indicate that the basic response of clays to cyclic loading is in several ways similar to sands.

Several researchers have developed relationships to define the low strain amplitude modulus,  $G_{\max}$ , for various clays using resonant column tests. Hardin and Black [1968] developed an equation of the form:

$$G_{\max} = A(t)F(e)(\bar{\sigma}_c)^{0.5} \quad (2-7)$$

where:

$e$  = void ratio,

$\bar{\sigma}_c$  = effective confining stress (kPa),

$F(e) = (2.973 - e)^2 / (1 + e)$ , and (2-8)

$A(t)$  = time-dependent soil constant in units of  $(\text{kPa})^{0.5}$ .

The  $F(e)$  term accounts for the increase in shear modulus with change in void ratio.  $A(t)$ , as defined by Hardin and Black [1968] for normally consolidated reconstituted kaolinite samples, is equal to 3270, in units of  $(\text{kPa})^{0.5}$ . This term is valid only for stiff clays with  $e < 1.5$ . Hardin's [1965] equation for the shear modulus of angular sand is of identical form, but with a different  $A(t)$  value.

Other values of  $A(t)$  have been determined for different clays. Marcuson and Wahls [1972] determined that, for Boston Blue Clay in various states, the  $A(t)$  varied from 2353 to 3119  $(\text{kPa})^{0.5}$ . However, for soft

clays, a new value for  $F(e)$  must be used, i.e.,  $F(e) = (4.4 - e)^2 / (1 + e)$ , and  $A(t) = 445 \text{ (kPa)}^{0.5}$ . Hardin and Black [1968] also suggested that  $A(t)$  may be a function of time after completion of primary consolidation.

Marcuson and Wahls [1972] developed Equation 2-7 to include for time after primary consolidation and the OCR of the clay by changing the definition of  $A(t)$ , for kaolinite, to:

$$A(t) = 3270(1 + 0.046 \log T_r)(OCR)^{0.5} \quad (2-9)$$

where  $T_r$  is defined as the ratio of a prescribed time to the time to 100% primary consolidation. The factor  $(1 + 0.046 \log T_r)$  was obtained from consolidated undrained data, and accounts for the increase in shear modulus with time, which is not due to void ratio changes. The increase in shear modulus with time is approximately 10% for kaolinite and 40% for bentonite per log cycle of  $T_r$ . For bentonite,  $A(t) = 171(1 + 0.242 \log T_r)(OCR)^{0.5}$ .

Marcuson and Wahls [1978] found a similar time effect for damping ratios. The damping ratio was found to decrease 12% for kaolinite, and 25% for bentonite, per log cycle of  $T_r$ . Time-dependent changes in the clay structure thus produce large changes in shear modulus and damping ratio at low shear amplitudes. However, for excitation levels above 0.1% shear strain, the nonlinear material behavior is likely to mask these time effects.

Natural clays are very different from the clays used in the research described above. The process of sedimentation followed by one-dimensional consolidation results in natural clays having anisotropic properties. Saada, et al. [1978] investigated the effects of anisotropy on the dynamic behavior of clays, and demonstrated that substantial differences existed between the moduli for undisturbed samples tested with either a vertical or horizontal orientation. Equation 2-7 was found to represent  $G_{\max}$  adequately if a factor was introduced to account for the degree of anisotropy in a sample. Saada, et al.

[1978] suggested that this factor is a function of the ratio of Young's modulus in the vertical and horizontal directions.

The effects of anisotropy and clay fabric are important parameters influencing dynamic response, which only reasonably can be accounted for by using undisturbed samples. Athanasopoulos and Richart [1983] studied the effect of stress release, which occurs during sampling, on the shear modulus of clays. It was found that the temporary release of confining pressure induces disturbances which cause a decrease in  $G_{max}$ . After reapplication of the original confining pressure, the clay, over time, regains the lost amount of  $G_{max}$ . A procedure was presented to establish the required time of application of the confining pressure to ensure that the measured  $G_{max}$  represents the in-situ value.

Previous research has concentrated either on using the resonant column to investigate parameters affecting  $G_{max}$  and damping characteristics at low strain amplitudes, or various types of cyclic tests to study the strain-dependency of the modulus and damping at high strain amplitudes. Kokusho [1980] developed a modified cyclic triaxial device which could measure strains from 0.0001% to 10%, thus enabling both low and high amplitude strain testing on the same sample, without resorting to a hybrid testing device. They used this device to study the effect of consolidation time and plasticity index on the dynamic properties of undisturbed clay samples over a wide strain range. Long-term consolidation tests were used to investigate the effect of consolidation time on  $G_{max}$ . The test results showed a continuous increase in modulus throughout primary consolidation. There was a distinct change in the rate at which the modulus increased following primary consolidation. Shear modulus continued to increase, but at a much lower rate. However, Kokusho, et al. [1982] reported that the shear modulus increased during secondary consolidation at a rate higher than that predicted, based on void ratio change using Equation 2-7 (modified for the clay being tested). The difference between the shear modulus increase predicted by Equation 2-7 and the actual increase in modulus implied that void ratio changes alone cannot

explain this secondary increase, which is probably due to chemical bonding effects.

The rate of secondary modulus increase is defined as  $\Delta G/G_{1000}$ , the increase in shear modulus per logarithmic cycle of time,  $\Delta G$ , divided by the modulus at 1000 minutes from the start of primary consolidation,  $G_{1000}$ . Kokusho, et al. [1982] related the rate of modulus increase to plasticity index, PI, since it is a parameter related closely to the chemical activity of the clay minerals.

Figure 2-50 is a plot of  $\Delta G/G_{1000}$  versus PI, including data from other researchers, and shows the empirical relationship developed:

$$\Delta G/G_{1000} = 0.027(PI)^{0.5} \quad (2-10)$$

The strain-dependent change of shear modulus has been shown to be almost negligible for strains less than 0.001%, and the modulus can therefore be defined as  $G_{\max}$ .

The variation of modulus ratio,  $G/G_{\max}$ , for normally consolidated samples in the strain range 0.001% to 10%, as obtained by Kokusho, et al. [1982], is shown in Figure 2-51. The specimens shown in this figure had a variety of plasticity indices, and were tested at a variety of confining pressures. Further tests indicated that confining pressure had little influence on the position of the modulus reduction curve. Therefore, the differences in the positions of the curves shown in Figure 2-51 were due to the effect of different plasticity indices. Note that the broken line representing Toyoura sand is in close agreement with the curve representing a nonplastic specimen.

The change in location of the curves due to plasticity index is shown in Figure 2-52, where the shear strain corresponding to four different modulus ratios is plotted against plasticity index. Bilinear approximation lines drawn in the figure indicate that in the interval,  $PI = 0$  to 40, the position of the strain dependent curve changes considerably and shifts to the right, as shown in Figure 2-51, according to the

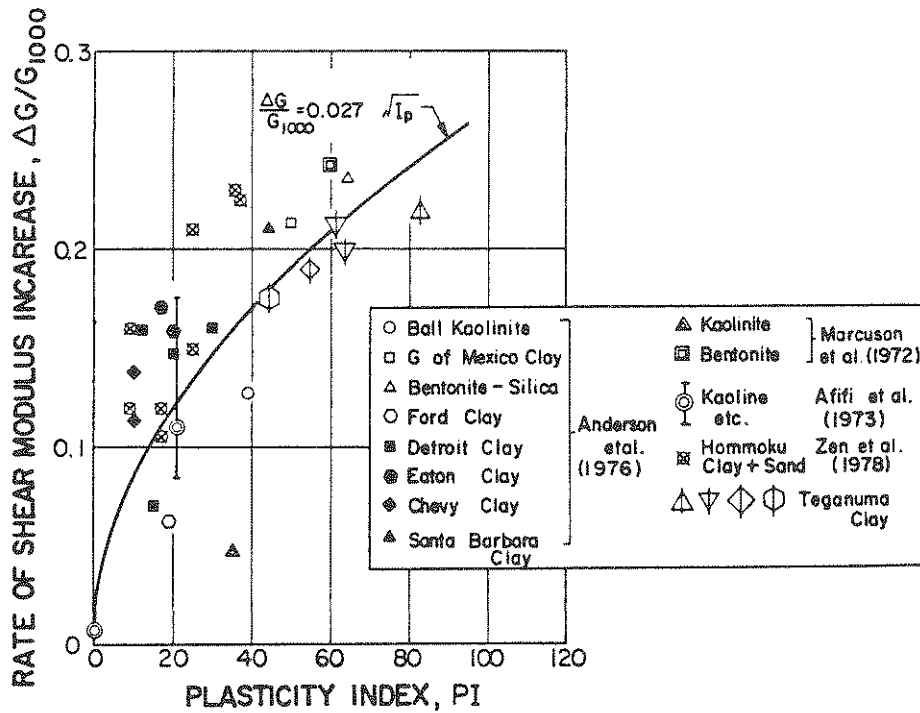


FIGURE 2-50. Relationship Between Modulus Increase Rate and Plasticity Index [after Kokusho, et al., 1982]

increase in PI, but for larger plasticity indices, the change becomes much smaller. Kokusho, et al. [1982] also found that consolidation history had a negligible effect on the position of the  $G/G_{max}$  versus shear strain curves.

Studies investigating the effect of consolidation history and strain dependency on damping ratio were also completed. Unusually, it was found that damping ratio decreased with increasing consolidation time, and although damping ratios did show differences due to plasticity, the differences were much less pronounced than those found for shear modulus, as shown in Figure 2-53.

#### 2.6.4 Dynamic Properties of Silts

Silts have been discussed in Section 2.6.2 as having cyclic strength and pore pressure generation properties somewhere between the extremes of clay and sand. While the data backing this assertion are sparse,

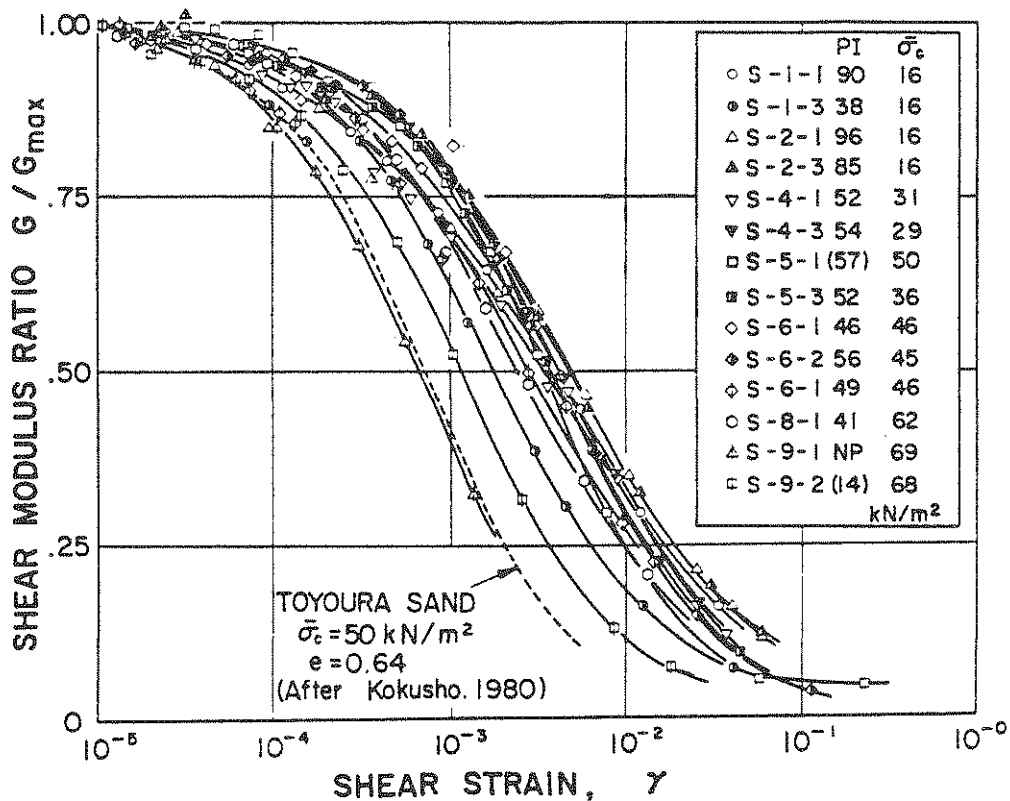


FIGURE 2-51.  $G/G_{\max}$  versus  $\log \tau$  Relationships for Normally Consolidated Specimens [after Kokusho, et al., 1982]

it seems a reasonable assumption that flow failure and liquefaction can occur in silts, but at higher levels of cyclic stress than required for sands. The effect of silt content on the steady-state strength of sand also has been discussed in Section 2.5.4 [Dobry, et al., 1985]. Increased silt content was found to decrease the slope of the steady-state line but, interestingly, have no effect on the steady-state strength envelope or pore pressure generation characteristics of a specimen tested in strain-controlled torsional shear tests.

Shen, et al. [1985] investigated the dynamic properties of a pure non-plastic silt using a free torsional vibration system. This device subjected a cylindrical specimen to a certain torque, which was then turned off, and the system was allowed to vibrate freely. The device

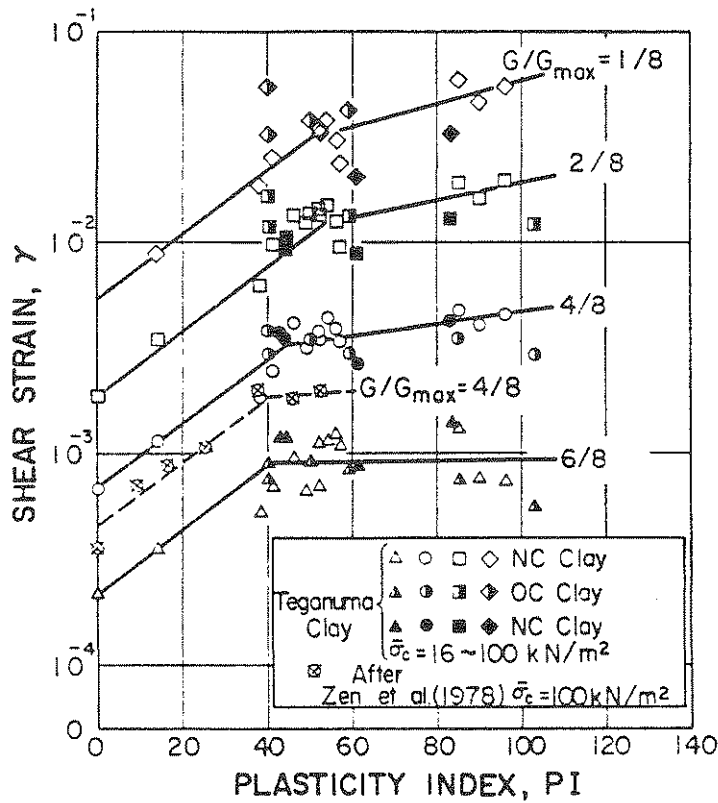


FIGURE 2-52. Shear Strain versus Plasticity Index Relationships for Different Modulus Ratios [after Kokusho, et al. 1982]

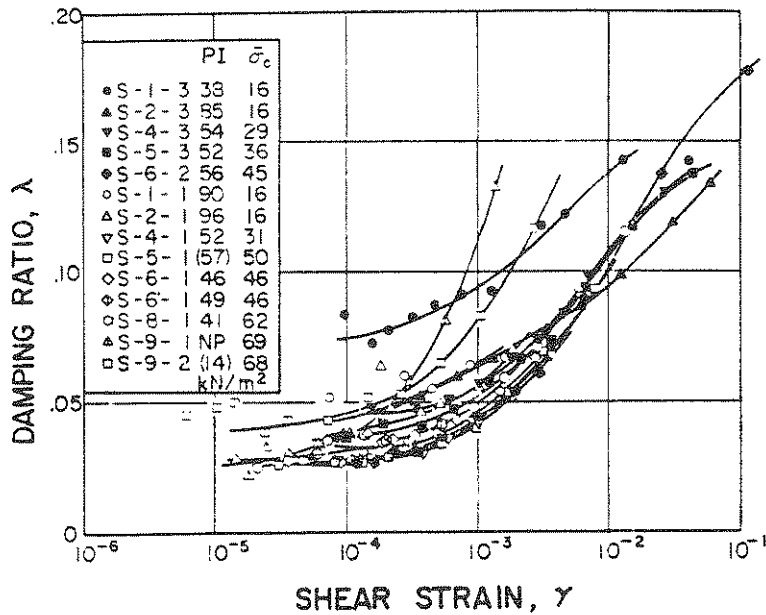


FIGURE 2-53. Strain-Dependent Changes of Damping Ratio for Normally Consolidated Specimens [after Kokusho, et al., 1982]

was capable of operating from 0.0005% to 0.1% shear strain. The acceleration trace from the first four cycles of free oscillation then was used to calculate shear modulus and damping values. Pore pressure and vertical displacement changes were monitored simultaneously. The effects of relative density, confining pressure, loading cycles, and initial shearing strain on the relationships between shearing strain amplitude and shear modulus/damping ratio were investigated in this study.

Some basic test results for the silt tested by Shen, et al. [1985] are given in Figure 2-54, which shows the variations of shear modulus, damping ratio, and pore water pressure under different shearing strain amplitudes. As expected,  $G$  decreases and damping ratio increases with increasing shearing strain. The threshold strain was found to be approximately 0.01%. Figure 2-54 also shows that higher relative density and confining pressure increases  $G$  and gives lower damping ratios. Shen, et al. [1985] also determined that overconsolidation had little influence on dynamic properties, but that application of an initial shearing strain decreases the value of  $G_{\max}$ . The effect of an initial shearing strain on the degradation of shear modulus was investigated, and it was determined that increased initial shearing strain from 0.001% to 0.01% caused an increase in pore pressure buildup, and a corresponding reduction in the shear modulus.

Figure 2-55 shows the values of maximum shear modulus, damping ratio, and pore pressure buildup after a given number of loading cycles. The tests were carried out undrained at strain amplitudes of 0.001 to 0.01%. The test results showed that the shear modulus decreased with increasing loading cycles, and that larger shearing amplitudes caused a larger reduction in modulus. From these results, it was concluded that the dynamic behavior of non-plastic silt is similar to that of sands.

Hardin and Drnevich [1972] proposed an equation to describe the degradation of shear modulus with respect to shear strain amplitude for dry sand:



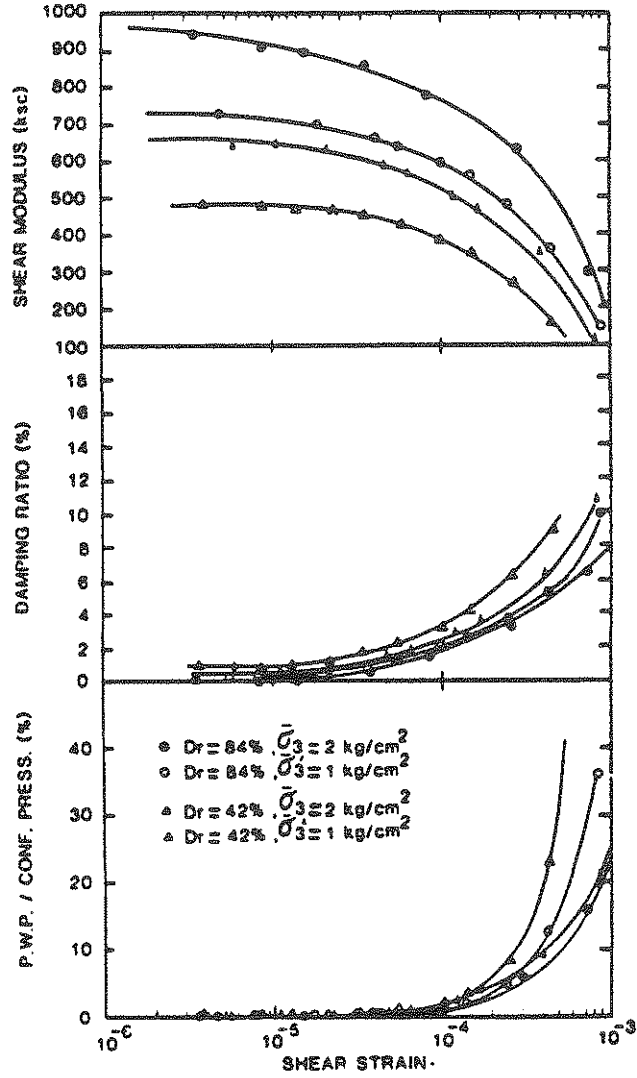


FIGURE 2-54. Influence of Shearing Strain Amplitude, Relative Density, and Confining Pressure on Dynamic Response [Shen, et al., 1985]

$$G/G_{\max} = 1/(1 + \gamma/\gamma_r) \quad (2-11)$$

where  $\gamma_r$ , the reference shearing strain, was defined as  $\tau_{\max}/G_{\max}$ ; where  $G_{\max}$  is the initial tangent modulus of a hyperbolic relationship of  $\tau$  versus  $\gamma$  from torsional shear tests, or the small strain modulus, and  $\tau_{\max}$  is the shear strength. This equation does not describe adequately the effect of pore water pressure in an undrained condition.

Shen, et al. [1985] developed an equation to characterize the effect

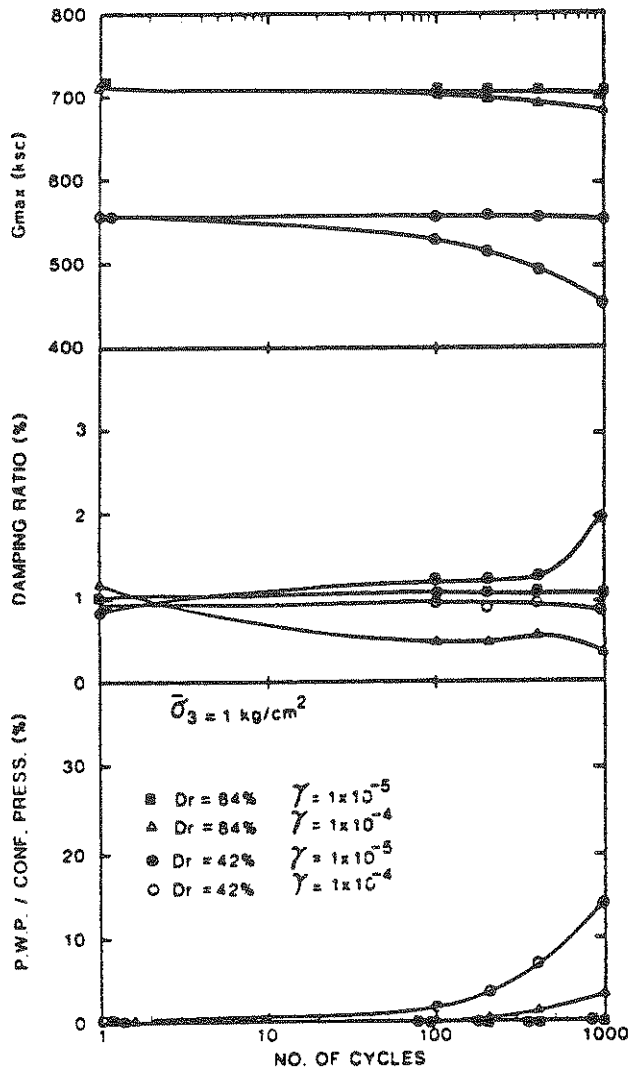


FIGURE 2-55. Influence of Number of Loading Cycles on Dynamic Response [Shen, et al., 1985]

of pore water pressure for the undrained condition:

$$G(\gamma, u)/G_{\max} = f_1(\gamma) \cdot g_1(u) \quad (2-12)$$

where:

$$f_1(\gamma) = 1/(1 + \gamma/\gamma_r), \quad (2-13)$$

$$g_1(u) = (\bar{\sigma}/\bar{\sigma}_c)^\alpha, \text{ and} \quad (2-14)$$

$\bar{\sigma}_c$  is the effective consolidation pressure.

The parameter  $\alpha$  was determined to be 0.5 from curve fitting of

undrained test results. The family of curves represented by Equation 2-12 is shown in Figure 2-56, which indicates that as pore pressure builds up in a specimen, the shear modulus relationship with shearing strain moves through different planes ( $\bar{\sigma}/\bar{\sigma}_c$ ), as indicated by curve AB. Shen also described a similar equation for damping ratio:

$$\lambda(\gamma, u)/\lambda_{\max} = f_2(\gamma) \cdot g_2(u) \quad (2-15)$$

where:

$$f_2(\gamma) = (\gamma/\gamma_r)/(1 + \gamma/\gamma_r), \text{ and} \quad (2-16)$$

$$g_2(u) = (\bar{\sigma}/\bar{\sigma}_c)\beta \quad (2-17)$$

$\lambda_{\max}$  is determined at a large shearing strain amplitude, and  $\beta$  was found to be 0.2.

A hybrid test device which uses the same electromagnetic system for both resonance and torsional shear testing [Isenhower, 1979] was used by Stokoe, et al. [1980] to investigate the shear modulus and damping characteristics of silty clays and clayey silts. The effect of shearing strain amplitude on normalized shear modulus for all the tests performed in the study was summarized in Figure 2-33. Unfortunately, no attempt was made to determine why such a large spread of modulus reduction curves occurred. Presumably, the varying plasticities of the specimens, as discussed in Section 2.6.3, had a large effect. Figure 2-34 showed a similar wide range for damping ratio versus shear strain curves. All the tests were performed drained, and therefore no information on pore pressure buildup during testing was obtained, although a useful comparison of results from the resonant column and torsional shear tests was made.

Figure 2-57 illustrates this comparison using the shear modulus from the first cycle of drained torsional shear loading, and presumably, after several thousand cycles of loading for the resonant column test. The results from both devices agree well, which is unusual, considering the wide discrepancy in number of loading cycles. However, above the approximate threshold strain of 0.01%, the torsional shear test

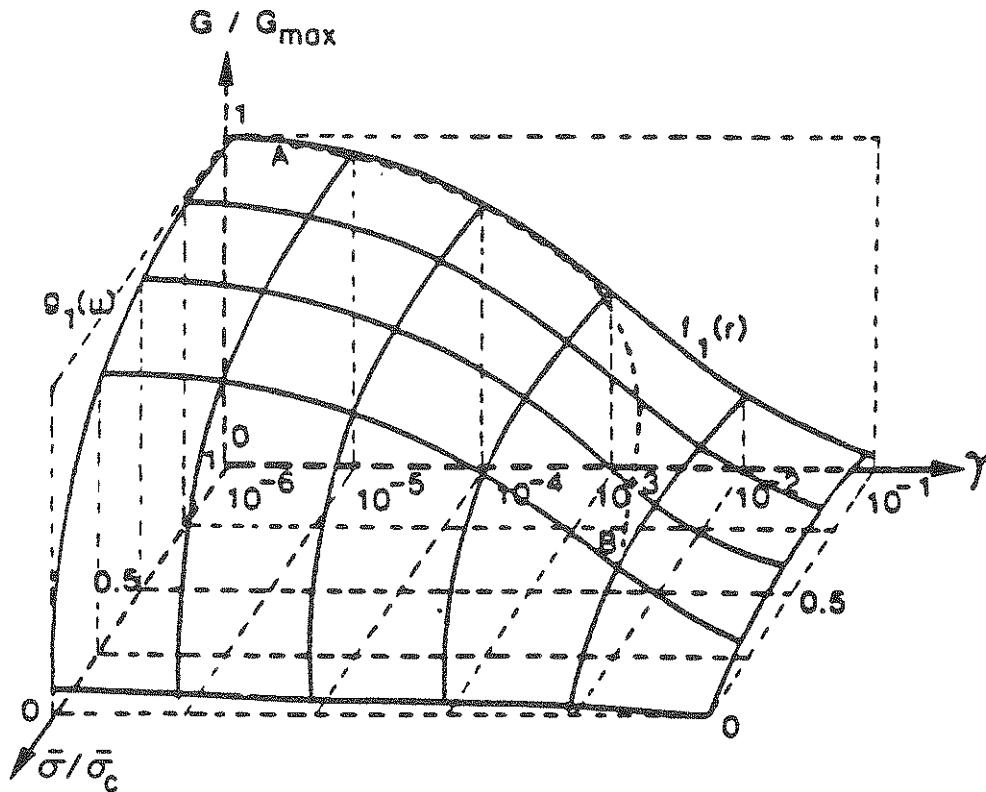


FIGURE 2-56. Degradation of Shear Modulus Ratio [after Shen, et al., 1985]

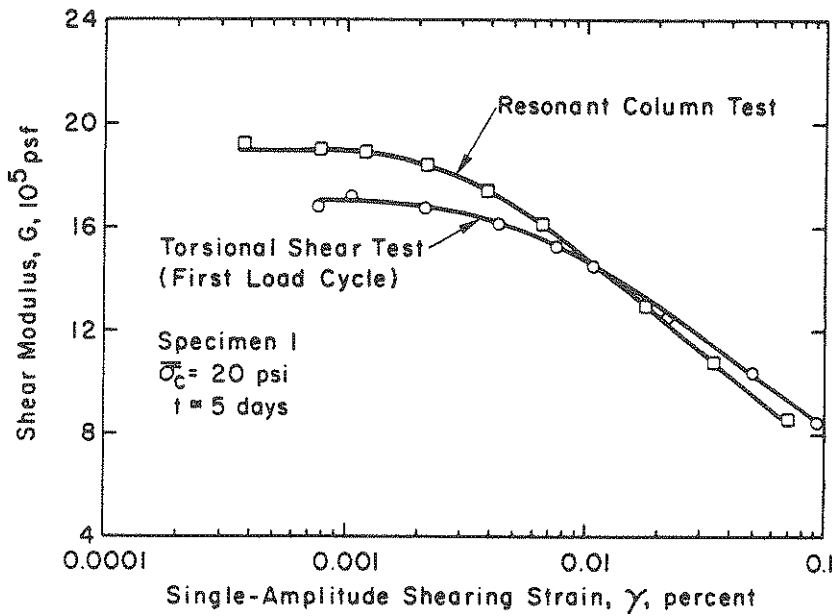


FIGURE 2-57. Comparison of Shear Moduli Measured by Torsional Shear and Resonant Column Tests [after Stokoe, et al., 1980]

does obtain a slightly higher modulus than the resonant column test, although this difference is less than might be expected. Alarcon-Guzman [1986], using a Drnevich hybrid testing device, only obtained agreement between resonant column and torsional shear tests on dry sands by using the tenth cycle of torsional shear loading.

The effect of plasticity index on the cyclic strength of plastic silts was discussed by Ishihara, et al. [1981] in a paper discussing the cyclic stability of mine tailings material. Results from cyclic stress-controlled triaxial tests on undisturbed plastic silt samples are shown in Figure 2-58. In the figure, the cyclic stress ratio required to cause 5% double amplitude or peak-to-peak strain is plotted versus plasticity index, and shows that cyclic strength tends to increase with increasing plasticity. However, this is a very weak correlation, and the figure also could be interpreted as showing that there was no effect of PI on the cyclic shear strength of the mine tailings.

Therefore, although there is little direct research available on the dynamic behavior of silts, some basic conclusions can be drawn:

1. Nonplastic silts display dynamic behavior in terms of shear modulus and damping which is similar in several ways to that of sands, and
2. Plastic silts show a wider range of variability and behavior, which depends to some extent on plasticity index. The characteristics of plastic silts are more typical of the dynamic response of clays.

## 2.7 CONCLUSIONS

Strain-controlled tests are in many ways superior to stress-controlled tests. Cyclic strain is a more fundamental parameter than cyclic stress in controlling pore pressure buildup during undrained cyclic loading, due to the existence of a threshold shear strain below which no excess pore pressures are generated. Using strain control makes tests much less sensitive to several factors, including specimen preparation method and relative density.

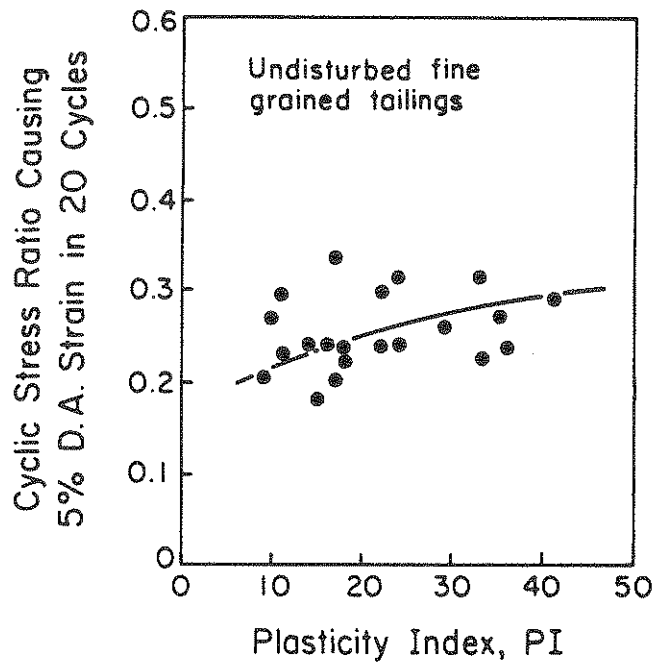


FIGURE 2-58. Relationship Between Cyclic Strength and Plasticity Index of Tailings [after Ishihara, et al., 1981]

A resonant column device is required to measure dynamic soil properties at small strains, 0.0001% to 0.1%. In particular, the variation of shear modulus and damping ratio with shear strain can be determined. However, the device operates at too high a frequency to study pore pressure buildup in undrained loading.

The torsional shear test has several advantages over the other test methods discussed. The test allows reproduction of the most general stress conditions, and can operate over a wide cyclic strain range, 0.02% to 10%. Specimens can be tested in either stress or strain control, and also failed monotonically at large shear strains. The effects of pore pressure buildup and number of loading cycles also can be evaluated.

## SECTION 3 EXPERIMENTAL PROGRAM

### 3.1 TEST APPARATUS

Resonant column and torsional shear tests have been used separately to determine dynamic soil properties over a wide strain range. Two types of equipment generally require the use of two different specimens, which are unlikely to have identical properties, so there is often no overlap between the results from the low strain resonant column tests and the higher strain torsional shear tests. This is a limitation when trying to establish shear modulus and shear strain relationships, or in determining the strain level at which pore pressures begin to buildup. These drawbacks were considered in the design of a hybrid device which combines a resonant column with a torsional shear loading system. The combination allows the evaluation of a single soil specimen's dynamic properties over the shear strain range of engineering interest.

The quasi-static torsional simple shear/resonant column apparatus used in this experimental program was designed by Professor Vincent P. Drnevich for Soil Dynamics Instruments, Inc. (S.D.I.), based on specifications provided in part by Professors Gerald Leonards and Jean Chameau, both of Purdue University. The apparatus, which is shown in Figure 3-1, can test solid or hollow cylinder specimens in torsion. Quasi-static loading may be either monotonic or cyclic, using either stress or strain control. Both quasi-static and dynamic loading may be applied simultaneously and controlled independently. The solid specimens are 71 mm in diameter. The hollow specimens may be constructed with a 71 mm outside diameter and 38 mm inside diameter, or a 100 mm O.D. and 71 mm I.D. The specimen height is roughly 193 mm. These specimen dimensions were selected to reduce the effects of end restraint [Saada and Townsend, 1981].

A specimen may be consolidated under either isotropic or anisotropic states of stress. However, an additional axial loading system must be

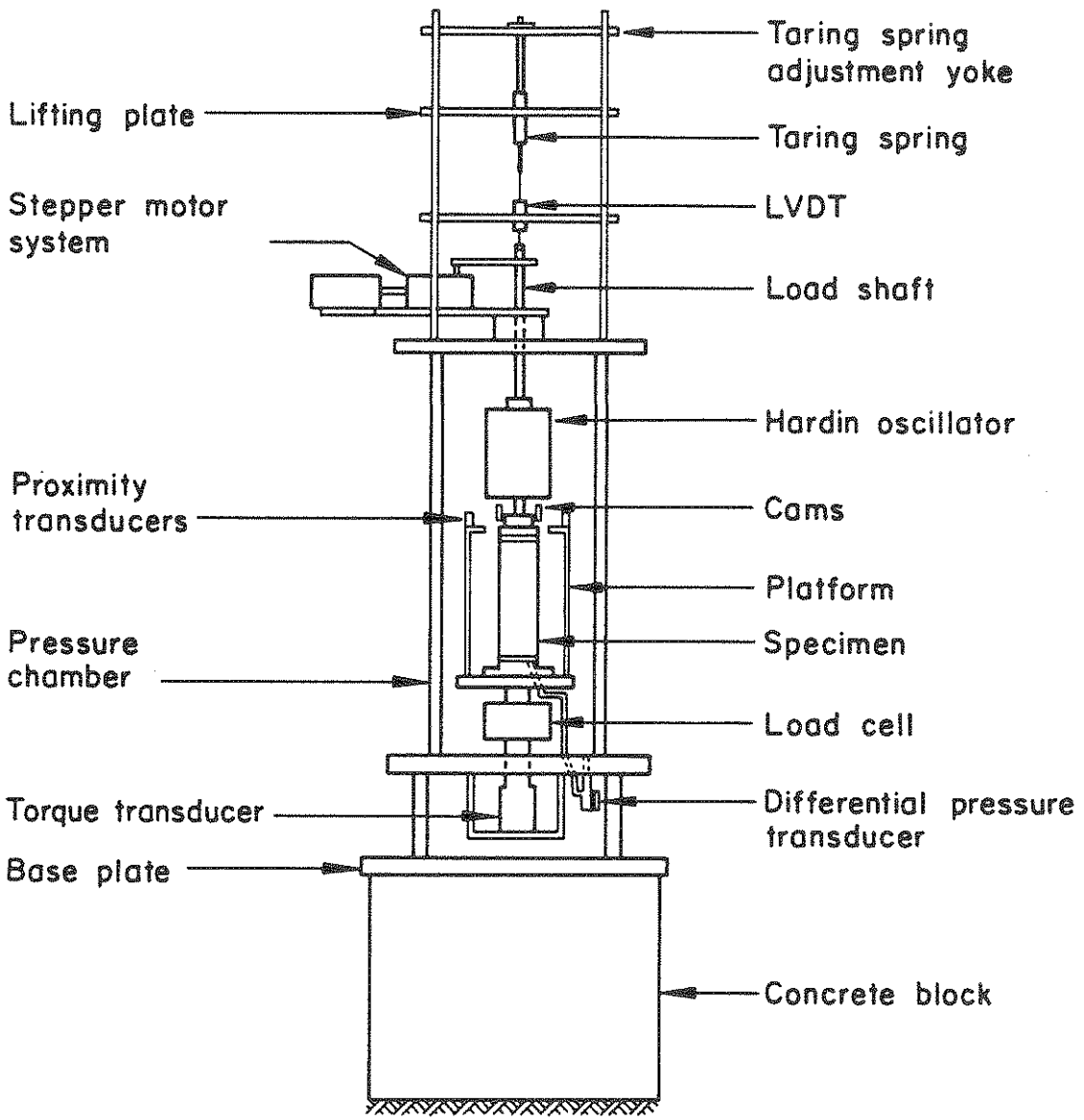


FIGURE 3-1. Quasi-Static Torsional Shear/Resonant Column Device



incorporated to achieve highly anisotropic consolidation states. Only limited anisotropic states can be obtained using weights placed on the loading axle, and controlled axial compression of the specimen to failure cannot be achieved.

Confining pressures up to 700 kPa can be applied inside the chamber to a specimen by means of silicon oil confining fluid. The chamber is filled only partly with silicon oil, to a level just below the rotation transducers. Air pressure then can be applied to the upper part of the chamber through a connection in the top plate. Silicon oil is nonconducting, so there is no chance of affecting the transducers or the resonant column within the chamber. Also, silicon oil is an improvement over water in reducing air penetration into a specimen.

The general transducer arrangement is shown in Figure 3-1. The effective confining pressures are measured by a differential pressure transducer located at the base of the apparatus. The axial load on the specimen is measured by a 3.0 kN load cell located within the chamber under the specimen platen. A 42.5 N-m torque transducer is positioned outside the chamber beneath the base. Changes in the length of the specimen are measured by a linearly variable differential transformer (LVDT) with 25 mm full displacement, located in a yoke above the stepper motor system. Proximity transducers, which focus on cams connected to the upper platen, measure the rotation of the specimen up to a maximum of 30 degrees. All transducers are connected to a signal conditioning unit, which provides power and amplification, and then to a PC-based computer data acquisition system. The computer enables simultaneous readout of all transducers, torsional shear control, and recording of data during a test.

Metal porous disks are used at the face of each platen to distribute or collect pore fluids. These disks have rough surfaces and are screwed into the platens to avoid slippage during testing. The bottom platen has two pressure lines: one connects to the differential pressure transducer, and may be connected to a volume change device, while the other is used for saturation, backpressure control, or drainage

during consolidation. The top platen has one pressure line which is used for drainage during saturation. Both top and bottom lines can also be connected to a vacuum supply.

### 3.1.1 Resonant Column System

A Hardin-type oscillator is used to apply torsional vibrations that vary sinusoidally with time [S.D.I., 1987; Alarcon-Guzman, et al., 1986]. The oscillator is basically a single degree of freedom system in which a spool-shaped spring couples a central mass to a hollow cylindrical mass which has a large rotational inertia. A sine wave generator produces a variable frequency sinusoidal voltage, which controls the current that powers the coils and permanent magnets of the oscillator. The coils and magnets are wired to produce a torque about the axis of the specimen. The large inertia mass of the oscillator provides a fixed reaction such that the forcing torque produces vibration of the central mass and specimen cap. The output of the sine wave generator is amplified to provide enough power to induce vibration of the specimen. The shear strains that can be produced vary between  $1 \times 10^{-4}\%$  and  $1.5 \times 10^{-2}\%$ , depending on the specimen geometry. The minimum strain limit is determined by the sensitivity of the displacement measuring system, and the maximum limit is controlled by the stiffness of the soil specimen and the torque capacity of the oscillator.

The oscillatory motion of the soil specimen is monitored by a piezoelectric accelerometer mounted on the top platen. The accelerometer produces an electric charge which is proportional to acceleration. A charge amplifier is used to convert the electrical charge to a voltage that can be read with a voltmeter. Since the motion is sinusoidal, the displacements can be determined from the measured acceleration values.

Figure 3-2 shows the wiring schematic for the resonant column system. During testing, the excitation frequency is adjusted to obtain resonance of the system. Resonance is determined by observing the

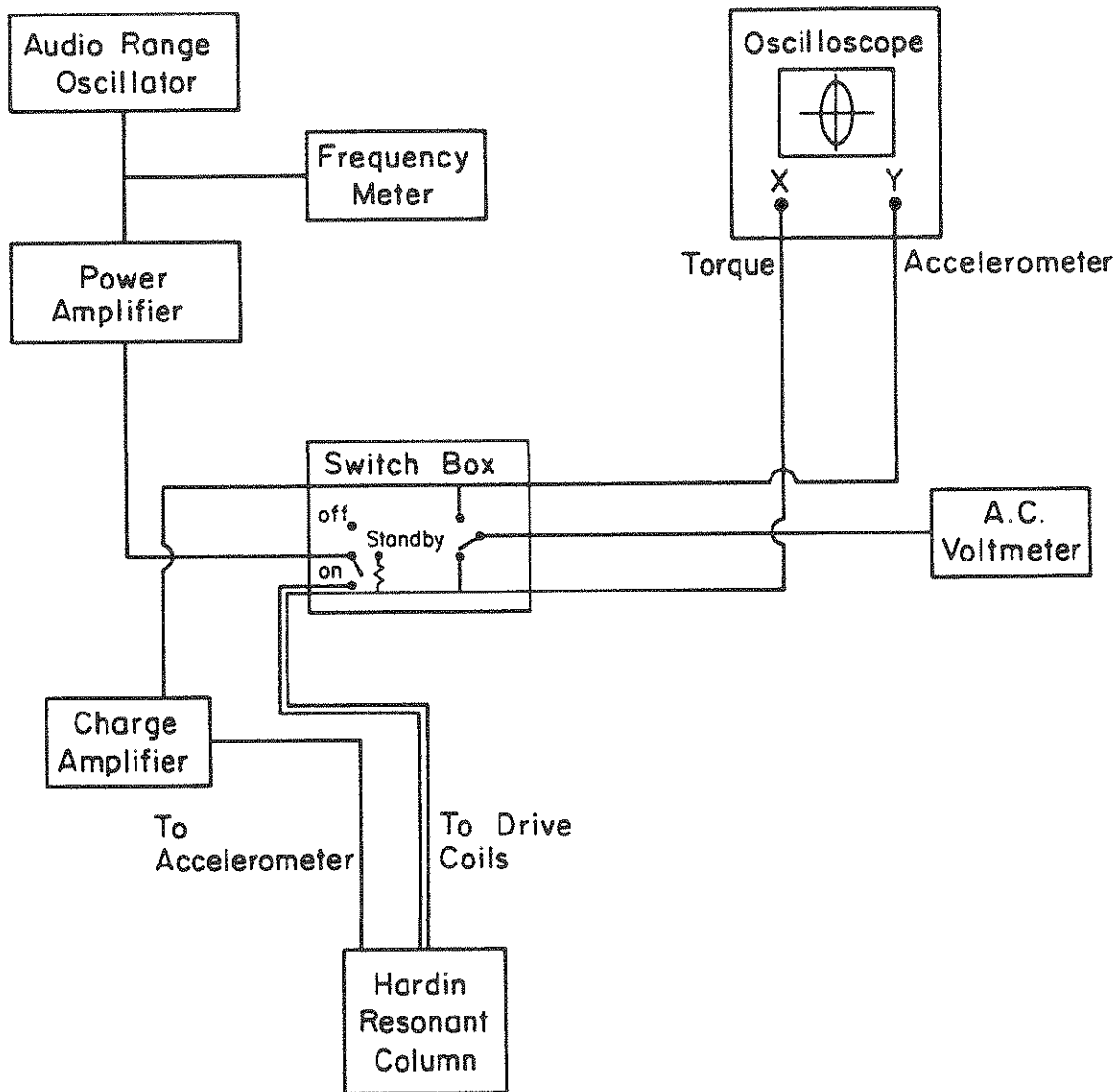


FIGURE 3-2. Wiring Schematic for Hardin Resonant Column

Lissajous figure formed on an X-Y oscilloscope by the torque and acceleration signals. First resonance occurs at the frequency for which the sinusoidal excitation torque and the acceleration signals are 90 degrees out of phase, i.e., the screen trace corresponds to an ellipse with vertical and horizontal axes.

The switch box controls the resonant column system. One switch has three settings: off, operational, and standby (standby allows determination of the applied torque before activation of the oscillator). The other switch has two settings which allow the voltmeter to read either the torque or accelerometer output.

The shear modulus and damping ratio are determined from the vibration response of the system, as defined by the torque and accelerometers output voltage at resonance, and by the system's resonant frequency. The resonant frequency of the system is used to determine the shear modulus. Damping is determined from either the magnification factor at resonance, or the decay in amplitude of the system undergoing free vibration. Pore pressure buildup during testing has to be carefully monitored, as operation at strain levels above a soil's threshold strain may cause rapid failure of the specimen. More detailed descriptions of the data reduction and operation procedures are contained in Appendix C.

### 3.1.2 Torsional Shear System

A quasi-static torsional load can be applied to a specimen by a torque motor system. The motor system, which is mounted on the pressure chamber lid, includes a stepper motor, rotary table, and sprocket system. The sprocket system consists of sprockets located on the top of the rotary table and on the piston, which are linked by two plastic-coated wire chains. The piston passes through the chamber lid and is fixed rigidly to the Hardin oscillator. The oscillator is fastened to the top platen by a special coupling. During assembly, the shaft is locked to the chamber lid. After the chamber lid is placed in position, the lock is released and the oscillator head lowered to meet the

top platen. The coupling is then completed with a long hex key inserted through the center of the hollow piston. Hence, rotation of the piston causes the oscillator and upper platen to rotate. Since the torsional oscillator has some torsional stiffness of its own, some small amount of torsional energy will be stored in the oscillator. However, this has been shown to have little practical effect [S.D.I., 1987].

The applied torsion passes through the cam assembly, upper platen, specimen, bottom platen, axial load transducer, and is finally reacted to by a torque transducer which is mounted under the pressure chamber base. The relative rotation between the bottom and top of the specimen is measured by two noncontacting displacement transducers located on a cylindrical platform. The platform is fastened to the bottom platen after zeroing of the transducers. The transducers measure the distance between nonconcentric circular cams, attached to the top platen, and the transducer faces. As the top platen rotates relative to the bottom, the distance between the cams and transducers changes, and hence the transducer output changes. Output from these transducers is linear for small rotations ( $\pm 5$  degrees), but varies with the sine of the rotation angle for larger rotations. The maximum rotation is 30 degrees in either direction. The system is designed to be unaffected by length changes of the specimen up to about 20 mm. However, it is very sensitive to lateral displacements, which can cause the transducers to go out of alignment. If the transducers cannot be zeroed, it is not possible to run a strain control test.

The stress and deformation limits for torsional testing for different specimen types are given in Table 3-1. The stress limits are based on the rated transducer maximums, and the strain limits are based on the rotation and vertical deformation limits. Monotonic tests can be performed to a maximum shear strain of roughly 19% using manual stepper motor control.

Control of the stepper motor and data acquisition systems is provided by a computer program, QSDATAWA. The program has four main functions:

TABLE 3-1. Stress and Deformation Limits of the Apparatus

Specimen	Solid	Hollow	Hollow
Outer diameter (mm)	71.1	71.1	101.6
Inner diameter (mm)	-	38.1	71.1
Length (mm)	193	193	193
Maximum cell pressure (kPa)	700	700	700
Maximum single amplitude shear strain (%)	7.8	9.3	14.4
Maximum axial strain (with an axial loader) (%)	10.5	10.5	10.5
Maximum shear stress (kPa)	401	524	228
Maximum axial stress (kPa)	760	1062	725

1. The Setup and Adjust menu allows for simultaneous monitoring of all six transducer outputs, and provides an average of the two rotation transducers. This menu is useful during specimen construction and assembly, when it is important to monitor the specimen to avoid excessive disturbance. Also, it should be used during saturation and consolidation procedures. The menu allows manual operation of the stepper motor at several speeds. From the zero position, the motor can move rotary table  $\pm$  65 degrees before limit switches disengage operation.

2. Monotonic Loading allows for shearing to some peak torque or rotation, with the option to return to a zero condition manually or automatically. Shearing rates can be selected, in terms of degrees per second, over a wide range. The program automatically prompts the user for all required information, including a data file name. Once the chosen values are confirmed, the display reverts to transducer outputs. The test is begun by pressing the PC's "F1" key, and may be

stopped manually at any time by pressing the "\" key. If the test is not stopped manually, it will stop according to the input torque or rotation limits reached, and store the data in the designated file on the computer's hard drive. During a test the torque and rotation values are updated on the screen, and the values for each of the transducer readouts are available on the signal conditioning meter.

3. Cyclic Rotation Testing allows for unipolar (one-way shearing) or bipolar (full shearing reversal) rotation to a specified rotation limit, in degrees. The number of cycles, cycle times, and a file name also must be specified before testing can begin. The number of data points taken per cycle varies, but is roughly 100 per cycle, and the maximum number of data points that can be taken is 2260. Therefore, the maximum number of cycles prescribed is effectively restricted, in one run, to between 20 to 25. If the data point/memory limit is reached during a test, the run will stop and a prompt will ask if the data acquired should be stored. Data reduction is done using a spreadsheet program, QSDATAVU. More detailed discussion of the data reduction program is contained in Appendix D. It usually is advantageous, if the cycles are to be analyzed using QSDATAVU, to restrict the number of cycles per run to between 5 and 10, to expedite data reduction. Approximate cycle times can range from 10 to 500 seconds (0.1 Hz to 0.002 Hz). Large cycle times should be used for runs where large pore pressure buildup is expected, i.e., the first 5 to 10 cycles. The test is started and can be stopped in a similar manner to a monotonic test. However, during testing, a plot of torque versus rotation is provided on the screen in real time. After the test is completed, all acquired data may be stored on the hard drive.

4. Cyclic Torque Testing is similar to rotation testing, except that cycle reversals occur at specified torque limits, rather than rotation limits. Results obtained from the data reduction procedures give stress-strain hysteresis loops for each cycle. From these loops, the shear modulus,  $G$ , and damping ratio,  $\lambda$ , can be calculated for every cycle of interest, as shown in Figure 3-3. The pore pressure buildup at the end of each cycle is obtained directly from the recorded data.

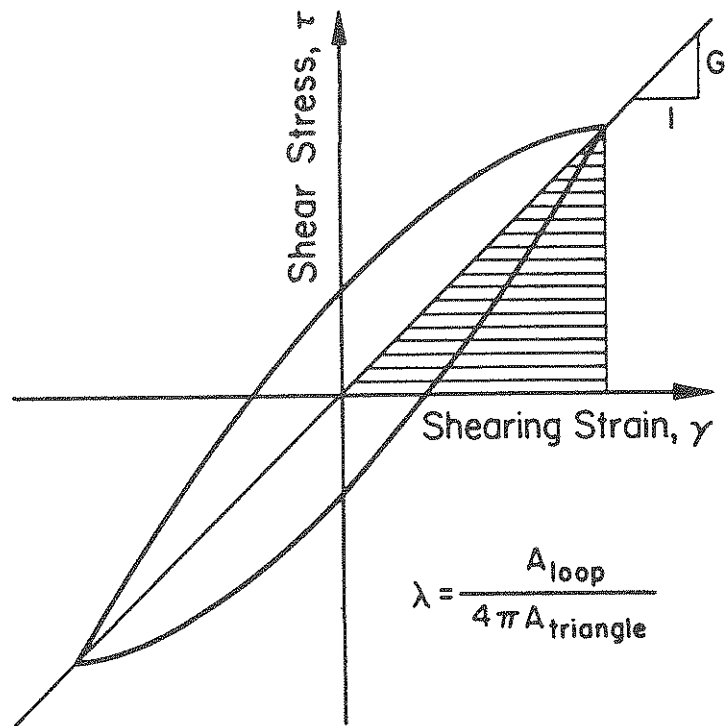


FIGURE 3-3. Definition of Secant Modulus,  $G$ , and Hysteretic Damping Ratio,  $\lambda$

### 3.2 MATERIAL PROPERTIES

The basic silt selected for this study is a nonplastic, finely ground silica, obtained from the Pennsylvania Glass Sand Company, and known as PGS 120 silt. This material was selected for several reasons. As discussed in Section 2, rough bounds exist on grain size distribution curves to delineate the liquefaction limits for clean granular materials. Figure 3-4 shows an approximate lower limit for potentially liquefiable soils [Tsuchida, 1970]. The coarse PGS 120 silt selected as the baseline material for this study has a grain size distribution for greater than the 40 percent passing size similar to the lower limit for potentially liquefiable soils, as given by Tsuchida [1970]. The PGS 120 silt, however, has a substantially higher fines content than Tsuchida's lower limit for most liquefiable soils.

Shen, et al. [1985] conducted laboratory tests on Tianjin silt,



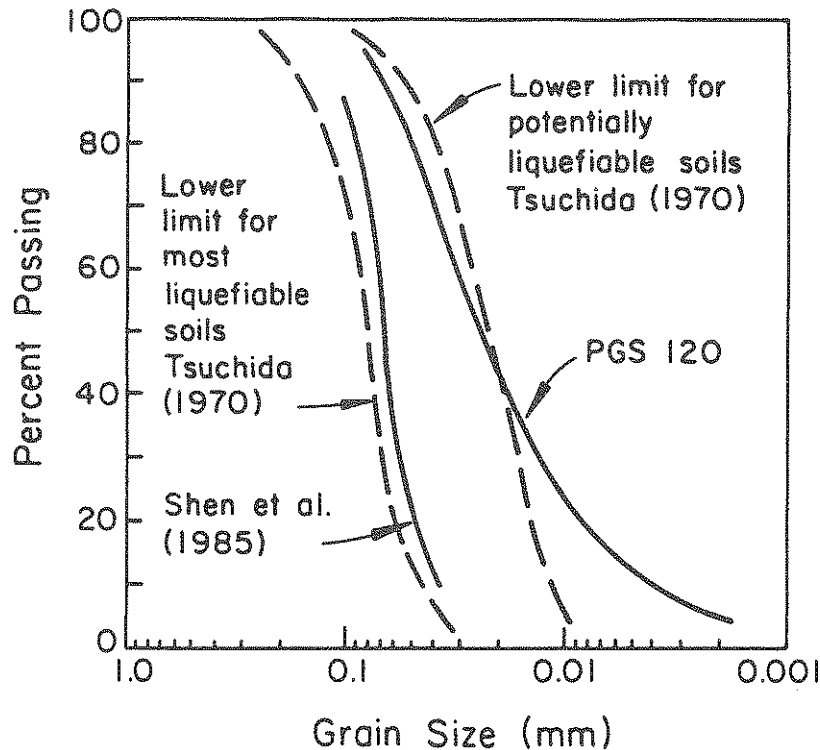


FIGURE 3-4. Grain Size Distributions for Silt Testing

obtained from a site in Tianjin, China that had experienced soil liquefaction during the 1976 Tangshan earthquake. The approximate grain size distribution for this silt, also shown in Figure 3-4, is only slightly finer than the lower limit for most liquefiable soils. They reported, as discussed in Section 2, that the dynamic response of the Tianjin silt, in terms of shear modulus, damping, and pore pressure generation, was similar in behavior to that of sand.

Therefore, the PGS 120 silt selected as the baseline material for this study is a borderline material with respect to liquefaction potential, if judged by grain size distribution alone. Table 3-2 indicates some basic PGS 120 silt properties. The maximum void ratio was determined in accordance with ASTM D4254-83 [ASTM, 1988b], method B. The minimum void ratio, however, was determined by using a standard Proctor mold and hammer, and a range of energies to compact the silt. Then, assuming a hyperbolic unit weight versus compaction energy relationship,

TABLE 3-2. Properties of PGS 120 Silt

Composition	Ground silica
Specific gravity	2.65
D <sub>90</sub>	0.068 mm
D <sub>10</sub>	0.004 mm
Uniformity coefficient	C <sub>u</sub> = 7.3
Minimum void ratio	0.5
Maximum void ratio	1.35
USCS classification	ML
Liquid limit	22%
Plastic limit	-
Plasticity index	N.P.

the maximum unit weight, and hence minimum void ratio, was calculated.

Figure 3-5 shows the plot of applied energy to applied energy divided by unit weight. The reciprocal of the gradient of the straight line gives the maximum unit weight. The  $e_{max}$  and  $e_{min}$  values are in general agreement with those quoted in Lambe and Whitman [1969] for an inorganic silt, i.e., 1.1 and 0.4, respectively.

### 3.2.1 Plasticity Control

To investigate the effects of plasticity on the dynamic behavior of PGS 120 silt, various percentages of a plastic clay were added to the pure silt. Adding small percentages, by weight, of Kaolin (Peerless No. 1) slightly alters the plasticity of the silt without significantly altering the grain size distribution. Addition of up to 10 percent Kaolin by weight was found to increase the plasticity index of

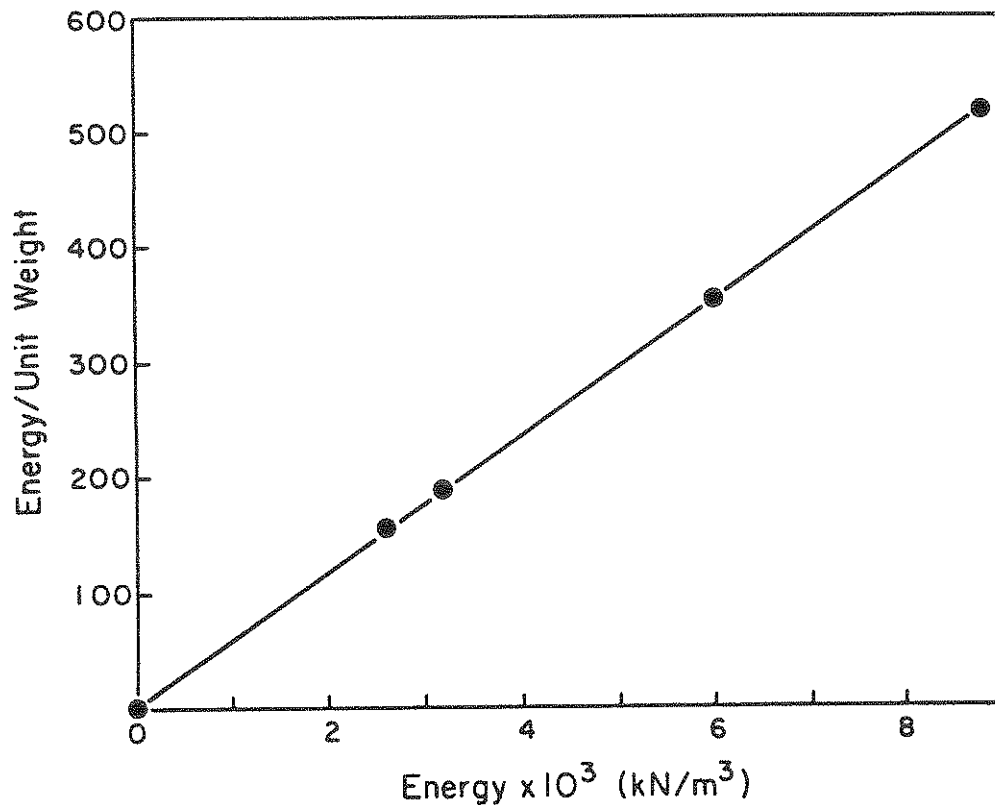


FIGURE 3-5. Energy/Unit Weight versus Energy

the silt from zero to roughly 4%, and the liquid limit was increased to 25%. Field experience with fine-grained soils has indicated that those materials with liquid limits (LL) less than about 35%, less than roughly 15% finer than 0.005 mm, and water contents near the liquid limit may be vulnerable to liquefaction [Wang, 1979]. Thus, by controlling the amount of Kaolin added to the silt, levels of plasticity below those listed above can be achieved.

Several Atterberg limits tests were performed according to ASTM D4318-84 [ASTM, 1988c] on several silt/clay mixes, and the results are shown in Figures 3-6 and 3-7. Figure 3-6 shows a linear relationship between liquid limit and percentage of clay. Sivapullaiah and Sridharan [1985] also have shown that, for silt/clay mixes, a linear relationship between clay percentage and liquid limit exists for relatively low clay percentages. Figure 3-7 shows the linear relationship between plasticity index and liquid limit for different silt/clay

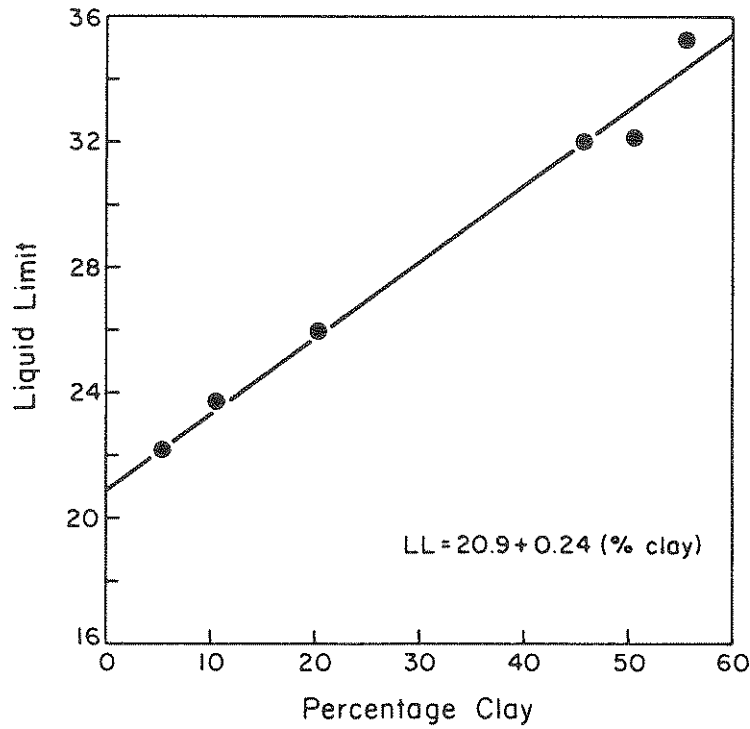


FIGURE 3-6. Liquid Limit versus Percentage Clay

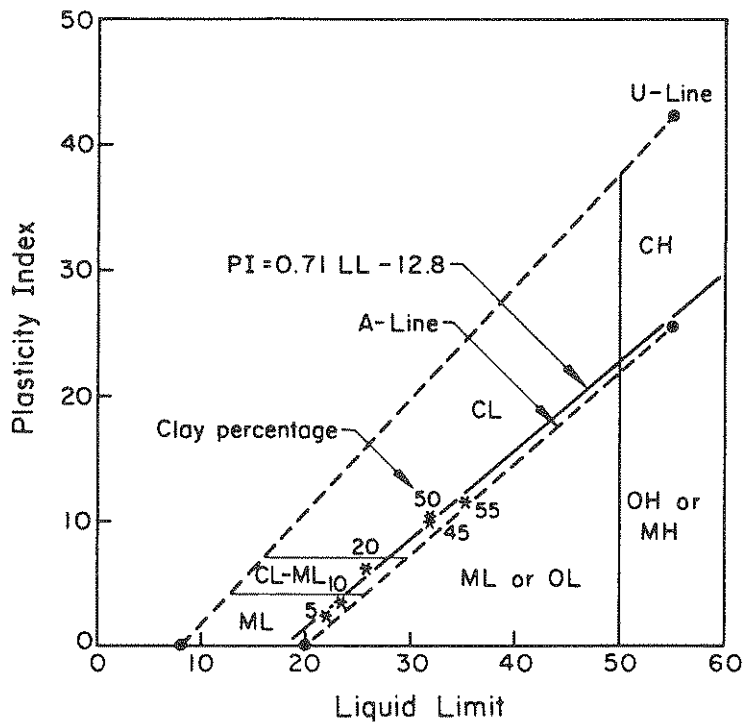


FIGURE 3-7. Plasticity Index versus Liquid Limit for Various Silt/Clay Mixes

mixes and the USCS soil classification boundaries.

Resonant column and torsional shear tests were carried out on pure silt specimens and specimens with clay additions of 10% and 20% by weight. These give plasticity properties below the limits described by Wang [1979] above. The plasticity limits for these clay percentages are given in Table 3-3, along with those for the pure PGS 120 silt.

### 3.2.2 Specimen Preparation

A number of oedometer tests were carried out to determine if a PGS 120 silt slurry could be consolidated into a sample suitable for trimming, the rationale being that if a block sample of the silt was consolidated, then several nominally uniform specimens could be trimmed from the block. The results of these tests showed that a pure silt specimen, since it was nonplastic, would require in-place preparation to a controlled physical state, and could not be trimmed from a block. The minimum percentage of Kaolin that would allow block trimming following consolidation from a slurry was 10% by weight. Therefore, it was decided to compact specimens to controlled relative densities in a split mold using the undercompaction method [Ladd, 1978] to ensure uniformity of preparation.

Many sample preparation techniques have been developed, and different techniques have been shown to produce different cyclic strengths [Mulilis, et al., 1978]. The method of undercompaction has, however, been shown to lead to more consistent and repeatable results. The method helps to minimize particle segregation, and can be used to prepare specimens over a wide range of relative densities. The method also can be used to determine a material's optimum cyclic strength at a given dry unit weight. The key feature about this preparation method is that reproducible specimens can be constructed at selected relative densities.

A spreadsheet program (SAMPREP) was developed to record specimen dimensions, weights, and miscellaneous test data. It also follows

TABLE 3-3. Plasticity Properties of Mixes

Clay Percentage	Liquid Limit (%)	Plastic Limit (%)	Plasticity Index (%)
0	22.0	-	N.P.
10	23.3	19.6	3.7
20	25.7	20.3	5.4

through the stages involved in constructing a specimen using under-compaction. A printout of this spreadsheet is given in Appendix B.

### 3.3 TESTING PROCEDURES

The resonant column and torsional shear testing performed for this study was carried out undrained, on saturated, isotropically consolidated specimens. The following is a brief discussion of the stages undertaken in a typical test:

1. The specimen was constructed to the desired relative density. A relative density of 50% was selected for most of the tests. This relative density has been used frequently for sand testing, making direct comparisons possible without additional corrections. In addition, specimens with relative densities of above roughly 65% can be difficult to prepare.

2. Saturation was achieved by allowing water to seep through the specimen. The cell pressure was maintained at 103 kPa, and the back-pressure at 69 kPa, while the top drainage line was left open. Thus, a 69 kPa pressure gradient across the specimen was used to maintain flow for up to two days. The time required for saturation depended on the specimen density and percentage of added clay. At these saturation pressures, the top and bottom of the specimen were subjected to effective stresses of roughly 103 kPa and 34.5 kPa, respectively. The

effect of these stresses was allowed for by later consolidating the whole specimen to an effective confinement of at least 100 kPa. To ensure an adequate level of saturation the pore pressure parameter,  $B$ , was measured as the cell pressure was increased. Backpressures of at least 500 kPa were required to ensure that  $B$  was greater than 0.9. Appendix B-2 contains a step by step saturation method.

3. Consolidation to the desired confining stress was performed after an acceptable level of saturation was reached. Consolidation was monitored using the axial length change LVDT. Primary consolidation, for the low plasticity silts tested, was complete within a few minutes. A uniform effective confining stress of roughly 100 KPa was chosen for each test.

4. After consolidation, the drainage lines were closed and effective pressure changes monitored in the specimen for at least 15 minutes. If large pressure losses occurred, the specimen was not used for further testing. The most common sources of leaks were damaged membranes or leaking connections within the pressure chamber.

5. The shear modulus,  $G_{\max}$ , of the specimen was determined using the resonant column test at small (roughly  $10^{-4}\%$ ) shear strains. A series of resonant column tests was then carried out at increasing levels of shear strain. The effective pressure was monitored carefully, and if pore pressure buildup began to occur, resonant column testing was stopped at that strain level. The concept of a threshold shear strain level determining the level at which pore pressure begins to increase was discussed in Section 2. To assess the effects of strain history, sometimes only a  $G_{\max}$  test was carried out before continuing to torsional shear loading.

6. After resonant column testing was complete, strain-controlled torsional shear testing was carried out at much greater shear strain levels than used in the resonant column phase. Usually, 100 cycles of rotation-controlled torsional loading was performed. The data from this test were then used to calculate the shear modulus after loading cycles 1, 5, 10, 20, 50 and 100.

7. Final specimen dimensions were taken after completion of a test, and the water content and relative density were determined.

To characterize a specimen's response over a wide strain range, at least four different tests were required, with each test using a different level of torsional shear strain amplitude.

#### 3.4 SUMMARY

The quasi-static torsional simple shear/resonant column device was described in some detail. The general arrangement of the device and its transducer systems, as well as operational stress and deformation limits, were presented. The resonant column and torsional shear systems were described and operating procedures discussed.

Material properties such as maximum/minimum density, Atterberg limits, and grain size distributions were presented for the test silt. Atterberg limits also were given for the silt-clay mixes, and relationships between plasticity index and liquid limit were determined for various clay percentages.

The undercompaction method of sample preparation was determined to be suitable for this experimental program, the important factor being that this preparation method has been shown to allow construction of reproducible specimens at selected relative densities. A relative density of 50% was chosen for most of the tests.

An outline of the test sequence, including specimen saturation, consolidation, resonant column, and torsional shear procedures, was presented.



## SECTION 4 TEST RESULTS

### 4.1 INTRODUCTION

#### 4.1.1 Test Conditions

A summary of all tests presented in this section is given in Table 4-1. All of the tests shown were carried out on solid 71.1-mm-diameter PGS 120 silt specimens, with Kaolin clay (Peerless No.1) contents of 0%, 10%, or 20% by weight, and constructed to a relative density of 50% (based on the silt  $e_{max}$  and  $e_{min}$ ). An isotropic effective confining stress of roughly 100 kPa was used for each test. The general test procedure was to carry out resonant column tests, at successively higher strain amplitudes, until pore pressure generation began to occur, and then to perform a strain controlled torsional simple shear test at a predetermined cyclic strain level. All tests were carried out with the drainage lines to the specimen closed, i.e., undrained. From the resonant column test data, shear modulus and damping ratio values could be determined at different levels of shear strain. From the torsional shear test data, shear modulus,  $G$ , damping ratio,  $\lambda$ , and pore pressure ratio,  $\Delta u/\bar{\sigma}_c$ , values were determined at one level of cyclic strain, but for different load cycles.

Test SI-18 was a large strain monotonic test which was required for the calculation of the silt's effective stress friction angle,  $\bar{\phi}$ . The test was carried out using computer control of the stepper motor in the "Setup and Adjust" mode of the program, QSDATAWA, and manually recording the transducer data at different rotations. The rotation transducers, having only a limited range of  $\pm 30$  degrees, were removed and rotation determined from the scale on the rotary table.

The discussion of the results has been divided into three sections which describe the effect of shear strain level, number of loading cycles, and plasticity on the dynamic properties and pore pressure generation characteristics of the silt. The normalization procedures

TABLE 4-1. Test Summary

Test No.	$\bar{\sigma}_c$ (kPa)	% Clay by Weight	PI (%)	Test Type <sup>a</sup>	Cyclic Strain $\gamma_{cy}$ (%) <sup>b</sup>
SI-11	105	0	0	RC TS	0.001 0.029
SI-13	98	0	0	RC TS	0.005 0.17
SI-15	93	0	0	RC TS	0.0001 0.087
SI-16	104	0	0	RC TS	0.0001 0.87
SC-1	116	10	3.7	RC TS	0.00006 0.87
SC-2	109.5	10	3.7	RC TS	0.0035 0.17
SC-3	97	10	3.7	RC TS	0.0038 0.087
SC-4	98.5	10	3.7	RC TS	0.004 0.029
SC-5	103.5	20	5.4	RC TS	0.0042 0.17
SC-6	105	20	5.4	RC TS	0.0046 0.087
SC-7	107	20	5.4	RC TS	0.0044 0.029
SC-8	108	20	5.4	RC TS	0.0046 0.87
SI-18	106	0	0	RC TS	Monotonic Test to $\gamma = 17.5\%$

<sup>a</sup>RC = resonant column; TS = torsional shear

<sup>b</sup>For RC testing,  $\gamma_{cy}$  = upper limit  $\gamma_{cy}$ ; for TS testing,  $\gamma_{cy}$  = test  $\gamma_{cy}$

used in the data analysis are discussed below.

#### 4.1.2 Normalization Procedure

If a given soil was tested in direct simple shear, triaxial compression, and torsional simple shear, each test would demonstrate different shear stress-shear strain behavior, particularly if the soil was saturated and the testing was done without allowing drainage. Some of the differences in behavior would be due to the boundary conditions imposed by the given apparatus, e.g., end platen restraint, membrane penetration, specimen configuration, stress application, etc. Others would be due to shortcomings in the theories used for data reduction. Even for a given test apparatus, there is difficulty in reconciling stress-strain data from tests on the same soil but tested at different confining stresses or different stress states.

Drnevich [1981] has shown that, for a given soil, incrementally normalized data from different types of tests are relatively independent of the test used. Normalized data also have been shown to be more insensitive to sample disturbance. The effects of variations in specimen preparation also are reduced. The normalization procedure used in this section is based on that presented by Drnevich [1981], in which normalized stress-strain curves can be obtained by use of maximum shearing stress to normalize shear stress, and a reference strain to normalize shear strain. The reference strain,  $\gamma_r$ , is defined as:

$$\gamma_r = \tau_{\max}/G_{\max} \quad (4-1)$$

where:

$\tau_{\max}$  = maximum shearing stress as dependent on effective stress level, and

$G_{\max}$  = initial tangent shear modulus as dependent on effective stress level.

$G_{\max}$  can also be defined as the low strain amplitude shear modulus determined from resonant column testing. Also, Drnevich [1981]

defines  $G_{\max}$  and  $\tau_{\max}$  to be functions of effective stress state. Therefore, using the Mohr-Coulomb failure criteria, and for torsional shear testing:

$$\tau_{\max} = \bar{\sigma}_c \tan \bar{\phi} \quad (4-2)$$

where:

$\bar{\sigma}_c$  = effective confining stress, and

$\bar{\phi}$  = effective stress friction angle.

Also, from Hardin and Drnevich [1972],  $G_{\max}$  may be defined as proportional to the square root of effective confining stress, therefore:

$$G_{\max} = F(\bar{\sigma}_c)^{0.5} \quad (4-3)$$

where:

F = a soil constant for undrained tests.

The constant, F, can be determined from equations based on void ratio, plasticity, and overconsolidation ratio. Alternatively, a low strain amplitude resonant column test can be used to determine  $G_{\max}$  at a specific level of effective confining stress, and therefore allow direct calculation of F. Using this method, a new value for F was calculated directly for each specimen.

Since both  $\tau_{\max}$  and  $G_{\max}$  are functions of the effective confining stress, they will change as pore pressure changes occur during shearing. Thus, the normalizing parameters vary with stress points along the stress path. Figure 4-1 shows the stress paths for an undrained monotonic torsional shear test on a contractive specimen, and indicates how  $\tau_{\max}$  changes as excess pore pressure,  $\Delta u$ , builds up due to torsional shearing ( $u_0$  is the initial static pore pressure in the specimen). Also, the effective confining stress at point B will be less than that for point A, and thus  $G_{\max}$  also changes. Note for an isotropic torsional shear test,  $q$  equals the applied shear stress, and  $\bar{p}$  will equal the two-dimensional mean effective stress.

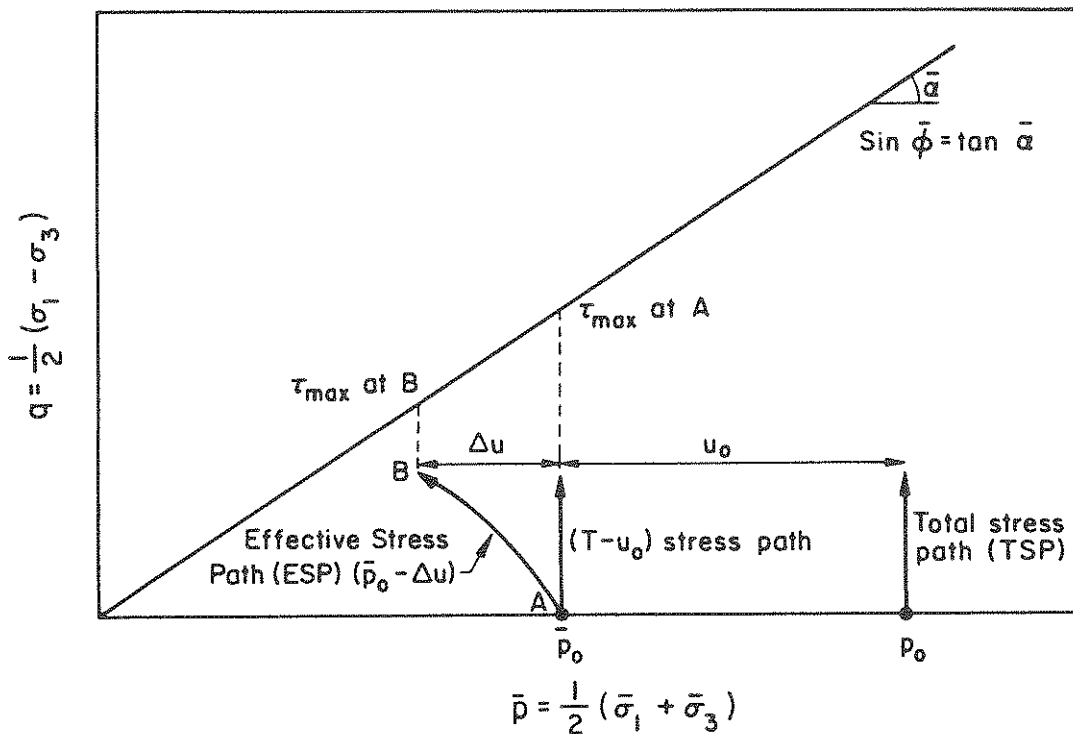


FIGURE 4-1. Stress Paths for an Isotropic Undrained Monotonic Torsional Shear Test

To determine the effective stress angle of friction required for the normalization calculation of  $\tau_{\max}$ , a monotonic torsional shear test was run on a pure silt specimen to roughly 17% shear strain. The results of this test are given in Figures 4-2, 4-3, 4-4, and 4-5. The shear stress-shear strain plot is given in Figure 4-2. The figure also shows a peak shear stress and subsequent loss of strength, which is characteristic of a contractive material. Thus, for a placement relative density of 50%, the silt behaves in a contractive manner, which indicates that the material is susceptible to not only cyclic mobility, but also liquefaction flow failure. A steady state of deformation may be occurring beyond 12% shear strain, but from the figure, it appears that shear resistance is slowly increasing with increasing shear strain. This behavior is illustrated more clearly by Figure 4-3, which shows the effective stress path for the test, and indicates a small amount of shear resistance at zero effective

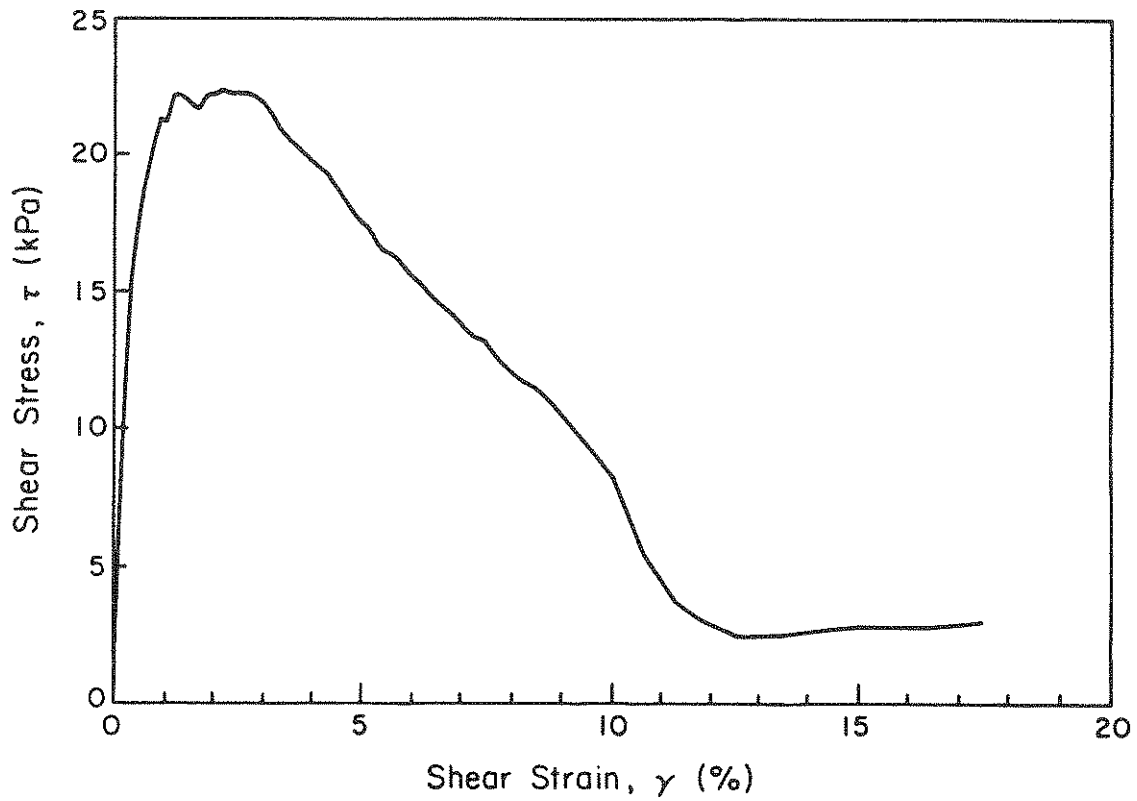


FIGURE 4-2. Shear Stress versus Shear Strain for a Monotonic Torsional Shear Test

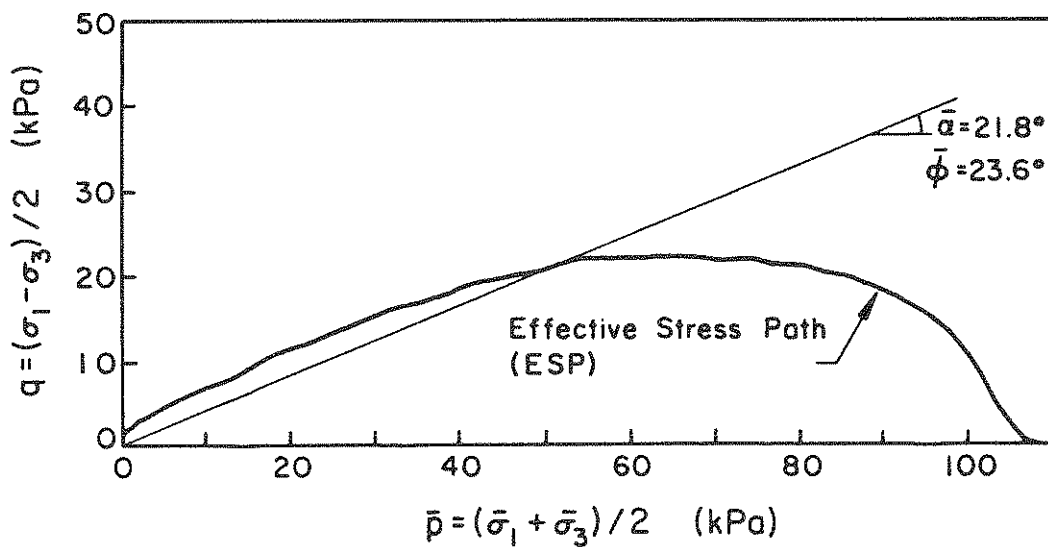


FIGURE 4-3. Effective Stress Path and Failure Envelope for a Monotonic Torsional Shear Test on Silt

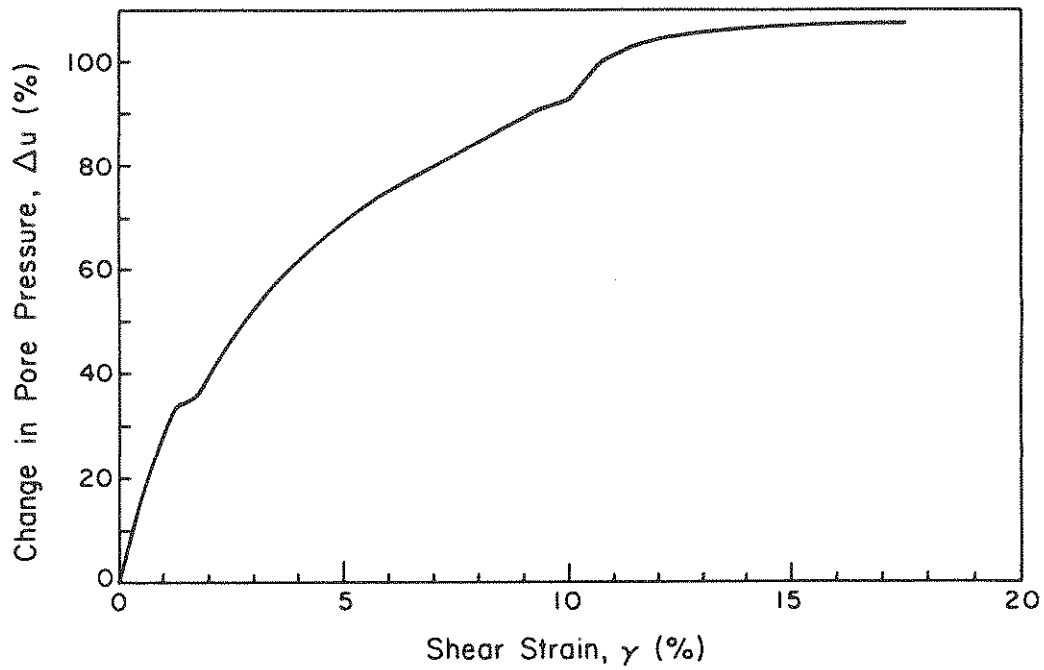


FIGURE 4-4. Pore Pressure Change versus Shear Strain for a Monotonic Torsional Shear Test

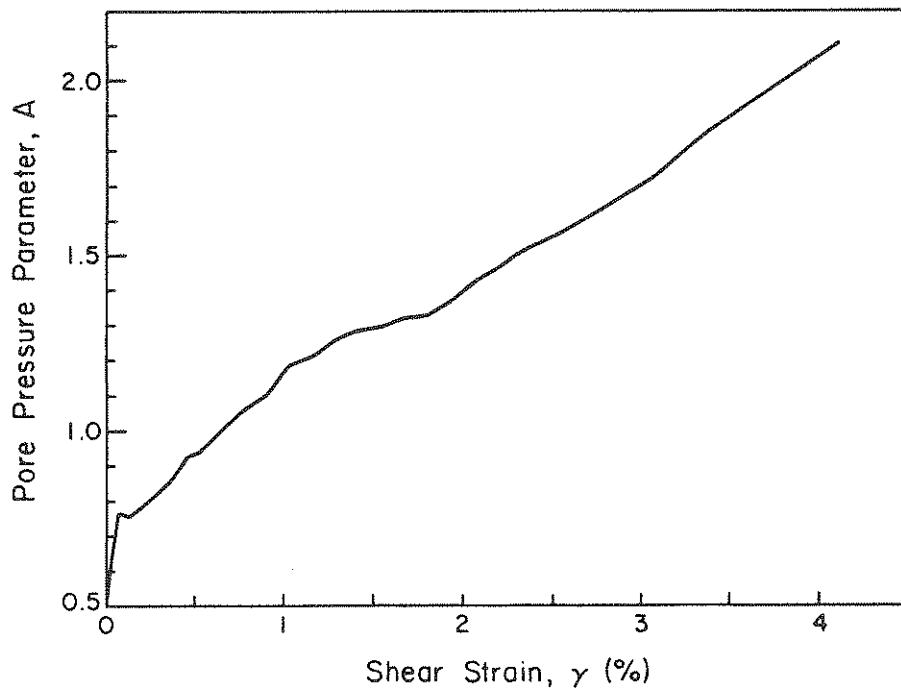


FIGURE 4-5. Pore Pressure Parameter A versus Shear Strain for a Monotonic Torsional Shear Test

confining stress. This apparent shear resistance at zero effective stress was due to the shear resistance of the membrane and the pressure tubing to the top platen. Figure 4-3 also shows the estimated position of the Mohr-Coulomb failure envelope, which gives a  $\bar{\phi} = 23.6$  degrees ( $\tan \bar{\alpha} = \sin \bar{\phi}$ ). The position of this envelope was determined by drawing a line parallel to the effective stress path for  $\bar{p} < 40$  kPa, and passing through the origin.

Figure 4-4 indicates the pore pressure buildup with increasing shear strain, and Figure 4-5 shows the increase in the pore pressure parameter A with increase up to the peak shear stress. For an isotropically consolidated monotonic torsional shear test:

$$A = (\Delta u + \tau) / 2\tau \quad (4-4)$$

where:

$\Delta u$  = change in pore pressure, and

$\tau$  = shear stress.

## 4.2 RESONANT COLUMN AND TORSIONAL SHEAR RESULTS

### 4.2.1 Effect of Cyclic Shear Strain Level

Figure 4-6 shows normalized shear modulus plotted against normalized shear strain for four tests on pure silt specimens. Resonant column results have been combined with torsional shear results on the same figure. For the torsional shear tests,  $G/G_{\max}$  curves have been drawn for 1 and 100 cycles of loading. Several important trends are apparent from this figure. Normalized shear modulus decreases with increasing shear strain and increasing number of loading cycles above the threshold strain. The threshold strain for this material was approximately 0.004%. Also, the effect of number of loading cycles on  $G/G_{\max}$  increases as shear strain increases. Note that the shape of the curves shown in Figure 4-6 is typical for this type of relationship, and that the torsional shear data matches well with the resonant column data.



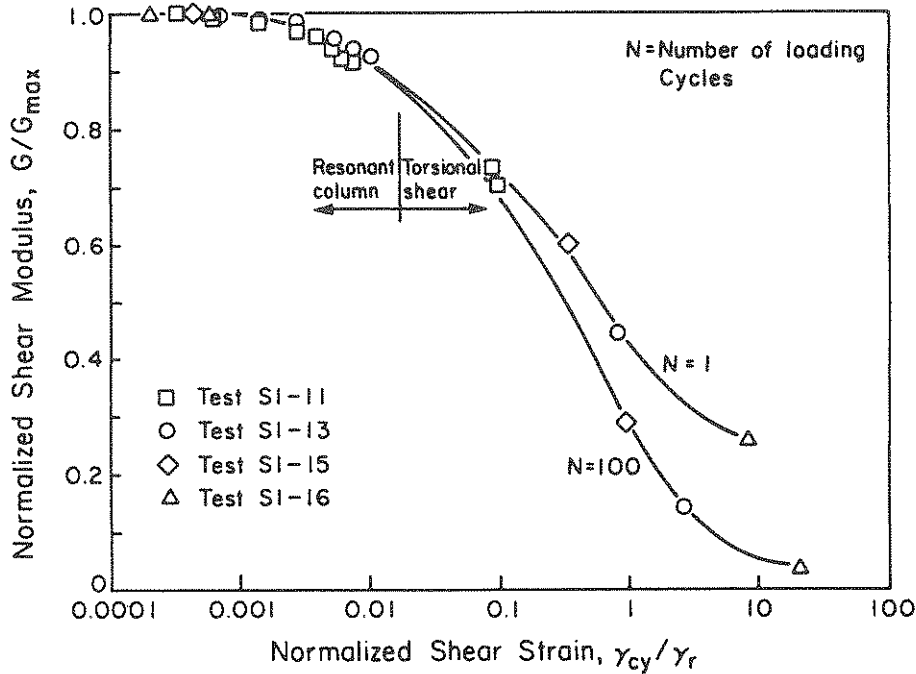


FIGURE 4-6. Normalized Shear Strain versus Normalized Shear Modulus for 0% Clay

Figure 4-7 shows normalized pore pressure increase plotted against normalized shear strain for pure silt specimens. The effect of loading cycles is illustrated by curves representing 1 and 100 loading cycles. Thus, pore pressure generation increases as shear strain increases and as number of cycles increases. The effect of number of loading cycles is most important at moderate levels of cyclic strain, i.e., at high cyclic strains, maximum pore pressure increase will occur in one cycle, but at low strains, number of loading cycles has little or no effect.

The threshold strain,  $\gamma_t$ , for pore pressure generation was found for all the specimens tested to be roughly 0.004%. Chung, et al. [1984] indicated a threshold strain level of 0.002% for resonant column tests on sands. Dobry, et al. [1981] indicated a threshold strain level based on 10 cycles of torsional shear loading of 0.01%. These differences confirm that threshold strain level is not an entirely

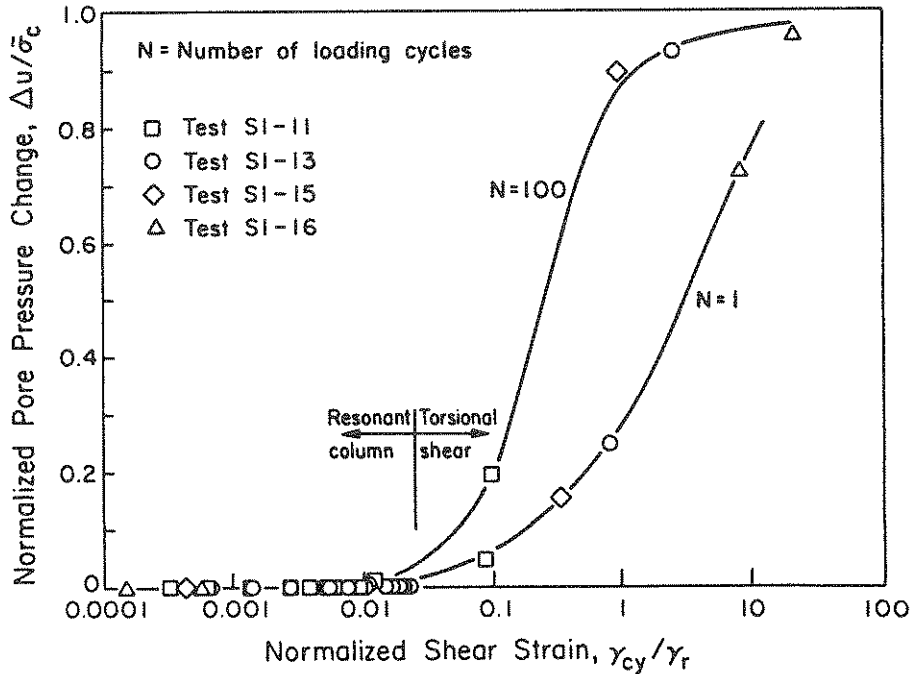


FIGURE 4-7. Normalized Shear Strain versus Pore Pressure Ratio for 0% Clay

fundamental soil property, since it is apparently dependent on number of loading cycles and soil type.

Figure 4-8 shows normalized damping ratio,  $\lambda / \lambda_{\min}$ , plotted against normalized shear strain for pure silt. The damping ratio at low strain amplitude is  $\lambda_{\min}$ . Note that, adjacent to each torsional shear test point, the number of loading cycles has been indicated. The results, especially for the torsional shear tests, show a wide variation, which is typical of damping ratio results in general [Seed and Lee, 1970]. However, several general conclusions still can be drawn. As cyclic shear strain increases, damping ratio increases, and as the number of loading cycles increases, damping ratio decreases. Also, the effect of number of loading cycles probably becomes greater as cyclic shear strain increases.

Figure 4-9 shows cyclic shear stress,  $\gamma_{cy}$ , plotted against cyclic

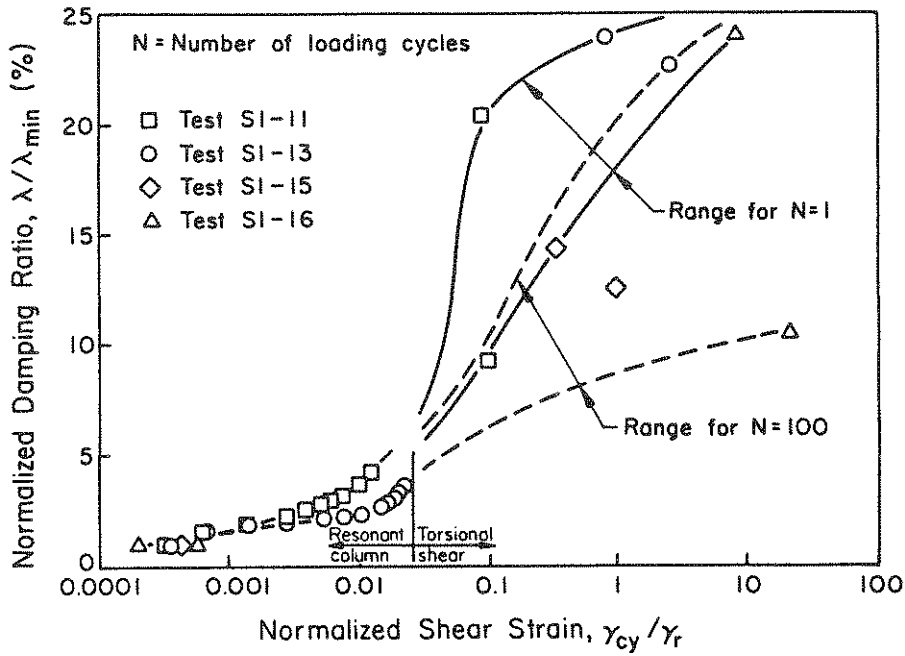


FIGURE 4-8. Normalized Damping Ratio versus Normalized Shear Strain for 0% Clay

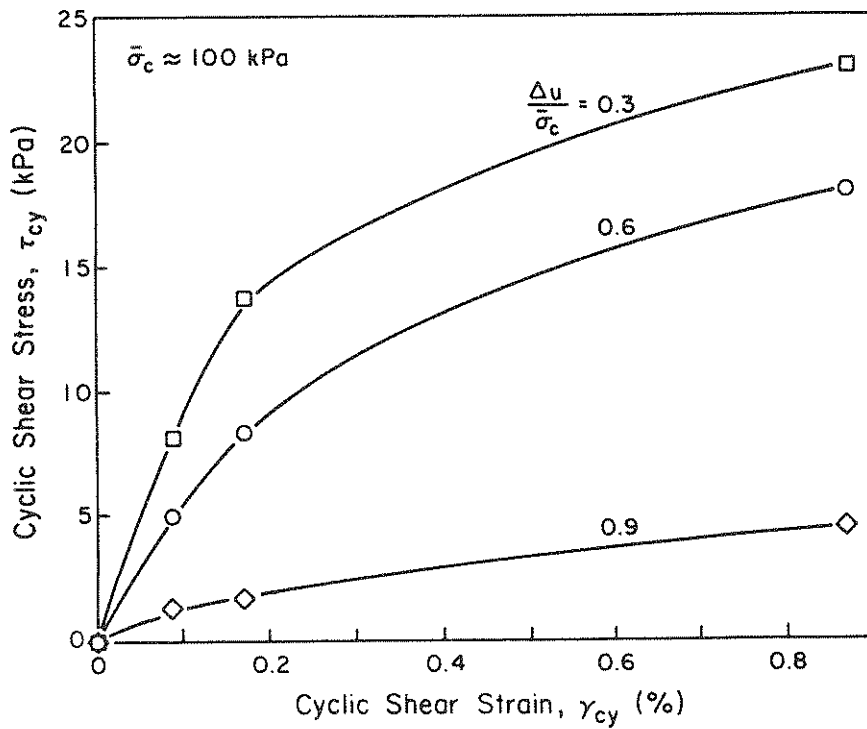


FIGURE 4-9. Cyclic Shear Stress versus Cyclic Shear Strain for 0% Clay and Various Levels of Pore Pressure Ratio

shear strain for a pure silt. Lines representing different levels of pore pressure ratio show the reduction in cyclic shear stress at constant strain amplitude that occurs as the pore pressure ratio increases.

#### 4.2.2 Effect of Number of Loading Cycles

Torsional shear tests can be used to illustrate the effect of number of loading cycles. Figure 4-10 shows number of cycles plotted against shear modulus for pure silt. Curves for different levels of cyclic strain also are shown on the figure. Note that the shear modulus has not been normalized, in order to show some actual modulus magnitudes. However, the trends apparent in this figure are unaffected by normalization. The figure, therefore, indicates that shear modulus decreases as number of loading cycles or  $\gamma_{cy}$  increases. Approximately 50% of the maximum decrease in shear modulus due to increased number of cycles occurred within the first 10 loading cycles. The magnitude of the reduction in  $G$  with increasing  $N$  becomes lower as  $\gamma_{cy}$  decreases. Note that the silt has a very low shear modulus for a confining pressure of 100 kPa, i.e., it is approximately one quarter that of Ottawa 20-30 sand tested under comparable conditions. Only values up to 20 cycles are shown for the highest level of cyclic shear strain, 0.87%, because generally after 20 cycles, no further modulus degradation or pore pressure increase occurs.

Figure 4-11 shows number of cycles plotted against pore pressure ratio for pure silt. Curves for four torsional shear tests at different levels of cyclic strain are shown on the figure. Trends apparent from this figure are similar to those determined from Figure 4-7. As number of loading cycles or the level of cyclic strain increases, the pore pressure ratio increases. The effect of increasing cycles has less effect on the specimens subjected to the lowest, 0.029%, and the highest, 0.87%, levels of cyclic strain. Approximately 60% of the maximum pore pressure increase due to increasing numbers of load cycles occurred within the first 10 loading cycles.

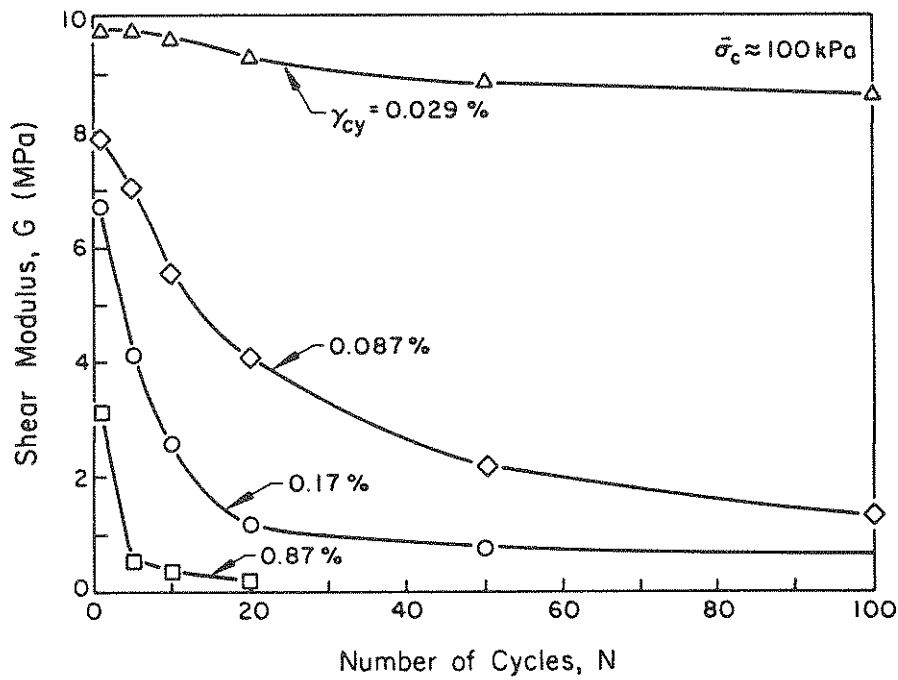


FIGURE 4-10. Number of Cycles versus Shear Modulus for 0% Clay and Different Levels of  $\gamma_{cy}$

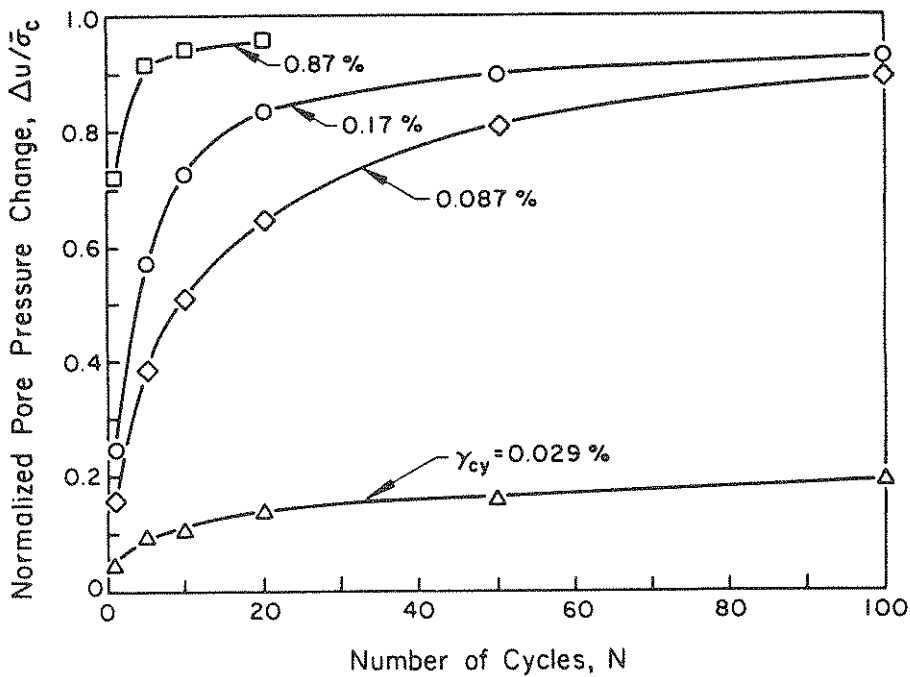


FIGURE 4-11. Number of Cycles versus Pore Pressure Ratio for 0% Clay and Different Levels of  $\gamma_{cy}$

Figure 4-12 shows number of cycles plotted against damping ratio for pure silt at different levels of cyclic shear strain. A number of general trends are apparent, even though the results are more inconsistent than the pore pressure ratio and shear modulus results. As the number of cycles increases or the cyclic shear strain level decreases, the damping ratio decreases. However, for  $\gamma_{cy} = 0.087\%$  and  $0.17\%$ , the damping ratio actually increases between cycles 10 and 50, and then decreases again between cycles 50 and 100. The maximum decrease in damping ratio with increasing number of cycles occurs at the largest cyclic shear strain level.

#### 4.2.3 Effects of Plasticity

The effects of plasticity were studied by adding amounts of Peerless No. 1 Kaolin clay to the PGS 120 silt. The general trends which have been discussed in sections 4.2.1 and 4.2.2 hold equally true for the specimens tested with 10% and 20% clay fractions. As discussed in Section 3, the effect of adding clay to the silt is primarily to increase a specimen's plasticity. Although other effects, such as change in grain size distribution and the maximum and minimum void ratios, cannot be dismissed, by keeping the change in clay percentage low, the dominant effect on a specimen is the change in its plasticity, i.e., from a nonplastic silt to a low plasticity clayey silt.

Figure 4-13 shows normalized shear strain plotted against normalized shear modulus for one cycle of torsional shear loading. The figure has curves drawn for different clay contents for both the resonant column and torsional shear test results. The figure shows that the increased plasticity has shifted the shear modulus curve slightly to the right for both sets of results. Factors that could influence the position of these curves include confining stress, void ratio changes, degree of saturation, and strain rate. However, as the tests were carried out using identical procedures, these factors should affect every test to the same extent.

Figure 4-14 shows pore pressure ratio plotted against normalized shear

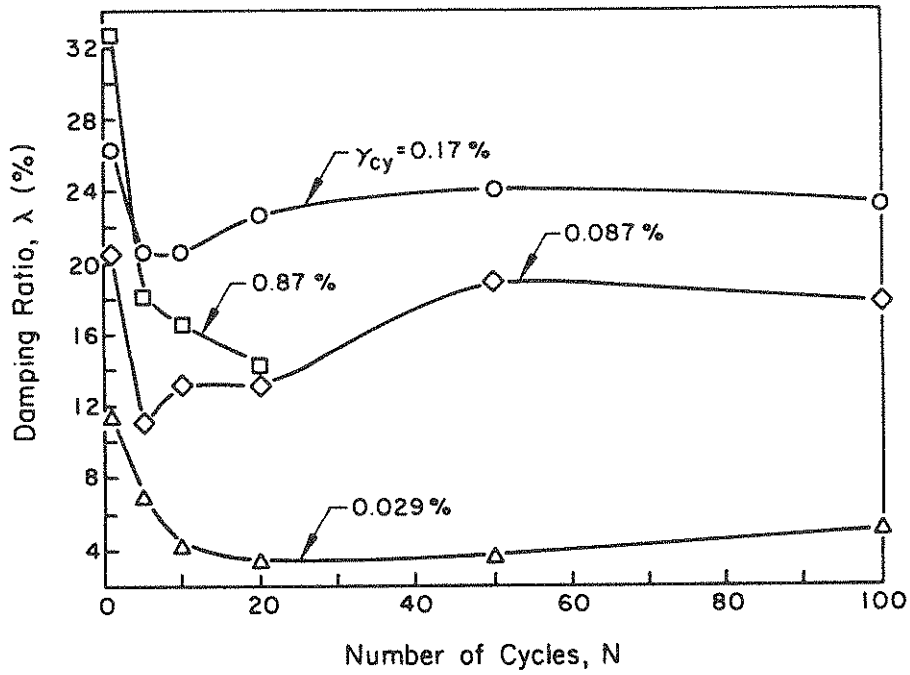


FIGURE 4-12. Number of Cycles versus Damping Ratio for 0% Clay and Different Levels of  $\gamma_{cy}$

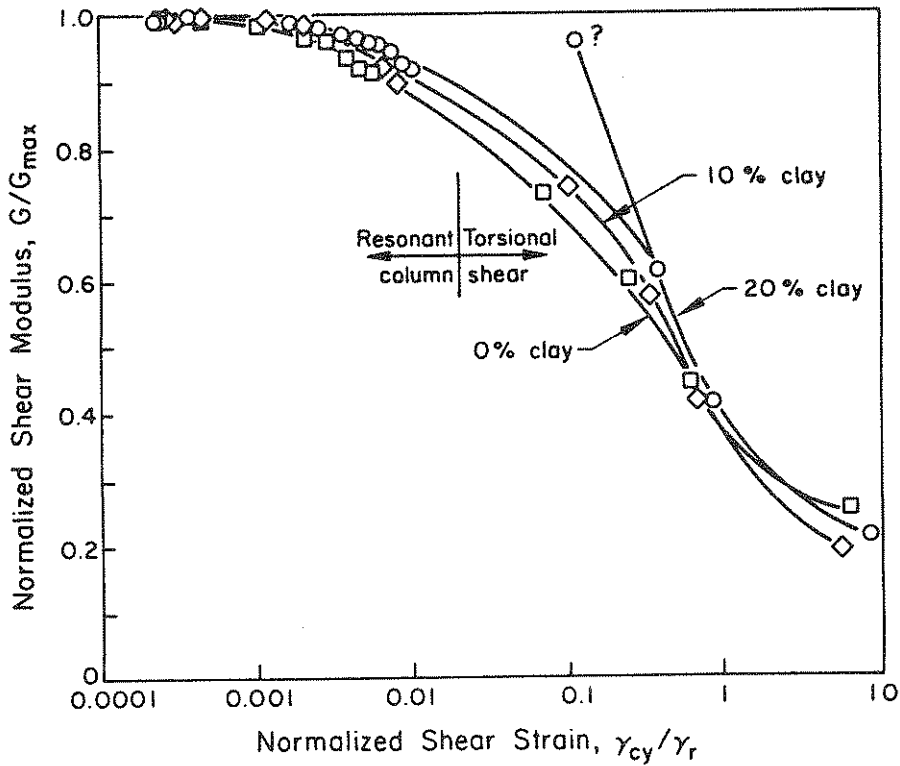


FIGURE 4-13. Normalized Shear Modulus versus Normalized Shear Strain for One Cycle of Torsional Shear Loading and Clay Fractions of 0%, 10%, and 20%

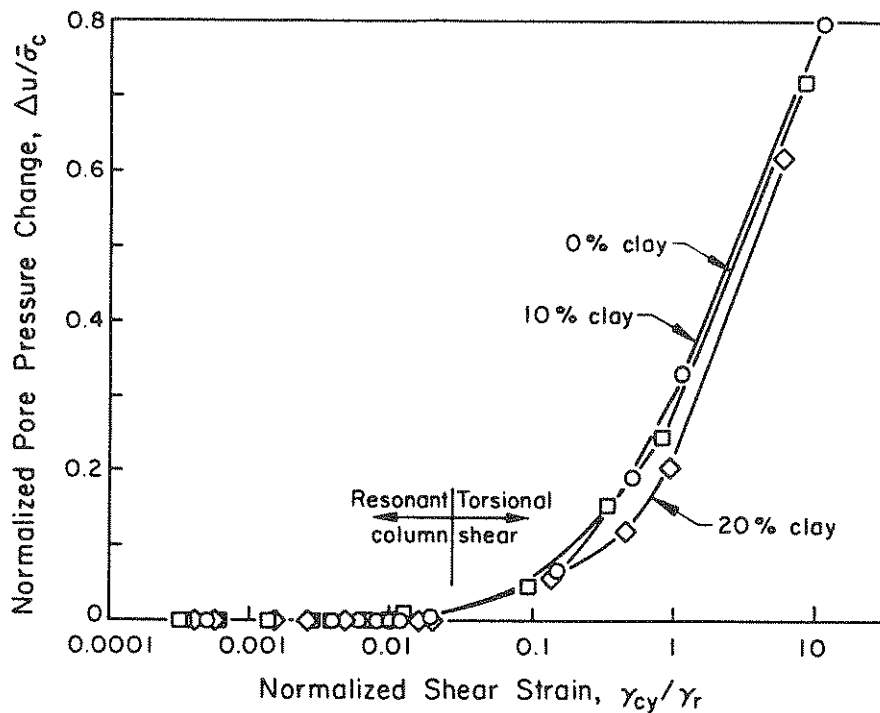


FIGURE 4-14. Pore Pressure Ratio versus Normalized Shear Strain for One Cycle of Torsional Shear Loading and Clay Fractions of 0%, 10%, and 20%

strain for one cycle of torsional shear loading. Curves for different clay fractions are also indicated. The 0% and 10% clay pore pressure ratio curves are very similar, but the 20% clay curve is distinctly lower. Thus, increasing clay percentage (increasing plasticity) decreases pore pressure generation potential.

Figure 4-15 shows normalized damping ratio plotted against normalized shear strain for one cycle of torsional shear loading. From the torsional shear tests, there is no clear trend discernable for the effect of increased clay percentage, so a range for one loading cycle for all the materials tested is shown on the figure. However, the resonant column tests show a clear decrease in value for increasing clay content, although the decrease appears slightly greater for the 10% clay than the 20% clay.



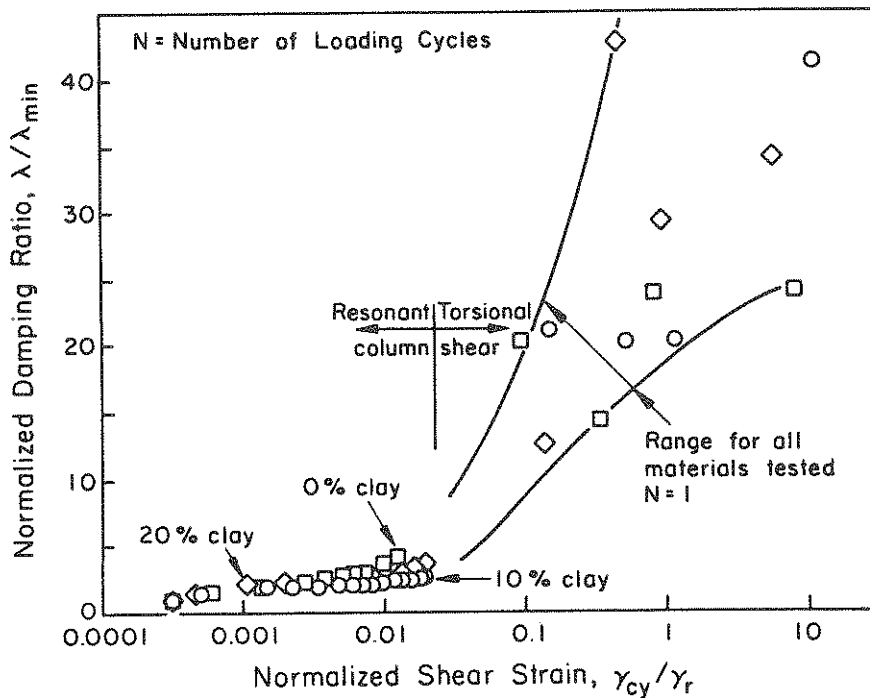


FIGURE 4-15. Normalized Damping Ratio versus Normalized Shear Strain for One Cycle of Torsional Shear Loading and Clay Fractions of 0%, 10%, and 20%

Figure 4-16 shows shear modulus plotted against number of load cycles at a cyclic torsional shear strain level of 0.17%. The figure also shows curves for different clay percentages, and indicates that the magnitude of shear modulus degradation for increasing load cycles is substantially decreased as clay percentage is increased.

Figure 4-17 shows pore pressure ratio plotted against number of load cycles at a cyclic torsional shear strain level of 0.17%, and for clay fractions of 0%, 10%, and 20%. The curve for the 10% clay plots above the curve for 0% clay, but the difference is not significant, and the pore pressure responses can be considered as being approximately equal. But the curve for 20% clay plots well below the other curves, and thus can be considered as having lower pore pressure generation potential. Therefore, increased clay percentage above roughly 10% significantly reduces the excess pore pressure generation capability

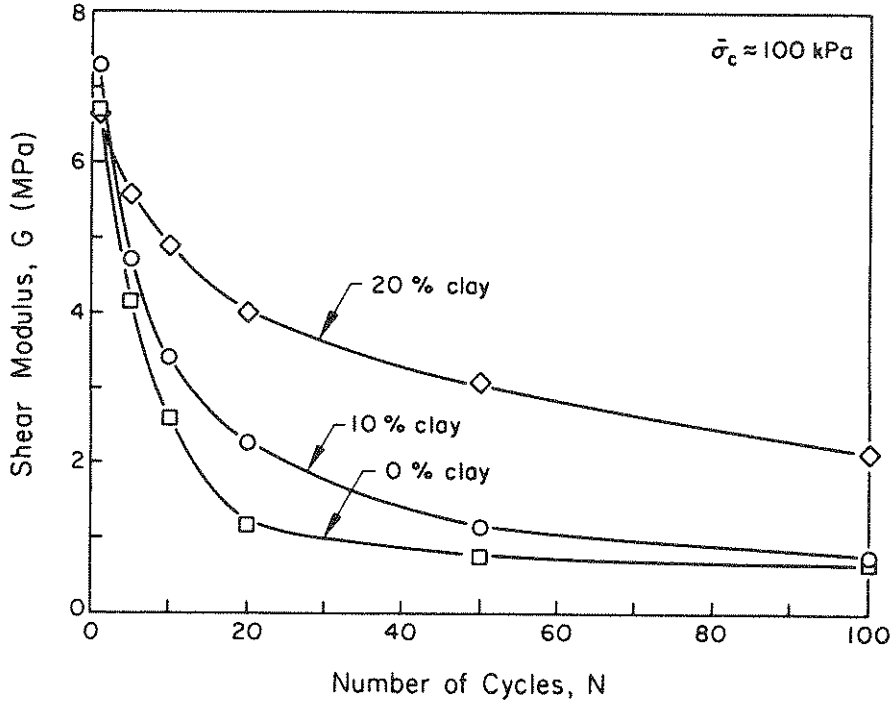


FIGURE 4-16. Shear Modulus versus Number of Loading Cycles for  $\gamma_{cy} = 0.17\%$  and Clay Fractions of 0%, 10%, and 20%

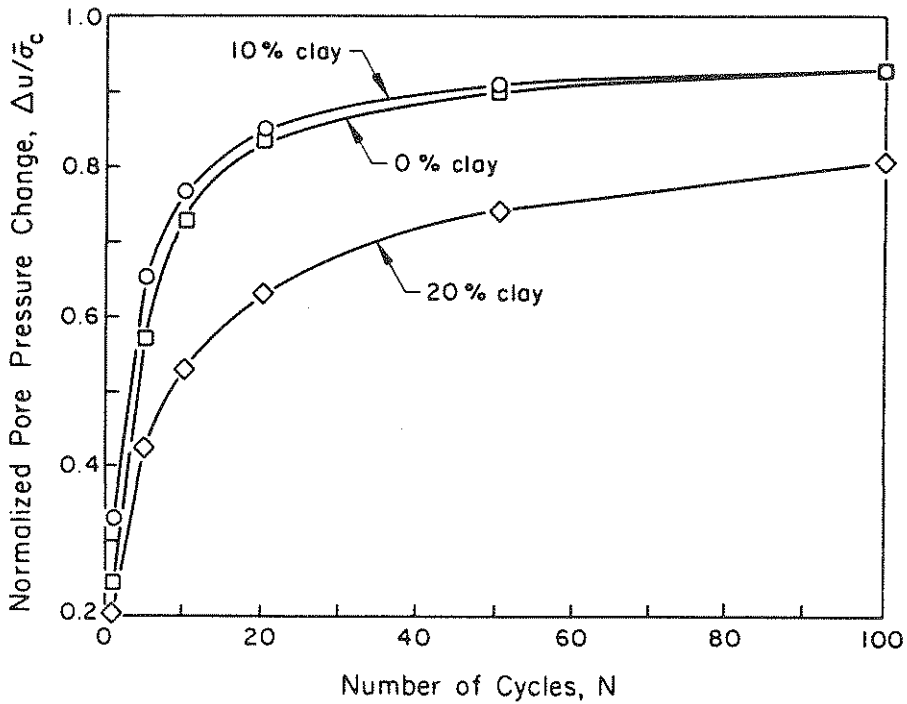


FIGURE 4-17. Pore Pressure Ratio versus Number of Load Cycles for  $\gamma_{cy} = 0.17\%$  and Clay Fractions of 0%, 10%, and 20%

of a specimen.

Figure 4-18 shows damping ratio against number of loading cycles at a cyclic torsional shear strain level of 0.17%, and for clay fractions of 0%, 10% and 20%. The figure shows that increased plasticity increases the degradation effect of the load cycles.

#### 4.3 COMPARISONS WITH SAND AND CLAY

A major problem with finding results for suitable comparison is that, as discussed in Section 2, different apparatus and testing and specimen preparation techniques lead to different cyclic stress-strain behavior. Also, stress-controlled test data cannot easily be compared with strain-controlled test data. Another problem is that results are often quoted with respect to shear strain and not normalized shear strain. However, Figures 4-19, 4-20, and 4-21 show, in a general way, the relationship between the test silt and previous researchers' test results, and commonly quoted property ranges for clays and sands.

Figure 4-19 shows normalized shear modulus plotted against shear strain for a range of materials. The clay (USCS classification MH) curve is based on resonant column data from Isehower [1979], and has a PI = 45%. The range for sands is based on a compilation of testing data by Seed and Idriss [1970], using several different test devices and procedures. The curve shown for pure silt is for one cycle of torsional loading. Comparison of the data in Figure 4-19 shows that the curve for the PGS 120 silt lies within the range for sands up to 0.01% strain, but beyond 0.01%, approaches the clay curve.

Figure 4-20 shows a comparison of the pore pressure generation characteristics of sand, silt, and clay for one cycle of torsional shear loading. The curve for sand was taken from a figure by Dobry, et al. [1982] for Monterey No. 0 sand, tested in a strain control cyclic triaxial test, at a  $D_r = 45\%$ . The pore pressure buildup curve for normally consolidated clay (OCR = 1) was taken from direct simple shear test data given by Dobry and Vucetic, [1987]. The pure silt curve is for a specimen preparation  $D_r = 50\%$ . Comparison of these

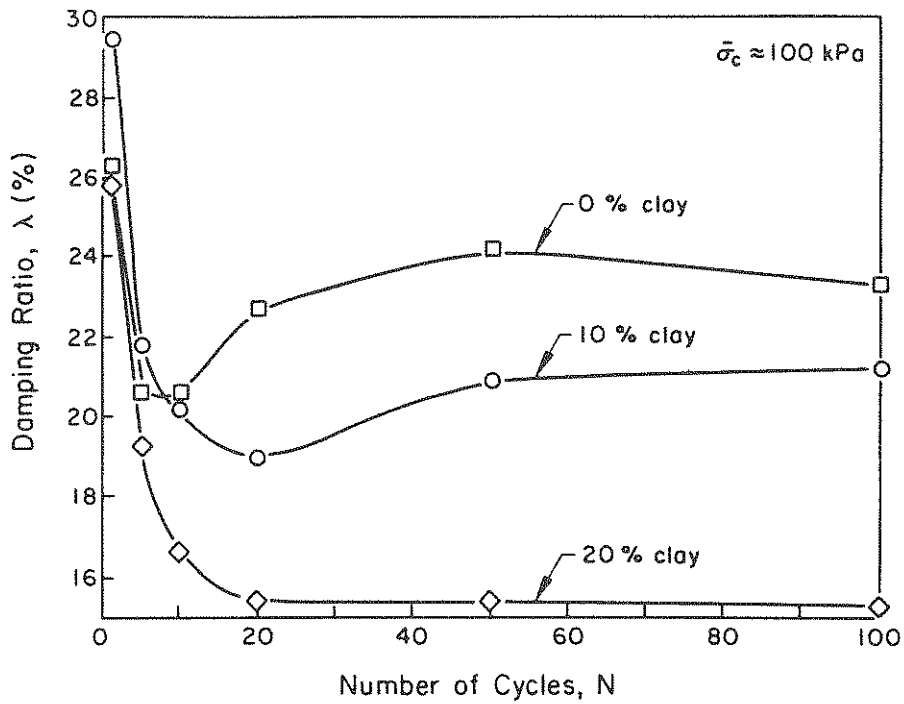


FIGURE 4-18. Damping Ratio versus Number of Load Cycles for  $\gamma_{cy} = 0.17\%$  and Clay Fractions of 0%, 10%, and 20%

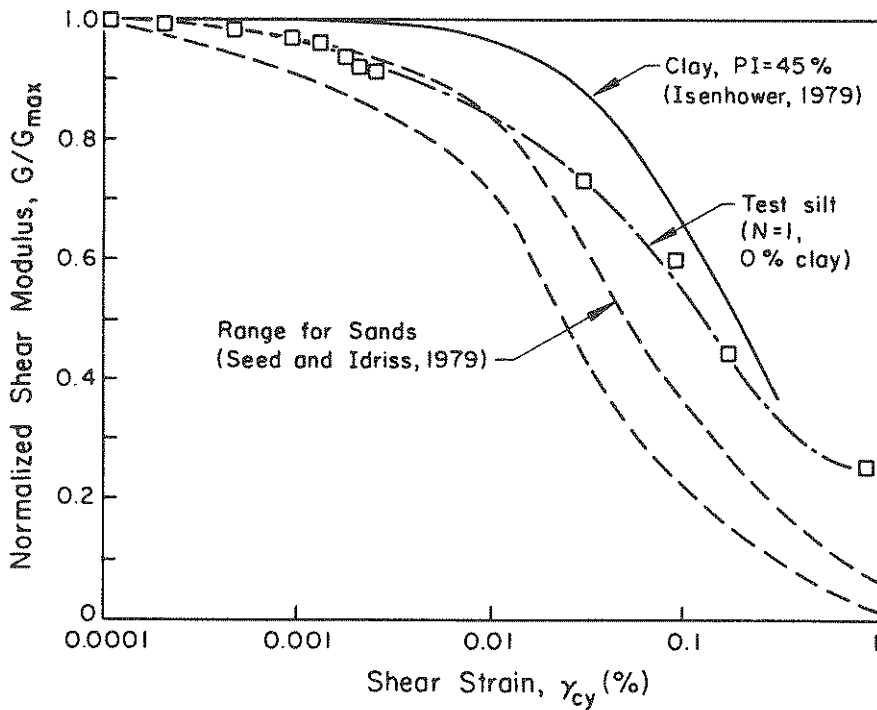


FIGURE 4-19. Shear Modulus versus Shear Strain for a Range of Materials

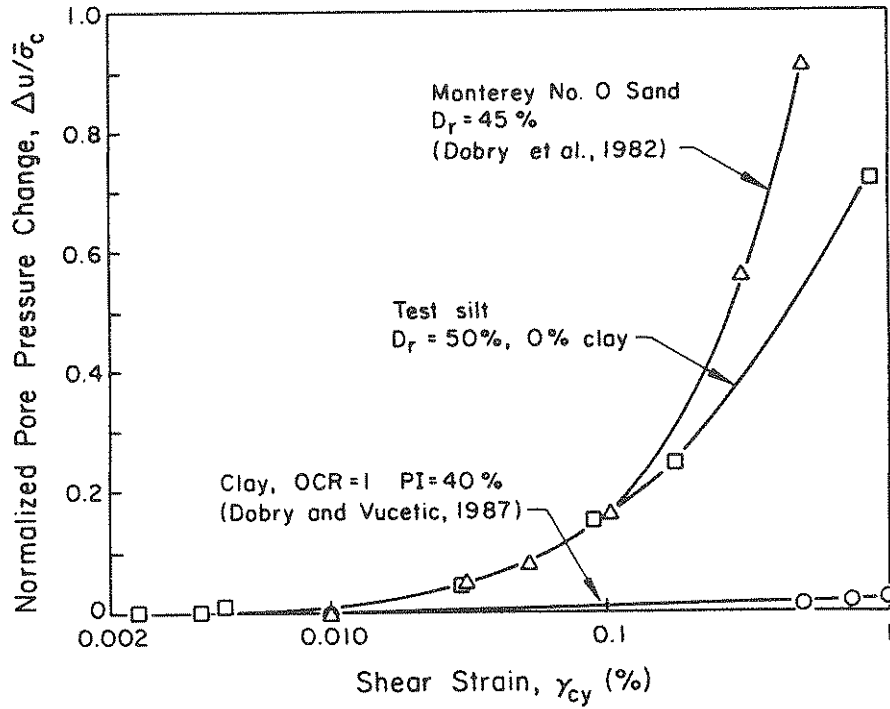


FIGURE 4-20. Pore Pressure Ratio versus Cyclic Shear Strain for Sand, Clay, and Silt

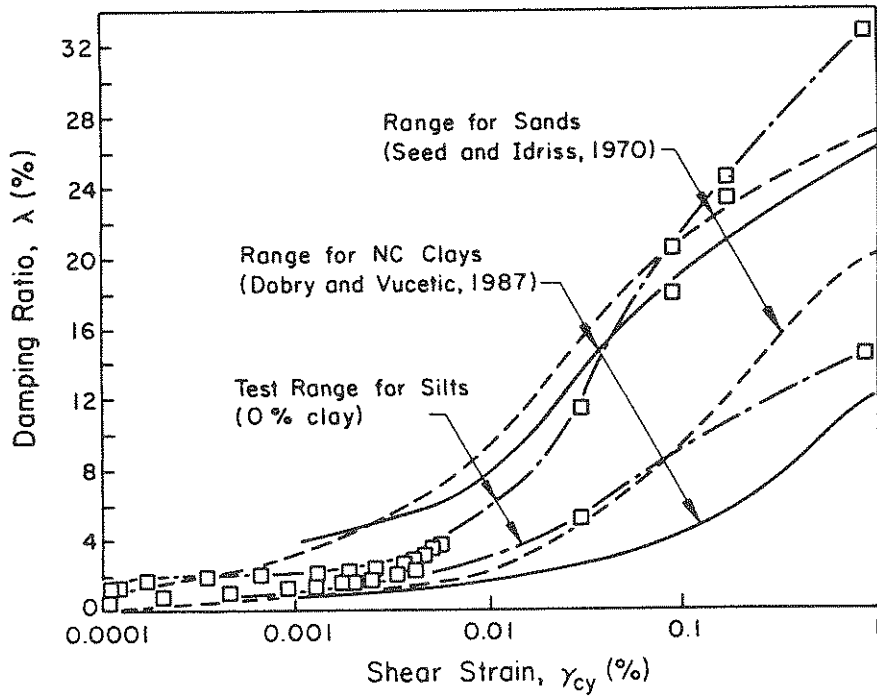


FIGURE 4-21. Damping Ratio versus Shear Strain; Ranges for Sand, Clay, and Silt

TABLE 4-2. Summary of Cyclic Loading Results

Increasing Factor	Pore Pressure Ratio, $\Delta u/\bar{\sigma}_c$	Shear Modulus Ratio, $G/G_{\max}$	Damping Ratio, $\lambda$
Plasticity Index, PI	Decreases with PI (Figure 4-14)	Increases with PI (Figure 4-13)	Decreases with PI (Figure 4-18)
Cyclic Strain, $\gamma_{cy}$	Increases with $\gamma_{cy}$ (Figure 4-7)	Decreases with $\gamma_{cy}$ (Figure 4-6)	Increases with $\gamma_{cy}$ (Figure 4-8)
Number of Loading Cycles, N	Increases with N - only above the threshold strain level of 0.004% (Figure 4-7)	Decreases with N - effect more pronounced at large $\gamma_{cy}$ values (Figure 4-6)	Generally decreases with N, especially at large $\gamma_{cy}$ values (Figure 4-12)

Note: Figure numbers in brackets illustrate described effects.

three curves in Figure 4-20 indicates that, although the silt had a higher relative density than the sand, and even though triaxial tests are known to produce slightly lower levels of pore pressure generation than torsional shear tests [Bhatia, et al., 1985], their pore pressure generation curves were very similar. The clay, however, generates almost no pore pressure increase during shearing.

Figure 4-21 shows a plot of damping ratio versus shear strain for ranges of sands, clays, and silts. The damping ratio range for sands is based on a compilation of data presented by Seed and Idriss [1970]. The range for normally consolidated clays is from a data summary presented by Dobry and Vucetic [1987]. The pure silt range of results is based on combined resonant column and torsional shear data. The torsional shear data is based on 1 to 100 cycles of loading. The figure indicates that the silt range lies, in general, partly in both the sand and clay ranges.

#### 4.4 SUMMARY AND CONCLUSIONS

The results of the monotonic and cyclic testing were presented. The monotonic test indicated that the silt, at  $D_r = 50\%$ , behaves in a highly contractive manner, and that the effective friction angle,  $\bar{\phi} = 23.6$  degrees. An effective stress normalization procedure, utilizing reference strain and maximum shear stress, was presented and used in many of the figures to help remove specimen variability effects and to clarify the results.

General conclusions from cyclic testing are given in Table 4-2. Comparisons with different types of material indicated that the overall results obtained for the silt testing were within reasonable ranges. The most striking comparison described was between the pore pressure generation characteristics of sand, silt, and clay, which showed that sand and silt behavior was very similar. This indicates that a loose silt deposit has a similar liquefaction potential to that of a loose sand deposit.





## SECTION 5 CONCLUSIONS AND RECOMMENDATIONS

### 5.1 GENERAL CONCLUSIONS

The literature review discussed the different types of equipment available for dynamic soil testing, and outlined some of the theories that have been used to describe the cyclic loading response of saturated soils. Also, the response of silty soils was considered to have been largely neglected, even though cases of liquefaction of silts in the field have been documented. In addition, the small amount of existing research clearly indicates that nonplastic silt's dynamic response is very similar to that of sand, and the belief that silts are too fine-grained to liquefy is false.

The apparatus discussion focused on the resonant column and torsional shear devices. These two types of apparatus have been combined into one hybrid device known as the quasi-static torsional simple shear/resonant column. This device, operating procedures, and the experimental program are discussed in detail in Section 3.

A resonant column is necessary to investigate the variation of dynamic properties, shear modulus, and damping ratio at small shear strains. The torsional shear test now is recognized as having superior capabilities for determining soil behavior under earthquake loading, because it allows reproduction of the most general stress conditions and can operate over a wide strain range. The apparatus can be used to determine dynamic soil properties and the effects of number of loading cycles and pore pressure buildup. Specimens can be tested in either strain or stress control. Cyclic strain control testing is recommended because cyclic strain is a more fundamental parameter in controlling pore pressure generation in saturated undrained testing, and strain control tests are much less sensitive to specimen preparation methods and relative density effects.

Types of testing, as described in Section 4, concentrated on basic

isotropic saturated undrained and cyclic strain control tests, in an effort to determine the response of a nonplastic and low plasticity silt to cyclic loading. Plasticity was controlled by adding varying amounts of clay to the pure silt. The essential findings were as follows:

1. The dynamic response of the silts was found to be very similar to that of sands. An important finding was the similarity between silts and sands in the magnitude of pore pressure response with varying strain level. This indicates that loose silt deposits, which are currently considered safe from liquefaction on the grounds that their grain size distribution curves are outside the generally accepted boundaries for potentially liquefiable soils, should be reevaluated.

2. Increased plasticity reduced the silt's level of pore pressure response. This reduction, however, was not significant for plasticity index values of roughly 5 or less.

3. A threshold strain level of approximately 0.004% was found for pore pressure generation under 2000 cycles of resonant column testing. However, the usual level quoted for threshold strain is 0.01%, which is based on 10 cycles of loading. Therefore, this result confirms that threshold strain level is dependent upon other parameters, and in particular, on the number of loading cycles.

4. The general trends observed in the silt's dynamic response, and the effect of increased plasticity, are in accordance with previous studies.

## 5.2 EQUIPMENT RECOMMENDATIONS

Installation of an axial loader would simplify the operation of maintaining isotropic stress conditions during a test. More importantly, an axial loading system would enable study of the effect of anisotropic stress conditions on dynamic properties. In addition, pore pressure generation characteristics and standard axial loading of specimens to failure can be examined.

The rotation measuring transducers have a limited rotation range, are

highly sensitive, and require great care and special apparatus assembly procedures to be able to zero them properly. Large strain, greater than 10%, testing is possible only by using the rotation scale on the rotary table and manual control of the stepper motor. It would be worthwhile to investigate alternative means of measuring rotations (i.e., some type of rotary transducer fixed to the chamber lid may be appropriate for large strain measurements).

The differential pressure transducer does not allow independent measurement of the cell and pore water pressures. This is a limitation when attempting accurate measurement of the pore pressure B parameters.

Torque values have to be calculated by using a reduction factor of 0.8 on peak torque values below 0.8 N-m. This correction, described in Appendix A, is necessary because of low torque nonlinearity in the response of the torque transducer.

### 5.3 AREAS FOR FURTHER RESEARCH

There is still a great deal of research to be carried out to classify the dynamic response of silts and the effect of plasticity on that response. Several areas which may warrant additional investigation include the following:

1. Establishment of relationships between confining pressure and  $G_{max}$ , with varying PI, would improve the accuracy of the effective stress normalization procedure.
2. A study of the effect of varying relative density on the dynamic properties is a necessary step in the determination of a general dynamic response model for the silt.
3. Drained tests using volume measurements should be carried out to establish the volumetric change characteristics of the material.
4. A sand and clay series of tests would be useful to obtain precise behavioral differences. Such a series of tests would also enable comparison with other apparatus, if a standard test sand was used.

5. Hollow cylinder testing should also be carried out and compared with solid specimen testing.

6. Increasing the PI by using clay additions of up to 50% would produce a clearer picture of the effects of plasticity on the silt/clay's dynamic properties.

7. A series of anisotropic tests should be carried out because, although isotropic tests are useful in determining basic responses to dynamic loading, they do not realistically model the actual in-situ stress state.

8. Effects of loading history or prestraining could be investigated by using staged testing and reconsolidation between stages.

9. Time effects on modulus changes, especially for the more plastic specimens, should also be investigated. If they are not investigated, then the saturation and consolidation times for specimens at the same plasticity level at least should be kept constant.

10. Further large strain monotonic testing at varying void ratios would enable the determination of the steady-state line for the silt, and better characterization of the effect of plasticity on static strength.

**SECTION 6**  
**NOTATION**

A	pore pressure parameter
B	$\Delta u/\Delta \sigma_3$ = pore pressure parameter
c	specimen radius at which $\tau$ is calculated
CLRL	critical level of repeated loading
CLS	cyclic limit state
CSL	critical stress level
$C_r$	average slope of recompression line
$C_u$	uniformity coefficient = $D_{60}/D_{10}$
d	diameter
$D_r$	relative density
$D_{50}$	grain diameter corresponding to 50% passing
E	Young's modulus
e	void ratio
$e_{max}$	maximum void ratio
$e_{min}$	minimum void ratio
$e_o$	initial void ratio
F	soil constant = $G_{max}/(\bar{\sigma}_o)^{0.5}$
G	shear modulus
$G_{max}$	maximum shear modulus
$G_{1000}$	shear modulus 1000 minutes from the start of primary consolidation
I.D.	inner diameter
J	polar moment of inertia
K	$\bar{\sigma}_3/\bar{\sigma}_1$ = principal stress ratio
$K_c$	$\bar{\sigma}_{1c}/\bar{\sigma}_{3c}$ = consolidation stress ratio
$K_o$	$\bar{\sigma}_h/\bar{\sigma}_v$ = coefficient of earth pressure at rest
LL	liquid limit
L	length of specimen
N	number of cycles
$N_{eq}$	equivalent number of uniform stress cycles
$N_L$	number of cycles to liquefaction
$n_t$	number of cycles to flow failure triggering

$N_{50}$	number of cycles to $u = 0.5(\bar{\sigma}_{3c})$
OCR	overconsolidation ratio
O.D.	outside diameter
$\bar{p}$	$(\bar{\sigma}_1 + \bar{\sigma}_3)/2$ , stress path parameter
PI	plasticity index
PL	plastic limit
$q$	$(\sigma_1 - \sigma_3)/2$ , stress path parameter
$q_{cr}$	steady-state shear resistance
$q_s$	static shear stress
$R$	$\Delta\sigma_d/2\bar{\sigma}_{3c} = \tau/\bar{\sigma}_o =$ cyclic stress ratio
$r$	$N/N_L =$ cycle ratio
$r_i$	inside radius
$r_o$	outside radius
$r_u$	$u/\bar{\sigma}_{3c} =$ pore pressure ratio
SS	steady state
$S_{us}$	steady-state shear strength
$T$	applied torque
$T_{eq}$	selected earthquake period
$T_r$	time/time to 100% consolidation = time factor
$u$	pore pressure
$\Delta u$	change in pore pressure
$u^*$	$\Delta u/\bar{\sigma}_{3c} =$ pore pressure ratio
$u_t^*$	pore pressure ratio at triggering of flow failure
$u_s^*$	pore pressure ratio at steady-state
$u_f$	limiting value of residual pore pressure
$\alpha$	shape factor
$\bar{\alpha}$	effective stress angle of friction in $\bar{p}, q$ space
$\bar{\alpha}_s$	angle of steady-state strength envelope
$\beta$	shape factor
$\epsilon_v$	axial strain
$\gamma$	shear strain
$\gamma_{cy}$	cyclic shear strain
$\gamma_{in}$	initial applied shear strain
$\gamma_r$	$\tau_{max}/G_{max} =$ reference shear strain
$\gamma_t$	threshold shear strain

$\bar{\phi}$	effective angle of shear resistance
$\bar{\sigma}$	effective stress
$\bar{\sigma}_a$	effective axial stress
$\Delta\sigma_a$	cyclic deviator stress
$\bar{\sigma}_c$	effective confining stress
$\sigma_d$	deviator stress = $(\sigma_1 - \sigma_3)$
$\sigma_{dc}$	consolidation deviator stress
$\sigma_{df}$	deviator stress at failure
$\bar{\sigma}_o$	initial effective confining stress
$\bar{\sigma}_{oct}$	$1/3(\bar{\sigma}_1 + \bar{\sigma}_2 + \bar{\sigma}_3)$ = effective octahedral stress
$\bar{\sigma}_{o-oct}$	reference effective octahedral stress
$\sigma_h$	total horizontal stress
$\bar{\sigma}_h$	effective horizontal stress
$\sigma_v$	total vertical stress
$\bar{\sigma}_v$	effective vertical stress
$\sigma_1$	major principal stress
$\sigma_2$	intermediate principal stress
$\sigma_3$	minor principal stress
$\bar{\sigma}_{1c}$	effective consolidation major principal stress
$\bar{\sigma}_{3c}$	effective consolidation minor principal stress
$\bar{\sigma}_{3s}$	effective confining stress at steady-state conditions
$\tau$	shear stress
$\tau_{cy}$	cyclic shear stress
$\tau_{eq}$	peak shear stress amplitude
$\tau_s$	static shear stress
$\theta$	angular rotation
$\kappa$	recompression index expressed on the natural logarithm scale
$\mu$	Poisson's ratio
$\lambda$	damping ratio
$\lambda_{min}$	minimum value of damping ratio





**SECTION 7**  
**REFERENCES**

- Afifi, S. S. and F. E. Richart, Jr., "Stress History Effects on Shear Modulus of Soils," Soils and Foundations, JSSMFE, Vol. 13, No. 1, Jan. 1973, pp. 77-95.
- Alarcon-Guzman, A., "Cyclic Stress-Strain Behavior of Sands," Ph.D. Thesis, Purdue University, West Lafayette, IN, Aug. 1986.
- Alarcon-Guzman, A., J. L. Chameau, and G. A. Leonards, "A New Apparatus for Investigating the Stress-Strain Characteristics of Sands," Geotechnical Testing Journal, ASTM, Vol. 9, No. 4, 1986, pp. 204-212.
- American Society for Testing and Materials, "Standard Test Method for Modulus and Damping of Soils by the Resonant-Column Method," Annual Book of Standards, D4015-87, Vol. 4.08, Philadelphia, PA, 1988a, pp. 507-525.
- American Society for Testing and Materials, "Standard Test Method for Minimum Index Density of Soils and Calculation of Relative Density," Annual Book of Standards, D4254-83, Vol. 4.08, Philadelphia, PA, 1988b, pp. 566-572.
- American Society for Testing and Materials, "Standard Test Method for Liquid Limit, Plastic Limit, and Plasticity Index of Soils," Annual Book of Standards, D4318-84, Vol. 4.08, Philadelphia, PA, 1988c, pp. 573-583.
- Anderson, D. G. and R. D. Woods, "Time-Dependent Increase in Shear Modulus of Clay," Journal of Geotechnical Engineering, ASCE, Vol. 102, No. GT5, May 1976, pp. 525-537.
- Athanasopoulos, G. A. and F. E. Richart, Jr., "Effect of Stress Release on Shear Modulus of Clay," Journal of the Geotechnical Engineering Division, ASCE, Vol. 109, No. 10, Oct. 1983, pp. 1233-1245.
- Bhatia, S. K., J. Schwab, and I. Ishibashi, "Cyclic Simple Shear, Torsional Shear, and Triaxial - A Comparative Study," Proceedings, Advances in the Art of Testing Soils Under Cyclic Conditions, ASCE, New York, NY, 1985, pp. 232-254.
- Casagrande, A., "Liquefaction and Cyclic Deformation of Sands - A Critical Review," Proceedings, 5th Panamerican Conference on Soil Mechanics and Foundation Engineering, Buenos Aires, Argentina, 1975, pp. 81-133. (Also published as Harvard Soil Mechanics Series No. 88, Jan. 1976, Harvard University, Cambridge, MA.)

- Castro, G., "Liquefaction and Cyclic Mobility of Saturated Sands," Journal of the Geotechnical Engineering Division, ASCE, Vol. 101, No. GT6, June 1975, pp. 551-569.
- Castro, G. and S. J. Poulos, "Factors Affecting Liquefaction and Cyclic Mobility," Journal of the Geotechnical Engineering Division, ASCE, Vol. 103, No. GT6, June 1977, pp. 501-516.
- Chang, C. S., C. L. Kuo, and E. T. Selig, "Pore Pressure Development During Cyclic Loading," Journal of the Geotechnical Engineering Division, ASCE, Vol. 109, No. 1, January 1983, pp. 103-107.
- Chen, A. T. F. and K. H. Stokoe II, "Interpretation of Strain-Dependent Modulus and Damping from Torsional Soil Tests," U.S. Geological Survey Report, NTIS-PB-298749/AS, July 1979, 45 p.
- Chung, R. M., F. Y. Yokel, and H. Wechsler, "Pore Pressure Buildup During Resonant Column Testing," Journal of the Geotechnical Engineering Division, ASCE, Vol. 110, No. GT2, Feb. 1984, pp. 247-261.
- Chung, R. M., F. Y. Yokel, and V. P. Drnevich, "Evaluation of Dynamic Properties of Sands by Resonant Column Testing," Geotechnical Testing Journal, ASTM, Vol. 7, No. 2, June 1984, pp. 60-69.
- Committee on Earthquake Engineering, Commission on Engineering and Technical Systems, Liquefaction of Soils During Earthquakes, National Research Council, National Academy Press, Washington, D.C., 1985.
- De Alba, P., H. B. Seed, and C. K. Chan, "Sand Liquefaction in Large-Scale Simple Shear Tests," Journal of the Geotechnical Engineering Division, ASCE, Vol. 102, No. GT9, Sept. 1976, pp. 909-927.
- De Alba, P., K. Baldwin, V. Janoo, G. Roe, and B. Celikkol, "Elastic Wave Velocities and Liquefaction Potential," Geotechnical Testing Journal, ASTM, Vol. 7, No. 2, June 1984, pp. 77-87.
- Dobry, R., K. H. Stokoe II, R. S. Ladd, and T. L. Youd, "Liquefaction Susceptibility from S-Wave Velocity," Proceedings, Specialty Conference on In-Situ Testing to Evaluate Liquefaction Susceptibility, ASCE, 1981.
- Dobry, R., R. S. Ladd, F. Y. Yokel, R. M. Chung, and D. Powell, "Prediction of Pore Water Pressure Buildup and Liquefaction of Sands During Earthquakes by the Cyclic Strain Method," Building Science Series 138, National Bureau of Standards, Washington, D.C., 1982.
- Dobry, R., A. Vasquez-Herrera, R. Mohamad, and M. Vucetic, "Liquefaction Flow Failure of Silty Sand by Torsional Cyclic Tests," Proceedings, Advances in the Art of Testing Soils Under Cyclic Conditions, ASCE, New York, NY, 1985, pp. 29-50.

- Dobry, R. and M. Vucetic, "Dynamic Properties and Seismic Response of Soft Clay Deposits," Proceedings, International Symposium on Geotechnical Engineering of Soft Soils, Vol. 2, Mexico City, Aug. 1987, pp. 51-87.
- Drnevich, V. P. and F. E. Richart, Jr., "Dynamic Prestraining of Dry Sand," Journal of the Soil Mechanics and Foundations Division, ASCE, Vol. 96, No. SM2, Mar. 1970, pp. 453-469.
- Drnevich, V. P., "Undrained Cyclic Shear of Saturated Sand," Journal of the Soil Mechanics and Foundations Division, ASCE, Vol. 98, No. SM8, Aug. 1972, pp. 807-825.
- Drnevich, V. P., B. O. Hardin, and D. J. Shippy, "Modulus and Damping of Soils by the Resonant Column Method," Dynamic Geotechnical Testing (STP 654), ASTM, Philadelphia, PA, 1978, pp. 91-125.
- Drnevich, V. P., "Resonant Column - Problems and Solutions," Dynamic Geotechnical Testing (STP 654), ASTM, Philadelphia, PA, 1978, pp. 384-398.
- Drnevich, V. P., "Evaluation of Sample Disturbance Using the 'Reference Strain' Concept," Soil Mechanics Series 26, University of Kentucky, May 1979.
- Drnevich, V. P., "Normalized Stress-Strain for Undrained Shear Tests," Laboratory Shear Strength of Soil (STP 740), Eds. R. N. Yong and F. C. Townsend, ASTM, Philadelphia, PA, 1981, pp. 387-409.
- Drnevich, V. P., "Recent Developments in Resonant Column Testing," Proceedings, Richart Commemorative Lectures, Ed. R. D. Woods, ASCE, New York, NY, 1985, pp. 79-107.
- Dyvik, R., R. Dobry, G. E. Thomas, and W. G. Pierce, "Influence of Consolidation Shear Stresses and Relative Density on Threshold Strain and Pore Pressure During Cyclic Straining of Saturated Sand," Miscellaneous Paper GL-84-15, U. S. Army Corps of Engineers, July 1984.
- Egan, J. A. and D. A. Sangrey, "Critical State Model for Cyclic Load Pore Pressure," Proceedings, Specialty Conference on Earthquake Engineering and Soil Dynamics, Vol. 1, ASCE, New York, NY, 1978, pp. 410-423.
- Finn, W. D. L., P. L. Bransby, and D. J. Pickering, "Effect of Strain History on Liquefaction of Sand," Journal of the Soil Mechanics and Foundations Division, ASCE, Vol. 96, No. SM6, Nov. 1970, pp. 1917-1934.

- Finn, W. D. L., D. J. Pickering, and P. L. Bransby, "Sand Liquefaction in Triaxial and Simple Shear Tests," Journal of the Soil Mechanics and Foundations Division, ASCE, Vol. 97, No. SM4, Apr. 1971, pp. 639-659.
- Finn, W. D. L., K. W. Lee, C. H. Maartman, and R. Lo, "Cyclic Pore Pressures Under Anisotropic Conditions," Proceedings, Earthquake Engineering and Soil Dynamics, Vol. 1, ASCE, New York, NY, 1978, pp.457-470.
- Hardin, B. O., "The Nature of Damping in Sands," Journal of the Soil Mechanics and Foundations Division, ASCE, Vol. 91, No. SM1, Jan. 1965, pp. 63-97.
- Hardin, B. O. and W. L. Black, "Vibration Modulus of Normally Consolidated Clay," Journal of the Soil Mechanics and Foundations Division, ASCE, Vol. 94, No. SM2, Feb. 1968, pp. 353-369.
- Hardin, B. O., "Suggested Methods of Test for Shear Modulus and Damping of Soils by the Resonant Column," Special Technical Publication (STP 479), ASTM, Philadelphia, PA, 1970, pp. 516-529.
- Hardin, B. O. and V. P. Drnevich, "Shear Modulus and Damping in Soils: Design Equations and Curves," Journal of the Soil Mechanics and Foundations Division, ASCE, Vol. 98, No. SM7, July 1972, pp. 667-692.
- Hight, D. W., A. Gens, and M. J. Symes, "The Development of a New Hollow Cylinder Apparatus for Investigating the Effects of Principal Stress Rotation in Soils," Geotechnique, Vol. 33, No. 4, Dec. 1983, pp. 355-383.
- Holtz, R. D. and W. D. Kovacs, An Introduction to Geotechnical Engineering, Prentice-Hall, Inc., Englewood Cliffs, NJ, 1981.
- Isenhower, W. M., "Torsional Simple Shear/Resonant Column Properties of San Francisco Bay Mud," M. S. Thesis, University of Texas, Austin, 1979, 307 p.
- Isenhower, W. M., K. H. Stokoe II, and J. C. Allen, "Instrumentation for Torsional Shear/Resonant Column Measurements Under Anisotropic Stresses," Geotechnical Testing Journal, ASTM, Vol. 10, No. 4, Dec. 1987, pp. 183-191.
- Ishibashi, I. and M. A. Sherif, "Soil Liquefaction by Torsional Simple Shear Device," Journal of the Geotechnical Engineering Division, ASCE, Vol. 100, No. GT8, Aug. 1974, pp. 871-887.
- Ishibashi, I., M. A. Sherif, and C. Tsuchiya, "Pore-Pressure Rise Mechanism and Soil Liquefaction," Soils and Foundations, JSSMFE, Vol. 17, No. 2, June 1977, pp. 17-27.

- Ishibashi, I., M. A. Sherif, and W. L. Cheng, "The Effects of Soil Parameters on Pore Pressure Rise and Liquefaction Prediction," Soils and Foundations, JSSMFE, Vol. 22, No. 1, Jan. 1982, pp. 39-48.
- Ishibashi, I., M. Kawamura, and S. K. Bhatia, "Torsional Simple Shear Testing for Drained and Undrained Cyclic Testing," Proceedings, Advances in the Art of Testing Soils Under Cyclic Conditions, ASCE, New York, NY, 1985, pp. 232-254.
- Ishihara, K. and S. Li, "Liquefaction of Saturated Sand in Triaxial Torsion Shear Test," Soils and Foundations, JSSMFE, Vol. 12, No. 2, June 1972, pp. 19-39.
- Ishihara, K. and S. Yasuda, "Sand Liquefaction in Hollow Cylinder Torsion Under Irregular Excitation," Soils and Foundations, JSSMFE, Vol. 15, No. 1, Mar. 1975, pp. 45-59.
- Ishihara, K. and H. Takatsu, "Effects of Overconsolidation and  $K_0$  Conditions on the Liquefaction Characteristics of Sands," Soils and Foundations, JSSMFE, Vol. 19, No. 4, Dec. 1979, pp. 60-68.
- Ishihara, K., Yasuda, S. and Yokota, K., "Cyclic Strength of Undisturbed Mine Tailings," Proceedings, International Conference on Recent Advances in Earthquake Engineering and Soil Dynamics, Vol. 1, ASCE, New York, NY, 1981, pp. 53-58.
- Ishihara, K., "Post-Earthquake Failure of a Tailings Dam Due to Liquefaction of the Pond Deposit," Proceedings, International Conference on Case Histories in Geotechnical Engineering, Vol. 3, ASCE, New York, NY, 1984, pp. 1129-1143.
- Iwasaki, T., F. Tatsuoka, and Y. Takagi, "Shear Moduli of Sands Under Cyclic Torsional Shear Loading," Soils and Foundations, JSSMFE, Vol. 18, No. 1, Mar. 1978, pp. 40-56.
- Kokusho, T., "Cyclic Triaxial Test of Dynamic Soil Properties for Wide Strain Range," Soils and Foundations, JSSMFE, Vol. 20, No. 2, June 1980, pp. 45-60.
- Kokusho, T., Y. Yoshida, and Y. Esashi, "Dynamic Properties of Soft Clay for Wide Strain Range," Soils and Foundations, JSSMFE, Vol. 22, No. 4, Dec. 1982, pp. 1-18.
- Kovacs, W. D., H. B. Seed, and C. K. Chan, "Dynamic Moduli and Damping Rates for a Soft Clay," Journal of the Soil Mechanics and Foundations Division, ASCE, Vol. 97, No. SM1, Jan. 1971, pp. 59-75.
- Ladd, R. S., "Specimen Preparation and Cyclic Stability of Sands," Journal of the Geotechnical Engineering Division, ASCE, Vol. 103, No. GT6, June 1977, pp. 535-547.

- Ladd, R. S., "Preparing Test Specimens Using Undercompaction," Geotechnical Testing Journal, ASTM, Vol. 1, No. 1, Mar. 1978, pp. 16-23.
- Lambe, T. W. and R. V. Whitman, Soil Mechanics, John Wiley and Sons, New York, NY, 1969, 553 p.
- Lee, K. L. and H. B. Seed, "Cyclic Stress Conditions Causing Liquefaction of Sand," Journal of the Soil Mechanics and Foundations Division, ASCE, Vol. 93, No. SM1, Jan. 1967, pp. 47-70.
- Lee, K. L. and A. Albaisa, "Earthquake-Induced Settlements in Saturated Sands," Journal of the Geotechnical Engineering Division, ASCE, Vol. 100, No. GT4, Apr. 1974, pp. 387-406.
- Marcuson, W. F. and H. E. Wahls, "Time Effects on Dynamic Shear Modulus of Clays," Journal of the Soil Mechanics and Foundations Division, ASCE, Vol. 98, No. SM12, Dec. 1972, pp. 1359-1373.
- Marcuson, W. F. and H. E. Wahls, "Effects of Time on Damping Ratio of Clays," Dynamic Geotechnical Testing (STP 654), ASTM, Philadelphia, PA, 1978, pp. 126-147.
- Mulilis, J. P., H. B. Seed, C. K. Chan, J. K. Mitchell, and K. Arulandan, "Effects of Sample Preparation on Sand Liquefaction," Journal of the Geotechnical Engineering Division, ASCE, Vol. 103, No. GT2, Feb. 1977, pp. 91-107.
- Nemat-Nasser, S. and K. Takahashi, "Liquefaction and Fabric of Sand," Journal of the Geotechnical Engineering Division, ASCE, Vol. 110, No. GT9, Sept. 1984, pp. 1291-1306.
- Park, T. K. and M. L. Silver, "Dynamic Triaxial and Simple Shear Behavior of Sand," Journal of the Geotechnical Engineering Division, ASCE, Vol. 101, No. GT6, June 1975, pp. 513-529.
- Peacock, W. H. and H. B. Seed, "Sand Liquefaction Under Cyclic Loading Simple Shear Conditions," Journal of the Soil Mechanics and Foundations Division, ASCE, Vol. 94, No. SM3, May 1968, pp. 689-708.
- Poulos, S. J., G. Castro, and J. W. France, "Liquefaction Evaluation Procedure," Journal of Geotechnical Engineering, ASCE, Vol. 111, No. 6, June 1985, pp. 772-792.
- Pyke, R. M., "Settlement and Liquefaction of Sands Under Multi-Directional Loading," Ph. D. Thesis, University of California, Berkeley, 1973.
- Richart, F. E., Jr., D. G. Anderson, and K. H. Stokoe, II, "Predicting In-Situ Strain Dependent Shear Moduli of Soil," Proceedings, 6th World Conference on Earthquake Engineering, New Delhi, India, 1979, pp. 118-123.

- Saada, A. S., G. F. Bianchini, and L. P. Shook, "The Dynamic Response of Anisotropic Clay," Proceedings, Specialty Conference on Earthquake Engineering and Soil Dynamics, Vol. 2, ASCE, New York, NY, 1978, pp. 777-801.
- Saada, A. S. and F. C. Townsend, "State-of-the-Art Laboratory Strength Testing of Soils," Laboratory Shear Strength of Soil (STP 740), Eds. R. N. Yong and F. C. Townsend, ASTM, Philadelphia, PA, 1981, pp. 7-77.
- Saada, A. S., "On Cyclic Testing with Thin Long Hollow Cylinders," Proceedings, Advances in the Art of Testing Soils Under Cyclic Conditions, ASCE, New York, NY, 1985, pp. 1-28.
- Sangrey, D. A., D. J. Henkel, and M. I. Esrig, "The Effective Stress Response of a Saturated Clay Soil to Repeated Loading," Canadian Geotechnical Journal, Vol. 6, No. 3, 1969, pp. 241-252.
- Sangrey, D. A., G. Castro, S. J. Poulos, and J. W. France, "Cyclic Loading of Sands, Silts, and Clays," Specialty Conference on Earthquake Engineering and Soil Dynamics, Vol. 2, ASCE, New York, NY, 1978, pp. 836-851.
- Seed, H. B. and K. L. Lee, "Liquefaction of Saturated Sands During Cyclic Loading," Journal of the Soil Mechanics and Foundations Division, ASCE, Vol. 92, No. SM6, Nov. 1966, pp. 105-134.
- Seed, H. B. and I. M. Idriss, I. M., "Analysis of Soil Liquefaction: Niigata Earthquake," Journal of the Soil Mechanics and Foundations Division, ASCE, Vol. 93, No. SM3, May 1967, pp. 83-108.
- Seed, H. B. and I. M. Idriss, "Soil Moduli and Damping Factors for Dynamic Response Analyses," Report EERC 70-10, University of California, Berkeley, Sept. 1970.
- Seed, H. B. and I. M. Idriss, "Simplified Procedure for Evaluating Soil Liquefaction Potential," Journal of the Soil Mechanics and Foundations Division, ASCE, Vol. 97, No. SM9, Sept. 1971, pp. 1249-1273.
- Seed, H. B., P. P. Martin, and J. Lysmer, "Pore-Water Pressure Changes During Soil Liquefaction," Journal of the Geotechnical Engineering Division, ASCE, Vol. 102, No. GT4, Apr. 1976, pp. 323-346.
- Seed, H. B., K. Mori, and C. K. Chan, "Influence of Seismic History on Liquefaction of Sands," Journal of the Geotechnical Engineering Division, ASCE, Vol. 103, No. GT4, Apr. 1977, pp. 257-270.
- Seed, H. B., "Soil Liquefaction and Cyclic Mobility Evaluation for Level Ground During Earthquakes," Journal of the Geotechnical Engineering Division, ASCE, Vol. 105, No. GT2, Feb. 1979, pp. 201-255.

- Seed, H. B., K. Tokimatsu, L. F. Harder, and R. M. Chung, "The Influence of SPT Procedures in Soil Liquefaction Resistance Evaluations," Journal of the Geotechnical Engineering Division, ASCE, Vol. 111, No. 12, Dec. 1985, pp. 1425-1445.
- Selig, E. T. and C. S. Chang, "Soil Failure Modes in Undrained Cyclic Loading," Journal of the Geotechnical Engineering Division, ASCE, Vol. 107, No. GT5, May 1981, pp. 539-551.
- Shen, C. K., C. C. Ker, Z. Wang, and X. S. Li, "Dynamic Response of Silt," Proceedings, 2nd International Conference on Soil Dynamics and Earthquake Engineering, 1985, pp. 93-106.
- Sherif, M. A. and I. Ishibashi, "Dynamic Shear Moduli for Dry Sands," Journal of the Geotechnical Engineering Division, ASCE, Vol. 102, No. GT11, Nov. 1976, pp. 1171-1184.
- Sherif, M. A., I. Ishibashi, and C. Tsuchiya, "Saturation Effects on Initial Soil Liquefaction," Journal of the Geotechnical Engineering Division, ASCE, Vol. 103, No. GT8, Aug. 1977, pp. 914-917.
- Sherif, M. A., I. Ishibashi, and C. Tsuchiya, "Pore-Pressure Prediction During Earthquake Loadings," Soils and Foundations, JSSMFE, Vol. 18, No. 4, Dec. 1978, pp. 19-30.
- Shibata, T. and D. S. Soelarno, "Stress-Strain Characteristics of Sands Under Cyclic Loading," Proceedings, Japanese Society of Civil Engineers, No. 239, July 1975, pp. 57-65 (in Japanese).
- Silver, M. L. and H. B. Seed, "Volume Changes in Sands During Cyclic Loading," Journal of the Soil Mechanics and Foundations Division, ASCE, Vol. 97, No. SM9, Sept. 1971, pp. 1171-1185.
- Sivapullaiah, P. V. and A. Sridharan, "Liquid Limit of Soil Mixtures," Geotechnical Testing Journal, ASTM, Vol. 8, No. 3, Sept. 1985, pp. 111-116.
- Skogland, G. R., W. F. Marcusson, III, and R. W. Cunny, "Evaluation of Resonant Column Test Devices," Journal of the Geotechnical Engineering Division, ASCE, Vol. 102, No. GT11, Nov. 1976, pp. 1147-1158.
- Soil Dynamics Instruments, Inc., "Quasi-Static Torsional Simple Shear and Resonant Column Apparatus," Operation Manual Apparatus Serial No. 256, Lexington, KY, Sept. 1987.
- Stokoe, K. H., II, W. M. Isenhower, and J. R. Hsu, "Dynamic Properties of Offshore Silty Samples," Proceedings, 12th Offshore Technology Conference, Vol. 2, Houston, TX, 1980, pp. 289-292.



- Stokoe, K. H., II and P. F. Lodde, "Dynamic Response of San Francisco Bay Mud," Proceedings, Specialty Conference on Earthquake Engineering and Soil Dynamics, Vol. 2, ASCE, New York, NY, 1978, pp. 940-959.
- Tsuchida, H., "Prediction and Countermeasure Against the Liquefaction in Sand Deposits," Seminar Abstract, Port and Harbour Research Institute, 1970, pp. 3.1-3.33 (in Japanese).
- Vaid, Y. P. and D. Negussey, "A Critical Assessment of Membrane Penetration in the Triaxial Test," Geotechnical Testing Journal, ASTM, Vol. 7, No. 2, June 1984, pp. 70-76.
- Vaid, Y. P. and J. C. Chern, "Cyclic and Monotonic Undrained Response of Saturated Sands," Proceedings, Advances in the Art of Testing Soils Under Cyclic Conditions, ASCE, New York, NY, 1985, pp. 120-147.
- Wang, W., "Some Findings in Soil Liquefaction," Water Conservancy and Hydroelectric Power Scientific Research Institute, Beijing, China, Aug. 1979.
- Whitman, R. V. and P. C. Lambe, "Liquefaction: Consequences for a Structure," Proceedings, Soil Dynamics and Earthquake Engineering Conference, Vol. II, 1982, pp. 941-949.
- Whitman, R. V., "On Liquefaction," Proceedings, 11th International Conference on Soil Mechanics and Foundation Engineering, A. A. Balkema Publishers, Rotterdam, Netherlands, 1985, pp. 1923-1926.
- Woods, R. D., "Measurement of Dynamic Soil Properties," Proceedings, Specialty Conference on Earthquake Engineering and Soil Dynamics, Vol. 1, ASCE, New York, NY, 1978, pp. 91-178.
- Wright, D. K., P. A. Gilbert, and A. S. Saada, "Shear Devices for Determining Dynamic Soil Properties," Proceedings, Specialty Conference on Earthquake Engineering and Soil Dynamics, Vol. 2, ASCE, New York, NY, 1978, pp. 1056-1075.
- Youd, T. L., "Compaction of Sands by Repeated Shear Straining," Journal of the Soil Mechanics and Foundations Division, ASCE, Vol. 98, No. SM7, July 1972, pp. 709-725.
- Youd, T. L., "Packing Changes and Liquefaction Susceptibility," Journal of the Geotechnical Engineering Division, ASCE, Vol. 103, No. GT8, Aug. 1977, pp. 918-923.
- Zen, K., Y. Umehara, and K. Hamada, "Laboratory Tests and In-situ Seismic Survey on Vibratory Shear Modulus of Clayey Soils with Various Plasticities," Proceedings, 5th Japanese Earthquake Engineering Society Meeting, 1978, pp. 721-728 (in Japanese).



## APPENDIX A TRANSDUCERS

### A.1 INTRODUCTION

Manufacturers' specifications and calibration information on the axial load, torque, LVDT, and pressure transducers are given in detail by S.D.I. [1987]. The axial load and torque transducers were replaced after the first pressure chamber test using water, because the housings leaked and the strain gages shorted. The use of nonconducting silicon oil as a confining fluid eliminated the problem. Overall, however, the majority of problems that have occurred have been with the rotation measurement system and the torque transducer. The torque transducer is discussed in detail in section A.3.

The relative rotation between the bottom and the top of the specimen is measured by two noncontacting displacement transducers. They are located on a cylindrical platform, which is fastened to the lower platen of the apparatus. These transducers were made by Kaman Measuring Systems (Model KD-2350). The transducers allow for precision noncontact displacement measurements of metal targets, using a sensor and a signal conditioning package which has been incorporated into the Sensotec unit. The output voltage of the system is proportional to the distance between the face of the sensor and any metallic target. In the apparatus, the two transducers focus on nonconcentric circular cams attached to the top platen, and hence measure the distance between the cams and the transducer face. As the top platen rotates relative to the bottom, the separation distance changes, and therefore the transducer output changes. Thus, measurements of the rotation angles from the at rest position are made.

A number of problems were experienced with the transducers. They were initially impossible to zero, which meant that strain control or monotonic rotation limit tests could not be run. Full information on the calibration of the transducers was provided by S.D.I. so that recalibrations could be carried out. After recalibration, the transducers

were possible to zero. However, it was then found that the calibration factors changed as much as 50% between successive calibrations. The piston and resonant column connection was checked, and found insufficient to maintain a concentric alignment. Thus, with the cams rotating slightly off center, different calibration factors would result from different cam and transducer locations. The piston and the resonant column were returned to S.D.I., and the connection was redesigned. The new connection ensured a more rigid and concentric link. The cams also were redesigned with steeper face angles to increase the linear calibration range. Again, recalibrations were performed and zeroing was easier to accomplish. However, the calculated calibration factors should be rechecked every few months. A modified version of S.D.I.'s calibration procedure and plots from two actual calibrations are included below.

## A.2 CALIBRATION OF KAMAN TRANSDUCERS

### Setup Description:

1. Kaman transducers should be mounted in their holders and their holders should be fastened to the support table in the same manner as used in testing.
2. The spacing between the faces of the Kaman transducers should be equal to the mid-diameter of the cam plate plus 6.35 mm (0.25 in.). This will give a gap of 3.17 mm (0.125 in.) between the cam and each transducer when the cam is in the mid position.
3. The support table should be in position in the apparatus such that each cable for the Kaman transducer can be connected to the transducer. (It is essential that the same Kaman transducer, cable, and Kaman oscillator-demodulator always be connected together for accurate calibrations.) Connect the cable to the Kaman transducers.
4. Connect the other end of the cables to their respective Kaman oscillator-demodulator boxes located on the top of the Sensotec unit.
5. Connect the power-signal cables coming from the interior of the Sensotec to the respective Kaman oscillator-demodulator boxes. (Again, these cables must be connected to the same box as in the

original calibration.)

Preliminary Calibrations (must be done for each Kaman transducer):

1. The output from the Sensotec unit to the computer data acquisition daughter board should be disconnected at the rear of the Sensotec and the positive lead of a voltmeter connected to pin 11 of the DB 25 connector for Kaman transducer No. 1 (Channel 7 on Sensotec) and pin 9 for Kaman transducer No. 2 (Channel 8 on Sensotec). The negative lead to the voltmeter should be connected to chassis ground. Special circuitry inside the Sensotec for the Kaman transducers applies an offset (when switched in by the switch on the front panel of the Sensotec) and provides a gain of 5 to the Kaman oscillator-demodulator signal before it is sent to the computer or the display on the Sensotec. (The display on the Sensotec is set to read rotation in degrees and should not be used in the calibration process. Once all calibrations are complete, an adjustment of the scale for this meter is made.)

2. Power to the Sensotec and computer should be turned on.

3. Turn the offset switches to the off position (down).

4. Set the voltmeter to read d.c. voltages, using the 20 volt range.

5. Attach a 63.5 mm (2.5 in.) diameter aluminum target to a micrometer head and mount the head to the top of the Kaman support platform such that the micrometer reads zero when the flat plate is in contact with the face of the Kaman transducer. The plate should completely cover the face of the transducer.

6. Adjust the micrometer head such that a gap of 0.635 mm (0.025 in.) exists between the aluminum target and the face of the Kaman transducer.

7. Remove the tape covering the adjustment access holes on the side of the Kaman oscillator-demodulator box for the transducer being calibrated and adjust the ZERO control until a zero voltage output is viewed on the voltmeter.

8. Adjust the micrometer head such that a gap of 3.17 mm (0.125 in.) exists between the target and the face of the Kaman transducer.

9. Observe the output of the voltmeter. It should read 10.0 volts. If it does not, adjust the GAIN control of the Kaman oscillator-demodulator box until it reads 10.0 volts.

10. Adjust the micrometer head such that a gap of 5.08 mm (0.2 in.) exists between the target and the face of the Kaman transducer.

11. Observe the output of the voltmeter. It should read 13.0 volts. If it does not, adjust the FINE or COARSE LINEARITY controls of the Kaman oscillator-demodulator box until it reads roughly 13.0 volts.

12. Repeat steps 6 through 11 until all three points are within 0.2 volts of the desired value. It may be necessary to overadjust the LINEARITY control to speed up the convergence process.

13. Reset the target at a distance of 3.17 mm (0.125 in.) by use of the micrometer head and then turn on the offset for the channel being calibrated. It should be possible to adjust the offset potentiometer to bring the voltage reading on the voltmeter to zero.

14. Once the above calibrations are obtained, disconnect the voltmeter, replace the DB25 connector to the computer, and replace the tape over the adjustment holes of the Kaman oscillator-demodulator box. If the above calibration does not yield the above listed calibrations, first check the connections. If they are not the problem, then check the cables from the Kaman transducers to the oscillator-demodulator boxes for continuity or shorts. If they are not at fault, then the problem lies with either the Kaman transducer, the oscillator-demodulator box, or the power source to the oscillator-demodulator box. Each one of these can be checked by temporarily interchanging units.

#### Final Calibrations:

1. Follow the instructions given in the manual for setting up the apparatus for a test, except install the tubing spacers over the chamber rods and do not install the cast acrylic tube. The steps include:

- a) placing spacing tubes on the chamber rods,

- b) installing the chamber lid with torsional oscillator attached to piston and piston clamped in highest position, and
- c) lowering and centering, by eye, the cam plate in the gap of the Kaman transducers.
- d) Attach the taring spring to the piston and unlock the piston clamp. (This condition will minimize the friction in the system.)
- e) The position of the rotary table should be at the zero index. (Use the cursor arrow keys in the Set Up and Adjust option on the program QSCAL1V to do this.)
- f) The stepper motor system should be installed to the chamber lid and connected as in a test and the power to the system should be applied.

2. With the offset switches above Channels 7 and 8 on the Sensotec in the ON (up) position, and assuming that they have not been moved since completing the preliminary calibrations above, adjust the position of the Kaman transducers by translating and/or rotating the support platform for the Kaman transducers until the output of both Kaman transducers are near zero. (This should be monitored on the screen of the computer, which should be displaying the Set Up and Adjust option of the main menu. The output of the Sensotec meter also should register near zero when the rotary knob is placed in positions 7 and 8.) A visual check should verify that the cams are very close to their mid position. (The average gap between the Kaman transducers and the cams should be approximately 3.175 mm (0.125 in.).

3. By use of the manual control of the stepper motor in the Set Up and Adjust option, cause the stepper motor to rotate the rotary table in a clockwise direction until the index of the rotary table is at the 60 degree mark. This will cause the oscillator head to rotate 30 degrees in the clockwise direction. Inspect the position of the cams relative to the Kaman transducers. The faces of the cams should not have gone past the faces of the Kaman transducers, and the gaps

should be roughly equal to each other.

4. Read and record the outputs of both the computer screen and the Sensotec. The computer reading should be somewhere between 7 and 10 volts, and the Sensotec reading should be somewhere between 27 and 32.

5. Now with the manual control, cause the stepper motor to rotate the rotary table in the counterclockwise direction until the index is 60 degrees on the other side of zero (300 mark on the table scale). Inspect the position of the cams relative to the Kaman transducers. The faces of the cams should not have gone past the faces of the Kaman transducers, and the gaps should be roughly equal to each other.

6. Repeat step 4, above. This time, the readings should be in the same magnitude range, but have the opposite sign.

7. If in steps 3 or 5, above, the faces of the cams went beyond the face of the Kaman transducers, return the rotary table to the zero index and then manually adjust (rotate) the support platform in the direction needed to keep the faces of the cams within the faces of the Kaman transducer. The positioning of the support platform can be guided by observing the computer screen while making the adjustment. The readings of both transducers should be kept nearly the same, and the magnitude of the readings is proportional to the amount of rotation applied to the support platform. After adjusting, repeat steps 3 through 6.

8. Return the rotary table to the zero index. Turn off the offset switches for Channels 7 and 8 on the Sensotec and record the readings on the Sensotec meter for these two channels. These readings should be nearly the same and will be the readings to be used in future setups when adjusting the support platform. Record these values in section V of the apparatus manual. (The values displayed on the computer screen will probably be overranged and of no use.)

9. Turn the offset switches for Channels 7 and 8 back on and adjust the potentiometers below the switches until both of the rotation transducer channels read zero. (Either the Sensotec meter or the computer screen displayed values may be used for this, but it is



usually more convenient and accurate to use the computer screen displayed values.)

10. Return to the Main Menu of the program QSCALIV by pressing SHIFT 6 (the "^"), and then choose Option 3.

11. Place a formatted diskette in the B drive of the computer.

12. Two tests will need to be run, one at a small rotation limit in the range of 1 to 5 degrees, and one to the full capacity of the apparatus, 30 degrees. Only two pieces of information really need to be supplied, the rotation limit and the file name for storing the data acquired. Choose the file names to indicate the rotation limit and number of cycles chosen (e.g., RL02C1 would represent a rotation limit of 2 degrees and a test that consisted of 1 cycle). Note that input rotations apply to the rotary table and not the cams, i.e., a 60° rotation limit implies a 30° cam rotation limit.

13. To accept the selected items input and begin operation, follow the prompts in the program. The stepper motor will automatically rotate the oscillator head by 0.1 of the rotation limit and stop. Manually take and record the readings for both Channels 7 and 8 on the Sensotec. Then press any key and the next rotation increment will be applied. Continue doing this until all of the readings specified have been taken. At this time, the computer will prompt the user on whether to save or discard the computer-acquired data. If accepted, the data are written onto the diskette in the B drive with the same format as used by the program QSDATACQ.

14. Repeat the process for the cam rotation limit of 30 degrees.

15. Readings from Channels 7 and 8 of the Sensotec should be averaged and plotted against the rotation applied by the stepper motor. This will give a calibration for the Sensotec. (In general, the Sensotec meter readings should be close to the actual rotations, especially for rotations less than 20 degrees. As rotations approach 30 degrees, it is not uncommon for the difference to approach 10 percent.)

16. Data recorded on diskette can be imported to the spreadsheet program QSDATAVU.WR1, or simply manually recorded into a specially prepared spreadsheet. The data for the small rotation limit is fitted

with a straight line. The slope of this line is used as the baseline for the full range rotation limit. Figure A.1 shows the relationship between the actual and back-calculated cam rotations for a typical test. Then, for the full range rotation test, the log of the difference between the linear fit and the actual rotation readings versus the log of the voltage readings are fitted with straight lines, one in the positive region and one in the negative. Finally, a nonlinear equation is established which has two branches, one in the positive region and one in the negative region. Figure A-2 shows the calculated nonlinear equations fit to the exact rotation values. The final calibration factor has the form:

$$\text{Rot. (Deg.)} = (\text{PC Volt}) * \text{LCF} + 10^a * (\text{PC Volt})^b \quad (\text{A-1})$$

where:

- PC Volt is the average of the voltages read by the PC for the two rotation transducers,
- LCF is the linear calibration factor obtained from the test at the small rotation limit,
- a is the intercept in the fit of  $\log(\text{Diff})$  versus  $\log(\text{PC Volt})$ , and
- b is the slope of the fit of  $\log(\text{Diff})$  versus  $\log(\text{PC Volt})$ .

17. In the program QSDATAWA, the above calibration factors are given by:

$$\text{VRTCF} = \text{LCF} \quad [\text{Deg./Volt}] \quad (\text{A-2})$$

For the positive region,

$$\text{VRTCFPA} = 10^a$$

$$\text{VRTCFPB} = b$$

and for the negative region,

$$\text{VRTCFNA} = 10^a$$

$$\text{VRTCFNB} = b$$

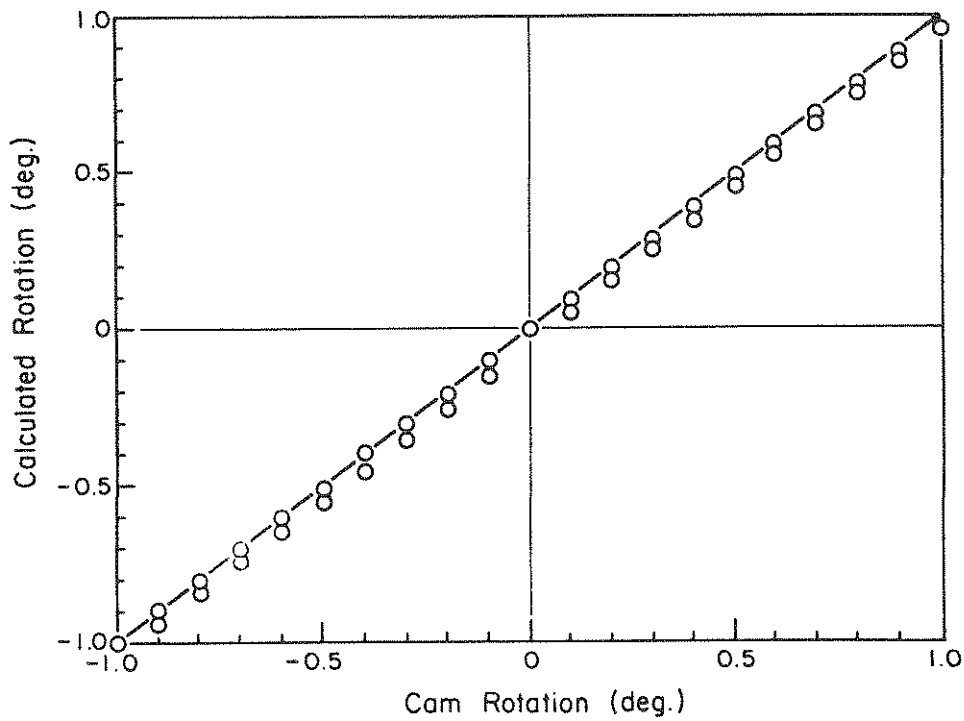


FIGURE A-1. Example of Linear Range Rotation Transducer Calibration

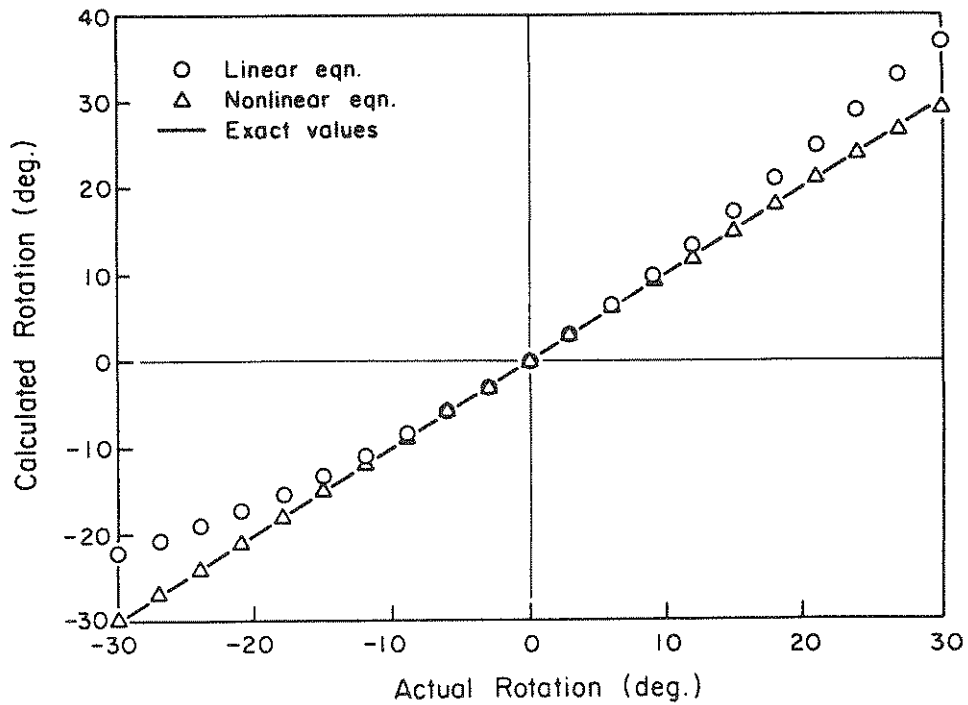


FIGURE A-2. Example of Nonlinear Range Rotation Transducer Calibration

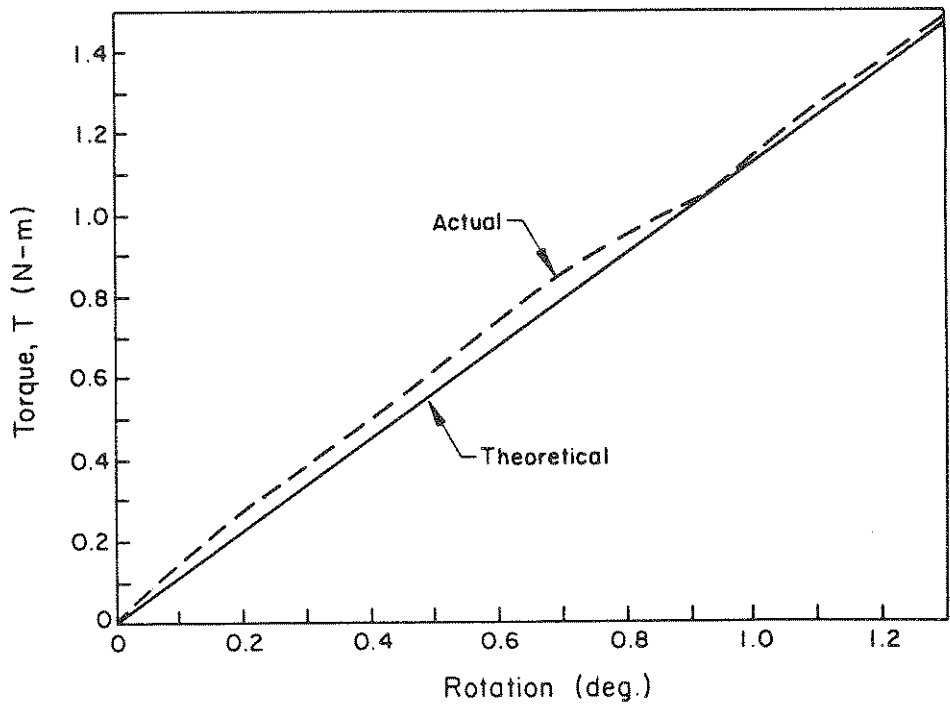


FIGURE A-3. Theoretical versus Actual Torque Transducer Readings

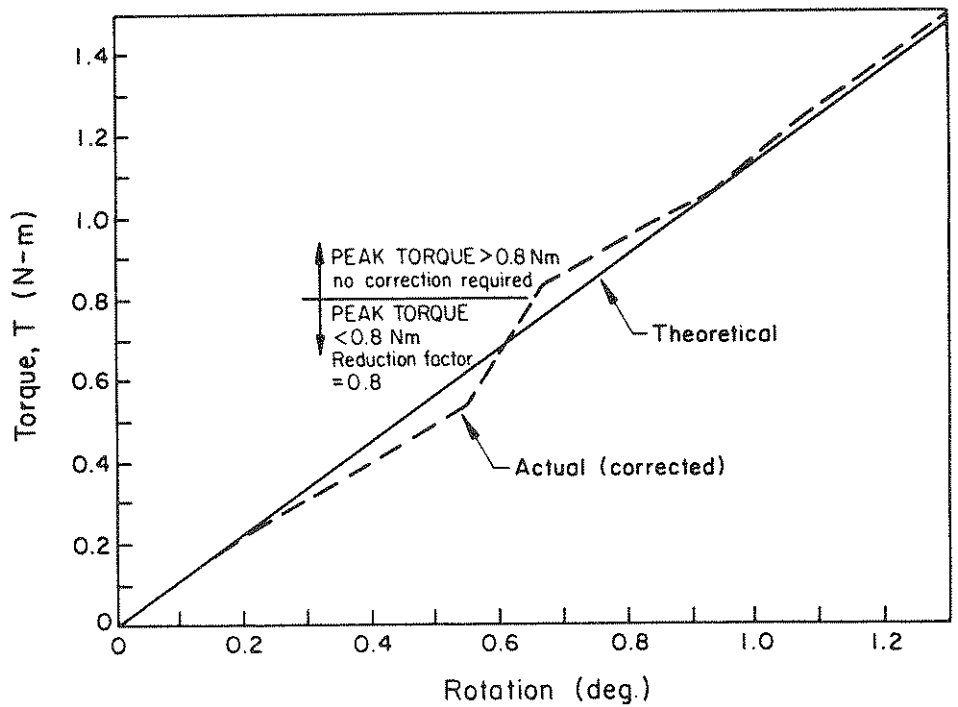


FIGURE A-4. Theoretical versus Corrected Torque Transducer Readings for 0.8 Correction Factor

where the a and b values for the positive region are different from those for the negative region.

### A.3 TORQUE TRANSDUCER CALIBRATION

The calibration of the torque transducer was checked because larger values of shear modulus were being obtained from the low strain amplitude torsional shear tests than the resonant column testing, which was clearly illogical. The calibration rod was used to check the torque transducer's output. The test was carried out by removing the porous disks and fixing the rod firmly to the platens. A standard low strain, to 1 degree, torsional shear test then was carried out. A theoretical value of torque was calculated for various rotation angles, from elasticity theory:

$$T = (G \theta J)/L \quad (A-3)$$

where:

T = torque,

G = shear modulus, for steel = 79,300 MPa,

$\theta$  = angle of rotation in radians,

J = polar moment of inertia, and

L = length of rod.

Figure A-3 shows the difference between the theoretical value calculated and the actual reading obtained from the transducer. Clearly, the transducer is reading too high; over 25% for some of the lower torque values. This low torque nonlinear behavior can be corrected by using a simple reduction factor of 0.8 applied to torque values below 0.8 N-m, which reduces the error to a maximum of 10%. This correction is shown in Figure A-4.



## APPENDIX B GENERAL OPERATIONS

### B.1 SOLID SPECIMEN PREPARATION

1. Saturate the pore drainage lines and porous disks by placing the upper platen directly on the lower platen and sealing the platens together with O-rings and a short length of membrane. Then connect the upper platen's pore line to its base plate connection. Be sure to tighten the connection with two 7/16-inch wrenches, one on the nut and the other on the center of the union. Check that the bottom platen's lines are also tight. Next, connect the top platen valve to a vacuum supply and the bottom platen valve to the backpressure water supply. Open the top platen valve and evacuate the system with maximum vacuum for about 30 minutes.

After evacuation, shut the valve to the upper platen and gradually open the bottom platen valve. The backpressure should be at no more than 35 kPa. The water will balloon the membrane, and after a few seconds, the pore water should be shut off. This procedure should produce a reasonably saturated system.

2. Several transducers should be adjusted at this point. Check the output of the torque transducer. If it is not registering zero, adjust the zero (coarse and/or fine) of Channel 3. If the upper platen with cam plate is sitting on the lower platen, remove it and then adjust the load cell output to zero by adjusting the zero of Channel 2. Finally, the pressure transducer output should be corrected to zero by adjusting the zero for Channel 1. None of these channels should require any further adjustment.

3. A procedure for construction of solid cylindrical specimens is given below:

- a) Check the vertical faces adjacent to the porous structures on the platens to see that they are clean

and free of scratches. Place a light coating of vacuum grease on each of these faces, and be careful not to get the vacuum grease into the porous structures.

- b) Put a wet filter paper disk on the bottom platen.
- c) Place the membrane over the lower platen. Ensure that the membrane is squarely in position and no vacuum grease gets on the portion of the membrane in contact with the soil.
- d) Carefully place three O-rings over the membrane on the lower platen.
- e) Check the split mold for soil particles and other debris. Put a light coating of vacuum grease on the places where the two halves of the mold meet. Apply a light coating of talcum powder on the inside of the mold. Position the split mold and fasten the halves by means of the wormscrew clamps. In the process, guide the membrane through the mold so that it protrudes from the top.
- f) Place three O-rings over the upper part of the mold and then fold the membrane over the top of the mold. Apply a vacuum to the space between the membrane and the mold. If the membrane is folded or creased, release the vacuum, remove the creases, and reevacuate. Should the application of the vacuum cause a hissing noise from within the mold, tighten the wormscrew clamps. If the hissing sound continues, replace the membrane.
- g) Specimen construction may now be carried out using the method of undercompaction. A spreadsheet program, SAMPREP, can be used to aide specimen prepa-



ration and as a testing record. Figure B-1 shows an example of an actual test. The spreadsheet, as shown in the figure, is set up for solid silt specimens, but easily can be adjusted for other materials and specimen sizes. The steps followed in the program correspond with those described by Ladd [1977] up to step 9. Step 10 gives the result of the saturation procedure. Step 11 gives a summary of the tests carried out on the specimen. Step 12 calculates the specimen's final unit weight, void ratio, saturation ratio, and relative density. Step 13 is set aside for general comments on the test.

- h) Once the material has been carefully placed into the membrane-lined mold, the top surface should be smoothed and made flush with the top of the split mold. Then a wet filter paper disk is placed on top of the specimen.
- i) Place the upper platen carefully on the top of the specimen, making sure the cams are orientated in the correct direction. The center of cam No. 1 should align with the hole in the chamber base through which the gold cable for rotation transducer No. 1 passes.
- j) Roll up the membrane from the mold onto the top platen. Through one of the pore lines, apply a vacuum at a level below that to be used as the effective consolidation stress to avoid overconsolidation effects. Vacuum from outlet 2 should be used. Usually, a vacuum equivalent to 30 to 50 kPa is sufficient.
- k) Roll the three O-rings into place on the upper platen. Once the O-rings are in place, roll the

Undercompaction Calculations  
AJW, July 88

-----  
Test No. SC-2  
Date 11/02/88  
-----

STEP 1 Addition of Water

For a  $S_r = 40\%$  aprox. water contents of between 14-17%  
should be used.  
Desired  $w = 15\%$   
Mass of Dry Silt = 2373.5 g  
Vol. of Water reqd. = 356.03 ml  
 $G_s = 2.65$

-----  
STEP 2 Calculate actual water content of material

$w = 15.2\%$

-----  
STEP 3 Mold Measurements  
[include membrane thickness]

Inside Diameter = 69.9 mm  
Outside Diameter = 0 mm  
Height = 193 mm  
Volume = 740630.2 mm<sup>3</sup>

-----  
STEP 4 Select Number of Layers

$nt = 9$   
Layer Ht. = 21.44 mm

Note: layer height should not exceed 25mm  
for high unit weights thinner layers should be used

-----  
STEP 5 Determine Total Wet Mass of Material Required

Silt  
Max. Dry Unit Weight = 17.3 KN/m<sup>3</sup> = 110.2 pcf  
Min. Dry Unit Weight = 11.1 KN/m<sup>3</sup> = 70.4 pcf  
Reqd Dry Unit Weight = 13.5 KN/m<sup>3</sup> = 85.91 pcf  
  
Relative Density = 49.61 %  
Projected Void Ratio = 0.93  
 $S_r = 43.51$   
Wet Mass Required = 1.1741 Kg  
Dry Mass Required = 1.0192 Kg  
Placement Unit Wt. = 15.552 KN/m<sup>3</sup> = 98.97 pcf

-----  
STEP 6 Layer Weight  
= 130.46 g

-----  
STEP 7 Selection of Undercompaction Percentage (Uni)  
Uni = 6 %

-----  
STEP 8 Calculation of Layer Heights (Solid Samples)  
[table must be changed for different n values]

FIGURE B-1. Sample Preparation and Test Data

Layer n	Un	Avg. Un	Hn	Layer Th.	Ht. Measured	
1	6	6.00	22.73	22.73	173.77	nt = 9
2	5.25	2.63	44.01	21.28	152.49	Ht = 193 mm
3	4.5	1.50	65.30	21.28	131.20	Uni = 6 %
4	3.75	0.94	86.58	21.28	109.92	Unt = 0 %
5	3	0.60	107.87	21.28	88.63	Rim Th. = 13 mm
6	2.25	0.38	129.15	21.28	67.35	
7	1.5	0.21	150.43	21.28	46.07	
8	0.75	0.09	171.72	21.28	24.78	
9	0	0.00	193.00	21.28	3.50	

Note: Ht Measured is dist from top of tamping foot to support rest bottom.  
i.e.rim thickness of support collar +Ht-Hn-tamping foot thickness  
Un = percent undercompaction in layer n  
Uni= percent undercompaction in first layer  
Unt= percent undercompaction in final layer  
Hn = height of specimen at top of layer n  
Ht = height of specimen

-----  
STEP 9 Construct Sample  
[see Ladd paper procedure, steps 9,10,11&12]  
-----

STEP 10 Saturate Sample  
B= 0.90 achieved at 90 psi back pressure  
Method: as SI-10 except sample saturated for 36 hrs.  
by opening and closing drainage line repeatedly  
-----

STEP 11 Testing Record

Test	Notes
RES. COL.	Resonance around 112 Hz, threshold strain = 0.004%
SC-RS-2A	R.L.=0.6 degs. C.T.=150s, Cycles=4, Samples=882
SC-RS-2B	R.L.=0.6 degs. C.T.=100s, Cycles=5, Samples=688
SC-RS-2C	R.L.=0.6 degs. C.T.=50s, Cycles=10, Samples=1021
SC-RS-2/DFI	R.L.=0.6 degs. C.T.=20s, Cycles=10, Samples=890
SC-RS-2/EGH	R.L.=0.6 degs. C.T.=20s, Cycles=20, Samples=1760

-----  
STEP 12 Final Measurements

Sample Height =	188.5 mm
Average Outside Dia.=	67.9 mm
Average Inside Dia. =	0 mm
Volume =	682559.7 mm <sup>3</sup>
Wet Mass =	1287.7 g
Dry Mass =	1028 g
Change in Dry Mass =	8.8 g (-ve indicates a reduction from step 5)
Weight of water =	259.7 g
w =	25.26 %
Sr =	88.14 %
e =	0.76
Dry Unit Wt. =	14.77 KN/m <sup>3</sup> = 94.03 pcf
Wet Unit Wt. =	18.51 KN/m <sup>3</sup> = 117.78 pcf
Relative Density =	69.40 %

-----  
STEP 13 Test General Comments  
i A long time was required for saturation due to decreased sample permeability.

FIGURE B-1. Sample Preparation and Test Data (completed)

membrane back over the rings. This will ensure that the membrane does not trap any confining fluid on the top platen. Next, remove the clamps on the mold, insert a screw driver into the slots on the mold, split the mold halves, and carefully remove them. Examine the specimen for any imperfections and to see that the construction process did not puncture the membrane.

## B.2 APPARATUS ASSEMBLY

### B.2.1 General Setup

During the assembly process, it is important to monitor the transducer outputs to ensure that the specimen remains as undisturbed as possible. This can be done either by using the Sensotec readouts and switching from one channel to another or, preferably, observing the computer monitor in the Setup and Adjust mode of the program QSDATAWA. This program is located in the subdirectory C:\QSAPP\DATAACQ, and is executed by typing: SETUP.

The cam assembly attaches to the upper platen of the specimen. The rotation transducers focus on these cams to determine the rotation of the top of the specimen. For solid specimens, the assembly is attached to the upper platen before the platen is placed on the specimen. For hollow specimens, it must be placed after the specimen construction is complete. It is important that each cam faces the transducer against which it was calibrated. To ensure proper orientation, the cams are labelled "1" and "2" to correspond with rotation transducer channels "1" and "2".

### B.2.2 Assembly Procedure

1. With the specimen, cams and upper platen in place, carefully lower the rotation transducer support platform into position. Throughout the assembly procedure, the specimen should be at a vacuum pressure of between 30 and 50 kPa. Once the platform is on the

mounting plate, put the four clamps in place, but do not tighten them. The support platform may now be rotated and/or translated to provide centering for the cams. Attach the gold transducer cables, which come through the chamber base, to the individual rotation transducers. With the rotation offset switches in the on (up) position, roughly zero the rotation readouts.

2. The four chamber tie rods should now be screwed into the chamber base. They should only be finger tight. Then place the support rods over the tie rods.

3. The chamber lid assembly, consisting of the Hardin oscillator, LVDT, taring spring, torque motor system, and rotary table tensioning system, should be resting on the wooden stand. If any of these systems are not in place or require maintenance, the S.D.I. operations manual, Section V, contains detailed assembly and adjustment instructions. The piston locking clamp and the piston adjustment yoke should both be securely tightened. The overhead crane should be in position over the chamber lid, with its lifting hook fixed to the lifting eye. The lifting eye is fastened to a plate bolted onto the threaded rods.

4. The chamber lid assembly may now be lifted and moved to a position over the support rods. Care should be taken that no electrical or pressure lines are damaged. The assembly should be lowered as slowly as possible onto the top of the tie rods, and no attempt should be made to drop the lid directly into its final position. It is difficult to avoid some specimen disturbance at this point, because the crane's lowering control is very coarse. The tie rods may now be guided carefully into the holes on the chamber lid. The chamber lid should be at a height where only a few millimeters of each rod can fit into its respective chamber lid hole. Once the tie rods are lined up properly, the chamber can be lowered onto the support rods. CAUTION: If the lid tips to one side and becomes jammed on a tie rod, under no circumstances should the overhead crane be used in an attempt to lift the chamber lid free. (If the crane is used, the whole device, including the concrete block, will be lifted off the ground, and the crane cannot support such a weight.) To free the jammed rod, the

other rods must be moved to their respective holes. When all the rods are in position, the lid will drop down onto the supports.

5. Disconnect the crane hook, install the four tightening hand knobs, and tighten them firmly. Tighten opposite knobs simultaneously.

6. Ensure that the piston height adjustment yoke is locked and the ends of the yoke are supported by nuts on the threaded rods. Note that the LVDT and taring spring should not be in position at this time. Also, the sprocket head cap screws, located on the piston sprocket, should be released. This sprocket has to be moved up when lowering the piston, and down when raising the piston. Release the piston locking clamp.

7. Observe the output of the axial load cell. It should be displaying the weight of the specimen, support platform, and upper platen, which for a solid specimen is roughly 50 N. Insert the long hex wrench into the hole within the piston. It should slide into a socket head cap screw located within the oscillator and rotate the screw when turned. The screw should be coated with silicon grease, or any suitable lubricant. Slowly lower the piston by turning the two nuts that support the piston yoke. As the piston is lowered, observe the coupling at the base of the oscillator. If the coupling is not concentric, loosen the hand knobs that secure the chamber lid and adjust the lid until concentricity is achieved. If concentricity is still not possible, the top platen must be moved into the correct position, and this will cause some specimen disturbance. As the coupling pieces approach each other, observe the output of the axial load transducer so that undue axial force is not inadvertently applied to the specimen. When the coupling pieces mate, the axial load should be adjusted to read between 50 and 70 N.

8. Rotate the handle of the long hex wrench inserted into the piston until the coupling pieces are firmly held together. During this connection process, the axial load should be monitored constantly, and the axial force on the sample maintained at roughly 50 N by adjusting the height of the piston. The torque transducer should also be monitored, and excessive rotation avoided.

9. With the cams now fixed in position, zero the rotation transducers. It is important that the average reading is approximately zero, and that the individual channels are also reading approximately zero. Then tighten the clamps holding the support platform in position. Potentiometers located on the Sensotec panel may be used as fine adjustment; they have an approximate range of  $\pm 3$  degrees.

10. The long hex wrench should now be used to unscrew the coupling, and then the piston adjustment yoke can be used to raise the piston back to its starting position. Again, the axial load transducer should be monitored to avoid excessive load on the specimen.

11. The chamber lid knobs should be unscrewed, the crane moved back into position, and the hook attached to the lifting eye. The piston clamp must also be tightened.

12. When hoisting the chamber lid assembly, it must be manually guided off the tie rods so that it is lifted evenly. If the lid is hoisted without manual support, it could lift unevenly and a tie rod become jammed. If this occurs, then the whole device might be lifted.

13. The chamber lid assembly should be moved to one side. The support rods can now be removed and the bottom O-ring groove examined to see that it is free of soil particles, and that the O-ring is in position. If the O-ring is not in position, it will require pre-stretching before it can be fitted. The top O-ring should also be checked.

14. Ensure that the ends of the cast acrylic tube are clean, and then carefully install the tube on the chamber base.

15. Position the chamber lid on the pressure chamber, as in step 4.

16. Disconnect the crane hook, install the four tightening hand knobs, and tighten them firmly. Tighten opposite knobs simultaneously. If these knobs are not tightened enough, then leaking from the top seal will occur at high pressures.

17. Release the piston locking clamp.

18. Lower the piston into position, as in step 7.

19. Tighten the resonant column and upper platen coupling, as in step 8.

20. The average rotation transducer reading should be approximately zero, and the individual channel readings should be no more than  $\pm 5$  degrees. The average rotation reading can be zeroed by adjusting the potentiometers. If zeroing cannot be achieved, then the procedure has to be repeated. This procedure will be simplified when an upper platen locking device is designed and constructed. The device will hold the upper platen in the correct position, to enable the rotation transducers to be zeroed without the recourse to steps 4 to 8 and 10 to 12.

21. Tighten the piston locking clamp. The sprocket head cap screws should now be locked, with the sprocket a few millimeters above the level of the opposing sprocket on the rotary table.

22. Unlock the piston adjustment yoke, move it into a position at 90 degrees to the threaded rods, and relock it. This yoke will be used to support additional axial weights during the saturation process.

23. Swing the yoke that contains the LVDT into place. Insert the plug into the piston and tighten it until the O-ring is within the piston and the plug is seated firmly. Level the yoke by adjusting the supporting nuts. Then zero the transducer by adjusting its position in the yoke.

24. Pull down the spring, which is attached to the uppermost yoke, and hook it into the eye on the rod above the LVDT. The load on the taring spring should read 23 to 24 lbs.

25. Loosen the piston clamp and observe the output of the axial load transducer. The load should be in the 30 to 50 N range. If it is not in this range, adjust the handnut protruding from the top of the uppermost yoke. Check that the average rotation is still reading zero and readjust if necessary.

26. Connect vacuum supply 1 to the chamber lid pressure connection and apply a vacuum of between 20 to 30 kPa, while maintaining a specimen vacuum of at least 50 kPa, i.e., at least an effective stress of 20 kPa. Open the valve on the carboy containing the silicon oil and unscrew its lid. Then open the valve on the bottom of the chamber. The chamber will start to fill with silicon oil. Close the



valve when the silicon oil is just over the maximum fill level and all of the membrane is covered. Close the valve and tighten the lid on the carboy.

27. Connect the pressure line to the rotary table tensioning system. This system helps to remove any backlash that may occur during cyclic testing. Also, the accumulator tank should be connected to allow for a more constant applied pressure to the piston.

28. Pressurizing and saturation procedures may now be started.

### B.3 SATURATION PROCEDURE

#### B.3.1 Setup

After the assembly procedure is complete, the chamber vacuum is removed and the pressure line switched to the cell pressure control panel. The specimen vacuum is reduced while the cell pressure is increased, so that effective pressure remains between 30 to 40 kPa. When the specimen vacuum pressure has been reduced to zero, close the top platen connection and remove the line. Then fix the backpressure line to the bottom platen connection. Ensure that this line is full of water and the backpressure interface is full of distilled, deaired water. The bottom platen valve now can be opened and the backpressure increased, to maintain an effective pressure of roughly 34 kPa. When the cell pressure is at 103 kPa and the backpressure at 69 kPa, the top platen line can be opened and water allowed to circulate through the sample. For these saturation pressures, a consolidation pressure of at least 100 kPa must be used to remove any overconsolidation effects.

The time required for effective saturation of a specimen varies, depending on its relative density and clay percentage. For a preparation relative density of roughly 50%, silt specimens of 0%, 10%, and 20% clay would require saturation times of roughly 24, 48, and 72 hours, respectively. A pore pressure parameter  $B = \Delta u / \Delta \bar{\sigma}_3$  of greater than 0.9 is desirable to ensure adequate saturation. If the B

determination procedure is attempted too quickly, then an acceptable B will not be achievable, even at the highest confining pressure of 700 kPa. During the saturation time, the backpressure interface chamber will have to be refilled at least once. This is done by closing the top platen drainage valve and allowing the pressure within the specimen to equalize for about 10 minutes. Then the bottom platen valve can be closed, the backpressure reduced to zero, and the panel main air and backpressure valves closed. The backpressure line is disconnected, and a vacuum applied to the interface air bladder from the vacuum 1 control position. Distilled, deaired water can now be drawn from a container into the chamber through the backpressure line, if the backpressure valve is opened. After filling, the backpressure valve should be shut off and the line reconnected to the bottom platen valve. The vacuum should be turned off and the backpressure main air turned up to its previous level. If any air is trapped in the interface chamber, it should be released by opening the valve on the chamber's lid. Backpressure now can be returned to the sample, the top platen valve reopened, and saturation continued.

To more effectively remove air from the specimen, it is useful to occasionally close the top platen drainage valve and allow the pressure in the specimen time to equalize. Then, on reopening the top platen valve, air bubbles should be seen in the top platen line. If no bubbles are seen, then the specimen is ready for the B determination procedure.

### B.3.2 B-Determination

1. Close the valve to the upper platen and wait 5 to 10 minutes for the pressure to equalize throughout the specimen. This valve should not be opened again until the end of the test, or unless a high enough B cannot be achieved. Increased clay percentage decreases the specimen's permeability, and therefore increases the time required for pressure equalization.

2. Close the valve to the bottom platen. The effective pressure should remain roughly constant. If the pressure increases, then

equalization is still occurring in the specimen. If the pressure decreases, it is possible that a leak is allowing chamber pressure to enter the specimen.

3. Table B-1 should be checked to determine if weights need to be added to the piston adjustment yoke. In general, the axial load should be kept at roughly 30 N, and the addition of extra weight at the higher pressures enables this to be done. A level of 30 N was selected to ensure that a negative axial load does not occur during a pressure increase. If additional weight is not added, then the specimen will suffer a necking failure. This is because the area of the piston shaft is acted on by atmospheric pressure, but in the chamber it is acted on by large positive pressures, so that there is a net upward force. Note that above an approximate chamber pressure of 380 kPa, the total weight of the whole resonant column and piston assembly becomes insufficient to prevent a necking failure.

4. When the effective pressure becomes constant, an increase in cell pressure may be applied. This increase, typically about 35 kPa, should be applied carefully, and the effective pressure increase caused by the chamber pressure increase recorded.

5. Increase the backpressure 35 kPa and open the valve to the bottom platen. Again, time must be allowed for pressure equalization.

6. The B coefficient can be calculated from  $B = \Delta u / \Delta \bar{\sigma}_3$  or  $(1 - \Delta \bar{\sigma} / \Delta \bar{\sigma}_3)$ . If  $B > 0.9$ , the procedure may be halted. If it is below 0.9, then steps 2 to 5 should be repeated. If the chamber pressure is at maximum and the B is still less than 0.9, then the chamber and backpressures should be reduced simultaneously back to 103 kPa and 69 kPa, respectively. As the chamber pressure is reduced, the axial load should also be reduced, as shown in Table B.1. The top drainage line should then be reopened and water again allowed to flow through the specimen for at least 24 hours before another attempt is made. This procedure will cause some specimen disturbance, and it is not recommended that the B determination process be started until it is reasonably certain that the sample is well saturated.

TABLE B-1. Additional Axial Load Requirements

Cell Pressure (kPa)	Additional Axial Load (N)	Loading Schedule (kg)
69.0	20	taring spring
137.9	40	taring spring
206.9	60	taring spring
275.9	80	taring spring
344.8	100	taring spring
379.3	110	+1 kg
413.8	120	+1 kg
448.3	130	+1 kg
482.8	140	+1 kg
517.2	150	+1 kg
551.7	160	+1 kg
586.2	170	+1 kg
620.7	180	+1 kg
655.2	190	+1 kg
689.7	200	+1 kg

#### B.4 SPECIMEN CONSOLIDATION

When a sufficient level of saturation has been achieved, the back-pressure can be adjusted to achieve the required consolidation stress level in the specimen. All tests carried out in this study were on specimens consolidated to roughly 100 kPa. Axial deformation, effective pressure, and time from the start of consolidation should be

recorded. A Taylor construction on a square root of time versus axial deformation plot can be used to determine the time required for 100% completion of primary consolidation.

#### **B.5 PRESSURE TEST**

After completion of primary consolidation, the specimen should be left at least another 15 minutes to allow for pressure equalization. Then the valve to the bottom platen (backpressure line) is closed, and as the top platen valve should already be closed, the specimen is isolated against further drainage. The effective pressure should now be recorded against time. A drop in the effective stress of up to about 5 kPa in 10 minutes is usual, but eventually the effective pressure should stabilize. Minor increases or decreases of up to 1 kPa can occur due to fluctuations in the supply pressure. But if a steady decrease occurs, then a leak must be present.

If a slow leak is present, then it is still possible to run an undrained test in which a large amount of pore pressure buildup is expected in the first few loading cycles. If a large leak occurs, then the test must be aborted. The most common sources of leaks are membrane damage and/or pressure connections within the chamber. If no leaks are present, then undrained resonant column and torsional shear testing can begin.

#### **B.6 APPARATUS DISASSEMBLY PROCEDURE**

1. After a test is complete, lower the chamber pressure, with the specimen still undrained, to about 100 kPa. As the chamber pressure is reduced, the axial load should also be reduced, as shown in Table B-1.

2. Open the carboy valve and unscrew the lid. Then open the drainage valve in the chamber base. The silicon oil should flow back into the carboy. Close the drainage valve when as much silicon oil as possible has been removed from the chamber. Close the carboy valve and reseal the top.

3. Reduce the chamber pressure to about 30 kPa. Attach a

vacuum line from supply 2 to the top platen. Open the top platen valve and slowly increase vacuum pressure to about 30 kPa, as the chamber pressure is decreased to zero. With the chamber pressure at zero, the cell pressure line can be disconnected. Also, the pressure lines to the rotary table tensioning system should be disconnected.

4. Tighten the piston clamp, and disassemble the taring spring and LVDT assembly. Loosen the piston adjustment yoke and turn it so that it again rests on the nuts screwed to the threaded rod. Tighten the piston adjustment yoke and release the piston's sprocket head screws, so that the sprocket can be moved down when the piston is raised.

5. Release the piston clamp.

6. The long hex wrench now should be used to unscrew the coupling, and then the piston adjustment yoke can raise the piston back to its starting position. The axial load transducer should be monitored to avoid excessive load on the specimen.

7. The chamber lid knobs should be unscrewed, the crane moved back into position, and the hook attached to the lifting eye. The piston clamp must also be tightened.

8. When hoisting the chamber lid assembly, it must also be guided manually off the tie rods, so that it is lifted evenly. If the lid is raised without manual support, it could lift unevenly and a tie rod become jammed. If this occurs, then the whole device might be lifted. The chamber lid assembly now can be returned to the wooden stand.

9. Remove the tension rods and carefully lift off the acrylic chamber.

10. Remove the clamps holding the rotation transducer support platform in position, and then remove the platform.

11. Measure the specimen dimensions.

12. Close the valve to the top platen, and switch the vacuum supply to the bottom platen.

13. Carefully remove the top platen, and remove the O-rings from the bottom platen.

14. The bottom of the membrane now can be folded up and the

specimen removed in one piece. Then the membrane is folded off completely, and the specimen weighed for a water content determination.





## APPENDIX C RESONANT COLUMN OPERATION

### C.1 INTRODUCTION

The Hardin resonant column can measure the dynamic properties of a specimen over a range of shear strains, and at a number of different testing stages. Low amplitude resonant column vibration, at less than 0.001%, is nondestructive and will not affect the specimen. Therefore, low amplitude vibration can be applied at any testing stage to monitor changes in stiffness and damping. In particular, it can be used during consolidation to determine when primary consolidation is complete. This is important for low permeability cohesive materials that take a long time to consolidate, but is not worthwhile for materials that consolidate rapidly. The procedure for doing this is to apply a small torque to the coils, adjust the frequency of oscillation until resonance occurs (established by observing the Lissajous figure on the oscilloscope), and taking readings of torque, acceleration, and frequency. A more detailed method for resonant column testing is given in section C.2 of this appendix.

Once consolidation is complete, undrained resonant column testing from low to high amplitudes can be carried out. The procedure for this phase is similar to low amplitude testing, except that after each reading, which takes about one minute to make, the power to the drive coils is increased. This process is continued until the desired amplitude is achieved or the limit of the apparatus is reached. The apparatus is limited by the current capacity of the drive coils, which is approximately 0.75 amps. This corresponds to a voltage reading of 2.7 Volts<sub>rms</sub> on the A.C. voltmeter when the switch on the control box is in the torque position. Also, saturated undrained testing should stop when pore pressure generation starts to occur, i.e., the threshold strain is exceeded, because any further testing at higher amplitudes is liable to cause excessive specimen disturbance, and eventually, rapid failure of the specimen.

Once high amplitude testing is complete, it is common practice to return to low amplitudes and make an additional test. If the resonant frequency at this low amplitude has not changed significantly from the frequency prior to the start of high amplitude testing, it can be said that the high amplitude testing was nondestructive to the soil. When this occurs, it is possible to consolidate the specimen to another stress level and perform additional testing.

After high amplitude testing, or instead of it, the specimen may be tested in torsional shear. However, resonance testing may be continued throughout the loading phase. The procedure consists of establishing a low amplitude resonance, and then maintaining resonance during the torsional loading phase by adjusting the frequency of oscillation. Torque, acceleration, and frequency readings are taken at each point where conventional data are taken. Unfortunately, at low amplitude testing, a large amount of signal distortion makes resonance determination difficult, and when the transformer for the torsional stepper drive motor is switched on, distortion increases and low amplitude testing becomes almost impossible. Thus, resonance testing during a torsional shear test is very difficult to accomplish. However, testing is possible at the end of cycle runs if the motor is disconnected. Full details on the calibration of resonant column devices are given by Drnevich [1978; 1985]. In particular, calibration details on the device used for this test program are given by S.D.I. [1987].

## C.2 TESTING PROCEDURE

The procedure described below enables the collection of data required for calculation of a specimen's shear modulus and steady state damping ratio. An additional procedure for calculation of a specimen's damping ratio by the amplitude decay method is also described briefly.

Before the electronics are switched on, the output level should be set to zero (the Channel 1 knob on the supply amplifier should be fully counterclockwise), and the switch on the control box set in the "off"

position. Also, the signal generator should be set for sine waves. All the electronics should be turned on and allowed to warm up for at least 30 minutes.

1. Adjust the frequency on the signal generator to roughly 110 Hz, and set the readout to the 10 second gate position.

2. Record the transducer readings for the specimen's effective pressure, axial load, and length. For drained resonant column testing, volume change should also be recorded.

3. Set the three-way switch on the control box to "standby," and the two-way switch to "torque."

4. Set the desired output level on the Channel 1 control of the supply amplifier. The output level will be registered on the A.C. voltmeter. The usual starting output level for low amplitude testing is 0.01 Volts.

5. The oscilloscope should be set for X-Y display. The X display is proportional to the torque applied by the coils, and the Y display is proportional to acceleration of the top platen. Adjust the volts/div controls until the trace is a reasonable size.

6. Set the switch on the control box to "off."

7. Simultaneously activate a timer and turn the switch on the control box to the "operational" position. The trace on the oscilloscope should form an ellipse.

8. Adjust the frequency on the signal generator. When the axes of the ellipse are vertical and horizontal, the system is at the so-called "resonant frequency."

9. Read and record the torque output from the A.C. voltmeter, and switch the control box to "accel."

10. Read and record the accelerometer output from the A.C. voltmeter.

11. Simultaneously switch the control box to "off" and turn the timer off.

12. Wait at least 20 seconds before recording the resonant frequency from the signal generator.

Steps 2 to 12 then can be repeated, should more readings be required.

With practice, the above steps can be carried out in less than a minute or two.

Damping may be determined by two different methods. The standard procedure is to calculate steady-state damping from the data obtained in the procedure described above. The amplitude decay method of damping ratio calculation may be used as a check on the steady-state values. The method requires the use of a storage oscilloscope. To obtain the data for the amplitude decay method, the system must first be at resonance. The oscilloscope should then be switched to the accelerometer (Y) time mode, and set to record the decaying motion on triggering. When the control box three-way switch is moved to the "off" position, the oscilloscope should be triggered, and will store several cycles of steady-state motion followed by decaying motion. The peak-to-peak amplitude for a cycle just after amplitude decay begins should be measured. Then the number of cycles to the location where the amplitude is 20% to 30% of the steady-state amplitude can be counted, and the peak-to-peak amplitude measured. However, if this number of cycles is greater than ten, then only record the peak-to-peak amplitude at the tenth cycle. The damping ratio then can be calculated from these data.

The steady state method is advantageous for measuring damping at high strain amplitudes because shearing strain amplitude does not vary during the measurement, whereas for the amplitude decay method, the average shearing strain amplitude for the measurement is lower than the steady-state amplitude at which resonance measurements are made. Also, the steady-state method is superior when testing hard specimens. Such specimens have material damping values that are about the same magnitude as the apparatus damping. The steady-state method allows the effects of apparatus damping to be taken into account, and enables specimen damping measurements to be made.

### C.3 DATA REDUCTION

A PC program, RC6-0987, was used for resonant column data reduction.

DATA REDUCTION : INITIAL CONDITIONS

APPARATUS TYPE : HARDIN TORSIONAL RESONANT COLUMN  
DATA REDUCTION PROGRAM BY DR.V.P.DRNEVICH, ET AL, DEC.,1981.  
MICROBASIC VERSION PROGRAMMED BY MARK ANDERSON, JUNE, 1982.  
MODIFIED FOR CORNELL DIRECTORY AND FILE NAMES, 4/88 HES  
MODIFIED FOR HOLLOW SAMPLES BY HES & AJW 4/88

RESONANT COLUMN DATA REDUCTION

TEST NAME : SI-13  
TEST IDENTIFICATION NUMBER : SI-13A1  
SOIL DESCRIPTION : SILT  
TEST OPERATOR : AJW  
TEST DATE : 10/6/88

APPARATUS CALIBRATION FACTORS

POLAR MASS INERTIA = .001166 Kg-M\*\*2  
ROT. MOTION C.F. FOR TORS. VIB. = 4.02 rad-Hz\*\*2/VRMS  
DAMPING COEFF. FOR TORS. MOTION = .0139 Kg-M\*\*2-Hz  
TORQUE-CURRENT FACTOR FOR TORS. MOTION = .01022 N-M/VRMS  
APPARATUS RESONANT FREQUENCY = 99.5 Hz

SYSTEM CHARACTERISTICS

LENGTH DIAL CALIBRATION FACTOR = 1 mm/unit  
BURETTE CALIBRATION FACTOR = -1 ml/unit  
PRESSURE CALIBRATION FACTOR = 1 kPa/unit  
AXIAL LOAD CALIBRATION FACTOR = 1 N/unit

SYSTEM CONDITIONS

INITIAL AXIAL LOAD READING = 0 N  
INITIAL BURETTE READING = 0 ml  
INITIAL LENGTH DIAL READING = 0 mm  
NUMBER OF DATA LINES = 12

SPECIMEN CHARACTERISTICS

MASS = 1.2781 Kg  
DIAMETER = .0684 M  
LENGTH = .188 M  
SPECIFIC GRAVITY = 2.65  
WATER CONTENT = 24.8 %  
DEGREE OF SATURATION = 83.45 %  
MASS DENSITY = 1850.1 Kg/M\*\*3  
VOID RATIO = 0.788  
ROTATIONAL INERTIA = 7.475E-04 Kg-M\*\*2

FIGURE C-1. Example RC6-0987 Output

RESONANT COLUMN DATA REDUCTION FOR HARDIN APPARATUS  
 DATA REDUCTION PROGRAM BY DR.V.P.DRNEVICH, ET AL, DEC., 1981.  
 MICROBASIC VERSION PROGRAMMED BY MARK ANDERSON, JUNE, 1982.  
 MODIFIED FOR CORNELL DIRECTORY AND FILE NAMES,4/88 HES

TEST NAME : SI-13  
 TEST IDENTIFICATION NUMBER : SI-13A1  
 SOIL DESCRIPTION : SILT  
 TEST OPERATOR : AJW

TEST DATE : 10/6/88

INPUT DATA :

LINE #	TIME (min)	CELL PRESSURE (kPa)	BACK PRESSURE (kPa)	AXIAL LOAD (N)	BURETTE READING (ml)	LENGTH READING (mm)	CURRENT READING (V-RMS)	ACCEL. READING (V-RMS)	RES. FREQ. (Hz)
1	1.00	98.700	0.000	0.000	0.000	0.000	0.0100	0.0210	107.00
2	1.00	98.500	0.000	0.000	0.000	0.000	0.0230	0.0400	106.90
3	1.00	98.200	0.000	0.000	0.000	0.000	0.0500	0.0820	106.80
4	1.00	98.200	0.000	0.000	0.000	0.000	0.0970	0.1550	106.70
5	1.00	98.100	0.000	0.000	0.000	0.000	0.1940	0.3020	106.20
6	1.00	98.000	0.000	0.000	0.000	0.000	0.2860	0.4350	105.90
7	1.00	98.000	0.000	0.000	0.000	0.000	0.3930	0.5870	105.60
8	1.00	98.000	0.000	0.000	0.000	0.000	0.5750	0.8040	104.80
9	1.00	98.100	0.000	0.000	0.000	0.000	0.6630	0.9000	104.40
10	1.00	98.000	0.000	0.000	0.000	0.000	0.7810	1.0170	104.00
11	1.00	97.900	0.000	0.000	0.000	0.000	0.8840	1.1100	103.60
12	1.00	97.800	0.000	0.000	0.000	0.000	0.9910	1.2000	103.30

OUTPUT DATA :

LINE #	TIME (min)	AXIAL STRESS (kPa)	AXIAL STRAIN (%)	VOID RATIO	EFF. CONF. (kPa)	PRIN. STRESS RATIO	KILO-CYCLES OF VIB.	SHEAR STRAIN (%)	SHEAR MODULUS (MPa)	DAMP. RATIO (%)
1	1.00	0.0	0.000	0.788	98.7	1.00	6.	0.0000892	17.335	1.03
2	1.00	0.0	0.000	0.788	98.5	1.00	0.	0.0001707	17.315	1.70
3	1.00	0.0	0.000	0.788	98.2	1.00	0.	0.0003505	17.214	1.94
4	1.00	0.0	0.000	0.788	98.2	1.00	0.	0.0006638	17.114	2.05
5	1.00	0.0	0.000	0.788	98.1	1.00	0.	0.0013055	16.613	2.19
6	1.00	0.0	0.000	0.788	98.0	1.00	0.	0.0018912	16.315	2.31
7	1.00	0.0	0.000	0.788	98.0	1.00	0.	0.0025666	16.018	2.41
8	1.00	0.0	0.000	0.788	98.0	1.00	0.	0.0035692	15.232	2.79
9	1.00	0.0	0.000	0.788	98.1	1.00	0.	0.0040261	14.843	2.97
10	1.00	0.0	0.000	0.788	98.0	1.00	0.	0.0045845	14.456	3.24
11	1.00	0.0	0.000	0.788	97.9	1.00	0.	0.0050424	14.072	3.49
12	1.00	0.0	0.000	0.788	97.8	1.00	0.	0.0054830	13.786	3.74

FIGURE C-1. Example RC6-0987 Output (completed)

This program uses apparatus calibration factors, specimen measurements, ambient stress conditions, and measured vibration data to calculate the specimen's shear modulus, damping ratio, and strain amplitude. Output from this program is shown in Figure C-1. The program has compatible terminology with the standard for resonant column testing procedure and data reduction, ASTM D4015-87 [1988a]. The model of the resonant column used in program is fully described by Drnevich [1985].





## APPENDIX D TORSIONAL SHEAR TESTING

### D.1 INTRODUCTION

Torsion is applied to the specimen by a torque motor system which attaches to the pressure chamber lid. The motor system causes the piston and Hardin oscillator to rotate. The applied torsion passes through the cam assembly, upper platen, specimen, axial load transducer, and finally is reacted to by the torque transducer, which is mounted beneath the chamber base. Except for some minor resistance provided by the tubing and two electrical cables, all applied torque is measured by the torque transducer.

The relative rotation between the bottom and the top of the specimen is measured by displacement transducers, which focus on the cam assembly. Output of these transducers is linear for small rotations, but becomes nonlinear for larger values of rotation.

The torque motor system consists of a stepper motor, rotary table, and a sprocket system. The overall gear reduction ratio is 180 to 1. The stepper motor moves in 0.0144 degree steps. Control of the stepper motor is provided by the microcomputer program QSDATAWA. The main menu of the program gives five selections:

1. Setup and Adjust,
2. Monotonic Loading,
3. Cyclic Rotation Controlled Testing,
4. Cyclic Torque Controlled Testing, and
5. Return to DOS.

The Setup and Adjust menu allows for simultaneous monitoring of all six transducer outputs. The outputs are in SI engineering units and are not necessarily consistent with the numbers on the Sensotec meter, as several calibration factors in the control program have been updated. If the operator wishes to hold a given set of displayed

values, this can be done by pressing the "\ " key. Pressing the "\ " again unfreezes the display. Manual control of the stepper motor in this mode is also possible. The default motor speed is "3" (no significant units). The speed can be increased up to "5" by use of the up arrow key, or decreased to "1" by use of the down arrow key. Starting the motor is accomplished by pressing the right arrow for clockwise motion, and the left arrow for counterclockwise motion. The motor may be stopped by pressing the "\ " key, or either the up or down arrows. From the zero position, the motor can move the rotary table only  $\pm 65$  degrees before the limit switches shut it off. The rotation applied to the specimen is one-half of the rotary table motion. Motion larger than this could cause wiring damage to the Hardin oscillator, and would put the rotation transducers out of range. However, for a solid sample run on manual control, the maximum achievable monotonic shear strain is 19%, for nominal specimen dimensions of diameter equal to 71.1 mm and height equal to 191 mm. The test control options are fully discussed in Section 3 under subsection 3.1.2.

## D.2 DATA RETRIEVAL

Data stored by the program QSDATAWA are in two ASCII files, one with a "HDR" extension and the other with a "DAT" extension. The file with the "HDR" extension contains all of the information selected from the menu in QSDATAWA when the test is setup, plus information on the actual number of cycles completed, total number of data points, and reason for test termination. The file with "DAT" extension contains the torque, rotation, effective pressure, axial load, and axial deformation data for the test.

A spread sheet program, QSDATAVU, is used to view the acquired data. To use the program, the data file name is placed in cell C7, and the drive/directory where this file is located in cell C6. By pressing the ALT and L keys simultaneously, a macro is executed that loads the data files, makes a number of calculations, and sets up plotting windows. Depending on the size of the data set, some adjustment of the sample number and time columns, using standard spreadsheet techniques,

may be required before the entire data range can be viewed. The plots may then be viewed by successive presses of the F6 key. Example plots for the first five cycles of a typical undrained rotation control test of axial load, axial deformation, torque, rotation, and pressure versus time are shown in Figures D-1, D-2, D-3, D-4, and D-6, respectively. Figure D-5 shows a plot of torque versus rotation.

Figure D-1 indicates that axial load increases rapidly on loading to some stable level. This increase, and the increase in axial deformation shown in Figure D-2, are due to the stiffness reduction caused by the cyclic loading, which enables an increase in the radial compression of the specimen by the cell pressure. Since the test is undrained, this radial compression will cause the axial load and axial deformation to increase slightly. The axial load of 0.03 kN, shown in Figure D-1, is equivalent to an axial stress of 7.5 kPa. To maintain perfectly isotropic conditions during a test, an axial loader linked to the axial load transducer would be required. The reduction in the peak sustainable torque with increasing loading cycles is shown in Figure D-3. Figure D-4 shows the controlled rotation cycles, and for this test, the rotation limit is shown to have been set at  $\pm 3$  degrees. Figure D-5 shows a plot of torque versus rotation, and illustrates the degradation of the specimen's stiffness with increasing load cycles. Figure D-6 shows the excess pore pressure generation in the specimen.

For stress and strain calculations, the final specimen length and diameter should be input into cells J7 and J8, respectively, in the spreadsheet program QSDATAVU. Stress and strain values can then be calculated for solid specimens. Stress and strain values are usually only calculated over the specific cycle of interest, because it is easier to use the plot of a single cycle for shear modulus and damping ratio determination. Some spreadsheet manipulation is required to produce these plots. In general, for cyclic strain control tests only, the stress-strain hysteresis loops for cycles 1, 5, 10, 20, 50, and 100 were plotted and analyzed. Figure D-7 shows a typical stress-strain plot for the first loading cycle of an undrained strain

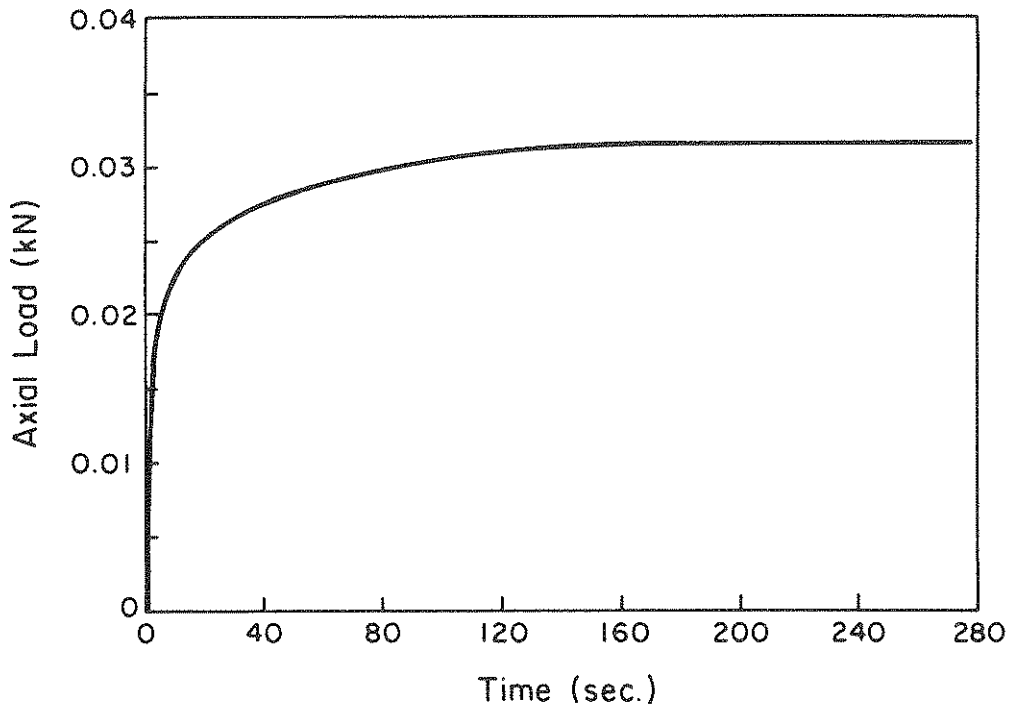


FIGURE D-1. Axial Load versus Time

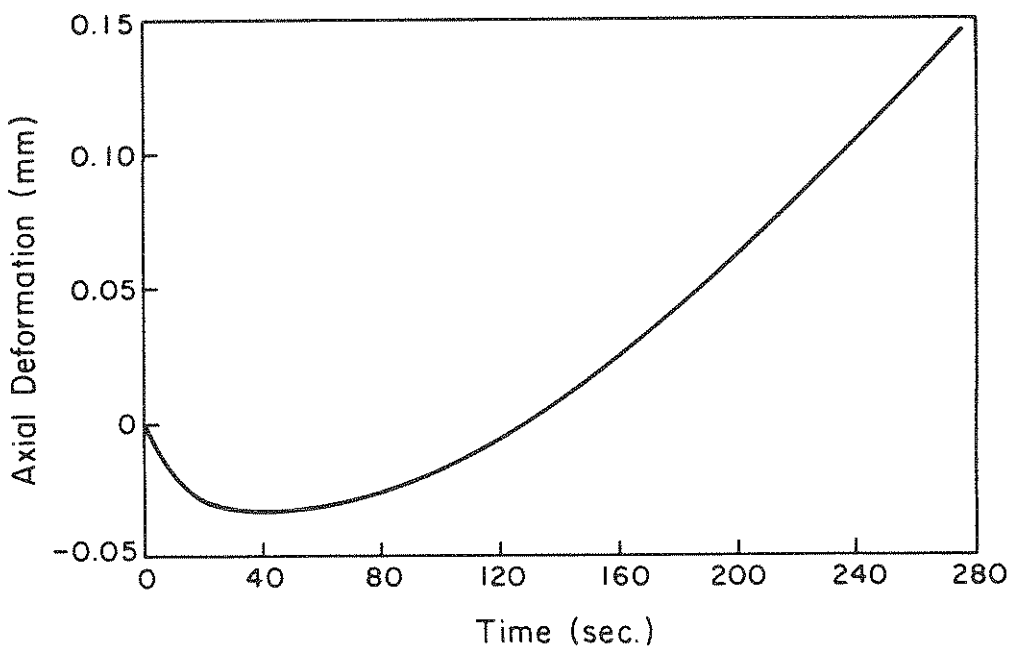


FIGURE D-2. Axial Deformation versus Time

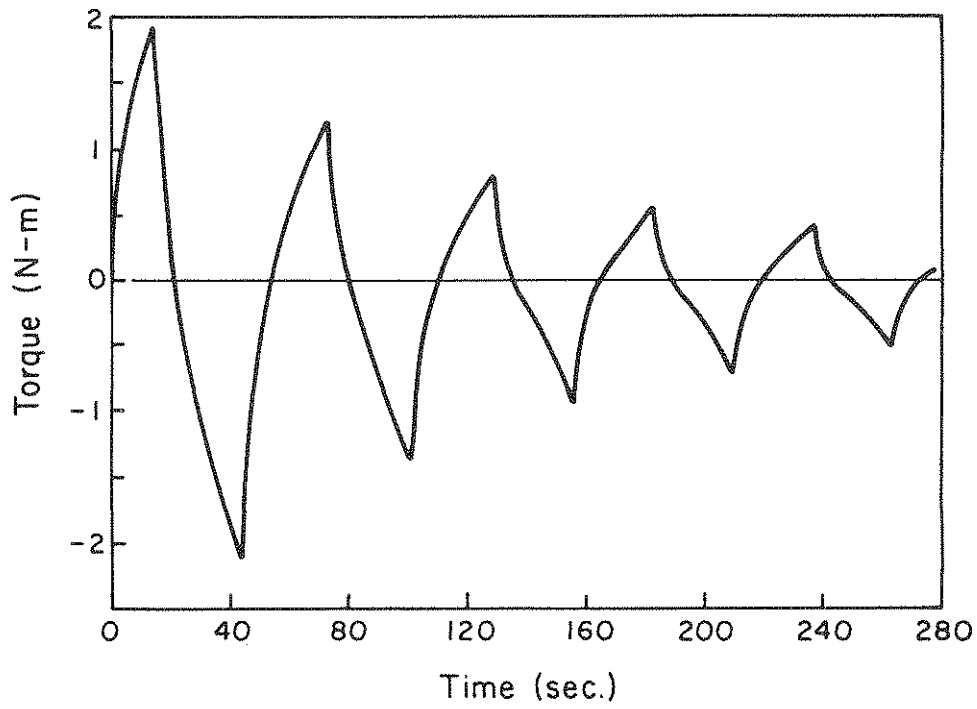


FIGURE D-3. Torque versus Time

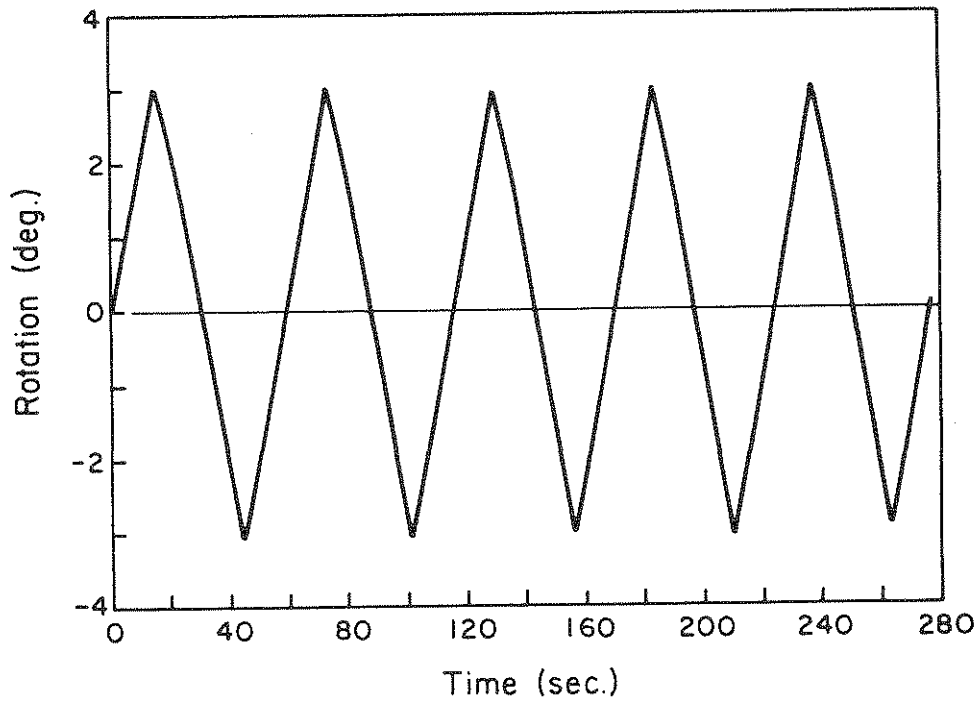


FIGURE D-4. Rotation versus Time

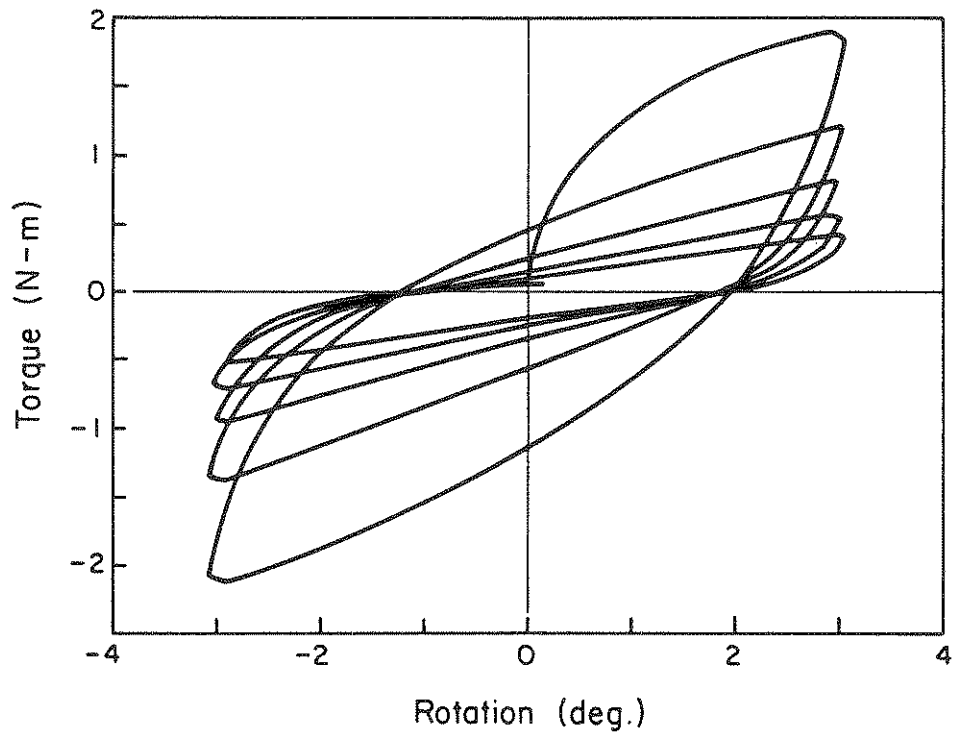


FIGURE D-5. Torque versus Rotation

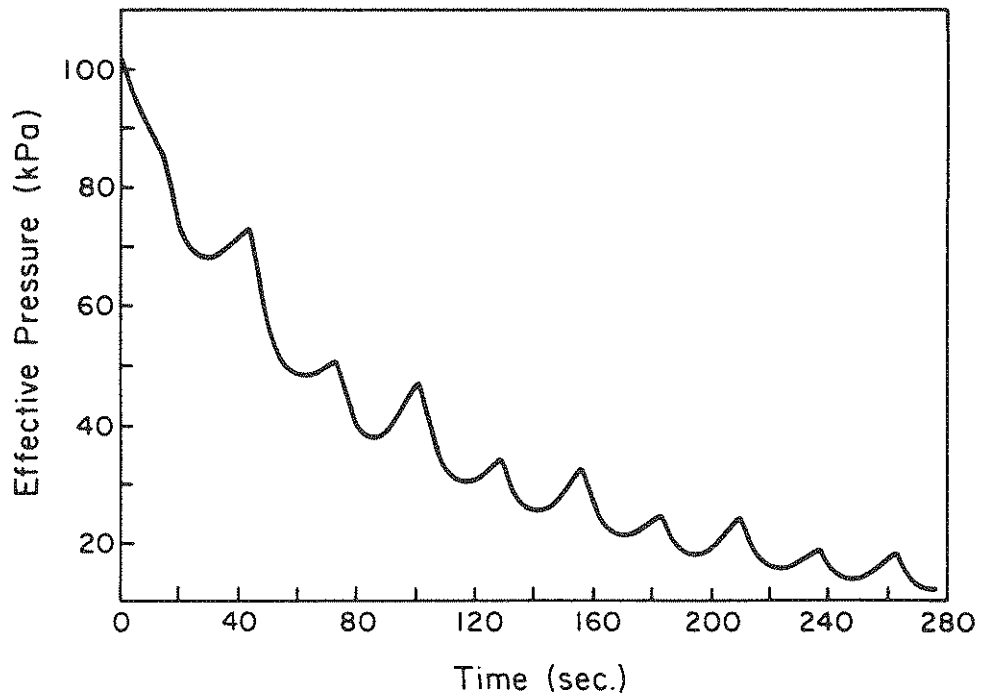


FIGURE D-6. Effective Pressure versus Time

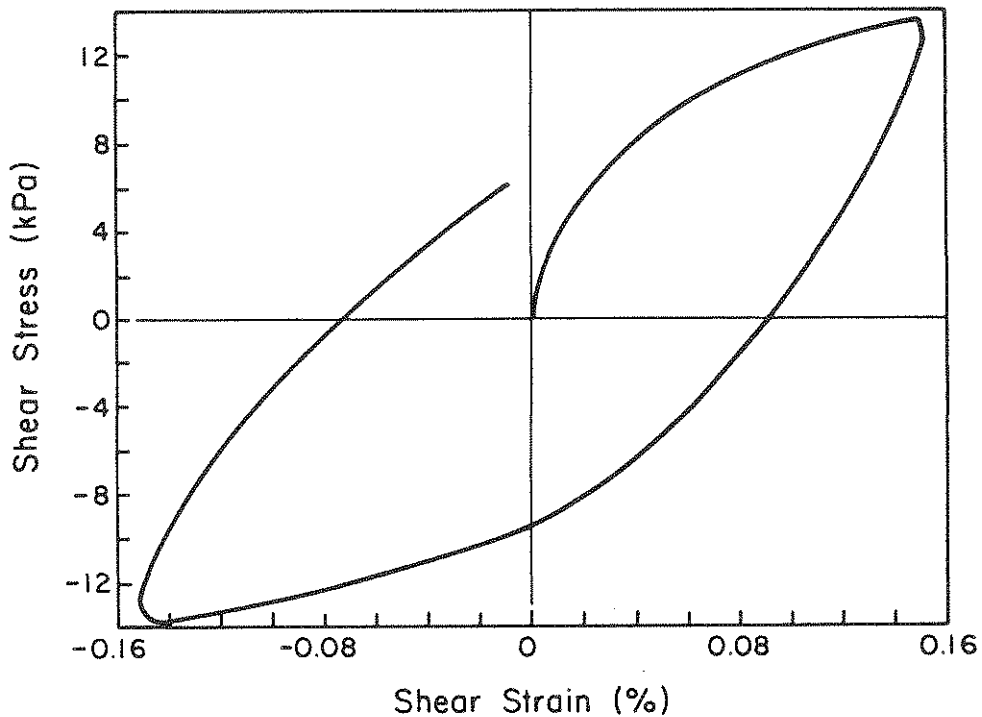


FIGURE D-7. Stress versus Strain

controlled test. The basis for the equations used to calculate stress and strain from torque and rotation are discussed below.

### D.3 STRESS AND STRAIN DISTRIBUTIONS

In torsional shear tests, shearing strain is calculated from the angle of rotation of the test specimen. However, the angle of rotation per unit length is not a good measure of shearing strain amplitude, because shearing deformation is constrained to vary linearly from zero at the axis of rotation to some finite value at the outside, as shown in Figure D-8.

Since soils have nonlinear stress-strain curves, shearing stress does not vary linearly across the radius of the specimen, even though shearing strain does. Therefore, a major problem in interpretation of data from torsional shear tests is determining the relationship between the measured torque-twist curve and the actual stress-strain

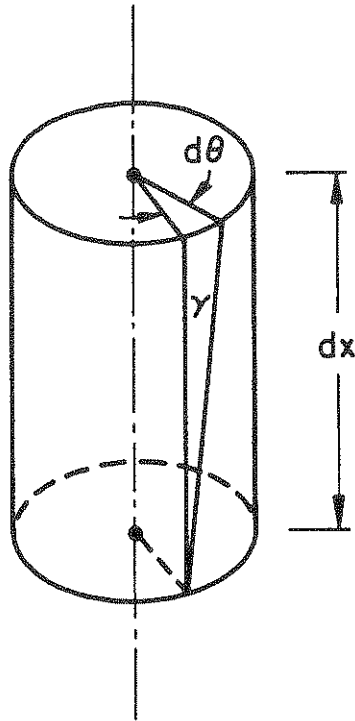


FIGURE D-8. Shearing Deformation in a Test Specimen

curve for the soil being tested. Isenhower, et al. [1987] presented procedures developed so that shearing stress can be calculated using relationships based on elastic theory, and the nonlinear behavior is accommodated in the procedure used to calculate shearing strain.

The procedure in reducing data from the torsional shear test is to use the torsion formula derived from elasticity theory. Shearing stress,  $\tau$ , is calculated from:

$$\tau = cT/J \quad (D-1)$$

where  $c$  = radius at which  $\tau$  is calculated,

$T$  = applied torque, and

$J$  = polar moment of inertia of the specimen;

$J = \pi(d^4/32)$  for a solid specimen with a diameter,  $d$ .

Shearing strain,  $\gamma$ , at a radius,  $c$ , is calculated from:



$$\gamma = \theta(c/L) \quad (D-2)$$

where  $\theta$  = angle of rotation in radians, and  
L = length of specimen.

Both stress and strain in the elastic relationships of Equations D-1 and D-2 are linear functions of the radius at which shearing stress and strain are calculated. The basic problem is to select a value of  $c$  that results in the best estimate of the true stress-strain curve for the level of stress calculated using elasticity theory. Chen and Stokoe [1979] studied this problem to find a value of  $c$  for solid specimens tested in torsional shear devices for which representative values of stress and strain could be calculated using Equations D-1 and D-2. The procedure also assumed a nonlinear stress-strain model, and then integrated the stress-strain curve over the radius of the specimen to calculate torque for a given angle of rotation. They next calculated shearing stress using Equation D-1, and shearing strain using Equation D-2, for an assumed value of  $c$ . The value of  $c$  was varied to ascertain the value that gave the greatest accuracy in reproducing the stress-strain relation originally assumed. Chen and Stokoe [1979] found that the value of  $c$  varied from  $0.41d$  for shearing strain amplitudes of  $0.001\%$ , to  $0.395d$  for shearing strains at  $0.1\%$ . Thus, it was recommended that a value of  $0.4d$  be used for all stress-strain calculations. Therefore, equations for the average stress and strain in solid cylindrical specimens become:

$$\tau = (0.4)32T/(\pi d^3) \quad (D-3)$$

$$\gamma = 0.4d\theta/L \quad (D-4)$$

These equations were used in the torsional shear data reduction procedures developed for this report.

A value of  $c = d/3$ , linear elastic behavior, is used in ASTM D4015-87 [1988a] for calculation of shearing strain and stress in the torsional resonant column test. This value is acceptable for small strain

amplitudes. Note that for full mobilization of shearing stress, a linear distribution of shear strain, and fully plastic behavior, the value of  $c$  used for shear stress determination is  $0.375d$ . But for shear strain determination, D4015-87 recommends  $c = d/3$ . Therefore, values for  $c$  given by Chen and Stokoe [1979] result in the same shear modulus (where  $G = \tau/\gamma$ ) as an elastic analysis, but at a higher shear strain level to simulate nonlinear behavior.

For hollow cylindrical specimens, Chen and Stokoe [1979] found that use of the average of the inside and outside radii resulted in only a slight error in predicting the assumed stress-strain relation. Therefore, for hollow specimens, a value of  $c$  equal to the average radius of the specimen is acceptable.

#### D.4 DETERMINATION OF SHEAR MODULUS AND DAMPING RATIO

In a linearly elastic material, the relationship between stresses and strains is linear. Thus, the shear modulus, which is the slope of the shear stress versus shear strain relationship, is constant, irrespective of the shear strain level. At very low shear strains, the deformations exhibited by soils can generally be considered elastic. However, as shearing takes place under increasing shear strains, the soil's response becomes increasingly nonlinear and inelastic. Hence, a soil's stress-strain response cannot be represented by a single modulus value.

The response of soils to seismic loading is usually investigated by means of cyclic loading, unloading, and reloading, which yields an approximately closed loop in the shear stress-shear strain space. This hysteresis loop reflects the nonlinear stress-strain characteristics of soils. Hence, a simple representation of this behavior often is made in terms of an equivalent secant shear modulus,  $G$ , and damping ratio,  $\lambda$ , as shown in Figure D-9. The shear modulus is defined as the slope of a straight line connecting the end points of the shear stress versus shear strain curve. Therefore, it can be calculated from:

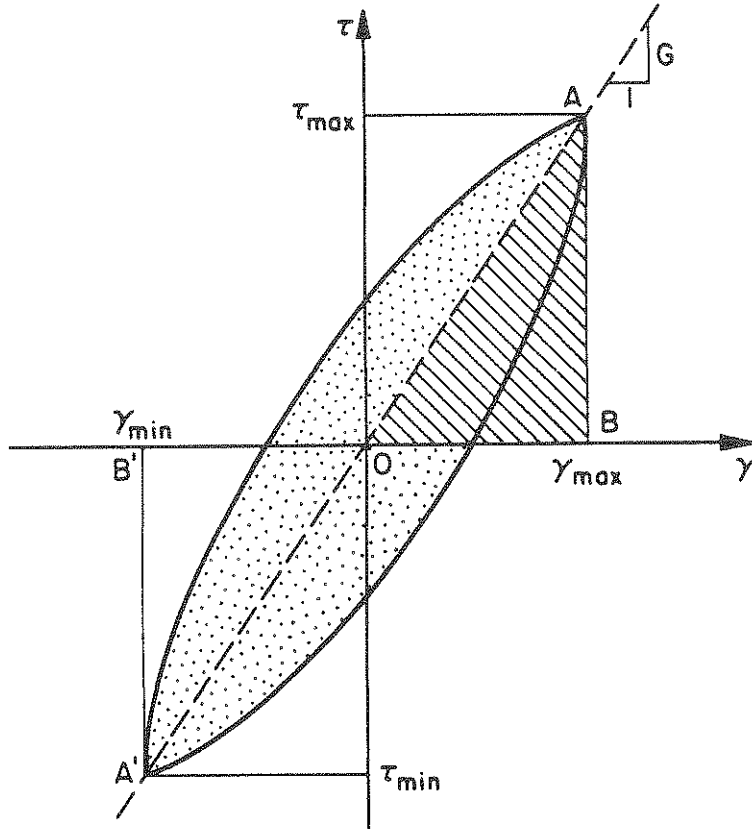


FIGURE D-9. Definition of Equivalent Hysteretic Shear Modulus and Damping Ratio

$$G = (\tau_{\max} - \tau_{\min}) / (\gamma_{\max} - \gamma_{\min}) \quad (D-5)$$

where  $\tau_{\max}$  = maximum (positive) shear stress,  
 $\tau_{\min}$  = maximum (negative) shear stress,  
 $\gamma_{\max}$  = maximum (positive) shear strain, and  
 $\gamma_{\min}$  = maximum (negative) shear strain.

The damping ratio,  $\lambda$ , is defined as the ratio of the energy dissipated per loading cycle (area inside the hysteresis loop) to two times the maximum elastic strain energy stored in the soil element. Therefore:

$$\lambda = \frac{1}{2} \frac{\text{Area of Hysteresis Loop}}{(\pi) \text{ Area of Triangles OAB and OA'B'}} \quad (D-6)$$

The area inside the hysteresis loop may be obtained by numerical

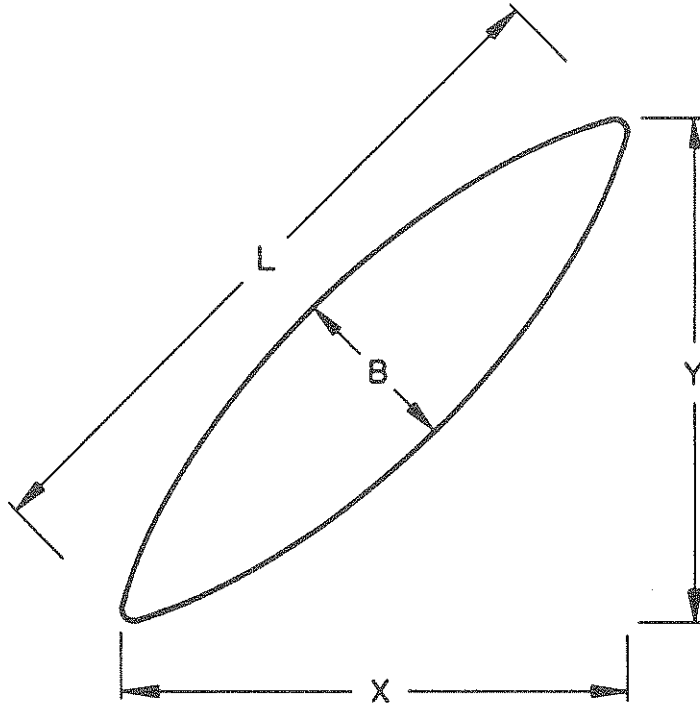


FIGURE D-10. Measurements of Hysteresis Loop

TABLE D-1. Comparison Between Methods of Damping Ratio Calculation

Test No.	Load Cycle	Damping Ratio (%)	
		Direct Area Measurement (Trapezoidal Rule)	Simplified Measurement (Equation D-8)
SC-5A	1	23.0	25.9
SC-5B	5	19.2	19.1
SC-5C	10	16.6	16.9
SC-5D	20	15.4	16.6
SC-5F	50	15.4	15.0
SC-5I	100	15.3	15.8

integration, or by the use of a planimeter. However, the area of the hysteresis loop can be closely approximated by assuming the loop to be an ellipse, and using the relationship:

$$\text{Area of Loop} = \pi LB/4 \quad (\text{D-7})$$

where L = major axis dimension, and  
B = minor axis dimension.

For this study, measurements were made of the hysteresis loop's vertical height, Y, horizontal width, X, and minor axis length, B, as shown in Figure D-10. Thus, the damping ratio was evaluated from:

$$\lambda = \frac{B(X^2 + Y^2)^{1/2}}{2XY} \quad (\text{D-8})$$

The accuracy of the equation was confirmed by comparison with direct area measurements, using the trapezoidal rule to determine the area within the hysteresis loop, as shown in Table D-1.



NATIONAL CENTER FOR EARTHQUAKE ENGINEERING RESEARCH  
LIST OF PUBLISHED TECHNICAL REPORTS

The National Center for Earthquake Engineering Research (NCEER) publishes technical reports on a variety of subjects related to earthquake engineering written by authors funded through NCEER. These reports are available from both NCEER's Publications Department and the National Technical Information Service (NTIS). Requests for reports should be directed to the Publications Department, National Center for Earthquake Engineering Research, State University of New York at Buffalo, Red Jacket Quadrangle, Buffalo, New York 14261. Reports can also be requested through NTIS, 5285 Port Royal Road, Springfield, Virginia 22161. NTIS accession numbers are shown in parenthesis, if available.

- NCEER-87-0001 "First-Year Program in Research, Education and Technology Transfer," 3/5/87, (PB88-134275/AS).
- NCEER-87-0002 "Experimental Evaluation of Instantaneous Optimal Algorithms for Structural Control," by R.C. Lin, T.T. Soong and A.M. Reinhorn, 4/20/87, (PB88-134341/AS).
- NCEER-87-0003 "Experimentation Using the Earthquake Simulation Facilities at University at Buffalo," by A.M. Reinhorn and R.L. Ketter, to be published.
- NCEER-87-0004 "The System Characteristics and Performance of a Shaking Table," by J.S. Hwang, K.C. Chang and G.C. Lee, 6/1/87, (PB88-134259/AS). This report is available only through NTIS (see address given above).
- NCEER-87-0005 "A Finite Element Formulation for Nonlinear Viscoplastic Material Using a Q Model," by O. Gyebi and G. Dasgupta, 11/2/87, (PB88-213764/AS).
- NCEER-87-0006 "Symbolic Manipulation Program (SMP) - Algebraic Codes for Two and Three Dimensional Finite Element Formulations," by X. Lee and G. Dasgupta, 11/9/87, (PB88-219522/AS).
- NCEER-87-0007 "Instantaneous Optimal Control Laws for Tall Buildings Under Seismic Excitations," by J.N. Yang, A. Akbarpour and P. Ghaemmaghani, 6/10/87, (PB88-134333/AS).
- NCEER-87-0008 "IDARC: Inelastic Damage Analysis of Reinforced Concrete Frame - Shear-Wall Structures," by Y.J. Park, A.M. Reinhorn and S.K. Kunath, 7/20/87, (PB88-134325/AS).
- NCEER-87-0009 "Liquefaction Potential for New York State: A Preliminary Report on Sites in Manhattan and Buffalo," by M. Budhu, V. Vijayakumar, R.F. Giese and L. Baumgras, 8/31/87, (PB88-163704/AS). This report is available only through NTIS (see address given above).
- NCEER-87-0010 "Vertical and Torsional Vibration of Foundations in Inhomogeneous Media," by A.S. Veletsos and K.W. Dotson, 6/1/87, (PB88-134291/AS).
- NCEER-87-0011 "Seismic Probabilistic Risk Assessment and Seismic Margins Studies for Nuclear Power Plants," by Howard H.M. Hwang, 6/15/87, (PB88-134267/AS). This report is available only through NTIS (see address given above).
- NCEER-87-0012 "Parametric Studies of Frequency Response of Secondary Systems Under Ground-Acceleration Excitations," by Y. Yong and Y.K. Lin, 6/10/87, (PB88-134309/AS).
- NCEER-87-0013 "Frequency Response of Secondary Systems Under Seismic Excitation," by J.A. HoLung, J. Cai and Y.K. Lin, 7/31/87, (PB88-134317/AS).
- NCEER-87-0014 "Modelling Earthquake Ground Motions in Seismically Active Regions Using Parametric Time Series Methods," by G.W. Ellis and A.S. Cakmak, 8/25/87, (PB88-134283/AS).
- NCEER-87-0015 "Detection and Assessment of Seismic Structural Damage," by E. DiPasquale and A.S. Cakmak, 8/25/87, (PB88-163712/AS).
- NCEER-87-0016 "Pipeline Experiment at Parkfield, California," by J. Isenberg and E. Richardson, 9/15/87, (PB88-163720/AS).

- NCEER-87-0017 "Digital Simulation of Seismic Ground Motion," by M. Shinozuka, G. Deodatis and T. Harada, 8/31/87, (PB88-155197/AS). This report is available only through NTIS (see address given above).
- NCEER-87-0018 "Practical Considerations for Structural Control: System Uncertainty, System Time Delay and Truncation of Small Control Forces," J.N. Yang and A. Akbarpour, 8/10/87, (PB88-163738/AS).
- NCEER-87-0019 "Modal Analysis of Nonclassically Damped Structural Systems Using Canonical Transformation," by J.N. Yang, S. Sarkani and F.X. Long, 9/27/87, (PB88-187851/AS).
- NCEER-87-0020 "A Nonstationary Solution in Random Vibration Theory," by J.R. Red-Horse and P.D. Spanos, 11/3/87, (PB88-163746/AS).
- NCEER-87-0021 "Horizontal Impedances for Radially Inhomogeneous Viscoelastic Soil Layers," by A.S. Veletsos and K.W. Dotson, 10/15/87, (PB88-150859/AS).
- NCEER-87-0022 "Seismic Damage Assessment of Reinforced Concrete Members," by Y.S. Chung, C. Meyer and M. Shinozuka, 10/9/87, (PB88-150867/AS). This report is available only through NTIS (see address given above).
- NCEER-87-0023 "Active Structural Control in Civil Engineering," by T.T. Soong, 11/11/87, (PB88-187778/AS).
- NCEER-87-0024 Vertical and Torsional Impedances for Radially Inhomogeneous Viscoelastic Soil Layers," by K.W. Dotson and A.S. Veletsos, 12/87, (PB88-187786/AS).
- NCEER-87-0025 "Proceedings from the Symposium on Seismic Hazards, Ground Motions, Soil-Liquefaction and Engineering Practice in Eastern North America," October 20-22, 1987, edited by K.H. Jacob, 12/87, (PB88-188115/AS).
- NCEER-87-0026 "Report on the Whittier-Narrows, California, Earthquake of October 1, 1987," by J. Pantelic and A. Reinhorn, 11/87, (PB88-187752/AS). This report is available only through NTIS (see address given above).
- NCEER-87-0027 "Design of a Modular Program for Transient Nonlinear Analysis of Large 3-D Building Structures," by S. Srivastav and J.F. Abel, 12/30/87, (PB88-187950/AS).
- NCEER-87-0028 "Second-Year Program in Research, Education and Technology Transfer," 3/8/88, (PB88-219480/AS).
- NCEER-88-0001 "Workshop on Seismic Computer Analysis and Design of Buildings With Interactive Graphics," by W. McGuire, J.F. Abel and C.H. Conley, 1/18/88, (PB88-187760/AS).
- NCEER-88-0002 "Optimal Control of Nonlinear Flexible Structures," by J.N. Yang, F.X. Long and D. Wong, 1/22/88, (PB88-213772/AS).
- NCEER-88-0003 "Substructuring Techniques in the Time Domain for Primary-Secondary Structural Systems," by G.D. Manolis and G. Juhn, 2/10/88, (PB88-213780/AS).
- NCEER-88-0004 "Iterative Seismic Analysis of Primary-Secondary Systems," by A. Singhal, L.D. Lutes and P.D. Spanos, 2/23/88, (PB88-213798/AS).
- NCEER-88-0005 "Stochastic Finite Element Expansion for Random Media," by P.D. Spanos and R. Ghanem, 3/14/88, (PB88-213806/AS).
- NCEER-88-0006 "Combining Structural Optimization and Structural Control," by F.Y. Cheng and C.P. Pantelides, 1/10/88, (PB88-213814/AS).
- NCEER-88-0007 "Seismic Performance Assessment of Code-Designed Structures," by H.H.-M. Hwang, J.-W. Jaw and H.-J. Shau, 3/20/88, (PB88-219423/AS).



- NCEER-88-0008 "Reliability Analysis of Code-Designed Structures Under Natural Hazards," by H.H.-M. Hwang, H. Ushiba and M. Shinozuka, 2/29/88, (PB88-229471/AS).
- NCEER-88-0009 "Seismic Fragility Analysis of Shear Wall Structures," by J.-W. Jaw and H.H.-M. Hwang, 4/30/88, (PB89-102867/AS).
- NCEER-88-0010 "Base Isolation of a Multi-Story Building Under a Harmonic Ground Motion - A Comparison of Performances of Various Systems," by F.-G. Fan, G. Ahmadi and I.G. Tadjbakhsh, 5/18/88, (PB89-122238/AS).
- NCEER-88-0011 "Seismic Floor Response Spectra for a Combined System by Green's Functions," by F.M. Lavelle, L.A. Bergman and P.D. Spanos, 5/1/88, (PB89-102875/AS).
- NCEER-88-0012 "A New Solution Technique for Randomly Excited Hysteretic Structures," by G.Q. Cai and Y.K. Lin, 5/16/88, (PB89-102883/AS).
- NCEER-88-0013 "A Study of Radiation Damping and Soil-Structure Interaction Effects in the Centrifuge," by K. Weissman, supervised by J.H. Prevost, 5/24/88, (PB89-144703/AS).
- NCEER-88-0014 "Parameter Identification and Implementation of a Kinematic Plasticity Model for Frictional Soils," by J.H. Prevost and D.V. Griffiths, to be published.
- NCEER-88-0015 "Two- and Three- Dimensional Dynamic Finite Element Analyses of the Long Valley Dam," by D.V. Griffiths and J.H. Prevost, 6/17/88, (PB89-144711/AS).
- NCEER-88-0016 "Damage Assessment of Reinforced Concrete Structures in Eastern United States," by A.M. Reinhorn, M.J. Seidel, S.K. Kunnath and Y.J. Park, 6/15/88, (PB89-122220/AS).
- NCEER-88-0017 "Dynamic Compliance of Vertically Loaded Strip Foundations in Multilayered Viscoelastic Soils," by S. Ahmad and A.S.M. Israil, 6/17/88, (PB89-102891/AS).
- NCEER-88-0018 "An Experimental Study of Seismic Structural Response With Added Viscoelastic Dampers," by R.C. Lin, Z. Liang, T.T. Soong and R.H. Zhang, 6/30/88, (PB89-122212/AS).
- NCEER-88-0019 "Experimental Investigation of Primary - Secondary System Interaction," by G.D. Manolis, G. Juhn and A.M. Reinhorn, 5/27/88, (PB89-122204/AS).
- NCEER-88-0020 "A Response Spectrum Approach For Analysis of Nonclassically Damped Structures," by J.N. Yang, S. Sarkani and F.X. Long, 4/22/88, (PB89-102909/AS).
- NCEER-88-0021 "Seismic Interaction of Structures and Soils: Stochastic Approach," by A.S. Veletsos and A.M. Prasad, 7/21/88, (PB89-122196/AS).
- NCEER-88-0022 "Identification of the Serviceability Limit State and Detection of Seismic Structural Damage," by E. DiPasquale and A.S. Cakmak, 6/15/88, (PB89-122188/AS).
- NCEER-88-0023 "Multi-Hazard Risk Analysis: Case of a Simple Offshore Structure," by B.K. Bhartia and E.H. Vanmarcke, 7/21/88, (PB89-145213/AS).
- NCEER-88-0024 "Automated Seismic Design of Reinforced Concrete Buildings," by Y.S. Chung, C. Meyer and M. Shinozuka, 7/5/88, (PB89-122170/AS).
- NCEER-88-0025 "Experimental Study of Active Control of MDOF Structures Under Seismic Excitations," by L.L. Chung, R.C. Lin, T.T. Soong and A.M. Reinhorn, 7/10/88, (PB89-122600/AS).
- NCEER-88-0026 "Earthquake Simulation Tests of a Low-Rise Metal Structure," by J.S. Hwang, K.C. Chang, G.C. Lee and R.L. Ketter, 8/1/88, (PB89-102917/AS).
- NCEER-88-0027 "Systems Study of Urban Response and Reconstruction Due to Catastrophic Earthquakes," by F. Kozin and H.K. Zhou, 9/22/88.

- NCEER-88-0028 "Seismic Fragility Analysis of Plane Frame Structures," by H.H.-M. Hwang and Y.K. Low, 7/31/88, (PB89-131445/AS).
- NCEER-88-0029 "Response Analysis of Stochastic Structures," by A. Kardara, C. Bucher and M. Shinozuka, 9/22/88, (PB89-174429/AS).
- NCEER-88-0030 "Nonnormal Accelerations Due to Yielding in a Primary Structure," by D.C.K. Chen and L.D. Lutes, 9/19/88, (PB89-131437/AS).
- NCEER-88-0031 "Design Approaches for Soil-Structure Interaction," by A.S. Veletsos, A.M. Prasad and Y. Tang, 12/30/88, (PB89-174437/AS).
- NCEER-88-0032 "A Re-evaluation of Design Spectra for Seismic Damage Control," by C.J. Turkstra and A.G. Tallin, 11/7/88, (PB89-145221/AS).
- NCEER-88-0033 "The Behavior and Design of Noncontact Lap Splices Subjected to Repeated Inelastic Tensile Loading," by V.E. Sagan, P. Gergely and R.N. White, 12/8/88, (PB89-163737/AS).
- NCEER-88-0034 "Seismic Response of Pile Foundations," by S.M. Mamoon, P.K. Banerjee and S. Ahmad, 11/1/88, (PB89-145239/AS).
- NCEER-88-0035 "Modeling of R/C Building Structures With Flexible Floor Diaphragms (IDARC2)," by A.M. Reinhorn, S.K. Kunnath and N. Panahshahi, 9/7/88, (PB89-207153/AS).
- NCEER-88-0036 "Solution of the Dam-Reservoir Interaction Problem Using a Combination of FEM, BEM with Particular Integrals, Modal Analysis, and Substructuring," by C.-S. Tsai, G.C. Lee and R.L. Ketter, 12/31/88, (PB89-207146/AS).
- NCEER-88-0037 "Optimal Placement of Actuators for Structural Control," by F.Y. Cheng and C.P. Pantelides, 8/15/88, (PB89-162846/AS).
- NCEER-88-0038 "Teflon Bearings in Aseismic Base Isolation: Experimental Studies and Mathematical Modeling," by A. Mokha, M.C. Constantinou and A.M. Reinhorn, 12/5/88, (PB89-218457/AS).
- NCEER-88-0039 "Seismic Behavior of Flat Slab High-Rise Buildings in the New York City Area," by P. Weidlinger and M. Ettouney, 10/15/88.
- NCEER-88-0040 "Evaluation of the Earthquake Resistance of Existing Buildings in New York City," by P. Weidlinger and M. Ettouney, 10/15/88, to be published.
- NCEER-88-0041 "Small-Scale Modeling Techniques for Reinforced Concrete Structures Subjected to Seismic Loads," by W. Kim, A. El-Attar and R.N. White, 11/22/88, (PB89-189625/AS).
- NCEER-88-0042 "Modeling Strong Ground Motion from Multiple Event Earthquakes," by G.W. Ellis and A.S. Cakmak, 10/15/88, (PB89-174445/AS).
- NCEER-88-0043 "Nonstationary Models of Seismic Ground Acceleration," by M. Grigoriu, S.E. Ruiz and E. Rosenblueth, 7/15/88, (PB89-189617/AS).
- NCEER-88-0044 "SARCF User's Guide: Seismic Analysis of Reinforced Concrete Frames," by Y.S. Chung, C. Meyer and M. Shinozuka, 11/9/88, (PB89-174452/AS).
- NCEER-88-0045 "First Expert Panel Meeting on Disaster Research and Planning," edited by J. Pantelic and J. Stoye, 9/15/88, (PB89-174460/AS).
- NCEER-88-0046 "Preliminary Studies of the Effect of Degrading Infill Walls on the Nonlinear Seismic Response of Steel Frames," by C.Z. Chrysostomou, P. Gergely and J.F. Abel, 12/19/88, (PB89-208383/AS).

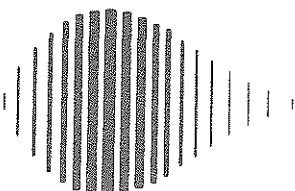
- NCEER-88-0047 "Reinforced Concrete Frame Component Testing Facility - Design, Construction, Instrumentation and Operation," by S.P. Pessiki, C. Conley, T. Bond, P. Gergely and R.N. White, 12/16/88, (PB89-174478/AS).
- NCEER-89-0001 "Effects of Protective Cushion and Soil Compliancy on the Response of Equipment Within a Seismically Excited Building," by J.A. HoLung, 2/16/89, (PB89-207179/AS).
- NCEER-89-0002 "Statistical Evaluation of Response Modification Factors for Reinforced Concrete Structures," by H.H-M. Hwang and J-W. Jaw, 2/17/89, (PB89-207187/AS).
- NCEER-89-0003 "Hysteretic Columns Under Random Excitation," by G-Q. Cai and Y.K. Lin, 1/9/89, (PB89-196513/AS).
- NCEER-89-0004 "Experimental Study of 'Elephant Foot Bulge' Instability of Thin-Walled Metal Tanks," by Z-H. Jia and R.L. Ketter, 2/22/89, (PB89-207195/AS).
- NCEER-89-0005 "Experiment on Performance of Buried Pipelines Across San Andreas Fault," by J. Isenberg, E. Richardson and T.D. O'Rourke, 3/10/89, (PB89-218440/AS).
- NCEER-89-0006 "A Knowledge-Based Approach to Structural Design of Earthquake-Resistant Buildings," by M. Subramani, P. Gergely, C.H. Conley, J.F. Abel and A.H. Zaghw, 1/15/89, (PB89-218465/AS).
- NCEER-89-0007 "Liquefaction Hazards and Their Effects on Buried Pipelines," by T.D. O'Rourke and P.A. Lane, 2/1/89, (PB89-218481).
- NCEER-89-0008 "Fundamentals of System Identification in Structural Dynamics," by H. Imai, C-B. Yun, O. Maruyama and M. Shinozuka, 1/26/89, (PB89-207211/AS).
- NCEER-89-0009 "Effects of the 1985 Michoacan Earthquake on Water Systems and Other Buried Lifelines in Mexico," by A.G. Ayala and M.J. O'Rourke, 3/8/89, (PB89-207229/AS).
- NCEER-89-R010 "NCEER Bibliography of Earthquake Education Materials," by K.E.K. Ross, 3/10/89, (PB90-109901/AS).
- NCEER-89-0011 "Inelastic Three-Dimensional Response Analysis of Reinforced Concrete Building Structures (IDARC-3D), Part I - Modeling," by S.K. Kunnath and A.M. Reinhorn, 4/17/89, (PB90-114612/AS).
- NCEER-89-0012 "Recommended Modifications to ATC-14," by C.D. Poland and J.O. Malley, 4/12/89.
- NCEER-89-0013 "Repair and Strengthening of Beam-to-Column Connections Subjected to Earthquake Loading," by M. Corazao and A.J. Durrani, 2/28/89, (PB90-109885/AS).
- NCEER-89-0014 "Program EXKAL2 for Identification of Structural Dynamic Systems," by O. Maruyama, C-B. Yun, M. Hoshiya and M. Shinozuka, 5/19/89, (PB90-109877/AS).
- NCEER-89-0015 "Response of Frames With Bolted Semi-Rigid Connections, Part I - Experimental Study and Analytical Predictions," by P.J. DiCorso, A.M. Reinhorn, J.R. Dickerson, J.B. Radzinski and W.L. Harper, 6/1/89, to be published.
- NCEER-89-0016 "ARMA Monte Carlo Simulation in Probabilistic Structural Analysis," by P.D. Spanos and M.P. Mignolet, 7/10/89, (PB90-109893/AS).
- NCEER-89-0017 "Preliminary Proceedings of the Conference on Disaster Preparedness - The Place of Earthquake Education in Our Schools, July 9-11, 1989," 6/23/89, (PB90-108606/AS).
- NCEER-89-0018 "Multidimensional Models of Hysteretic Material Behavior for Vibration Analysis of Shape Memory Energy Absorbing Devices, by E.J. Graesser and F.A. Cozzarelli, 6/7/89.

- NCEER-89-0019 "Nonlinear Dynamic Analysis of Three-Dimensional Base Isolated Structures (3D-BASIS)," by S. Nagarajaiah, A.M. Reinhorn and M.C. Constantinou, 8/3/89.
- NCEER-89-0020 "Structural Control Considering Time-Rate of Control Forces and Control Rate Constraints," by F.Y. Cheng and C.P. Pantelides, 8/3/89.
- NCEER-89-0021 "Subsurface Conditions of Memphis and Shelby County," by K.W. Ng, T-S. Chang and H-H.M. Hwang, 7/26/89.
- NCEER-89-0022 "Seismic Wave Propagation Effects on Straight Jointed Buried Pipelines," by K. Elhmadi and M.J. O'Rourke, 8/24/89.
- NCEER-89-0023 "Workshop on Serviceability Analysis of Water Delivery Systems," edited by M. Grigoriu, 3/6/89.
- NCEER-89-0024 "Shaking Table Study of a 1/5 Scale Steel Frame Composed of Tapered Members," by K.C. Chang, J.S. Hwang and G.C. Lee, 9/18/89.
- NCEER-89-0025 "DYNA1D: A Computer Program for Nonlinear Seismic Site Response Analysis - Technical Documentation," by Jean H. Prevost, 9/14/89.
- NCEER-89-0026 "1:4 Scale Model Studies of Active Tendon Systems and Active Mass Dampers for Aseismic Protection," by A.M. Reinhorn, T.T. Soong, R.C. Lin, Y.P. Yang, Y. Fukao, H. Abe and M. Nakai, 9/15/89, to be published.
- NCEER-89-0027 "Scattering of Waves by Inclusions in a Nonhomogeneous Elastic Half Space Solved by Boundary Element Methods," by P.K. Hadley, A. Askar and A.S. Cakmak, 6/15/89.
- NCEER-89-0028 "Statistical Evaluation of Deflection Amplification Factors for Reinforced Concrete Structures," by H.H.M. Hwang, J-W. Jaw and A.L. Ch'ng, 8/31/89.
- NCEER-89-0029 "Bedrock Accelerations in Memphis Area Due to Large New Madrid Earthquakes," by H.H.M. Hwang, C.H.S. Chen and G. Yu, 11/7/89.
- NCEER-89-0030 "Seismic Behavior and Response Sensitivity of Secondary Structural Systems," by Y.Q. Chen and T.T. Soong, 10/23/89.
- NCEER-89-0031 "Random Vibration and Reliability Analysis of Primary-Secondary Structural Systems," by Y. Ibrahim, M. Grigoriu and T.T. Soong, 11/10/89.
- NCEER-89-0032 "Proceedings from the Second U.S. - Japan Workshop on Liquefaction, Large Ground Deformation and Their Effects on Lifelines, September 26-29, 1989," Edited by T.D. O'Rourke and M. Hamada, 12/1/89.
- NCEER-89-0033 "Deterministic Model for Seismic Damage Evaluation of Reinforced Concrete Structures," by J.M. Bracci, A.M. Reinhorn, J.B. Mander and S.K. Kunnath, 9/27/89, to be published.
- NCEER-89-0034 "On the Relation Between Local and Global Damage Indices," by E. DiPasquale and A.S. Cakmak, 8/15/89.
- NCEER-89-0035 "Cyclic Undrained Behavior of Nonplastic and Low Plasticity Silts," by A.J. Walker and H.E. Stewart, 7/26/89.









National Center for Earthquake Engineering Research  
State University of New York at Buffalo